STRUCTURAL INVESTIGATION OF THE EVOLUTION, MECHANISM AND ASSEMBLY OF THE FLAGELLAR MOTOR

Josie Liane Ferreira

Imperial College London

Department of Life Sciences

Submitted for the Degree of *Doctor of Philosophy*

April 2019

Copyright declaration

The copyright of this thesis rests with the author. Unless otherwise indicated, its contents are licensed under a Creative Commons Attribution-Non Commercial 4.0 International Licence (CC BY-NC). Under this licence, you may copy and redistribute the material in any medium or format. You may also create and distribute modified versions of the work. This is on the condition that: you credit the author and do not use it, or any derivative works, for a commercial purpose. When reusing or sharing this work, ensure you make the licence terms clear to others by naming the licence and linking to the licence text. Where a work has been adapted, you should indicate that the work has been changed and describe those changes. Please seek permission from the copyright holder for uses of this work that are not included in this licence or permitted under UK Copyright Law.

Declaration of originality

I declare that all work presented in this thesis is entirely my own, under the supervision of Dr Morgan Beeby, unless otherwise stated. All work that was done by colleagues is appropriately highlighted and all published work is appropriately referenced and reprinted with permission.

Abstract

The evolution of molecular machines is fundamental to the development of pathogenesis in bacteria. This drives the adaptation to new lifestyles and the colonisation of novel niches. One such machine is the bacterial flagellum, an extracellular motility device which enables cells to actively seek out favourable environments. The flagellum is a vital virulence factor in many bacteria including the important human pathogen, *Salmonella enterica*. Studying the evolution, mechanism, assembly and regulation of the flagellum will shed light on how modifications in this large molecular machine facilitate life in different environments.

At the base of the flagellum is the flagellar motor, which converts electrochemical potential, via the stator complexes, into torque. Torque is then transmitted up the periplasmic rod to rotate the extracellular hook, and filament. The γ-proteobacterium, *Salmonella*, has a highly dynamic flagellar motor, perfectly poised for encountering different environments. Surprisingly, this gut pathogen has evolved a different mode of swimming and an environmental niche which is distinct from its close aquatic relatives. Here, using a combination of techniques, I studied the flagellar motor *in situ* and show that *Salmonella's* motor is not native but is a β-proteobacterial motor acquired from an ancestor of *Bordetella*. This new, adaptive motor may have provided a selective advantage to enable *Salmonella's* enteropathogenic lifestyle. Interestingly, the non-enteric, γ-proteobacteria that retained native γ-motors, swim faster than *Salmonella* but fare poorly in low nutrient environments. I show that these bacteria have a distinct mechanism for down regulation of motility, for entry into a sessile state. These cells eject their flagella in nutrient limited environments and actively plug the partial structure that is left behind in the outer membrane. I next work towards providing a more detailed understanding of the dynamic mechanism of stator complex incorporation, and finally, provide a novel mechanism for the regulation of rod length. Together, enabled by recent technological advances in the field of electron cryotomography, this work provides insight into some of the fundamental outstanding questions into the evolution, mechanism and regulation of the flagellum.

Dedicated to Nana, one of the strongest, smartest women that I am lucky to know. Thank you for instilling a desire for knowledge in our family.

Acknowledgments

Firstly, a huge thank you to Morgan. I am grateful for many things including your ability to see the big picture when I got stuck on the details. For your effort to make me not just a good researcher but a good scientist and getting me involved in peer reviewing, supervising and presenting. For your ever optimistic approach and encouragement. I have developed hugely as a person and a scientist over the past few years, much of which is thanks to you, and I am so grateful for the experience.

To the Beeby lab - Teige, Louie, Florian, Eli, Amanda and Bonnie. Thanks for the endless lab meeting discussions, the Lego building, the constant debates and for making so much of my PhD a lot of fun. To Florian, Eli and Julius - thank you for always taking time to help me in the lab and pass on your respective expertise (of which you have so many!).

Thank you to Thomas Meier and Neil Fairweather for your advice throughout my PhD and for giving insight that can only come from speaking to experts outside the field. And to Peter Rosenthal, Kelly Hughes and Fabienne Chevance for offering me your time and wisdom and encouraging me from the start of my PhD when I felt very overwhelmed. And thank you to Tillman Pape for teaching me about microscopes in the most relaxed and fun way and to Paul Simpson for continuing this.

To Mark, Ollie, Marion, Olga, Dan, Nats and Cian – I can't think of a better bunch of people to go through a PhD with. And to Shiv, Xander, Anna, Ram and Beebs. Thank you for making me forget about the lab and making London such fun.

To my extended family and the memory of Mit (who I know would have loved to tinker with our microscopes). Thank you for being a big ball of love, fun, encouragement and inspiration. I hope to one day live up to Mandy's description of me as a "genius of tiny things".

Thank you to my team - mum, dad, Mick and Ali. The best team anyone could ask for. Thank you for always cheering me on so loudly and for all the long, tight hugs. Having a strong, happy foundation of love to go home to after tough weeks makes everything easier. You are four incredible people.

And finally, thank you to my Rahim. Thank you for listening to all the ups and downs and always managing to make me laugh at the end of it. You've been such a huge, wonderful part of this journey.

Table of Contents

Copyright declaration....2
Declaration of originality....2
Abstract....3
Acknowledgments....5
List of Figures....11
Abbreviations....14
Chapter 1 Introduction....15
1.1 The bacterial flagellum....16
1.1.1 Structure, regulation and assembly....17
1.1.2 Mechanism of rotation....19
1.1.3 The flagellum for swimming....22
1.1.4 The flagellum in *Salmonella* pathogenesis....23
1.1.5 Studying the flagellum *in situ*....26
1.2 Introduction to Single Particle Analysis and Electron Cryotomography....26
1.2.1 The tomographic "missing wedge"....29
1.2.2 Hardware and theory....30
1.2.2a The electron gun, mean free path, scattering and dose....30
1.2.2b Electron lenses, the CTF and defocus....32
1.2.2c Gaining contrast: Apertures and energy filters....33
1.2.2d Image detection: Direct Detector Devices, magnification and Nyquist frequency....35
1.2.3 Data collection....37
1.2.3a Automated data collection....37
1.2.3b Tilt increment....37
1.2.3c Tilt scheme....38
1.2.4 Data processing....39
1.2.4a Preprocessing: Motion correction, CTF-correction and exposure filtering....39
1.2.4b Tilt-series alignment....41
1.2.4c Tomogram reconstruction....42
1.2.4d Sub-tomogram averaging....43
1.2.4e Resolution determination: Fourier Shell Correlation....43
1.3 Using ECT to study the *Salmonella* flagellar motor....44
1.4 Thesis overview....45
Chapter 2 Acquisition of the enteric flagellar motor by an ancestor of *Salmonella*....48
2.1 Chapter Summary....48
2.2 Introduction....49
2.2.1 Differences between the enterics and other γ-proteobacteria....49
2.2.1a Type and placement of flagella....49
2.2.1b Swimming behaviour....50
2.2.1c Motor structure....51
2.2.2 What makes the enteric bacteria different?....52
2.2.3 The β-proteobacteria....53
2.2.4 Spotlight on technique: Phylogenetic analysis....55

2.3 Results 57
2.3.1 Phylogenetic studies towards understanding the Horizontal Gene Transfer 57
2.3.2 Genetic context substantiates horizontal gene transfer 58
2.3.3 Structural investigations of the horizontal gene transfer 65
2.3.3a Subtomogram average of the "donor" bacterial motor 65
2.3.3b Subtomogram average of the "acceptor" bacterial motors 68
2.3.4 Structural comparisons of the *Bordetella* and *Plesiomonas* flagellar motors with the *Salmonella* flagellar motor 72
2.4 Discussion 74
2.4.1 *Salmonella* traded two highly specialised motors for one more general motor 75
2.4.2 Could the new flagellar motor have enabled colonisation of the gastrointestinal tract? 77
2.4.3 Why doesn't the *Plesiomonas shigelloides* lateral motor have a clear C-ring? 78
2.4.4 What is the extra density in both of the *Plesiomonas* FlhAs? 79
2.5 Materials and methods 81
2.5.1 Bacterial growth 81
2.5.2 Phylogenetic analysis 81
2.5.3 Negative stain grid preparation 82
2.5.4 Negative stain EM imaging 82
2.5.5 Cryo-grid preparation 82
2.5.6 Tilt-series collection 82
2.5.7 Tomogram reconstruction 83
2.5.8 Subtomogram averaging 83
2.5.9 Δ*fliC* strain construction 83
Chapter 3 The switch to a sessile state: deactivation of the bacterial flagellum under nutrient depletion 85
3.1 Chapter Summary 85
3.2 Introduction 86
3.2.1 Motility in the γ-proteobacteria 86
3.2.2 Transition from motile to sessile states 88
3.3 Results 89
3.3.1 γ-proteobacteria swim slower at increasing cell densities 89
3.3.2 Decrease in swimming speed coincides with loss in flagella 90
3.3.3 γ-proteobacteria eject flagella at the base of the distal rod 91
3.3.4 Ejected flagella leave behind a relic of a former motor which remains in the outer membrane of old poles 93
3.3.5 Flagellar ejection is widespread in the γ-proteobacteria 95
3.3.6 Flagellar ejection and rebuilding occurs in bacteria with only a single polar flagellum 97
3.3.7 Relics show differences between sheathed and unsheathed filaments 97
3.3.8 Subtomogram averaging reveals novel plug in relic structure 97
3.3.9 Relics can be purified by a MotX (T-ring) affinity purification 99
3.3.10 Revealing the protein that makes up the plug density 101
3.3.11 Confirmation that structures are relics and not assembly intermediates 101

3.3.12 Ejection "caught in the act" reveals immediate appearance of the plug density and break-point of ejection 102
3.3.13 Relics are no longer connected to the inner membrane 103
3.3.14 Relic and flagellar genes are interspersed in the same operon 104
3.3.15 Placement of motors and relics is not random and suggests a common placement mechanism 104
3.3.16 Flagellar ejection is not caused by mechanical breakage or mechanosensing 106
3.3.17 Ejection occurs in response to nutrient depletion 107
3.3.18 Ejection mechanism is distinct from *Caulobacter crescentus* 109
3.3.19 Precursor and relic structures enable a model for assembly and ejection of the γ-proteobacterial flagellum to be proposed 111
3.4 Discussion 113
3.4.1 Structures are relics and not assembly intermediates 113
3.4.2 The appearance of a plug density suggests a specific cellular response 114
3.4.3 Evolution is a "tinkerer" 115
3.4.4 An active mechanism of flagellar ejection 116
3.4.5 Possible selective benefit of flagellar ejection 116
3.4.6 Potential applications and future work 117
3.5 Materials and methods 118
3.5.1 Cell Growth 118
3.5.2 Swimming Speed Videos 119
3.5.3 Negative stain EM 119
3.5.4 Purification of relics 120
3.5.5 2D classification of relic particles 120
3.5.6 PEG precipitation to recover ejected flagella 120
3.5.7 SDS-PAGE gel electrophoresis of recovered flagella 121
3.5.8 Mean number of flagella in a population 121
3.5.9 Electron Cryo-Tomography Sample Preparation 121
3.5.10 ECT Data Acquisition 122
3.5.11 Tomogram reconstruction 122
3.5.12 Subtomogram Averaging 123
3.5.13 Segmentation 123
3.5.14 Periplasmic distance measurements 123
3.5.15 Clark-Evans distribution analysis 124
3.5.16 Nutrient depletion assay 124
3.5.17 Minimal medium assay 124
3.5.18 Strain construction 124
3.5.19 Motility plates 125
3.5.20 cdiGMP over-expression 125
Chapter 4 Mechanism of rotation: Structural studies of the flagellar stator complexes 126
4.1 Chapter Summary 126
4.2 Introduction 127
4.2.1 The stator complexes 127
4.2.2 Experimental approaches to probe stator complex dynamics 128
4.2.3 Visualising the stator complexes *in situ* 132
4.2.4 The enigmatic protein, FliL 132

4.3 Results 134
4.3.1 Towards visualising the stator complexes in *Salmonella in situ* 134
4.3.1a Ensuring sufficient building blocks 134
4.3.1b Mimicking a high-load environment 136
4.3.1c Imaging the *Salmonella* stators *in situ* 136
4.3.2 Towards a high resolution structure of the stator complex 142
4.3.3 Cryo-EM analysis of $MotA_4B_2$ 144
4.4 Discussion 146
4.4.1 Direct visualisation of the dynamic nature of the stator complexes 146
4.4.2 So, how many stator complexes are there in the *Salmonella* flagellar motor? 146
4.4.3 Importance of visualising stator complexes *in situ* 147
4.4.4 Next steps for *in situ* visualisation 147
4.4.5 Future for single particle analysis studies 148
4.5 Materials and methods 149
4.5.1 Bacterial growth 149
4.5.2 Mini-cell purification 149
4.5.3 Negative stain grid preparation 150
4.5.4 Negative stain EM imaging 150
4.5.5 FliC bivalent antibody tethering 150
4.5.6 Cryo-grid preparation 150
4.5.7 Tilt-series collection 151
4.5.8 Tomogram reconstruction 151
4.5.9 2D-classification 151
4.5.10 Δ*fabH* and Δ*motAB* strain construction 151
4.5. 11 FliL plasmid construction 152
4.5.12 MotAB plasmid construction 152
4.5.13 Protein purification (adapted from protocol from the Blair lab) 152
4.5.14 SDS-PAGE electrophoresis 154
4.5.15 Western blot analysis 154
Chapter 5 Assembly of the flagellar rod and broader implications of periplasmic architecture 155
5.1 Chapter Summary 155
5.2 Introduction 157
5.2.1 Flagellar assembly within the context of the cell envelope 157
5.2.2 Length control of the flagellar rod 159
5.2.3 Braun's lipoprotein 161
5.2.4 Rcs stress response 162
5.2.5 Other periplasm spanning complexes 162
5.3 Results 164
5.3.1 FlgG* polyrods do not interact with the outer membrane 164
5.3.2 Lpp provides membrane stability in *Salmonella* 166
5.3.3 Length of LppA dictates periplasmic distance in *Salmonella* 166
5.3.4 Periplasmic distance controls rod length 170
5.3.5 Altering the length of the flagellar rod affects *Salmonella* motility 171
5.3.6 LppA maintains outer membrane stability in *E. coli* 172
5.3.7 Instability of outer membrane results in impaired Rcs network activity 174

5.3.8 Constitutive Rcs response in Δ*mdoG* cells is due to a decreased periplasmic width 174
5.3.9 Length of Lpp dictates periplasmic distance in *E. coli* 175
5.3.10 Increasing the periplasmic distance inhibits activation of Rcs network in response to stress 177
5.3.11 Increased periplasmic distance can be compensated for by increasing RcsF linker length 178
5.3.12 Lpp acts as both a tether and a column 178
5.4 Discussion 181
5.4.1 Flagellar length control 181
5.4.2 Rcs response 183
5.4.3 Role of Lpp 185
5.4.4 Gram-negative cells without Lpp 185
5.4.5 Relevance to other systems and future work 185
5.5 Materials and Methods 187
5.5.1 Strain growth 187
5.5.2 Cryo-EM data collection 188
5.5.3 Membrane measurements 188
5.5.4 Construction of *lpp* length mutants (Performed by Eli Cohen and Abir Asmar) 188
5.5.5 Construction of the *lpp*ΔK58 mutant (Performed by Abir Asmar) 189
5.5.6 Construction of RcsF+7 (Performed by Abir Asmar) 189
5.5.7 β-Galactosidase assay (Performed by Abir Asmar) 189
5.5.8 Swimming and Swarming Motility Assays (Performed by Eli Cohen) 190
5.5.9 Isolation, Transmission Electron Microscopy and Measurement of Flagellar Structures (Performed by Eli Cohen) 190
Chapter 6 Summary and recent developments 191
6.1 Thesis summary 191
6.2 Developments in ECT which would benefit this work 195
6.2.1 FIB-milling 195
6.2.2 Phase plates 196
6.2.3 Continuous tilt-series collection 196
References 198
Appendix 1: Custom script for periplasmic width 217
Appendix 2: Permissions to reprint figures 219

List of Figures

Fig. 1.1: The bacterial flagellum. 16
Fig. 1.2: The assembly of the *Salmonella* flagellum. 21
Fig. 1.3: *Salmonella's* type three secretion systems. 25
Fig. 1.4: ECT overview. 28
Fig. 1.5: Missing wedge. 29
Fig. 1.6: The electron microscope. 31
Fig. 1.7: The Contrast Transfer function and envelope function. 34
Fig. 1.8: Tilt schemes. 39
Fig. 1.9: CTF correction. 40
Fig. 1.10: Back-projection for tomographic reconstruction. 42
Fig. 1.11: Methods to make cells smaller for ECT. 45
Fig 2.1: Placement of flagella in the enterics is different from other γ-proteobacteria. 50
Fig. 2.2: The swimming trajectory of γ-proteobacteria. 51
Fig 2.3: A collection of γ-proteobacterial flagellar motor structures. 52
Fig 2.4: Enteric γ-proteobacteria have a β-proteobacterial flagellum. 54
Fig. 2.5: Taxonomic tree of β- and γ-proteobacteria. 59
Fig. 2.6: Tree showing flagellar phylogeny. 60
Fig. 2.7: Schematic of horizontal gene transfer. 61
Fig. 2.8: Unrooted phylogenetic trees of individual flagellar proteins are congruent with overall flagellar tree. 63
Fig. 2.9: Unrooted C-ring protein phylogeny is not congruent with overall flagellar tree. 64
Fig. 2.10: Chromosomal context of flagellar genes supports HGT. 65
Fig 2.11: Optimisation of sample for collection of *Bordetella bronchiseptica* motor. 66
Fig 2.12: The structure of the *Bordetella bronchiseptica* flagellar motor. 67
Fig 2.13: Optimisation of sample for collection of *Plesiomonas shigelloides* lateral flagellar motor. 68
Fig 2.14: The structure of the *Plesiomonas shigelloides* lateral flagellar motor. 70
Fig 2.15: The structure of the *Plesiomonas shigelloides* polar flagellar motor. 71
Fig 2.16: The β-like motor has dynamic stator complexes. 73
Fig. 2.17: The *Salmonella* flagellar motor is structurally similar to the *Bordetella* motor. 74
Fig. 2.18: *Salmonella* swapped two specialised flagellar motors for one more general motor. 76
Fig. 2.19: Extra density in *Plesiomonas* FlhA is also seen in the SPI-1 injectisome homologue. 80
Fig. 3.1: The non-enteric γ-proteobacteria have polar Na+-driven flagella. 87
Fig 3.2. γ-proteobacteria with N+-driven polar flagellar motors swim slower at later growth stages. 89
Fig 3.3. Decrease in swimming speed at later growth stages is due to loss of flagella. 91
Fig 3.4: Ejected flagella with hooks accumulate in the supernatant of late growth stage *P. shigelloides*. 92
Fig. 3.5: Partial flagella structures appear alongside full flagella. 93
Fig. 3.6: *P. shigelloides* cells lysed prior to imaging show multiple relic structures at the pole. 94

Fig 3.7: Relics of old flagella are seen at the poles of widespread γ-proteobacteria. 96
Fig 3.8: Subtomogram averages of intact flagella and relic highlights novel plug protein. 98
Fig. 3.9: Analysis of sub-tomogram averages. 99
Fig 3.10: Relic structures are made of flagellar proteins and can be pulled-down and visualised by negative stain EM. 100
Fig 3.11: Partial flagella motors are not assembly intermediates. 102
Fig 3.12: Ejection "caught in the act". 103
Fig 3.13: Relic structures are not attached to the inner membrane. 104
Fig 3.14: Relic genes are interspersed with core flagella genes in the same operon. 104
Fig 3.15: Positioning of relic and flagella is the same, suggesting a common placement mechanism. 106
Fig 3.16: Ejection of flagella does not require a flagellar filament. 107
Fig 3.17: Ejection is triggered by nutrient depletion. 110
Fig 3.18: Ejection in γ-proteobacteria is not triggered by the same mechanism as *Caulobacter crescentus*. 111
Fig 3.19: Multiple assembly intermediates provide the basis for a model of flagellar ejection. 112
Fig 4.1: Structural analysis of the stator complex 128
Fig. 4.2: Studying the dynamics of the stator complex 130
Fig. 4.3: The stator complexes are not seen in subtomogram averages of *Salmonella*. 131
Fig. 4.4: FliL forms a ring within the stator complexes 133
Fig. 4.5: Overexpression of MotAB and FliL. 135
Fig. 4.6: Tethering flagellar filaments with a bivalent antibody sticks filaments together. .. 137
Fig. 4.7: Constructed strain has a low yield of motors per tomogram. 138
Fig. 4.8: Tethering filaments to increase load recruits stator complexes 139
Fig. 4.9: FabH deletion limits cell size. 140
Fig. 4.10: Schematic showing final strain for imaging. 141
Fig. 4.11: Data collection of final strain. 141
Fig. 4.12: Assessing purified MotAB from a collaborator by negative stain EM. 142
Fig. 4.13: Assessing purified MotAB-MBP from a collaborator by negative stain 2D class averaging. 143
Fig. 4.14: Assessing MotAB-MBP purified in-house by negative stain 2D class averaging. 144
Fig. 4.15: Cryo-EM analysis of the stator complex. 145
Fig. 5.1: The Gram-negative cell envelope 158
Fig. 5.2: Δ*lppA* rescues motility in FlgG* mutants 160
Fig. 5.3: The structure of Braun's lipoprotein (Lpp). 161
Fig. 5.4: Rcs stress response network. 163
Fig. 5.5: FlgG* mutants produce long rods *in situ.* 165
Fig. 5.6: LppAB maintains outer membrane integrity in *Salmonella* by tethering it to peptidoglycan. 167
Fig 5.7: Periplasmic integrity is lost in *lpp* deletion strains but not in *lpp* length variants 168
Fig 5.8: The periplasmic distance changes with LppA length variants in *Salmonella.* 169
Fig. 5.9: Periplasmic distance within an individual cell is tightly controlled 170
Fig. 5.10: Rod length is altered by periplasmic distance. 171
Fig. 5.11: Altering the length of the rod affects *Salmonella* motility. 172
Fig. 5.12: Lpp is involved in membrane maintenance in *E. coli*. 173
Fig. 5.13: Lpp must be linked to peptidoglycan for Rcs network to function. 175

Fig. 5.14: *lpp* length dictates periplasmic distance in *E. coli*. 176
Fig. 5.15: Increased periplasmic distance inhibits the Rcs response to stress. 177
Fig. 5.16: Extending the RcsF linker compensates for increased periplasmic distance. 179
Fig. 5.17: Lpp acts as both a tether and a support column.....180
Fig. 5.18: Model for flagellar rod length control in *Salmonella*.....182
Fig. 5.19: Model for control of Rcs response by periplasmic width.....184

Abbreviations

PMF: Proton Motive Force

HBB: Hook-basal-body

SPI: Salmonella Pathogenicity Island

T3SS: Type Three Secretion System

TLR5: Toll-like Receptor 5

SCV: *Salmonella* Containing Vacuole

HGT: Horizontal Gene Transfer

EM: Electron Microscopy

SPA: Single Particle Analysis

ECT: Electron Cryo-Tomography

STA: Subtomogram Averaging

SNR: Signal to noise ratio

CTF: Contrast Transfer Function

FEG: Field Emission Gun

DDD: Direct Detection Device

MAP: Monolithic Active Pixel

CMOS: Complementary Metal–oxide–semiconductor

WBP: Weighted back-projection

SIRT: Simultaneous Iterative Reconstruction Technique

FSC: Fourier Shell Correlation

MSA: Multiple Sequence Alignment

ML: Maximum Likelihood

FSA: Fast Statistical Alignment

cdG: Cyclic di-Guanylate Monophosphate

LC-MS: Liquid chromatography–mass spectrometry

CW: Clockwise

CCW: Counter clockwise

Rcs: Regulation of capsular synthesis

EMDB: Electron microscopy Database

PDB: Protein Database

Chapter 1

Introduction

The acquisition and evolution of molecular machines is fundamental to the development of pathogenesis in bacteria. This drives the adaptation to new lifestyles and the colonisation of novel niches. The acquisition of a motility device provides clear selective advantages. When nutrients become scarce, motile cells can move on to nutrient rich environments and proliferate, rather than remaining to compete for limited resources. If this is coupled to a system that detects and responds to environmental signals, a sophisticated lifestyle where cells can actively search for ideal environments or sites of infection and avoid unfavourable ones, is enabled. The swimming of a microbe however, is constrained within specific physical boundaries.

Bacteria and other microbes live in a low Reynolds number world, where momentum is insignificant due to the overwhelming viscous drag of the fluid [1,2]. This means that repetitive motion results in zero net movement, regardless of relative speed. A clam which swims on the macroscale by slowly opening its shell and then quickly shutting it, in the microscale would only repetitively move forward and backward in place. Due to the lack of momentum, as soon as a force is removed, cells of this size stop moving. A non-reciprocal form of motion is therefore required by organisms on this scale [1]. Although multiple methods of bacterial motility have been described including twitching using a type IV pilus "grappling hook" [3] or gliding [4], the most common and best studied device for bacterial motility is the bacterial flagellum, used by about two-thirds of motile bacteria [5].

Relevant publication: Ferreira JL, Matthews-Palmer TRS, Beeby M. Electron Cryo-Tomography. Cellular Imaging. Springer, Cham; 2018. pp. 61–94. [6]

1.1 The bacterial flagellum

The bacterial flagellum is an intricate molecular machine, self-assembled from over 20 unique structural proteins. These proteins have a wide range of copy numbers, from one up to tens of thousands. ~90% of flagellar protein makes up the rigid flagellar filament and motility is driven via its rotation, exerting thrust for propulsion [7]. At the base of the flagellum is a rotary motor made up of a rotor, which rotates with respect to the cell membranes, and a set of stator complexes. A rod, acting as an axial driveshaft, connects the motor to the flexible extra-cellular hook, or universal joint, which in turn is connected to the flagellar filament.

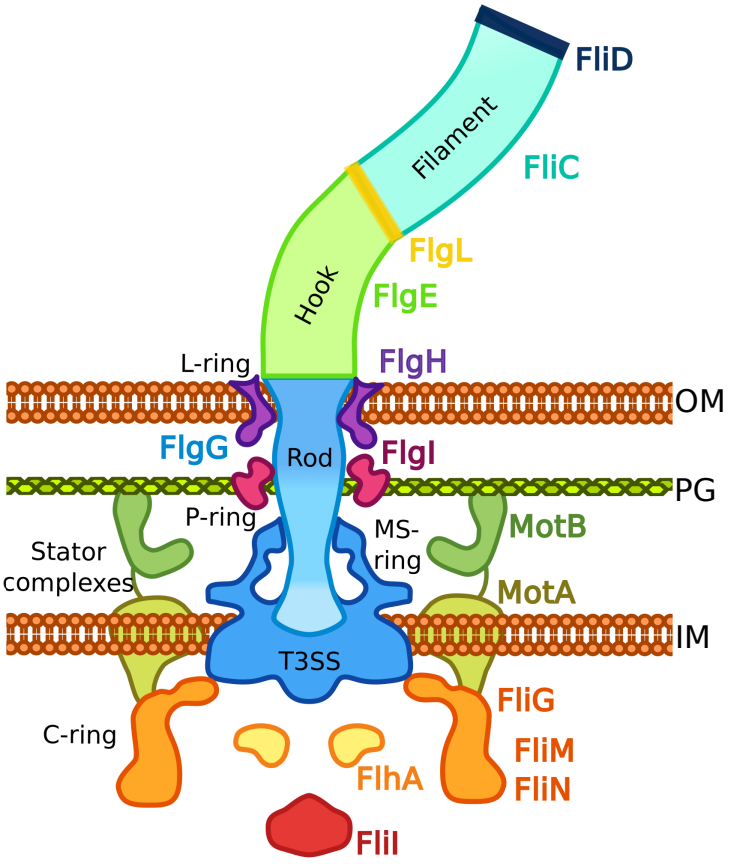


Fig. 1.1: The bacterial flagellum.
The bacterial flagellum is a self-assembled molecular machine made of multiple proteins. The structural proteins names are coloured to match their relative structures. OM = outer membrane, PG = peptidoglycan, IM = inner membrane.

1.1.1 Structure, regulation and assembly

The sequential, orchestrated expression from ~50 genes [8,9] culminates in the self-assembly of a complex molecular machine which reaches from the cytoplasm to multiple microns beyond the cell body, often multiple times the length of the bacterial cell. The flagellum can be structurally divided into two components, the basal body (composed of the flagellar rotor, and set of stator complexes) and the extracellular components (made primarily of the hook and filament) (Fig. 1.1). Of the ~50 genes, about half code for structural flagellar proteins and the rest are involved in the detection of environmental factors and regulation of assembly. The importance of motility and complexity of the flagellar motor means that an intricate set of regulators control all aspects of flagellar biogenesis from tight temporal, hierarchical control of protein expression to regulation of self-assembly including specific localisation, spacing, and length control. The assembly process is divided into three stages: early, middle, and late with three classes of genes (1, 2, and 3 respectively) (Fig. 1.2).

Early (Class 1 genes): Initiation

The only class 1 genes encode the master regulator of flagellar assembly. In response to environmental factors and point in the cell cycle [10], FlhC and FlhD are expressed and the $FlhD_4C_2$ complex is assembled. This recruits RNA polymerase (RNAP) and $\sigma 70$ to drive the translation of class 2 genes (Fig. 1.2).

Middle (Class 2 genes): Basal body and hook assembly

Class 2 genes code for structural components of the basal body and hook as well as regulators of class 3 genes held inactive by chaperones (FliA:FlgM, FliD:FliT) [11].

The self-assembly centres around a type three secretion system (T3SS) embedded in the inner membrane. The T3SS, the mechanistic core of which is made up of five conserved proteins (FlhA, FlhB, FliP, FliQ and FliR), coordinates secretion and assembly

by playing roles in both substrate-specificity, and the energisation of secretion. All five proteins are essential for secretion [12] and are conserved not only within flagella but also in the injectisomes (a family of needle-like structures for secretion of effector proteins, self-assembled via a T3SS). Proteins are secreted through a ~2nm channel in the growing flagellar structure [13] and substrates therefore need to pass through the narrow channel unfolded or partially folded [14]. Both the proton motive force (PMF), which may act via a proton pore in the TM-domain of FlhA [15,16], and ATP-hydrolysis via an associated ATPase in the cytoplasm, are utilised for energising the secretion of substrates. It is thought that only the PMF is essential while the ATPase only enhances secretion efficiency [15,17,18] however, a recent *in vitro* study of reconstituted basal bodies within inner membrane vesicles (no PMF) however, demonstrated that FliI alone, without PMF can drive protein export [19].

The T3SS sits within the MS ring, in the inner membrane, which is made of multiple copies of a single protein, FliF. In the cytoplasm, mounted onto the MS ring is the C-ring, made from a ring of 34 copies of FliG with FliM and FliN built onto it. The C-ring proteins, FliM and FliN, are dynamic and move in and out of tight association with the C-ring. The copy number associated with the C-ring is altered depending on the rotational bias of the motor [20,21] and up to 45 copies of FliM are attached when the motor is rotating counter clockwise (CCW) [22]. The extra copies may act to increase the C-ring diameter [23], however this remains unclear. Within the C-ring sits FliI, a hexameric ATPase as well as other proteins homologous to components of the F/V-type ATPases (FliI homologous to the α/β subunits, FliJ the γ subunit and FliH the b/δ subunits [24–26]).

The axial components are secreted through the export gate. Scaffold proteins cap the growing structure and promote the re-folding and polymerisation of secreted proteins, assembling them into place. This forms the proximal (FlgB, FlgC, FlgF) and distal (FlgG) rod, the hook (FlgE) and the filament (FliC). The P- (peptidoglycan) and L- (lipopolysaccharide) rings assemble around the rod and unlike all other axial components are secreted via the Sec-pathway. A molecular ruler protein, FliK, controls the length of axial components from the basal body, before the switch to filament. Until recently, the

length-control mechanism of the rod, before switching to secreting hook protein was unknown. In Chapter 5, I present results in collaboration with Kelly Hughes' lab where we elucidate this mechanism [27]. After the termination of rod polymerisation the hook is polymerised and FliK measures the correct hook length of ~55nm (±6nm) [28]. When the hook is ~55 nm in length, interaction of the FliK C-terminus with FlhB in the inner membrane leads to a switch to the late stage of flagella assembly (Fig. 1.2).

Late (Class 3 genes): The filament and stator complexes

Class 3 genes encode late stage proteins including the filament protein FliC, the stator complexes and the chemoreceptor proteins. The switch to late stage assembly releases σ28 (FliA) from the chaperone FlgM. FlgM is secreted through the growing filament and σ28 goes on to recruit RNAP to drive expression of class 3 genes. The filament cap FliD is released from FliT and helps to assemble the growing filament on top of the hook-filament junction. FliD forms a pentameric cap on the growing filament [29], helping to fold and polymerise FliC proteins. No length control mechanism is thought to act on the filament, however due to the passive diffusion of filament proteins the length plateaus at about 10 μm [30] (Fig. 1.2).

To provide the motor with torque, a set of ~11 stator complexes in *Salmonella*, (up to ~18 in other bacteria) composed of two proteins, MotA and MotB, assemble around the MS-ring, anchored in the inner membrane and interact with FliG on one end and to the peptidoglycan layer on the other. The association of stator complexes with the *Salmonella* flagellar motor is dynamic and the number of stator complexes assembled on the motor is dependent on the external load applied to the filament. I will explore this in Chapter 4.

1.1.2 Mechanism of rotation

The torque from the motor is generated by the electrostatic interaction between FliG in the rotor and the collection of stator complexes [31]. The stator complexes in *Salmonella*

utilise the proton motive force for energising the conformational change that leads to the rotation of the flagellar rotor. In some bacteria, most notably the marine bacteria genus *Vibrio*, the sodium motive force powers rotation. Motors driven by K^+ ions and divalent cations have also been described [32]. The rotation of the rotor by the stator complexes in turn transmits torque via the rod, to the hook and finally onto the filament which exerts thrust for propulsion. The P- and L- rings act as a bushing, allowing for rotation within the semi-rigid peptidoglycan layer and outer membrane. The C-ring and basal body are thought to rotate together as a FliG-FliF (which form the top of the C-ring and MS ring respectively) fusion motor remains functional [33].

At the centre of powering and initiating the rotation of the motor and eventually the flagellum, are the stator complexes. At present, a comprehensive understanding of the mechanism of action of the stators is hindered by the lack of detailed structural information, however, decades of biochemical and biophysical experiments have led to well-established models. In Chapter 4, I provide a detailed introduction into the stator complexes and present data towards gaining a better structural understanding of the stator complexes both *in situ* and of purified stator complexes. The stator complexes interact with FliG in the C-ring.

The size of the C-ring in flagellar motors differs significantly in different bacterial species. Alteration in the diameter of the C-ring leads to different FliG positioning. If FliG, the ring of proteins interacting with the stator complexes, is positioned further from the central axis of the flagellum, more FliG subunits will be needed to make up a complete ring, leading to more interaction sites for the stator complexes and perhaps a larger maximum number of stator complexes that can bind to the motor. It has been shown that the observed maximum torque of flagella from different species is proportional to that calculated using the radius of the C-ring, the number of stator complexes and the unit force of a single stator complex [34]. An increased C-ring diameter therefore leads to an increased maximum torque of the flagellar motor at high loads and an increased speed of the motor at low loads as the limiting speed of the flagellar motor has been shown to increase with number of bound stators [35].

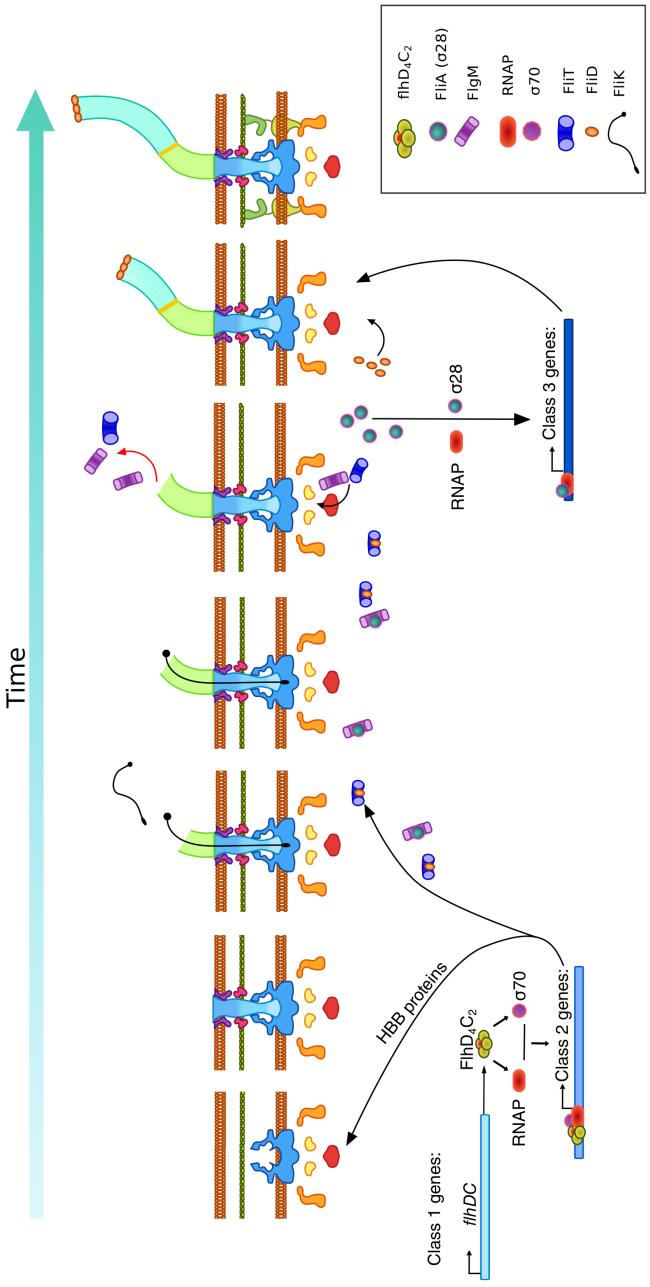


Fig. 1.2: The assembly of the *Salmonella* flagellum.
The assembly of the Salmonella flagellum is controlled by three classes of genes in a hierarchical process. Expression of $FlhD_4C_2$ from class 1 genes, leads to recruitment of RNAP and σ70 for activation of class 2 genes. Class 2 genes encode structural proteins for the hook-basal-body (HBB) as well as late stage genes held inactive by chaperones (FliT:FliD, FlgM:FliA). Once FliK has measured the correct hook-length, the switch to class 3 genes occurs. FlgM and FliT are secreted, releasing FliA to activate class 3 genes, and releasing FliD to cap the growing flagellar filament.

1.1.3 The flagellum for swimming

In *Salmonella* and the other enteric bacteria, where multiple flagella are spaced laterally over the cell ("peritrichous flagella"), motility is achieved by the concerted rotation of multiple flagella forming a coherent bundle. The rotation of the filament by the flagellar motor causes the filament to form a supercoil (helix). The rotation of the flagellar motor is reversible, allowing for alterations in the pattern of swimming. Smooth swimming runs occur when all motors rotate CCW, (when viewed from outside the cell) and the filaments form long pitched helices and assemble into a bundle. Cell tumbling or changes in direction occur when one or more motors rotate clockwise (CW), the filaments form a shorter-pitched helix and the flagellar bundle is displaced. This leads to characteristic chemotactic movement, biased towards moving up favourable gradients or down unfavourable ones [36,37]. A response regulator protein, CheY, is involved in transmitting the chemotactic signal from the chemoreceptors to the flagellar motor, via interactions with the switch component in the C-ring (FliM). Active (phosphorylated) CheY induces a change from CCW to CW via enhanced binding to FliM [38] leading to the dispersal of the flagellar bundle and a change in direction of the cell. The increased number of FliM proteins associated with the C-ring when rotating CCW, may increase sensitivity to CheY [22].

There is a large amount of variation between bacteria with regards to the placement and number of flagella on the cell body. This leads to differences in swimming styles. In bacteria with a single polar filament such as *Caulobacter crescentus,* CW motion of the flagellum thrusts the cell forwards whereas CCW motion pulls the bacterium backwards [39]. Alternatively, in some bacteria, such as *Rhodobacter sphaeroides*, the motor is unidirectional and rather alternates between starts and stops with the filament changing from an extended helix to a tight coil respectively [40]. When stopped, the cell is reoriented by Brownian motion. In the spirochetes, flagellar filaments do not exit the outer membrane but rather sit within the periplasmic space (endo-flagella) wrapping around the cell body. The rotation of the flagella cause the whole cell body to move forward in a cork-screw like motion [41]. The periplasmic flagella make spirochetes motile in viscous liquids that cause

bacteria with external filaments to get stuck [42–45] and even allows for penetration of tissue [46]. This large variation and diversity makes studying the flagellum an attractive system for studying a variety of questions, such as evolution, adaptation and pathogenesis.

1.1.4 The flagellum in *Salmonella* pathogenesis

An important human pathogen which proficiently uses its flagellum for pathogenesis is *Salmonella enterica sv. Typhimurium* (referred to as *S. enterica* or simple *Salmonella* in this thesis). *Salmonella* provides a valuable model system for studying the flagellum. Not only is it genetically tractable allowing us to probe its regulation, assembly, and mechanism but it also uses its flagellum as an effective virulence factor, allowing us to study the use of the bacterial flagellum as a pathogenesis tool. *Salmonella enterica* is a gut pathogen that causes food-borne disease in humans and a wide range of animals. The global burden of food-borne illnesses is substantial and *Salmonella enterica* is responsible for a large proportion of food-borne disease world-wide. Non-typhoidal *Salmonella* is estimated to cause 93.8 million cases of acute gastroenteritis resulting in 155,000 deaths each year, with a third of deaths being in children under 5 years of age. Of these cases, 85% are food-borne [47].

The acquisition of T3SSs played a major role in the evolution of modern day *Salmonella enterica* and may have had a prominent influence on the emergence of its enteropathogenic lifestyle. *Salmonella* acquired three T3SSs from different horizontal gene transfer (HGT) events; two injectisomes, *Salmonella* Pathogenicity Island (SPI) - 1 and SPI-2 [48,49] and a flagellum (Fig. 1.3). Injectisomes act as molecular syringes to export virulence-associated effector proteins into host cells [50,51]. The acquisition of the flagellum will be explored in Chapter 2.

The orchestrated assembly and action of *Salmonella's* three distinct T3SSs is central to its pathogenicity and essential to the establishment of infection [52,53]. *Salmonella* commonly infects its host via contaminated food and travels to the gut. The vertebrate gut is a harsh environment, with mechanical and chemical stresses as well as a

range of specialised symbiotic flora to compete with. At the site of infection, the first T3SS-assembled injectisome, SPI-1 [54] is assembled and required for uptake into the epithelial layer. *Salmonella* cells are engulfed by dendritic cells or Microfold cells. Once inside the lumen of the gut, *Salmonella* can be taken up by multiple different cell types including macrophages and neutrophils. Inside the host cell, *Salmonella* resides in a specialised vacuole, a *Salmonella* Containing Vacuole (SCV). Here, the second injectisome, SPI-2, is expressed [55]. This modulates the host cell, avoiding normal endosomal pathways, evading the host immune system and is essential for establishing systemic infection.

The third *Salmonella* T3SS, the flagellum, is a major virulence factor and plays multiple roles in pathogenesis [53]. Firstly, flagellar motility provides the cells the ability to actively search and respond to their environment. This gives *Salmonella* a huge advantage over non-flagellated cells reliant on Brownian motion or a diffusion-based search. In *Salmonella,* chemotaxis is essential for colitis induction and efficient colonisation of the intestinal epithelium in mice [56]. In conjunction with chemotaxis, *Salmonella* cells use near-surface swimming to target permissive infection sites [57]. Generic physical principles and flagellar motility dynamically entrap cells at surfaces, forcing them into a "scanning mode". This limits a complex 3-dimensional search into a simple 2-dimensional search for particular topological features, such as membrane ruffles, allowing efficient targeting of promising infection sites. Furthermore, the flagellum is a mechanosensor that senses arrival at a desired location, and stimulates swarmer-cell differentiation [58]. The importance of the flagellum is also implicated in attachment, induction of membrane-ruffling and invasion of host cells. Aflagellate *Salmonella* cells show a significant decrease in adherence to host cells, induction of membrane-ruffling and invasion, in human, avian, and murine models [59–61].

The flagellum also plays roles in evading the host immune system or contrarily stimulating it. Uniquely, *Salmonella* can undergo flagellar phase variation, as it encodes two variants of the main filament protein (FliC and FljB) [62,63], proposed to offer an alternative antigenicity, helping evade the host immune system [64]. However, at the site of infection, recognition by the host is important for *Salmonella* infection. It has been

shown that recognition of flagellin by Toll-like receptor 5 (TLR5) on human epithelia leads to the activation of NF-κB and interleukin-8 secretion leading to localised intestinal inflammation [65–67]. This is an important step in pathogenesis as *Salmonella* is unable to colonise murine intestinal epithelial cells in the absence of inflammation, attributed to increased competition from host gut flora [68]. Finally, late in infection the flagellum continues to play an important role in escaping infected cells leading to shedding and the spread of infection to new hosts.

There are still many unanswered questions about how the flagellum is self-assembled, its mechanism of rotation, its regulation and, its acquisition and evolution. *Salmonella* uses its flagellum as a highly effective pathogenicity device. Studying its flagellum is therefore of high importance and could provide fundamental understanding of this fascinating molecular machine.

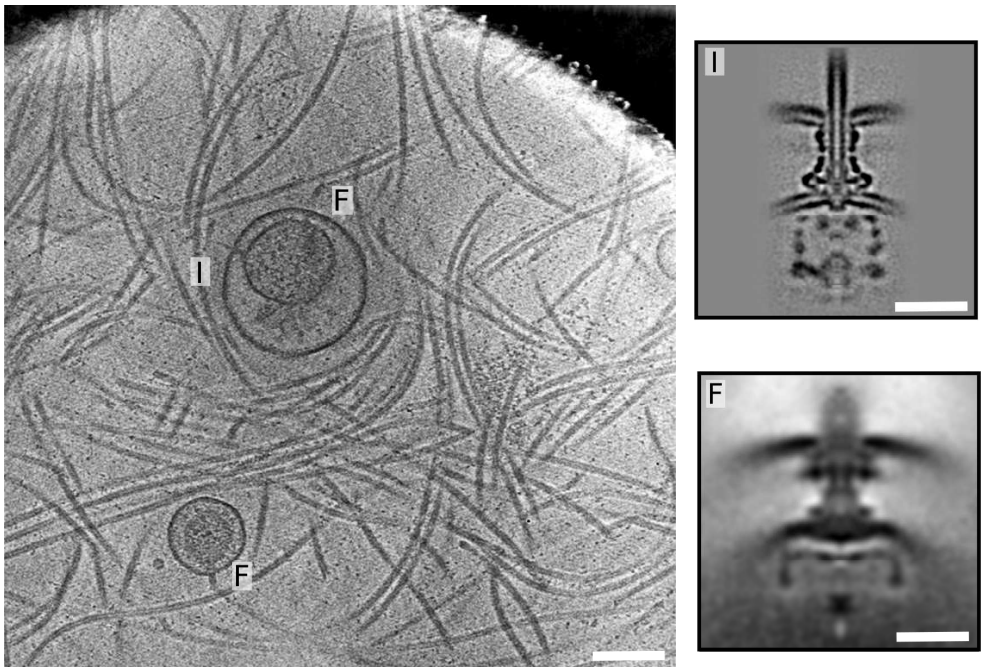


Fig. 1.3: *Salmonella's* type three secretion systems.
A cryo-tomogram of Salmonella cells showing two of its T3SSs, the SPI-1 injectisome labelled "I" and two flagella labelled "F". Scale bar = 200 nm. The boxes on the right are slices through the 3D structures of the injectisome (EMD-8544) and flagellum (EMD-3154) which were created using subtomogram averaging. Scale bar = 25 nm.

1.1.5 Studying the flagellum *in situ*

Studying the flagellar motor *in situ* to nanometre resolutions would provide the largest single leap in our understanding of its assembly and mechanism. Imaging large molecular complexes *in situ* however, is fundamentally difficult. Traditional techniques include negative stain electron microscopy (EM) where samples are preserved using heavy metal stains and "thin-sectioning" where samples are embedded in resin, and then sliced into thin enough sections to image with an electron microscope. These methods, although they have been instrumental in providing much of our understanding of biological ultrastructure, are limited in resolution by preparation artefacts.

The development of vitrification was hugely influential in providing a way to visualise native complexes without the use of heavy metals or plastic embedding. Vitrification, is a method that preserves samples in a near-native state [69], in a glass-like aqueous film. Samples are applied to an hydrophilic EM grid and plunged into a liquid cryogen (commonly ethane or an ethane/propane mixture [70]), cooled to liquid nitrogen temperatures. Due to a decreased cooling rate with increased thickness, specimens above a few microns thick however, suffer from increased incidence of crystalline ice formation, deforming and damaging the specimen. Vitrification by plunge freezing is therefore limited to bacterial cells or small eukaryotic cells. After vitrification the sample can be transferred directly to the microscope or stored in liquid nitrogen. The two main techniques used to image vitreous samples to obtain 3D structures using an electron microscope, are Single Particle Analysis (SPA) and electron cryotomography (ECT).

1.2 Introduction to Single Particle Analysis and Electron Cryotomography

SPA collects projection images of proteins or protein complexes that have been purified. Due to the random orientations of the purified proteins in buffer at the point of vitrification, the proteins are usually randomly oriented on the grid. Multiple projection images of the different orientations can then be used to computationally reconstruct the 3D structure. An important concept for understanding reconstruction of 3D data from 2D

projection images in both SPA and ECT is the "central slice theorem". This is the relationship, in Fourier space, between a 3D object and its 2D projection. The central slice theorem states that the Fourier transform of a 2D projection image represents a plane passing through the origin of the 3D Fourier transform of an object [71–74]. The 2D Fourier transforms of each projection image collected in SPA can therefore be used to calculate a 3D Fourier transform, the inverse of which gives the 3D structure.

The randomly oriented proteins are grouped or "classified" in 2D. This grouping is often based on a Maximum likelihood approach, using the data to calculate the likelihood that each particle belongs to a certain group. Each class is averaged to increase the signal to noise ratio (SNR). These 2D class averages are then used to produce the 3D structure.

SPA images purified complexes, and hence information on *in situ* structural dynamics and biological context is lost. ECT however, is an integrative imaging technique uniquely capable of providing mechanistic, dynamic, and contextual insights into biological systems at both molecular and cellular scales. Unlike SPA, where different orientations are imaged by collecting data of particles lying in different orientations on the grid, ECT images the same particle (often within its cellular context – e.g. a whole cell) from multiple orientations. A tilt series is collected by tilting the sample with respect to the electron beam and collecting projection images at each tilt angle (Fig. 1.4, 1.5). The projection images are then back-projected through a volume. The rays coming from the back-projections intersect and reinforce at points of mass in the original structure, leading to a 3D reconstruction from 2D projections. The power of ECT for obtaining high-resolution 3D structures relies on Subtomogram Averaging (STA) where the SNR of a structure is boosted by aligning and averaging many identical complexes ("subtomograms") found within one or multiple tomograms (Fig. 1.4).

To provide an understanding of tomography data collection and 3D reconstruction, I will go through details of the microscope hardware. Alongside this, I will explain some of the theory behind microscope components leading to image formation and detection. Finally, I will provide details of data collection and processing.

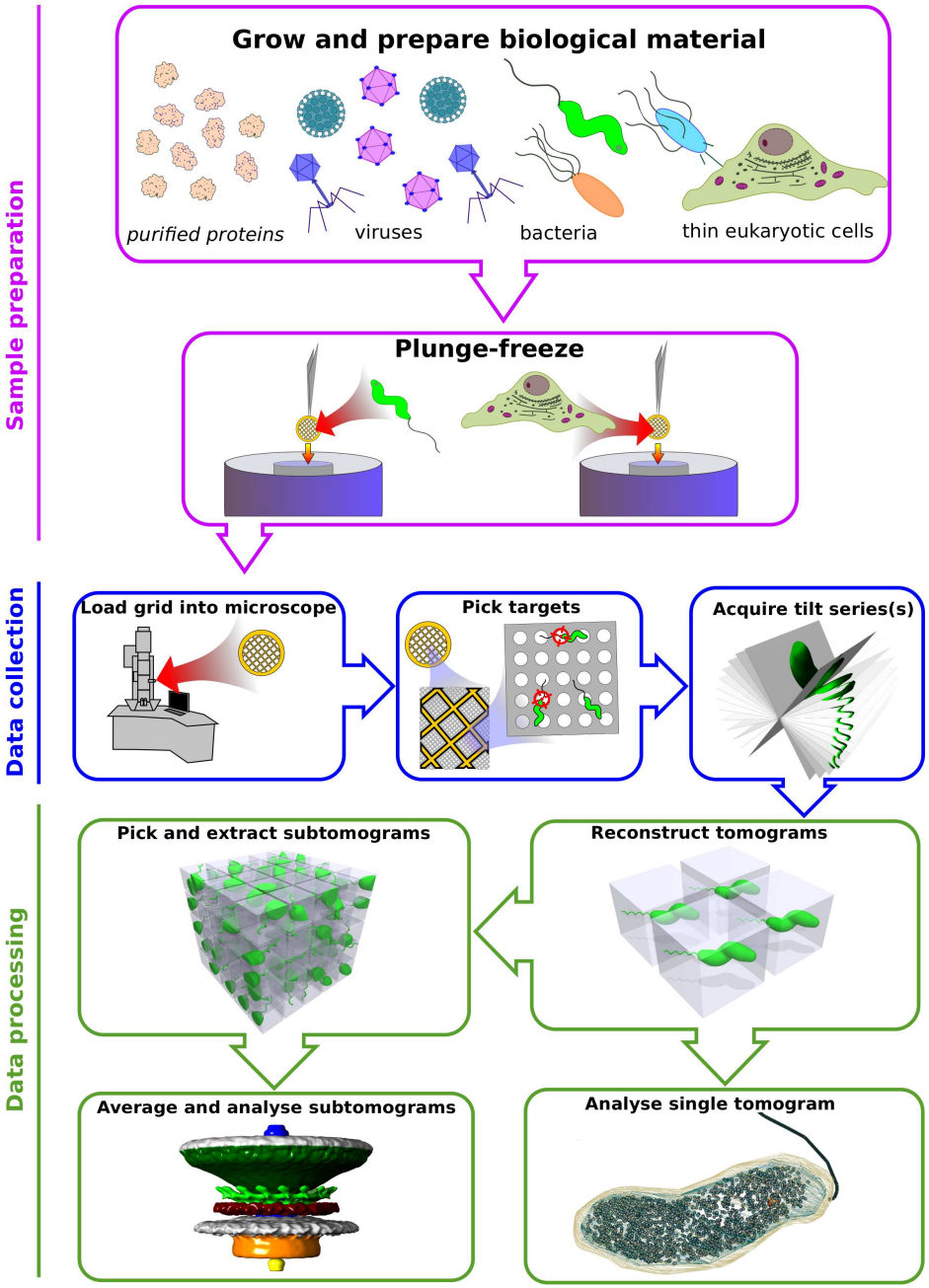


Fig. 1.4: ECT overview.
Small biological samples are vitrified by plunge freezing on EM grids. In the microscope targets are identified and tilt series are collected. Tomograms are reconstructed from the tilt series and can be analysed as a single tomogram or averaged using STA. Adapted from [6].

1.2.1 The tomographic “missing wedge”

Due to the slab geometry of the EM sample, there is a limit to the extent to which the specimen can be tilted as the thickness of the sample increases with increasing tilt angle. A grid tilted to ± 90° would be parallel to the beam, completely blocking electron penetration. A tilt series is therefore collected to a maximum of ~ ± 70° but practically often ± 60°. This means that the resolution along the axis parallel to the beam is greatly reduced, leading to anisotropic resolution. In 3D Fourier space the missing information is in the shape of a wedge and is therefore referred to as the “missing wedge”. In practice, this creates artefacts in tomograms, often smearing the appearance of structures along the axis parallel to the beam. The only way to fill in the missing data in 3D-fourier space is to use STA techniques where each individual subtomogram is orientated differently with respect to the electron beam and are therefore missing different parts of their data. By undergoing averaging, all 3D-fourier space can be filled, reducing the anisotropic resolution of the structure. Because the data collection is not continuous but rather discrete, small “missing wedges” of information in 3D-fourier space are also absent between tilts but these are also filled in with STA.

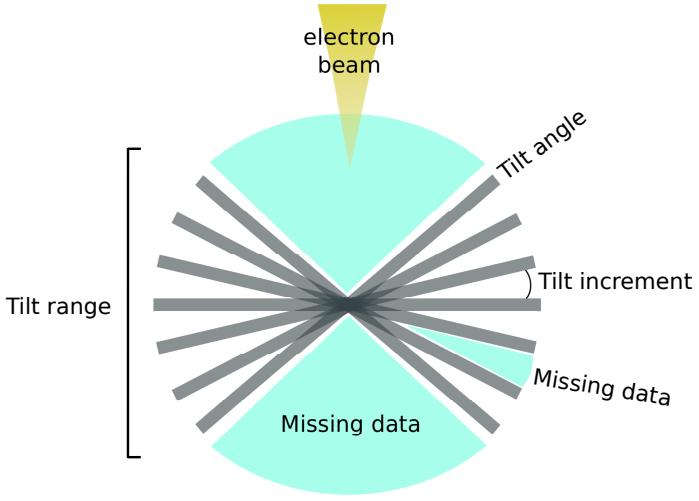


Fig. 1.5: Missing wedge.
Due to limitations in the tilt range of a sample, the sample is not imaged from all angles and there is missing some data. In 3D Fourier space this is in the shape of a wedge and is called the “missing wedge”. As discrete angles are sampled, there are also small missing wedges of information between tilts.

1.2.2 Hardware and theory

The electron microscope consists of a vertical column under high vacuum with an electron source at one end and a detector on the other. A series of lenses focus the electron beam. The basis of image formation in EM, without the need for highly scattering heavy metal stains, is enabled by the strong electron scattering of biological material - providing contrast.

1.2.2a The electron gun, mean free path, scattering and dose

Electron guns, at the top of the microscope, provide the electron source for imaging. Currently, the most commonly used electron gun for data collection is the field emission gun (FEG). The FEG is the most temporally and spatially coherent source, meaning that electrons are released from the gun at the same energy and in the same direction. A more coherent electron source results in more coherent scattered electrons, refocused to form a lower noise, higher resolution image. Different acceleration voltages or electron energies can be chosen, which dictates the wavelength and mean free path of the electron giving a specific penetration depth before the first scattering event. The mean free path of an electron at 200keV is ~ 150 nm and ~ 240 nm at 300keV. This makes EM ideal for samples below ~ 300 nm.

When electrons interact with biological material, they may deposit energy into the sample causing damage. Two main types of scattering events happen: elastic and inelastic. In EM, the image is formed by the interference of elastically scattered and unscattered electrons. Elastically scattered electrons conserve their energy but change direction. Inelastically scattered electrons lose energy and break bonds in the sample. This means that inelastically scattered electrons not only damage the sample, but also contribute incoherently to the image, creating noise. As sample thickness increases, the interaction of electrons with matter becomes problematic and the large amount of inelastic scattering events provides images that are uninterpretable [75].

Biological samples are particularly sensitive to radiation damage. The interplay between image formation and sample damage necessitates that the electron fluence ($e^-/Å^2$) is kept low, producing images with very low SNRs. Damage from the electron beam and hence the limited total electron dose tolerated by the sample is the largest limiting factor in resolution for ECT of frozen-hydrated biological samples. The electron dose problem, well known in SPA, is intensified in ECT where multiple projection images need to be acquired of a single object. Depending on the biological sample, the total fluence is set between 40 and 200 $e^-/Å^2$, divided between the entire tilt series, corresponding to 1-2 $e^-/Å^2$ per image. As a result, in single tomograms, the resolution is limited to the position and stoichiometry of protein domains rather than secondary structures or placement of atoms [76].

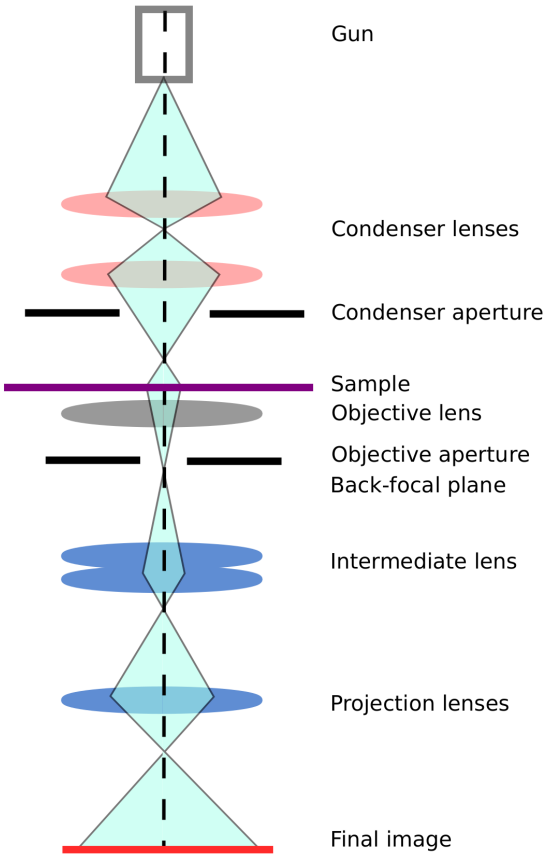


Fig. 1.6: The electron microscope.
The electron gun at the top of the column provides the electron source. Electrons are focused and projected by a series of electromagnetic lenses. Apertures remove highly scattered electrons. The final image is viewed on a fluorescent screen or on a detector.

1.2.2b Electron lenses, the CTF and defocus

Below the electron gun, inside the microscope column are a series of imperfect electromagnetic lenses, shaping the electron beam. Electron lenses are made from a large coil of copper wire held within a shell made from iron. By passing a current through the lenses a magnetic field is generated and this can be used to focus an electron beam due to the negative charge of the electrons. The microscope column contains a set of condenser lenses above the specimen and a series of objective, intermediate and projector lenses below the specimen. The main role of the condenser lens is to control the intensity of the beam. In newer microscopes a third condenser lens (C3) provides a constant parallel beam without the loss of beam coherence. The objective lens is the main magnifying lens, while the intermediate lens assists in magnifying the image. Finally, the projector lens aids in magnifying and projects the image onto the fluorescent screen or detector (Fig. 1.6).

Electromagnetic lenses are imperfect and therefore add spherical aberration to the image. Spherical aberration occurs due to the lens system acting irregularly on off-axis electrons and therefore failing to converge the beam at a common focal point. This spherical aberration changes the phase of scattered electrons. The phase alterations are dependent on the scattering angle (spatial frequency) which leads to oscillations in the contrast of an image with respect to resolution. The spherical aberration coefficient, electron acceleration voltage and defocus of the lenses all contribute to the Contrast Transfer Function (CTF), which modifies all images. The oscillations lead to certain spatial frequencies having negative contrast and some spatial frequencies having zero contrast, making interpretation of the image difficult (Fig. 1.7). The lowest spatial frequency that has zero contrast is referred to as the “first zero”. In 2D Fourier space, these contrast inversions produce a series of light and dark “Thon rings”, a relationship between the contrast and the spatial frequency (low spatial frequencies at the centre, high spatial frequencies at the edges).

The CTF is not the only function applied to the image, additional temporal and spatial aberrations lead to the envelope function, which acts to dampen signal as a function of resolution. Temporal aberrations are due to defects in the electron gun leading to electrons not being monochromatic (same energy). Spatial aberrations are also due to defects in the gun resulting in electrons emerging from the gun with different trajectories. Both of these affect high spatial frequency components more than low spatial frequency components. The CTF is therefore multiplied by the envelope function giving an oscillating function that weakens with respect to spatial frequency (Fig. 1.7).

Although the CTF causes contrast inversions and distortions of the image, a positive aspect is that it can be used to achieve strong phase contrast as it is a function of the defocus. By setting a defined defocus, the focal plane moves below the image plane, phase shifting the first zero in the CTF towards the lower spatial frequencies and gaining contrast at the lower end of the spectrum. As low spatial frequencies are the only discernible frequencies by eye, it is tempting to decrease the focus by a large amount. However, the increase in low spatial frequency contrast comes at a cost to the higher frequency resolution as it causes rapid oscillations in the CTF (contrast reversals) [77]. This means that only certain spatial frequencies gain adequate contrast and a balance needs to be struck between discerning the features by eye and later high resolution data acquisition (if for example high resolution STA is being used).

1.2.2c Gaining contrast: Apertures and energy filters

The low SNR of ECT makes interpretation of images difficult. To add contrast to the sample an aperture can be used. Apertures are annular metallic disks (often a laser-bored hole in a molybdenum sheet) that are placed at specific points along the microscope column. They are either fixed or adjustable and are thick enough to exclude electrons that are further from the optical plane than desired, allowing only axial electrons to pass through.

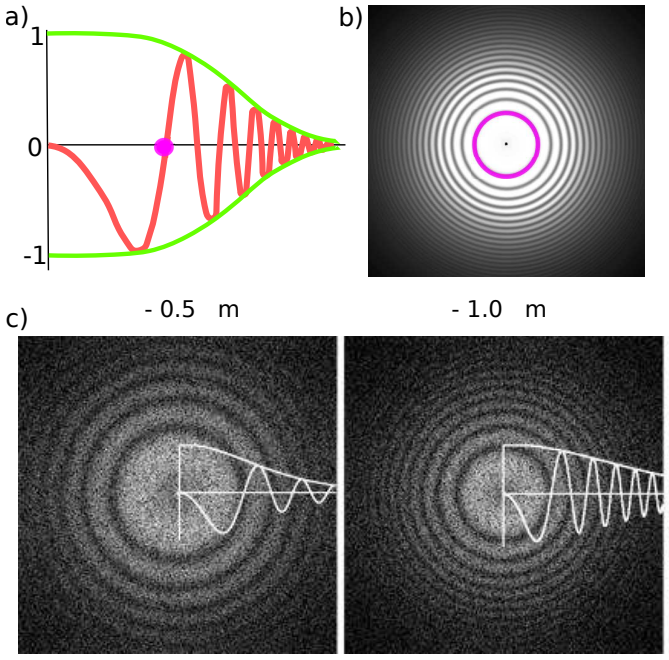


Fig. 1.7: The Contrast Transfer function and envelope function.
a) The CTF (orange), dampened by the envelope function (green). The pink dot is on the "first zero", the first contrast inversion. b) Power spectrum (Fourier transform of an electron micrograph) with radiating Thon rings. The centre is low spatial frequencies and the edges are high spatial frequencies. The first zero is in pink, as in a). This is a representation of contrast with respect to spatial frequency. c) The power spectrum at two different defocus values. An image taken closer to focus has a first zero at a higher spatial frequency and fewer high spatial frequency contrast inversions than an image taken at a higher defocus. Overlaid on the power spectra is the CTF and envelope function, (c) is adapted from [78].

Two important apertures are the condenser aperture and the objective aperture (Fig. 1.6). The condenser aperture, placed near the top of the column, is used to reduce spherical aberration by 'condensing' the coherence of the beam. The objective aperture, placed below the sample, enhances specimen contrast. All high angle scattered electrons will hit the aperture ring and only the lesser scattered or axial electrons are let through. This lessens the intensity of the beam as well as removing unwanted highly scattered electrons, the result of chromatic or spherical aberration or interaction with the sample. This is a good way to define the outline of features and works best with stained samples which produce strong scattering due to the high atomic number of the stain. However, even with cryo-

samples the objective aperture can add valuable contrast and allow for increased contrast of structures that may otherwise not be visible.

Another way to increase the SNR of the data is to use an energy filter. Energy filter transmission EM allows the selection of only electrons within a specific range of energy-loss to hit the detector. In other words, the chromatic error added by the loss of energy via inelastic scattering events is reduced. No structural information can be gained from inelastically scattered electrons, but they add background noise and decrease contrast [79]. An energy filter therefore reduces noise and produces higher contrast images, allowing images to be collected at lower defocus values, as well as lower electron doses, increasing the achievable resolution and giving good resolution images of samples up to 1 micron thick. High resolution structures from both STA and SPA are usually collected on microscopes with energy filters.

Energy filters are composed of magnetic prisms to bend the electron beam followed by a split aperture of varying widths, a series of magnetic lenses and finally the detector. The magnetic prisms bend the electron beam by 90 degrees (post-column filter), dispersing the electrons based on their energy loss. Electrons that are unscattered or elastically scattered and emerge from the sample with the incident electron energy pass through the slit and reach the detector. Inelastically scattered electrons, with lower energies, are bent more strongly and hit the filter, removing them from forming the image. The slit size and centre can be altered depending on the application. In cryo-EM the typical size of a slit is around 20eV (cantered at the incident energy of the electron beam) as inelastic scattering events are known to remove more than 10eVs worth of energy (typically 100-1000eV) [80] and the temporal coherence of current FEGs is extremely good. Energy filters have a very high energy resolution of ~ 1eV [81].

1.2.2d Image detection: Direct Detector Devices, magnification and Nyquist frequency

At the end of the column, after all the lenses, apertures and energy filter is the detector. A huge recent advancement in the field has been the development of Direct

Detector Devices (DDD). In DDDs the incident electron hits a back-thinned monolithic active pixel sensor (MAP) (based on the Complementary metal–oxide–semiconductor (CMOS) technology) directly and is converted to charge. The charge is very localised (i.e. small point spread function). The MAP is back-thinned, lowering the chance of electrons back scattering through the sensor in an unrelated location and hence decreasing the shot noise. Due to the stochastic nature of the interaction of electrons with the material of the MAPS chip, different count values (different amount of energy deposited) may be produced by individual electron events. However, new DDDs have a rapid frame rate, rapid electron detection algorithm and the ability to find the electron peak's centroid to subpixel accuracy ("counting mode") [82]. This means that each burst of counts can be interpreted as having come from one electron event. The rapid frame rate reduces the coincidence loss from detecting two electrons hitting the same pixel sequentially as one electron event. Therefore, in the final image, each electron contributes equally and provides meaningful information.

One of the main advantages of the DDDs is the ability to collect "movie-frames", dividing a single exposure into multiple frames. As the electron beam causes warping of the sample and movement of the specimen within the ice, images appear blurred, detrimentally affecting the quality of data. If sub-frames are collected, however, these can be computationally aligned and averaged, resulting in crisper images with better preservation of high spatial frequency data. This sub-frame alignment also allows easier prediction of the CTF of an image.

When collecting data, one choice that needs to be made is the magnification. The main consideration for choosing a magnification is field of view vs pixel size. At low magnifications a structure is captured by many fewer pixels than at higher magnifications. Higher magnifications therefore allow for finer sampling of the structure and therefore higher spatial frequencies are sampled. High magnification (small pixel sizes), however, decrease the field of view which may be important for understanding the cellular context of a sample or imaging multiple structures per tomogram. Higher magnifications also decrease the number of electrons per pixel resulting in a decreased SNR. For high

resolution subtomogram averaging, a small pixel size is more important than gaining information about the biological context and a magnification should be chosen based on the Nyquist-Shannon Sampling Theorem. The Nyquist-Shannon Sampling Theorem states that a signal can only be fully reconstructed if all frequency components are below half that of the sampling frequency or Nyquist frequency. In practical terms this means that the pixel size needs to be at least half of the desired resolution.

1.2.3 Data collection

1.2.3a Automated data collection

Depending on the biological questions, the sample may not be optimal for STA due to low numbers of particles per cell. Imaging the flagellar motor for example, may provide only one subtomogram per tomogram. As a single tilt series can take up to an hour to collect, this makes collecting the large number of particles needed for STA very difficult.

Modern tomography software programmes for controlling the microscope allow for almost fully-automated data collection (examples include Leginon [83], EPU (Thermo Fisher Scientific), and serialEM [84]. The user spends a considerable amount of time selecting targets to be imaged but after this the microscope can be left for multiple days collecting hundreds of tilt series.

1.2.3b Tilt increment

Crowther et. al. proposed that the resolution of a reconstructed tomogram is dependent on the tilt increment used to collect projection images, assuming that sampling is equidistant within the angular range (equal tilt increments) and ignoring the effect of the missing wedge (i.e. 180° sampling).

The Crowther Criterion states that: $d = \frac{\pi D}{N}$

where: d=resolution, D= diameter of spherical sample, N= number of projection images over a 180° range.

This means that higher resolutions are achieved by finer tilt increments due to the small "missing wedges" of information in 3D Fourier space unsampled between each tilt frame. Practically however, this is unrealistic as the tilt range and the total endurable electron dose is limited in cryo-tomography. The tilt increment must therefore be set to a size that accommodates the need to capture the highest spatial frequency of interest, while maximising the total electron dose per image to increase the signal to noise ratio. Choosing the tilt increment is also dependent on the final use for the tomogram. If the tomogram is collected for ultrastructural studies, a finer tilt increment (e.g. 1°) will increase the quality of the data, however this also lowers the number of electrons per tilt frame and therefore makes alignment of the tomogram more difficult. If the tomogram is being collected to do STA, a coarser tilt increment (e.g. 3°) can be used as the missing data between tilts will be filled in when subtomograms are averaged.

1.2.3c Tilt scheme

Traditionally tomograms were collected starting at a high tilt (e.g.: $+60^{o}$) and moved in a single sweep to the other extreme (-60°). The bidirectional tilt scheme starts at 0° and moves to +60° before jumping back to 0° and moving down to -60°. However, recent studies have suggested that sampling the entire set of low tilt angles (e.g. -25° to +25°) before moving onto the higher tilt angles will result in higher achievable resolution. Here, the thinnest part of the sample, where the best images are recorded before the sample has suffered from radiation damage, is imaged first. This scheme would for example move from +20° to -65° and then move from +20° to +65°. The dose symmetric or "Hagen" scheme has recently been developed to collect symmetric Fourier space information, evenly distributing sample damage (most at high tilt angles) and preserve high-resolution data [85]. This starts at 0° and moves evenly between positive and negative tilts (i.e. 0°, -3°, 3°, 6°, -6°, -9°, 9°… etc.). (Fig. 1.8).

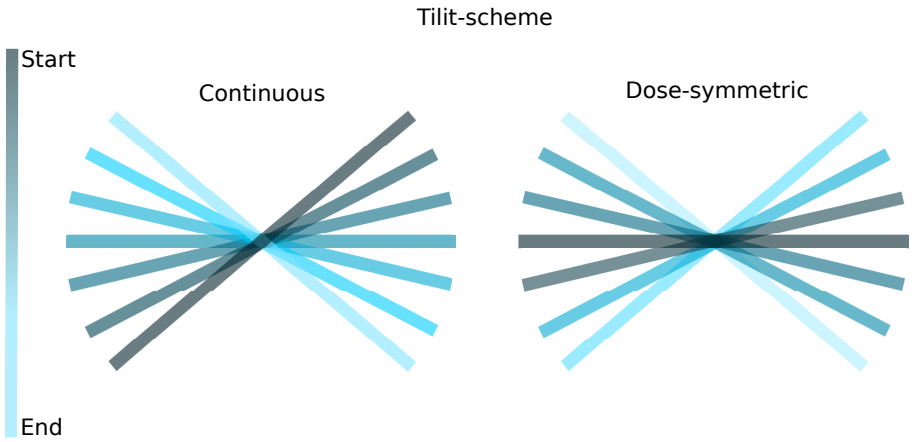


Fig. 1.8: Tilt schemes.
Traditionally the continuous tilt scheme was used, however recent development of the dose-symmetric scheme preserves high spatial frequencies.

1.2.4 Data processing

1.2.4a Preprocessing: Motion correction, CTF-correction and exposure filtering

Once a tilt series has been collected it needs to be reconstructed into a 3D tomogram. Before this, preprocessing of the tilt-images (individual projection images) must take place. If data was collected on a DDD collecting multiple movie frames, these frames should be aligned and averaged (motion correction). Next the defocus needs to be estimated and the CTF should be corrected for. Because we know the electron acceleration voltage and have an estimate of spherical aberration for each microscope we use, the CTF equation can be used to calculate the exact defocus that the data was collected at and a CTF curve can be generated to ensure the oscillations seen in the collected data (Thon rings) match the estimated defocus. The effects of the CTF can be corrected by phase flipping the frequencies with inverted contrast or by applying a Weiner filter (Fig. 1.9).

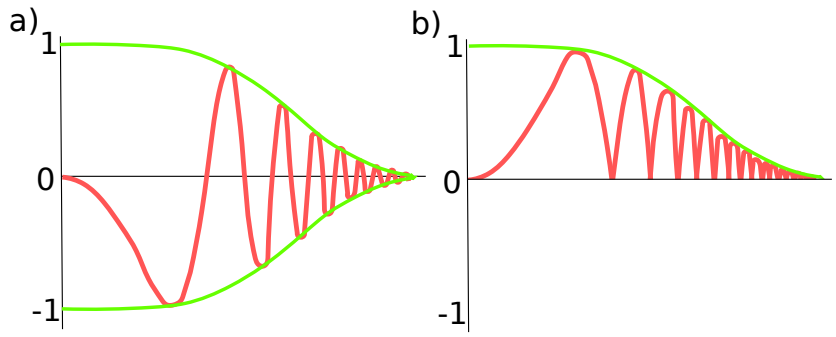


Fig. 1.9: CTF correction.
a) CTF (orange) with envelope function (green). b) After "phase flipping" all spatial frequencies with negative contrast have positive contrast.

In tomography, defocus estimation and CTF-correction are more complicated than in SPA due to most images in a tilt series being collected at an angle. The defocus is therefore not the same across the image. If the data is collected at eucentric height, a strip in the centre of the image will be at the expected defocus and the defocus will increase as you move towards on end of the image and will decrease as you move towards the other end of the image. To overcome this, defocus estimation and CTF correction can be done in strips parallel to the tilt axis. Although this strip-based approach accounts for changes in defocus due to tilting a planer sample, it does not account for alterations in defocus due to particles in the tomogram sitting at different Z heights. A new 3D CTF-correction approach has recently been developed to overcome this. novaCTF has been shown to allow calculation of higher-resolution STAs [86].

If the CTF cannot be fitted due to thickness of cells, lack of an energy filter, microscope or detector type, etc., the data can be filtered beyond the first zero (low-pass filtered), limiting achievable resolution but removing noise. This means all spatial frequencies that have contrast inversions are filtered out and only spatial frequencies that are lower than the first zero are kept.

If tomograms are being used for STA, higher doses can be used (especially with the Hagen scheme – see "tilt scheme" above) and the tilt series can then be "exposure

filtered". This accounts for the effect of beam-induced information loss as well as improving SNR in the reconstructed tomogram, which subsequently leads to faster convergence of alignment during STA. Exposure filtering leaves initial images, where no damage has been induced in the sample unfiltered but tilt images collected later, where specimen damage has occurred, are low pass filtered. This only keeps low spatial frequency information from later tilt images but all low and high-spatial frequency information from initial tilts with limited electron damage. Exposure filtering dampens Thon rings and CTF estimation should therefore be performed prior to exposure filtering.

If the data is being used to create a subtomogram average, the entire set of tilt angles can be used to align the frames but the final reconstruction can be calculated from only a subset of low tilt images before excessive dose and damage has occurred.

1.2.4b Tilt-series alignment

Before a tomogram can be computationally reconstructed, the precise orientations of each tilt frame relative to each other needs to be determined. Translations, rotations and small magnification changes relative to each frame must all be detected. The sample is often mixed with 5 – 20 nm diameter gold particles (fiducial markers) prior to vitrification for tilt series alignment. If fiducial markers were vitrified with the sample these can easily be used for tracking as they are high-density and easily visualised. As they are mixed with the sample prior to vitrification they are distributed throughout the sample and their accurate tracking in 2D can be used to create a coarse 3D lattice using cross-correlation algorithms. The 3D fiducial lattice model provides the information needed to correctly align the tilt series frames. If fiducials are not added prior to vitrification, high contrast areas of the sample can be used for tracking [87].

The tracked fiducial markers are often masked out before tomogram reconstruction as the high-density gold often produces reconstruction artefacts which may obscure features [88,89].

1.2.4c Tomogram reconstruction

Multiple algorithms can be used to computationally convert a set of 2D projection images into a 3D tomogram and are often computed in Real space, although still rely on the central slice theorem. These include Weighted back-projection (WBP) and simultaneous iterative reconstruction technique (SIRT). WBP acts by taking the densities in a tilt series and projecting them back through a 3D volume. Areas that include a real structure in the tomogram will be reinforced (Fig. 1.10). At the same time, the low-spatial frequencies are down-weighted as they contribute disproportionally. This retains high-spatial frequency information (good for STA) but results in lower contrast tomograms [89]. SIRT reconstruction algorithms are computationally expensive but result in high contrast tomograms. In SIRT reconstruction an iterative approach is used to minimise differences between the projection images in the tilt series and back projections from the computationally calculated tomogram [90].

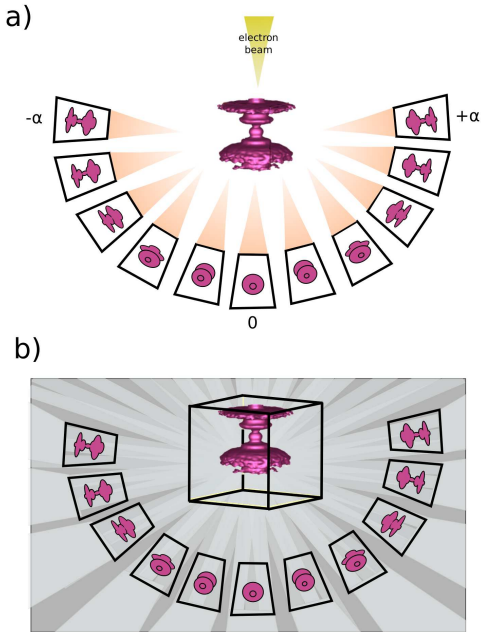


Fig. 1.10: Back-projection for tomographic reconstruction.
a) A tilt series is collected by tilting the specimen and collecting projection images at different tilt angles. b) The projection images from each tilt angle are back-projected through a volume and reinforce in areas of mass in the original structure.

1.2.4d Sub-tomogram averaging

STA assumes that the same structure in multiple copies in for example, the same cell or different cells are identical. The obscured high-spatial frequencies in the low SNR individual tomograms, as well as the missing information from the "missing wedge" can be recovered by aligning and averaging multiple copies of the same structure. STA works initially by superimposing subtomograms and aligning them. Depending on the sample, and the amount of information already known about the orientation of the sample, the alignment works by searching either in a restricted or global search. This search is six-dimensional, accounting for three translation directions and three rotation angles. A deterministic approach is used to identify ideal alignments [89,91]. Importantly, alignment searches need to take into account the artefacts of the missing wedge, which due to its random placement in the tomogram (dependent on orientation of the subtomogram on the grid) will results in structures looking different (e.g. smeared) in each subtomogram or missing from some subtomograms. If this is not handled correctly, subtomograms may align to the missing wedge. Once ideal alignments are identified, the subtomograms are averaged, filling all missing data in 3D Fourier-space, and boosting SNR leading to higher contrast and higher resolution structures. If symmetry is detected in the subtomogram average, this can be exploited to increase the SNR and resolution.

1.2.4e Resolution determination: Fourier Shell Correlation

To determine the resolution of the final subtomogram average, a Fourier Shell Correlation (FSC) coefficient is calculated. The gold standard approach is to use two independently aligned datasets that have been processed completely separately, but randomly splitting the data after processing is also commonly used. The FSC measures consistency between the two data sets, i.e. up to what spatial frequency are two different sets of data identical. The inverse of this frequency at a specified cut-off is given as the resolution. The cut-off is often set to 0.5 in STA or 0.143 if the gold standard approach used [92].

1.3 Using ECT to study the *Salmonella* flagellar motor

At present, ECT with STA is the only technique capable of studying large molecular complexes to nanometre resolution *in situ.* Due to its relatively recent development, there are still many bottlenecks in the process and tilt-series collection, tomographic reconstruction and STA can be labour intensive. The leap in resolution and structural detail from traditional cell-biological techniques however, are substantial. One of the important limitations in ECT, even with relatively thin bacterial cells, is thickness of the cell body. Outlined below are a few methods to overcome this.

The *Salmonella* cell body is ~1 micron thick. In ECT, thick samples produce more inelastic electron scattering, adding noise to an image, and when a sample is above 500nm thick, this may become prohibitive to image quality (especially if collection is on a microscope without an energy filter). Cells can be made thinner to overcome this. This can be done by growing them in minimal medium, using partial lysis with antibiotics or lysozyme [93] (Fig. 1. 11) or by using genetic manipulations to alter systems already used in the cell. A common method is the over-expression of FtsZ to produce "mini-cells" [94,95] (Fig. 1.11). FtsZ is a bacterial tubulin homologue which produces contractile rings at the future site of division. When this is over-expressed, multiple division sites form along the cell body, pinching off small cells. These mini-cells, although non-viable, provide a "native" environment in which to image molecular complexes without extra noise, from the thick cytoplasm, causing excessive inelastic scattering.

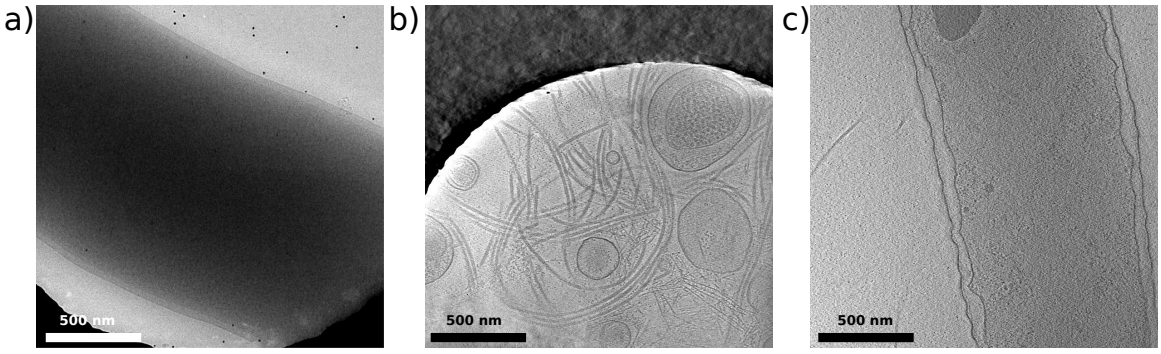


Fig. 1.11: Methods to make cells smaller for ECT.
a) A projection image of a cryo-preserved WT Salmonella cell. b) A slice through a cryo-tomogram of Salmonella mini-cells produced by the over-expression of FtsZ. c) Slice through a cryo-tomogram of a Bordetella bronchiseptica cell lysed using Penicillin G.

1.4 Thesis overview

The *Salmonella* flagellum is central to pathogenesis and a comprehensive understanding of its assembly, mechanism, and evolution at a molecular level will provide fundamental insights into *Salmonella* infection and the development of its enteropathogenic lifestyle.

In this thesis, I present work that used ECT and STA in combination with other techniques, to study the evolution, regulation, mechanism, and assembly of the bacterial flagellum. I will briefly outline each chapter below.

The *Salmonella* motor is the canonical motor which has been studied for decades to understand motility, self-assembly and pathogenesis. The swimming in *Salmonella* and other enteric bacteria however, is not only unrepresentative of the bacterial tree as a whole, but is also unrepresentative of the γ-proteobacterial clade to which it belongs. *Salmonella's* motor looks distinct, it has a distinct swimming style and it occupies a unique environmental niche.

In Chapter 2, I ask how a small group of bacteria could have colonised a new niche, developed a distinct swimming style and obtained a different flagellar motor from their close relatives. I show that an ancient horizontal gene transfer led to *Salmonella* acquiring a non-native flagellar motor from the β-proteobacteria, and by studying the acquisition of *Salmonella's* new flagellar motor, I discuss the possible selective benefits for this acquisition.

Although motility is important for bacteria, it is energy intensive and bacteria often move between motile and sessile states. Due to the motile state often being the infectious state, deactivation of the flagellum to stop swimming remains poorly studied and understood.

In Chapter 3, after finding that some bacteria stop swimming at high cell densities, I provide evidence for a novel mechanism for moving into the sessile state in the γ-proteobacteria. I show that polarly flagellated γ-proteobacteria eject their flagella under nutrient limited conditions, leaving behind partial flagellar structures in the outer membrane, which are plugged by a novel protein.

The *Salmonella* motor has dynamic stator complexes that only bind to the motor when the filament is put under a high load. Due to this dynamic nature, at present we do not know how many stator complexes can bind to the *Salmonella* motor, and what their arrangement is.

In Chapter 4, I ask what the arrangement and location of stator complexes in the *Salmonella* flagellar motor is. By developing a strain to image the stator complexes *in situ* and by doing initial SPA characterisation, I move towards providing a greater understanding of the stator complexes.

The self-assembly of the *Salmonella* flagellar motor has been studied intensely for decades and we have a good understanding of the assembly of most flagellar components. The last axial component whose assembly was not fully understood is the flagellar rod,

specifically what controls the length of the rod. The protein that makes up the flagellar distal rod (FlgG) has self-stacking capabilities and no molecular ruler has been identified.

In Chapter 5, I ask how the length of the *Salmonella* flagellar rod is controlled. I show that the periplasmic distance is the main determining factor for rod-length control. Due to this discovery, I then move on to asking what the broader implications of periplasmic width are, and show that another periplasmic spanning system, the Rcs-stress response system, also relies on the correct periplasmic architecture.

Chapter 2

Acquisition of the enteric flagellar motor by an ancestor of *Salmonella*

2.1 Chapter Summary

The γ-proteobacteria are a large group of diverse bacteria that include the human pathogens *Vibrio cholerae* and *Salmonella enterica*. All γ-proteobacteria use flagellar motility and the majority of species from this group are aquatic species with polar, Na^+-driven flagellar motors. The exceptions are the enteric bacteria, which include *Salmonella*, *Shigella*, *Yersinia* and *E. coli*. These bacteria are gut bacteria, both pathogenic and commensal, and swim with H^+-driven, peritrichous flagellar motors. What makes this group different, and how did a small group of bacteria achieve a new environmental niche and a mode of motility distinct from their close relatives?

Preliminary phylogenetic studies in the Beeby lab suggested that a horizontal gene transfer (HGT) of flagellar genes from the β-proteobacteria to the enteric bacteria, led to the enteric bacteria gaining a non-native flagellar motor. In this Chapter, I present subtomogram averages of flagellar motors from both the β- and γ-proteobacteria and compare these with the enteric motor from *Salmonella enterica.* As expected from phylogenetic studies, the non-native enteric motor is structurally similar to the native motors from β-proteobacteria while being structurally distinct from the motors of closely related γ-proteobacteria.

By analysing the structures, I consider the possible selective advantages of the HGT. I speculate that the acquisition of the non-native motor may have allowed the enteric bacteria to occupy a new niche and led to *Salmonella's* enteropathogenic lifestyle.

2.2 Introduction

The γ-proteobacteria are a large group of bacteria including multiple human pathogens such as *Vibrio cholerae* and *Salmonella enterica*. The majority of γ-proteobacteria use flagellar motility and most species from this group are aquatic species, including *Vibrio, Shewanella,* and *Pseudomonas*. The exceptions are the enteric bacteria which include *Salmonella, Shigella, Yersinia* and *E. coli*. These bacteria are gut bacteria, both pathogenic and commensal.

Having a small subset of the γ-proteobacteria occupying a different niche from the rest of the group is surprising. What makes the enteric bacteria different from the other γ-proteobacteria, enabling them to occupy a new environmental niche? One main difference between the enteric bacteria and the rest of the γ-proteobacteria, that I will explore below, is their mode of swimming.

2.2.1 Differences between the enterics and other γ-proteobacteria

2.2.1a Type and placement of flagella

Most γ-proteobacteria have polar flagella that are powered by Na^+-ions. They range from a single polar flagellum in species such as *Vibrio cholerae* and *Pseudomonas aeruginosa*, to multiple flagella on one pole in species such as *Vibrio fischeri* and *Plesiomonas shigelloides* (Fig. 2.1b). Some polar flagellates also have a secondary flagellar system. This secondary system produces non-chemotactic, lateral flagella which are expressed when cells sense a surface.

The lateral flagella system is used for swarming on solid surfaces. The enteric bacteria however, have proton-driven "peritrichous" flagella. Peritrichous flagella are chemotactic flagella that are arranged on the sides of the cell body (Fig. 2.1a) and are used for both swimming in liquid medium and swarming on solid surfaces.

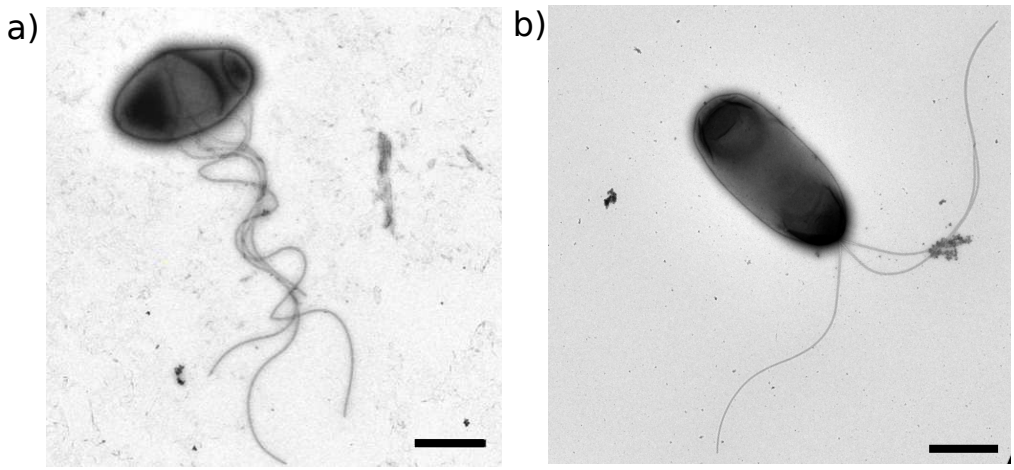


Fig 2.1: Placement of flagella in the enterics is different from other γ-proteobacteria. *Negative stain micrograph of a Salmonella cell (enteric bacterium) showing peritrichous flagella. Scale bar = 1 μm. b) Negative stain micrograph of a Plesiomonas shigelloides cell (γ-proteobacterium), showing polar flagella. Scale bar = 1 μm.*

2.2.1b Swimming behaviour

The peritrichous flagella in *Salmonella* rotate together in a counter clockwise (CCW) direction, to push the bacterium ("run"). When one or more motors change direction and turn in a clockwise (CW) direction, the bundle is dispersed and the cell body is reoriented ("tumble"). This type of swimming trajectory is known as a run-tumble and by altering the frequency of tumbles, the cell can control its chemotactic response (Fig. 2.2a). The straight swimming and reorientation of the cell for chemotaxis in the polarly flagellated γ-proteobacteria is distinct from this. In these bacteria a three-step cycle ("forward-reverse-flick") is used rather than the run-tumble. Polarly flagellated bacteria swim forward with CCW motor rotation ("forward"). When the direction of the motor is reversed to CW, the cell backtracks on itself ("reverse"). When the motor's rotational direction is changed again to continue swimming forward, the flagellum flicks sideways and the cell body is reoriented ("flick"). The direction is random and may take several forward-reverse-flick cycles to orient the cell for chemotaxis (Fig. 2.2b) [96].

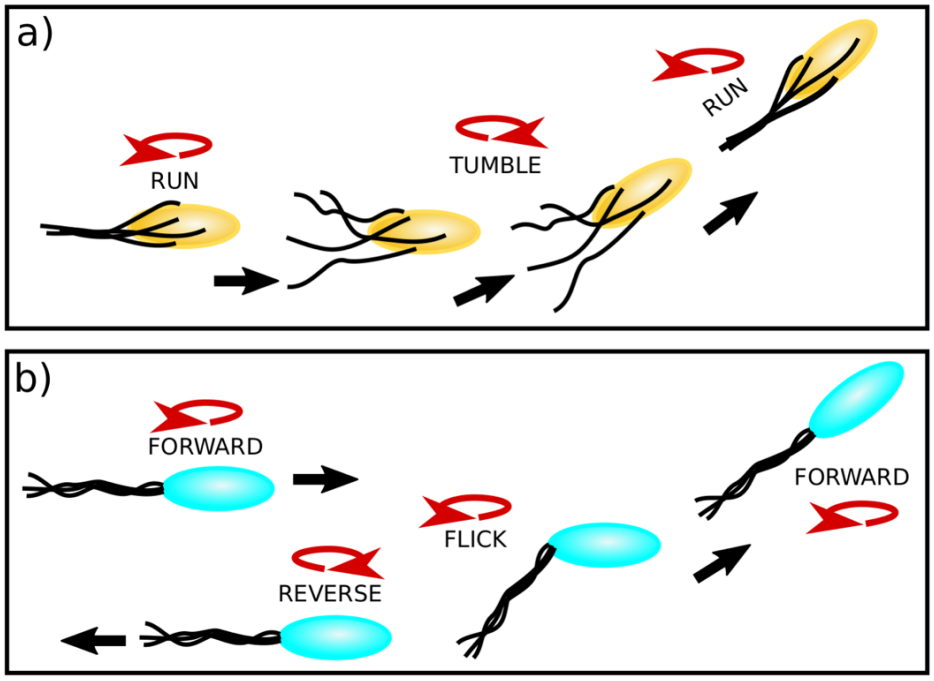


Fig. 2.2: The swimming trajectory of γ-proteobacteria.
a) The enteric bacteria with peritrichous flagella swim in a "run-tumble" trajectory. b) The polarly flagellated γ-proteobacteria swim in a "forward-reverse-flick" trajectory. Red arrows show direction of flagellar motor rotation.

Both groups of γ-proteobacteria can also "swarm" on solid surfaces. The enterics use the same set of H^+-driven peritrichous flagella, while the polarly flagellated γ-proteobacteria express a second set of proton-driven lateral flagella. Swarming motility is a concerted effort by a large group of bacteria, all using their flagella to move, often accompanied by high growth rates and cell elongation [97].

2.2.1c Motor structure

Not only do the enteric bacteria swim differently from the other γ-proteobacteria but the flagellar motors are also structurally distinct. The enteric bacteria have a stripped-down flagellar motor made only of the core, conserved flagellar proteins (Fig. 2.3). The polar flagellar motor from the other γ-proteobacteria are structurally more complex (Fig.

2.3). These motors have accessory proteins which have iteratively been added to the motor through evolution and are now all essential components. These accessory proteins include extra disks on the P- and L-rings that are thought to stabilise the stator complexes [34]. Some polar flagellar filaments are encased in a membrane sheath.

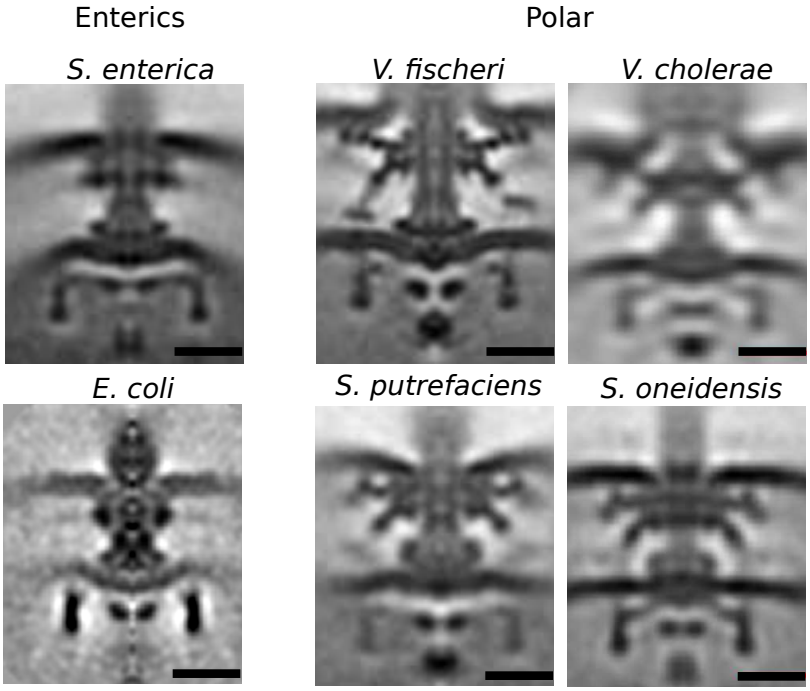


Fig 2.3: A collection of γ-proteobacterial flagellar motor structures.
On the left, the two enteric structures from Salmonella (EMD-3154) and E. coli (EMD-5311). On the right, the γ-proteobacteria with polar flagella: Vibrio fischeri (EMD-3155), Vibrio cholerae (EMD-5308), Shewanella putrefaciens (Structure from Dr. Florian Rossmann), Shewanella oneidensis (EMD-0467). Scale bar = 20 nm

2.2.2 What makes the enteric bacteria different?

The enteric bacteria clearly have a distinct form of swimming motility from the other γ-proteobacteria. Their flagella use different energy sources, are positioned differently on the cell and have diverse motor structures. The question remains: What makes this group different and how did a small group of bacteria within the γ-

proteobacteria achieve a new environmental niche and a mode of motility distinct from their close relatives?

Recent preliminary phylogenetic studies in the lab suggested an answer to this question (unpublished). When a phylogenetic tree was made of a selection of bacteria using a concatenation of core flagellar proteins, *Salmonella* and *E. coli* do not cluster with other γ-proteobacteria, but are found within the β-proteobacteria (Fig. 2.4). This shows that *Salmonella* and *E. coli* acquired a motor from the β-proteobacteria via a HGT. After the acquisition of the non-native β-proteobacterial motor, *Salmonella* subsequently lost its native γ-proteobacterial flagella. This new β-proteobacterial motor may have provided a selective advantage over the native γ-proteobacterial flagellar motor, allowing the transition from an aquatic species to the colonisation of the digestive tract.

2.2.3 The β-proteobacteria

The β-proteobacteria are a large group of bacteria including multiple human pathogens such as *Bordetella pertussis* which causes whooping cough and *Neisseria gonorrhoeae* and *Neisseria meninngitides* which cause gonorrhoea and meningitis respectively. The flagella in this group are peritrichous and chemotactic. A few species in this group also have a secondary non-chemotactic lateral flagellar system thought to be ancestral to the split of β- and γ-proteobacteria [98]. This group of bacteria occupy a large variety of ecological niches, from obligate pathogens living within human mucosal surfaces, to free-living species in soil and groundwater ecosystems.

In this Chapter, I aim to further the investigation into the HGT that took place from the β-proteobacteria to the γ-proteobacteria. A combination of thorough phylogenetic studies with *in situ* structural determination was used. The comparison of the β- and γ-proteobacterial flagellar motors allowed me to speculate on the possible selective advantages of the new flagellar motor to the enteric bacteria.

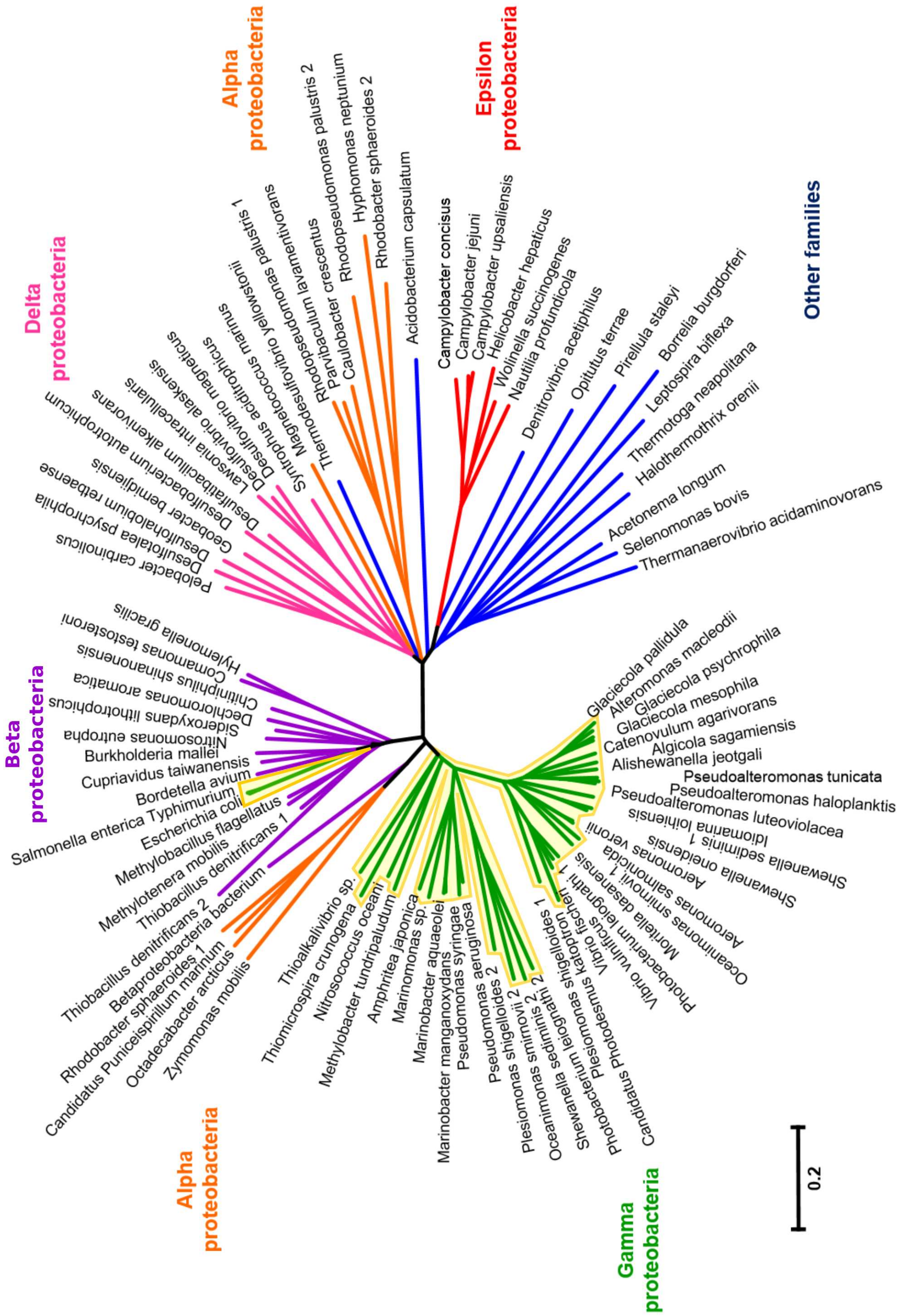


Fig 2.4: Enteric γ-proteobacteria have a β-proteobacterial flagellum.
A phylogenetic tree based on a concatenation of conserved flagellar genes, and coloured based on taxonomic classification. The γ-proteobacteria are highlighted in yellow. Salmonella and E. coli have flagella which are more similar to the β-proteobacteria than the γ-proteobacteria, suggesting a HGT of the flagellar genes from the β-proteobacteria to the enteric bacteria.

2.2.4 Spotlight on technique: Phylogenetic analysis

The characterisation of microorganisms has long been a focus and challenge in biology [99]. Although our understanding has since expanded [100], the tree of life, proposed in the early 1990's remains one of the most important organising principles in biology [101]. The aim of phylogenetic analysis is to gain an understanding of the evolutionary path of current-day organisms, using orthologous genetic loci, and the best assumptions available, to track the common ancestry of two sequences back to a specific event.

There are three main steps in phylogenetic analysis: 1) Selection of suitable phylogenetic marker and acquisition of molecular sequences, 2) Multiple sequence alignment, 3) Inference of phylogeny and analysis. These are described in detail below, and are used in this study as tools to understand the evolution of *Salmonella's* flagellar motor.

1). Bacterial genomes are highly dynamic and a significant proportion of bacterial genetic diversity occurs via HGT from even distantly related organisms [102]. The dynamic genomes may provide an explanation for the high level of adaptability to new environments. However, this flow of genomic information makes phylogenetic analysis based on single gene sequences problematic as multiple, conflicting evolutionary relationships will be expected from analysis based on different genes [103]. The use of a concatenation of multiple ribosomal protein sequences gives many benefits over methods based on a single gene, such as the commonly used 16S rRNA, providing a higher-signal tree at deeper evolutionary times. Importantly, it avoids artefacts that may arise when using genes with unrelated functions that are therefore subject to diverse evolutionary progressions.

2) Multiple sequence alignment (MSA) aligns homologous sites in the recorded sequences. This means it looks for corresponding positions originating from a common ancestor. Algorithms for MSA in general use a progressive technique, starting by aligning the two most homologous sequences and then expands the alignment for all other sequences, ending with the most distantly related [104].

3) A phylogenetic tree is finally created and analysed. Modern phylogenetic standards use Maximum Likelihood (ML) to predict tree structure. ML is a statistical method for estimating parameters in a statistical model that are unknown. This method aims to produce a tree topology which maximises the probability of observing the data given the model. Bootstrapping is then used to test how well the evolutionary model created fits the given data set. During bootstrapping, positions in the aligned sequences are randomly sampled with replacements, creating new bootstrap data-sets and bootstrap trees are created from these. These can be used to assess the reliability or "confidence" in each clade in the tree, depending on the proportion of bootstrap trees showing the same clade.

It is also useful to compare trees based on ribosomal proteins to those created using a gene or gene-cluster of interest, such as in this case the flagellum. This can give insight into molecular evolution, including highlighting HGTs, of specific proteins and protein complexes.

2.3 Results

2.3.1 Phylogenetic studies towards understanding the Horizontal Gene Transfer

Initial phylogenetic studies in the lab had identified that a HGT from the β-proteobacteria to the enteric bacteria had taken place. However, these were done using an outdated Parsimony method and focused on a broad set of bacteria from all clades of the proteobacteria phylum. I therefore set out to produce new phylogenetic trees using the current phylogenetic standards (Maximum Likelihood) as well as focusing only on the β- and γ-proteobacteria while expanding the number of bacteria within these clades, especially adding more enteric bacteria.

First, a taxonomic tree was created for a selection of β- and γ-proteobacteria including eight enteric bacteria (*Salmonella enterica, Escherichia coli, Yersinia pestis, Shigella flexineri, Enterobcter cloacae, Edwardsiella ictaluri, Serratia marcescens and Morgenella morganii*). In order to root the tree, an ε-proteobacterium, *Campylobacter jejuni*, was also included. This was chosen due to its placement in the universal tree (Fig. 2.4). The taxonomic tree was created using a concatenation of 15 conserved ribosomal protein sequences and all bacteria fell into their expected taxonomic clades (Fig. 2.5).

To understand the HGT, a phylogenetic tree based on the flagellar motor was created with the same bacterial species as in the taxonomic tree. The sequences of 10 core, conserved flagellar motor proteins were concatenated and used for the alignment and tree production. This tree represents the relation of flagellar motors, regardless of how closely related the species that they belong to are. In general, flagellar motors from taxonomically similar species are also closely related. This is the case in Fig 2.6, apart from the movement of one group of bacteria: the enteric bacteria. In the flagellar tree, the enteric bacteria have moved from the clade of γ-proteobacteria to nestled within the β-proteobacteria (Fig 2.6). Within the γ-proteobacteria, the lateral flagella are clustered as a distinct clade.

From a comparison of the two trees it is clear that a large HGT occurred, with the flagellar genes from the β-proteobacteria moving into the enteric bacteria and subsequent loss of the native γ-proteobacterial flagella from these species.

Trees were also made of the individual flagellar proteins included in the concatenated tree to ensure congruency (Fig. 2.8). All individual flagellar trees included in the final flagellar tree were congruent with one another and with the final concatenated tree. Importantly, all had the enteric bacteria clustered alongside the *Bordetella* species within the β-proteobacteria (Fig. 2.8). One interesting difference in the overall tree appearance of individual proteins was in the phylogenetic trees made from the proteins that make up the C-ring (FliG and FliM) (Fig. 2.9). These trees were incongruent with long branch lengths in the clade containing lateral flagella from γ-proteobacteria, suggesting a different selective pressure and faster divergence. As the FliM and FliG trees are incongruent they were not used in the final flagellar tree (Fig. 2.6).

2.3.2 Genetic context substantiates horizontal gene transfer

Although the *Salmonella* flagellar genes are dispersed in the chromosome in four distinct regions (Fig. 2.10a) the *Bordetella* flagellar genes are all in one chromosomal location (Fig. 2.10b). The genome arrangement of flagellar genes in one region would facilitate the HGT of an entire set of flagellar genes which would be difficult in other bacteria where flagellar genes are dispersed.

The GC content is also indicative of a HGT. The GC content of the *B. bronchiseptica* chromosome is 68.2% and as expected the GC content of the *B. bronchiseptica* flagellar genes is very similar (68.1%). The GC content of the *S. enterica* genome is 52.1% while the GC content of its flagellar genes is much higher than this (56.0%).

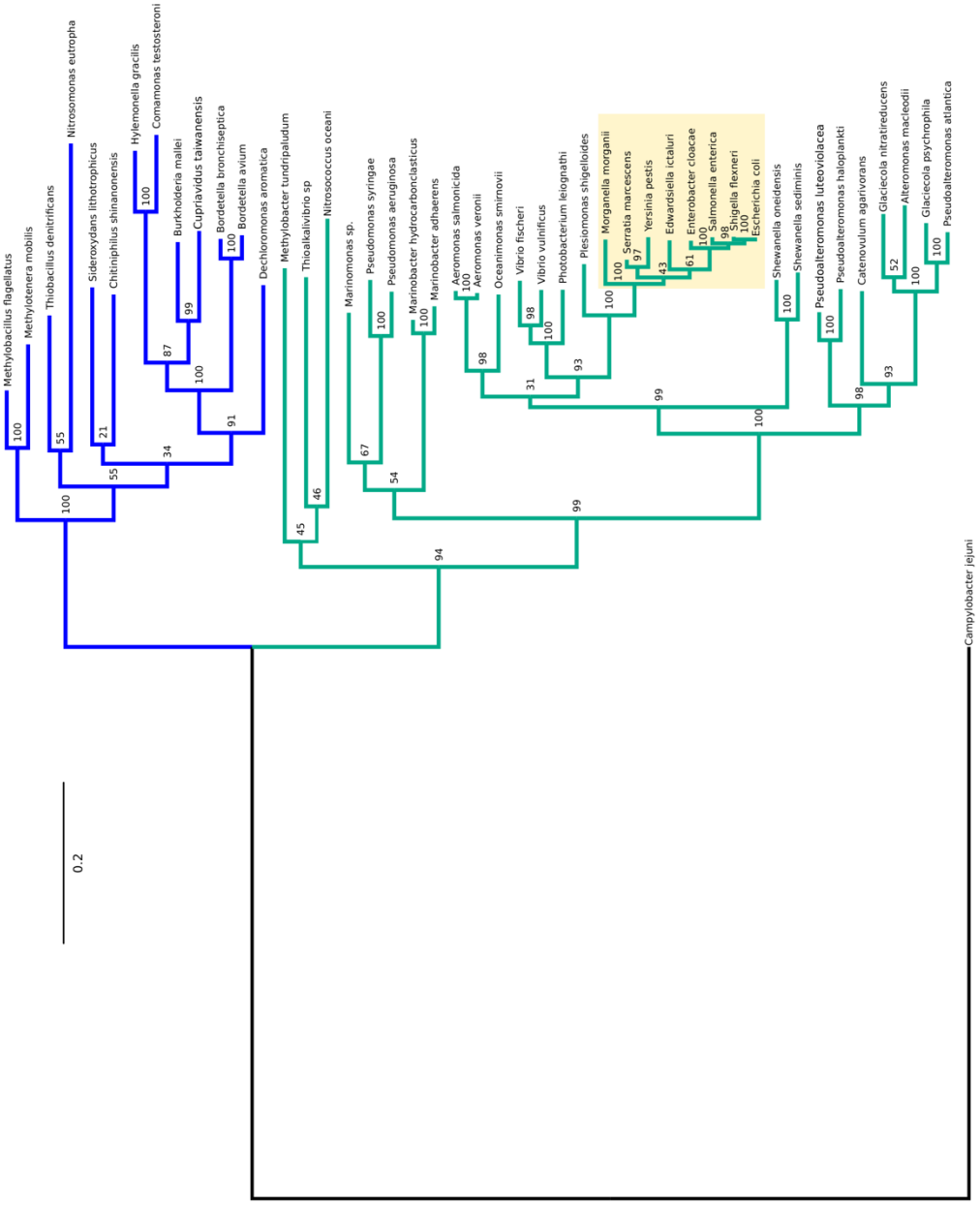


Fig. 2.5: Taxonomic tree of β- and γ-proteobacteria.
A phylogenetic tree based on a concatenation of 14 conserved ribosomal protein sequences. The γ-proteobacterial clade is in green and the β-proteobacterial clade is in blue. The eight γ- enteric bacteria included in the study are highlighted in yellow. The ε-proteobacterium, Campylobacter jejuni is used as an outlier to root the tree. The tree was bootstrapped 1000 times and bootstrap values are displayed on the nodes.

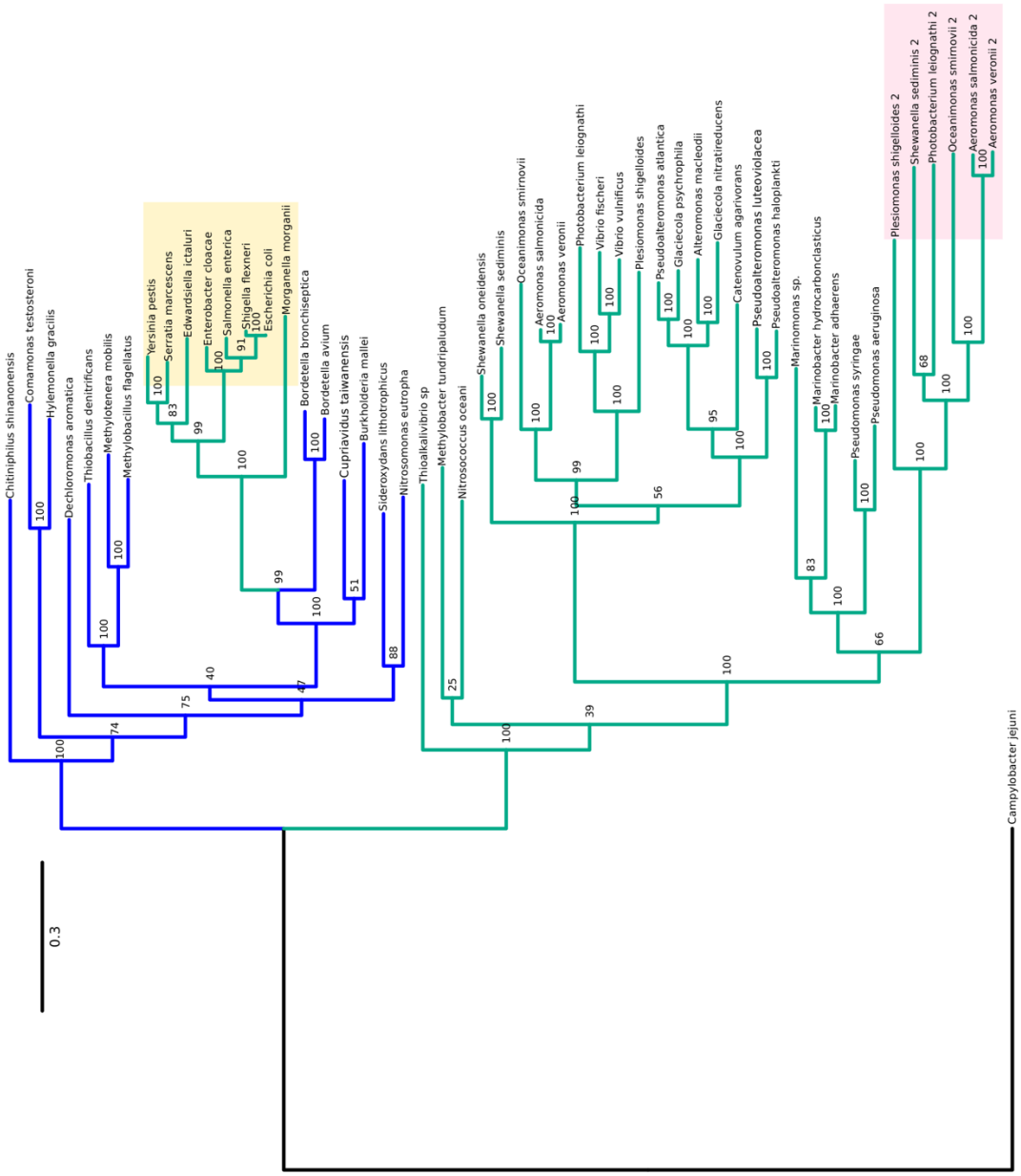


Fig. 2.6: Tree showing flagellar phylogeny.

A phylogenetic tree based on a concatenation of 10 core flagellar motor proteins. The γ-proteobacterial clade is in green and the β-proteobacterial clade is in blue. The γ-proteobacteria with polar and lateral systems are labelled with a 1 (polar) or 2 (lateral) and the lateral clade is highlighted in pink. The eight γ- enteric bacteria included in the study are highlighted in yellow. The γ- enteric bacteria are now grouped in a clade within the β-proteobacteria. This highlights a HGT that took place. The ε-proteobacterium, Campylobacter jejuni is used as an outlier to root the tree. The tree was bootstrapped 1000 times and bootstrap values are displayed on the nodes.

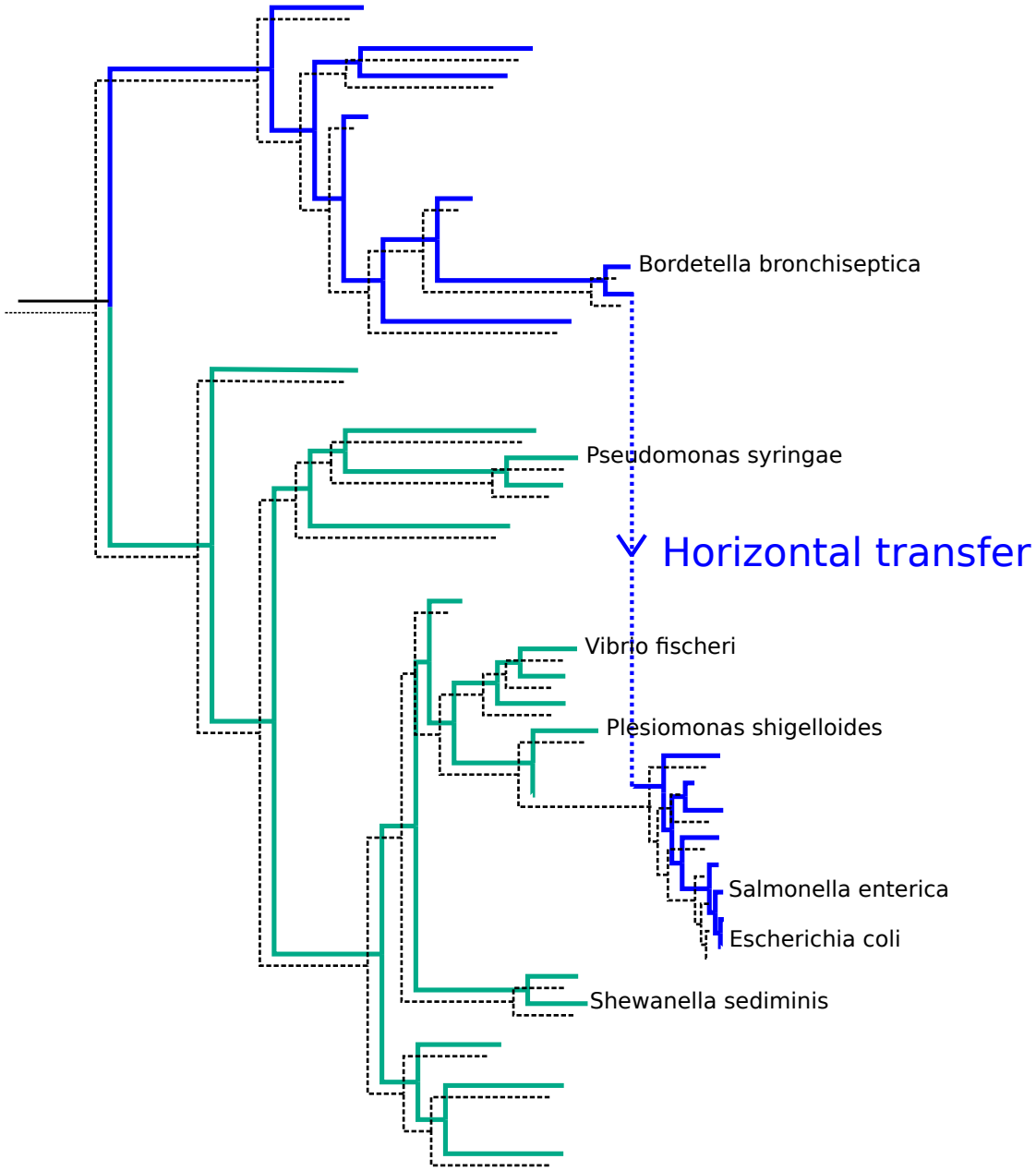
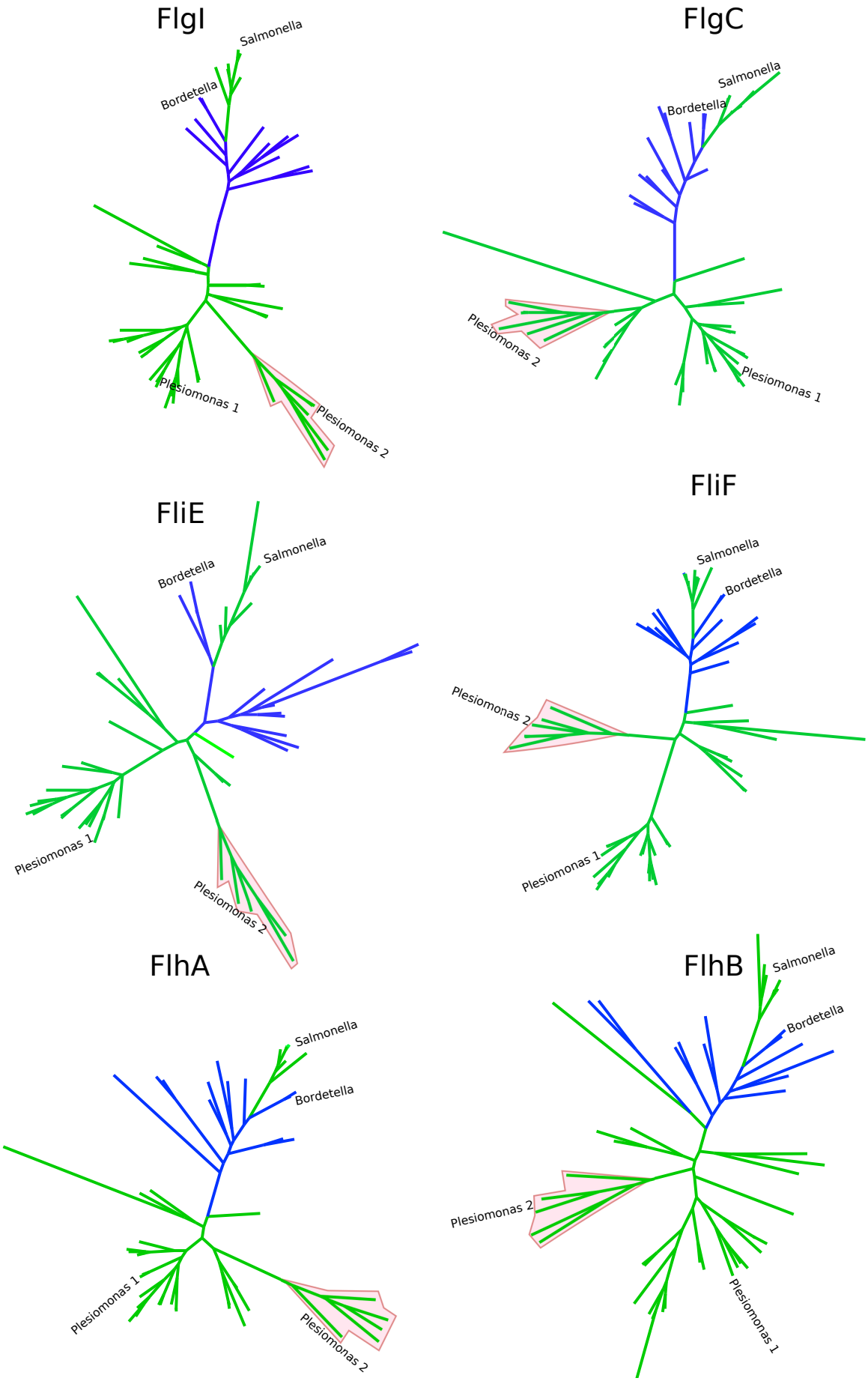


Fig. 2.7: Schematic of horizontal gene transfer.
A cartoon representing the HGT that took place. The species tree is represented in a black dotted line and the flagellar tree is represented in blue (β-proteobacteria) and green (γ-proteobacteria). This highlights that the only major difference between the taxonomic and flagellar trees is in one clade (the enterics) that moves from the γ-proteobacteria to within the β-proteobacteria. The blue dotted line highlights the HGT of DNA.


FlgI
Salmonella
Bordetella
Plesiomonas 1
Plesiomonas 2
FlgC
Salmonella
Bordetella
Plesiomonas 2
Plesiomonas 1
FliE
Bordetella
Salmonella
Plesiomonas 1
Plesiomonas 2
FliF
Salmonella
Bordetella
Plesiomonas 2
Plesiomonas 1
FlhA
Salmonella
Bordetella
Plesiomonas 1
Plesiomonas 2
FlhB
Salmonella
Bordetella
Plesiomonas 2
Plesiomonas 1

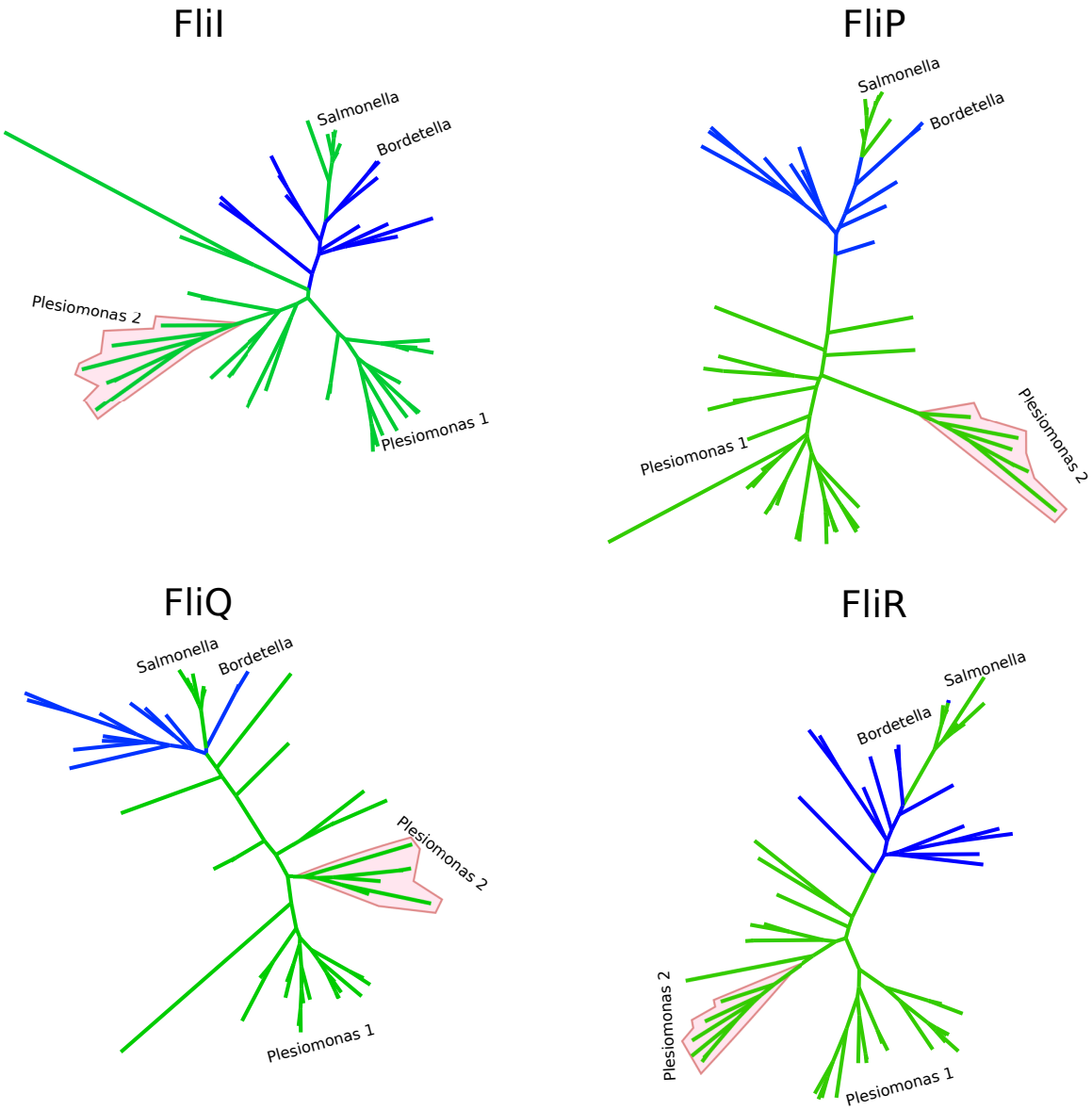


Fig. 2.8: Unrooted phylogenetic trees of individual flagellar proteins are congruent with overall flagellar tree.
Individual flagellar proteins (FlgI, FlgC, FliE, FliF, FlhA, FlhB, FliI, FliP, FliQ and FliR) show the same overall phylogeny. Blue = β-proteobacteria, Green = γ-proteobacteria, pink outline = lateral flagella from γ-proteobacteria, 1 = polar flagellum, 2 = lateral flagellum.

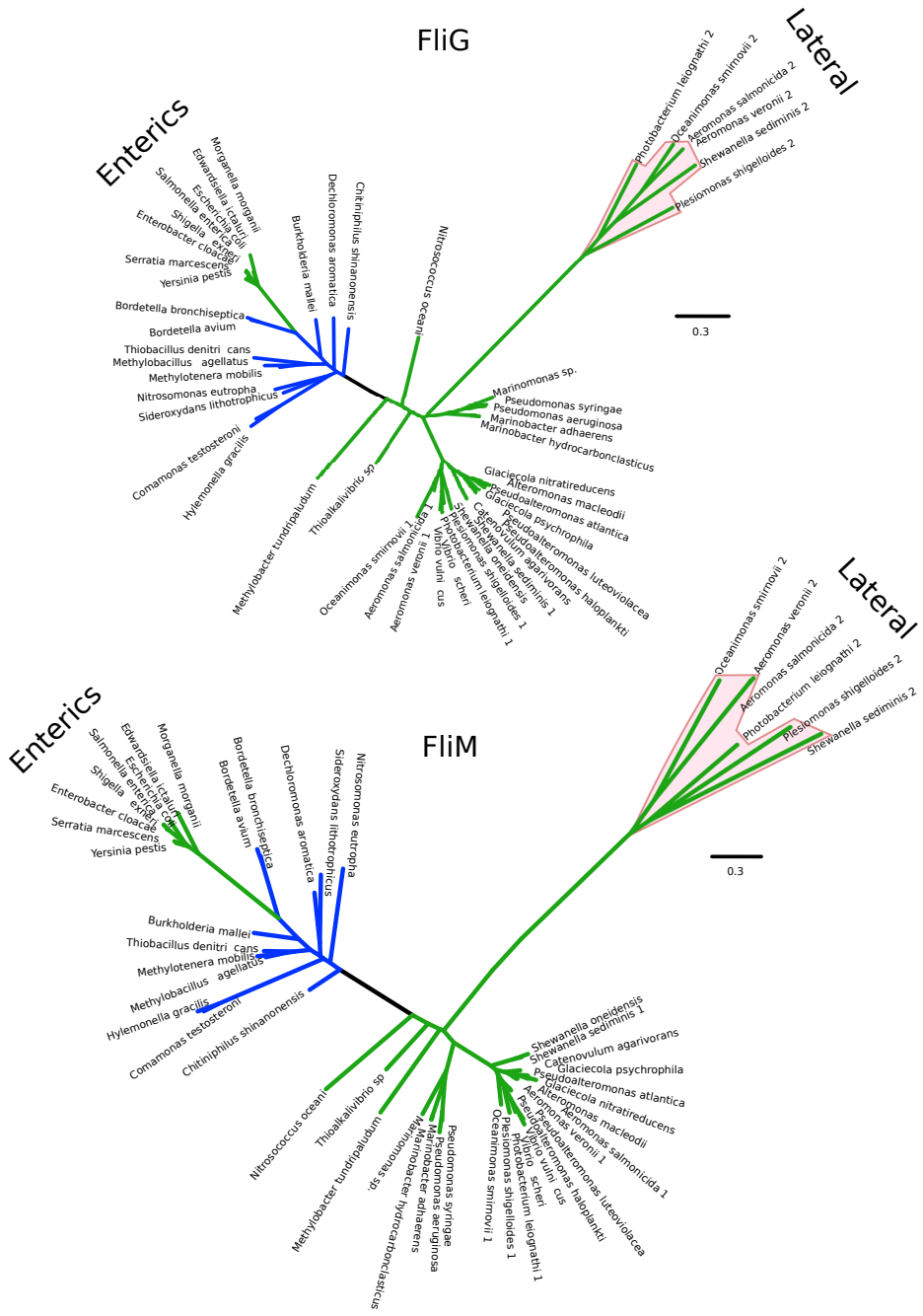


Fig. 2.9: Unrooted C-ring protein phylogeny is not congruent with overall flagellar tree.

The γ-proteobacterial lateral flagella have much longer branches in the FliM and FliG trees than other branches. Blue = β-proteobacteria, Green = γ-proteobacteria, pink outline = lateral flagella from γ-proteobacteria, 1 = polar flagellum, 2 = lateral flagellum.

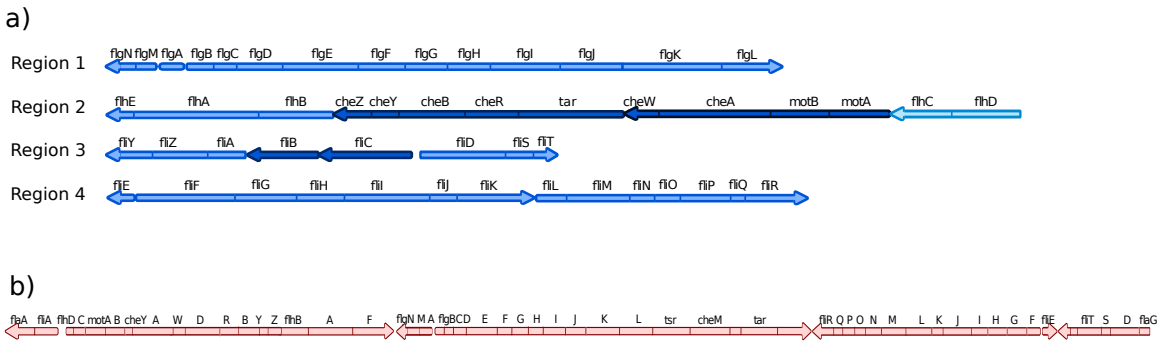


Fig. 2.10: Chromosomal context of flagellar genes supports HGT.
The flagellar genes in Salmonella are dispersed in four chromosomal regions. b) The Bordetella genes are all found in one chromosomal region supporting the easy transfer of the entire set of flagellar genes via a HGT event.

2.3.3 Structural investigations of the horizontal gene transfer

I next aimed to verify the HGT structurally, towards understanding the selective benefit of the new non-native enteric motor. To do this, I chose to image the β-proteobacterial flagellar motor that is most similar to the enteric flagellar motor as well as the γ-proteobacterial flagellar motor from the species that is most closely related to the enteric bacteria but still has a γ-like flagellar motor. These two species can be thought of as the "donor" bacterium and "acceptor" bacterium, respectively.

2.3.3a Subtomogram average of the "donor" bacterial motor

The closest related flagellar motor to the enteric motor is the motor from the *Bordetella* species. Although *Bordetella* is a β-proteobacteria, the enteric bacteria are found beside *Bordetella* in the flagellar phylogenetic tree (Fig. 2.6). From the placement in the flagellar tree we can assume that an ancestor of *Bordetella* was the donor bacterium that provided the new flagellar genes to an ancestor of *Salmonella*, and the other enteric

bacteria. Due to the closely related sequences of the flagellar motors from *Salmonella* and *Bordetella*, these two motors should have similar structures.

WT *Bordetella bronchiseptica* does not produce flagella under standard lab conditions (Fig. 2.11a), I therefore moved to a Δ*BvgS* strain (Bvg-), lacking part of the two component system involved in suppressing flagellar expression [105]. This strain produced peritrichous flagella under standard lab conditions (Fig. 2.11b-c). Due to the placement of flagella, and thickness of cells, and because over-expression of *ftsZ* failed to produce mini-cells in this strain, cells were gently lysed by treatment with Penicillin G (Fig. 2.12a). Lysis occurs due to the inability of cells to fix holes formed in the peptidoglycan layer in the presence of Penicillin G. Over 500 tomograms were collected, giving a total of 205 subtomograms (example in Fig. 2.12b) that were used for subtomogram averaging. As no symmetry was seen in the STA, the structure was radially averaged using C100 to increase the SNR (Fig. 2.12c).

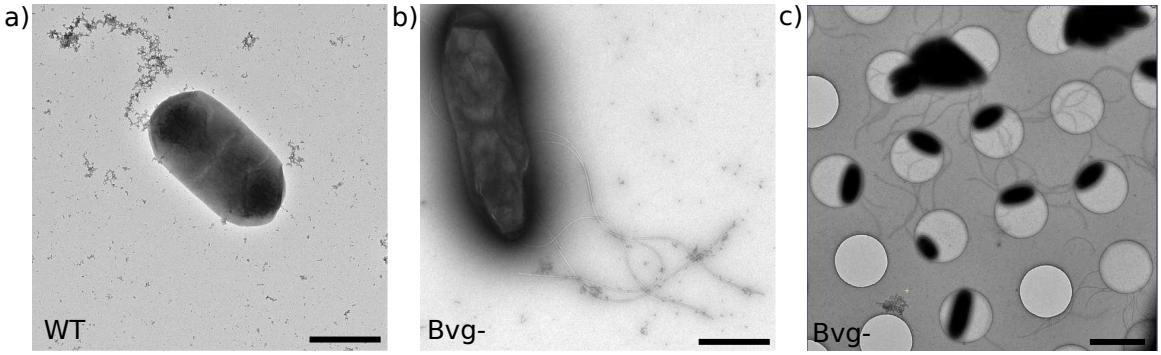


Fig 2.11: Optimisation of sample for collection of *Bordetella bronchiseptica* motor.
a) *WT B. bronchiseptica cell does not express flagella under standard lab conditions. Scale bar = 1 μm b) A B. bronchiseptica strain with a deletion in BvgS (Bvg-) constitutively expresses flagella. Scale bar = 1 μm c) Flagella are still seen on cells frozen on a cryo-grid. Scale bar = 2 μm*

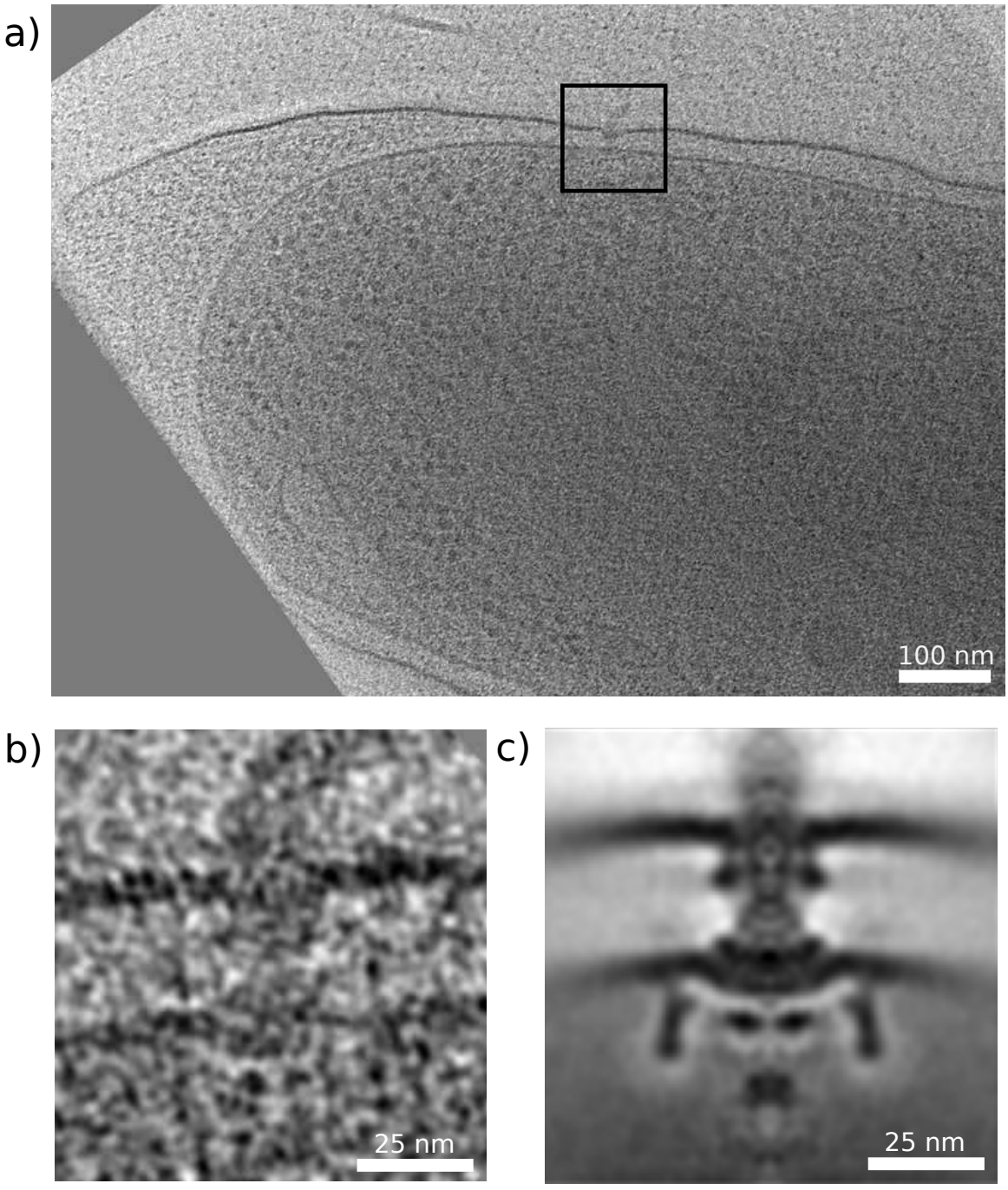


Fig 2.12: The structure of the *Bordetella bronchiseptica* flagellar motor.
a) Slice through a representative tomogram. Cells were gently lysed with Penicillin G prior to freezing. b) Example of a single subtomogram. c) Sub-tomogram average of the Bordetella bronchiseptica flagellar motor.

2.3.3b Subtomogram average of the "acceptor" bacterial motors

The closest related bacterium to the enteric bacteria that diverged from a common ancestor before the HGT took place, and therefore still possesses a native γ-proteobacterial flagellar motor, is *Plesiomonas shigelloides*. Due to the close taxonomic relation of *Plesiomonas* to the enteric bacteria, we can propose that an ancestor of modern-day enteric bacteria, such as *Salmonella* (from which *Plesiomonas'* motor is a direct descendant) once had a motor more similar to *Plesiomonas* than the motor that modern day *Salmonella* has now.

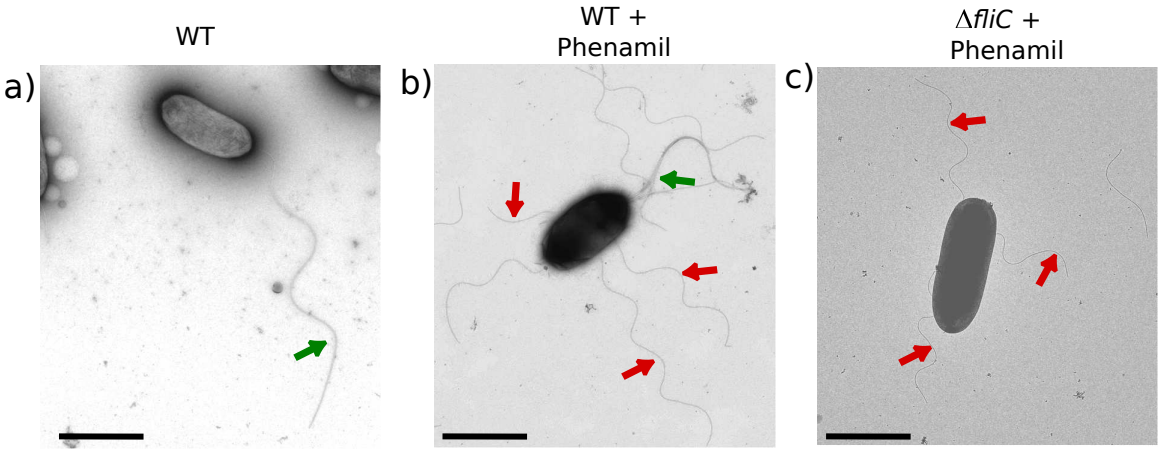


Fig 2.13: Optimisation of sample for collection of *Plesiomonas shigelloides* lateral flagellar motor.
a) WT cells only express polar flagella when grown in liquid medium. Scale bar = 1 µm b) Addition of the sodium-channel inhibitor Phenamil produces lateral flagella in liquid medium. Scale bar = 1 µm c) To distinguish between lateral and polar flagella, the polar flagellar filament protein (FliC) was deleted. The ΔfliC strain with addition of Phenamil results in cells with only lateral flagella. Scale bar = 1 µm. Green arrows point towards polar flagella (with long wave-forms), red arrows point towards lateral flagella (with short wave-forms).

In order to analyse the native γ-proteobacterial flagellar motor that the enteric bacteria lost after the HGT took place, *Plesiomonas shigelloides* was studied. To structurally understand the HGT, both polar and lateral flagellar systems need to be studied. When *P. shigelloides* cells are grown in liquid medium, only polar flagella are expressed and the lateral flagellar system is repressed (Fig. 2.13a). However, when the sodium channel inhibitor Phenamil was added, blocking powering of the polar motors, cells had both polar and lateral flagella (Fig. 3.13b). In order to differentiate the lateral from the polar motors (as lateral flagella are placed anywhere on the cell, including close to the pole), the polar filament protein fliC, was deleted. When in the presence of Phenamil, the resultant ΔfliC strain only contains lateral flagellar filaments (Fig. 2.13c). Due to the thickness of the cells, placement of flagella and inability to produce mini-cells with an ftsZ over-expression plasmid, cells were gently lysed by the addition of Penicillin G to the growth medium prior to freezing (Fig. 2.14a), as with *Bordetella* (Fig. 2.12a). 632 tomograms were collected, giving a total of 317 subtomograms. In some of the subtomograms a density for the C-ring was clearly seen (Fig. 2.14c), however in most of the subtomograms no clear C-ring density was seen (Fig. 2.14b). In the subtomogram average, a faint, short C-ring is seen (Fig. 2.14d). As no symmetry was seen in the STA, the structure was radially averaged using C100 to increase the signal to noise ratio (Fig. 2.14d).

Due to the placement of the polar motors on the thinnest area of the cell, data collection of the polar flagellar motor was done using WT cells without extra thinning from lysis. 107 tomograms were collected and a total of 389 subtomograms (Fig. 2.15a) were used for the STA. As 13-fold symmetry was clearly seen (Fig. 2.15d), the average was symmetrised by C13 to increase the signal to noise ratio (Fig. 2.15c, e).

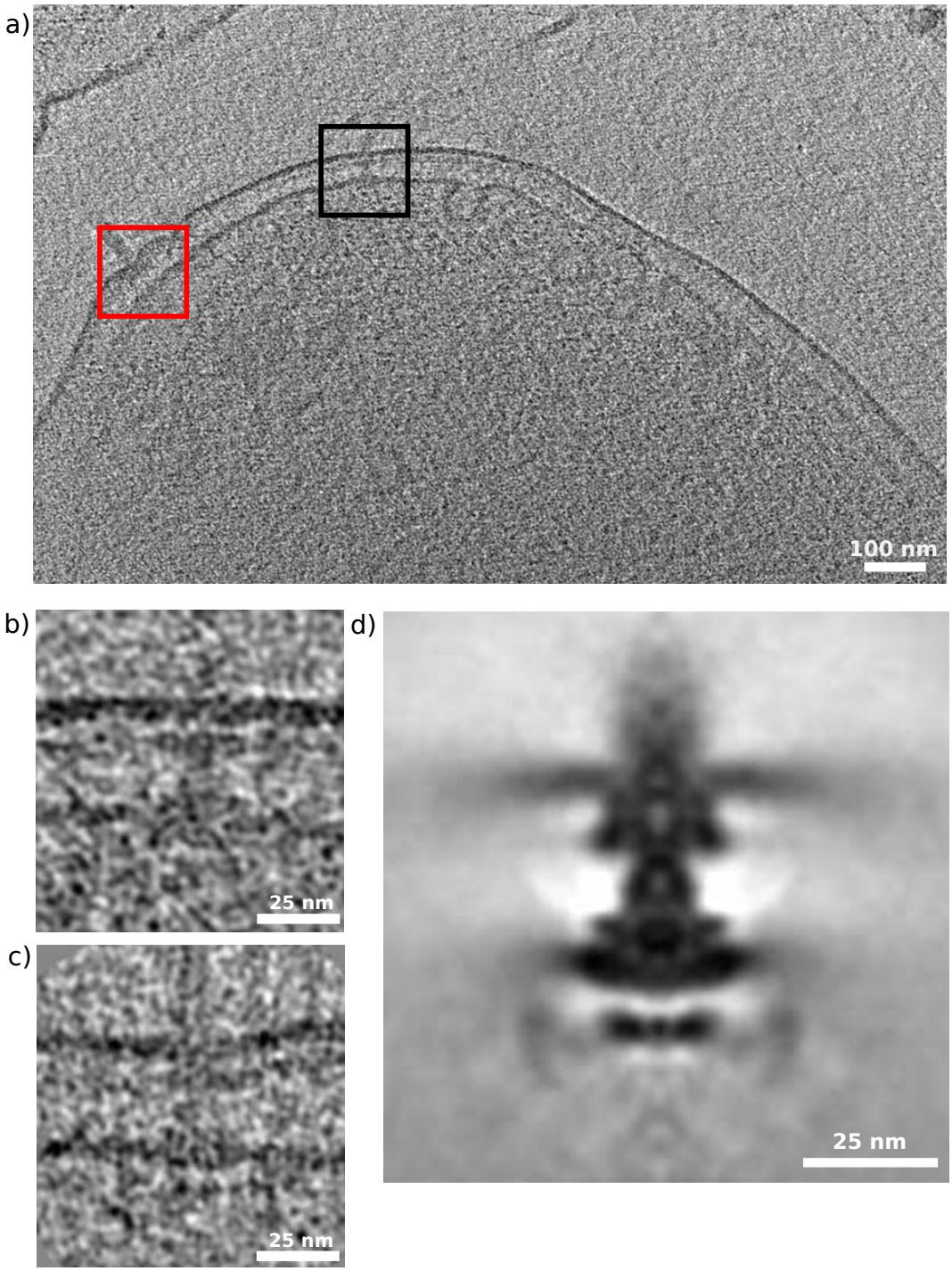


Fig 2.14: The structure of the *Plesiomonas shigelloides* lateral flagellar motor.
a) Slice through a representative tomogram. Cells were gently lysed with Penicillin G prior to freezing. Red box highlights polar motor and black box highlights lateral motor. b) Example of a single subtomogram without a clear density for a C-ring. c) Example of a single subtomogram with a clear density for a C-ring d) Sub-tomogram average of the Plesiomonas shigelloides lateral flagellar motor.

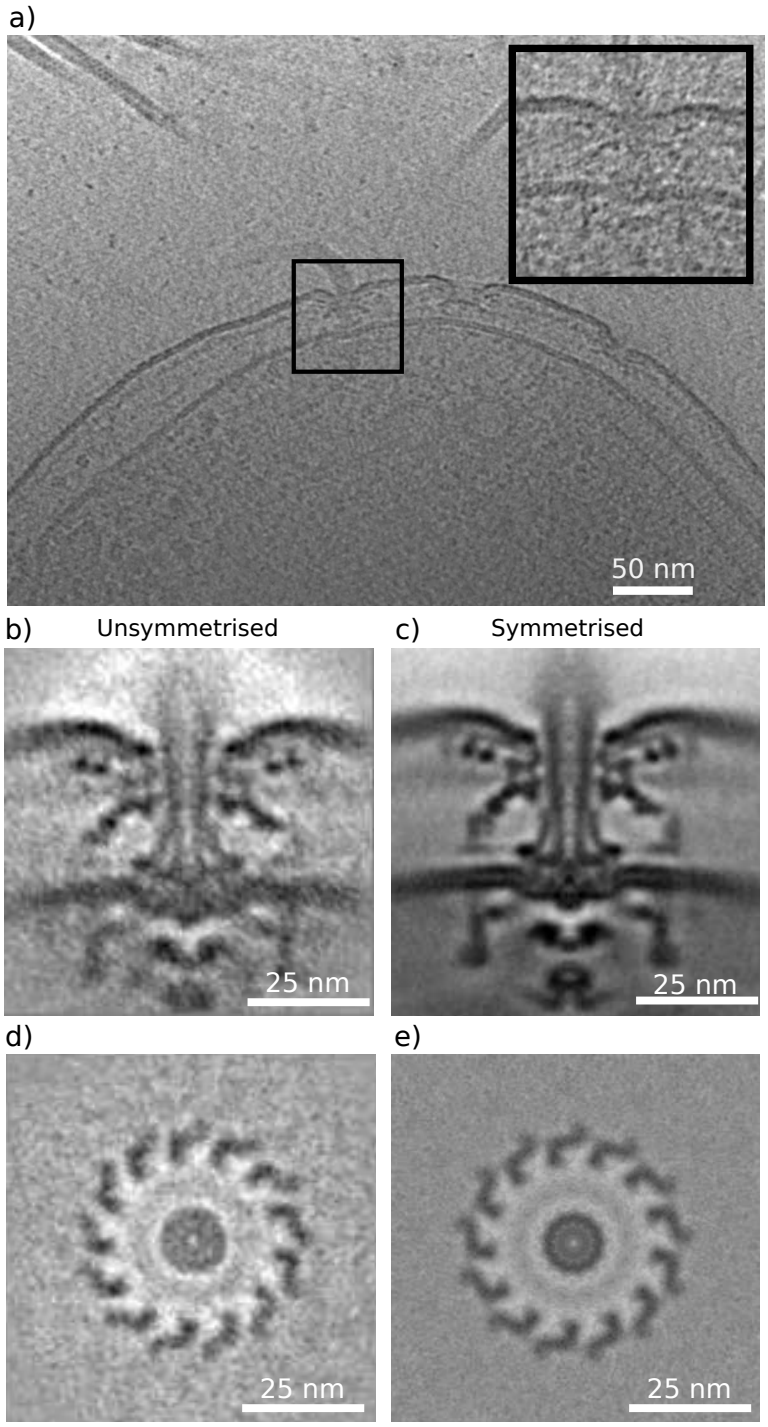


Fig 2.15: The structure of the *Plesiomonas shigelloides* polar flagellar motor.
a) Slice through a representative tomogram. Inset shows example subtomogram. b) Subtomogram average P. shigelloides polar flagellar motor before applying symmetry. c) Sub-tomogram average of the P. shigelloides polar flagellar motor after C13 symmetry was applied. d) 13-fold symmetry clearly seen in the stator complexes prior to applying 13-fold symmetry. e) Increased SNR after 13-fold symmetry was applied.

2.3.4 Structural comparisons of the *Bordetella* and *Plesiomonas* flagellar motors with the *Salmonella* flagellar motor

The *Salmonella* and *Bordetella* motors are remarkably similar at this resolution (Table 1 and Fig. 2.16). All measurements taken from sub-tomogram averages are the same (Table 1). The *Plesiomonas* polar motor is the most different, and like other polar γ-proteobacterial flagellar motors imaged to date (Fig. 2.3), this motor has multiple accessory proteins. This motor also has clear protein densities where the stator complexes are expected to be, but which are missing in the other three structures (Fig. 2.16). The *Plesiomonas* lateral flagellar motor is very simple, lacking any additional proteins and has a faint density where the C-ring is expected. Due to the extra disks made of accessory proteins on the polar *P. shigelloides* motor, the P-ring is lower in this motor (Table 1).

Table 1: Structural comparisons of the four γ- and β-proteobacterial flagellar motors.

	C-ring radius	IM to OM	MS-ring to P-ring	P-ring to OM
Salmonella	20 nm	29 nm	15 nm	10 nm
Bordetella	20 nm	29 nm	15 nm	10 nm
Plesiomonas lateral	22 nm	32 nm	15 nm	10 nm
Plesiomonas polar	22 nm	32 nm	13 nm	12 nm

A table listing four different measurements taken from the centre of each protein density.

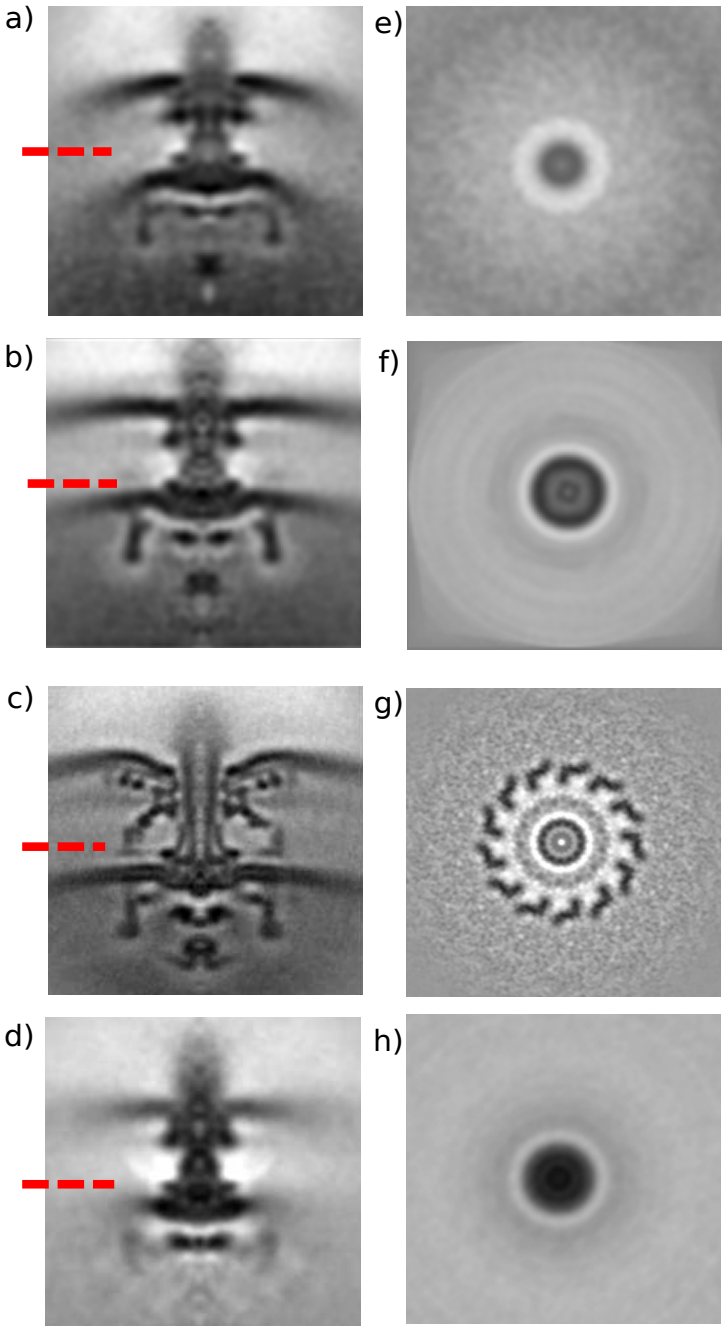


Fig 2.16: The β-like motor has dynamic stator complexes.
Left-hand panel: Slice through the subtomogram averages of a) Salmonella b) Bordetella bronchiseptica c) Plesiomonas shigelloides polar d) Plesiomonas shigelloides lateral. Red line points to expected position of the stator complexes. Right-hand panel: Subtomogram averages rotated around the red line in the top panel to show a cross section through the stator complexes in e) Salmonella f) Bordetella bronchiseptica g) Plesiomonas shigelloides polar h) Plesiomonas shigelloides lateral.

2.4 Discussion

In this Chapter, I show that the enteric bacteria do not have a native γ-proteobacterial flagellar motor but rather acquired it via a HGT from the β-proteobacteria. By comparing phylogenetic trees made from either a concatenation of ribosomal proteins or core flagellar proteins, it is clear that the enteric bacteria do not have flagellar motors that are similar to the motors from closely related bacteria, but rather have motors similar to the β-proteobacteria. By studying the subtomogram averages of the motors from the "donor" and "acceptor" bacteria, I structurally confirm the HGT. The structures show that the enteric motor from *Salmonella* (γ) is not only genetically but also structurally more similar to the *Bordetella* motor (β) than the *Plesiomonas* motors (γ) (Fig. 2.17).

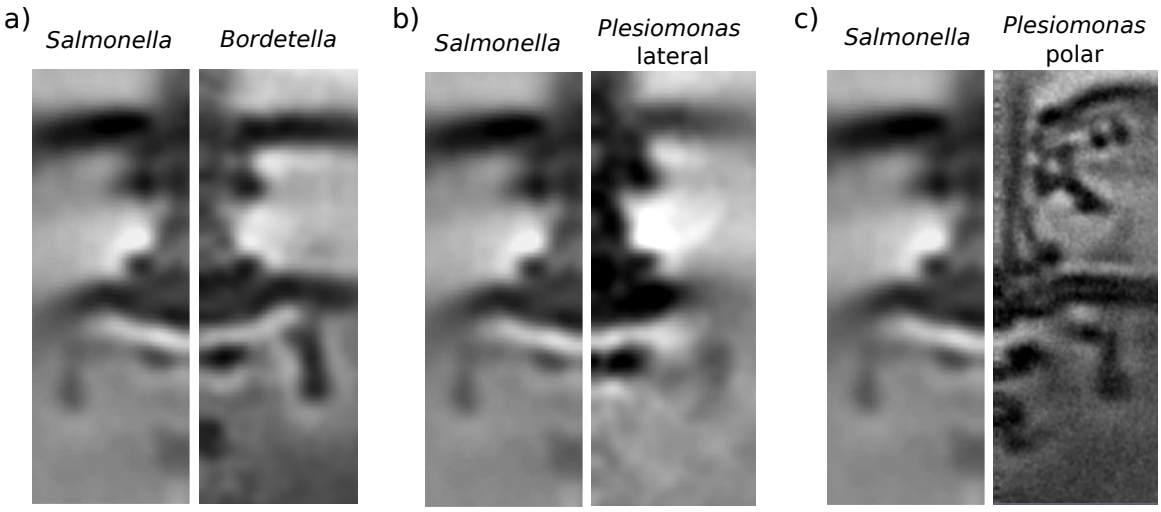


Fig. 2.17: The *Salmonella* flagellar motor is structurally similar to the *Bordetella* motor.
a) Salmonella motor (left) compared with the Bordetella motor (right). b) Salmonella motor (left) compared with the Plesiomonas lateral motor (right). c) Salmonella motor (left) compared with the Plesiomonas polar motor (right). Note: The Salmonella motors are slightly rotated to make the membranes parallel.

When analysing the structures, one of the main differences between the β-like motor and the γ-like motor, is the appearance of stator complexes in the γ-like polar motor (Fig. 2.16). This structural difference is likely due to a difference in stator complex occupancy in the different flagellar motors. It has been shown previously that the stator complexes in the enteric motor are dynamic and only assemble on the motor when more torque is required due to increased load (See Chapter 4). Due to the dynamic nature of these stator complexes, they do not appear in subtomogram averages. The polar motor from *P. shigelloides* however, has clear stator complexes showing that in this motor the stator complex occupancy is higher and the motor is always running at a high torque.

2.4.1 *Salmonella* traded two highly specialised motors for one more general motor

The enteric bacteria swapped two native γ-proteobacterial flagella for one, non-native β-proteobacterial flagellum (Fig. 2.18). The native γ-proteobacterial flagella are both highly specialised. The lateral flagellum is only used for swarming on solid surfaces, is not chemotactic, can only rotate in a CCW direction, and uses proton motive force for powering rotation [106–108]. The polar motor is only used for swimming in liquid medium, is chemotactic and is powered by the sodium motive force. The polar motor has high occupancy stators, a constant high torque and energy expenditure. The peritrichous motor of *Salmonella* is a more general motor. It is used for both swimming and swarming, is driven by protons and has dynamic stators giving it variable torque and energy expenditure. This is summarised in Table 2.

The native γ-proteobacterial motors are extremely specialised for two separate modes of motility. The high-torque, Na^+-driven polar motors ensure very fast, directed motility in liquid medium. The lateral motors are only expressed when on a solid surface.

Table 2: Functional comparisons of the three γ-proteobacterial flagella.

	***Plesiomonas* lateral**	***Plesiomonas* polar**	***Salmonella***
Function	Swarming	Swimming	Swarming and swimming
Chemotaxis	Non-chemotactic	Chemotactic	Chemotactic
Energy source	Protons	Sodium ions	Protons
Torque	?	Constant high	Variable
Energy expenditure	?	Constant high	Variable
Overall	Specialised	Specialised	General

A table listing the important functional aspects to be considered.

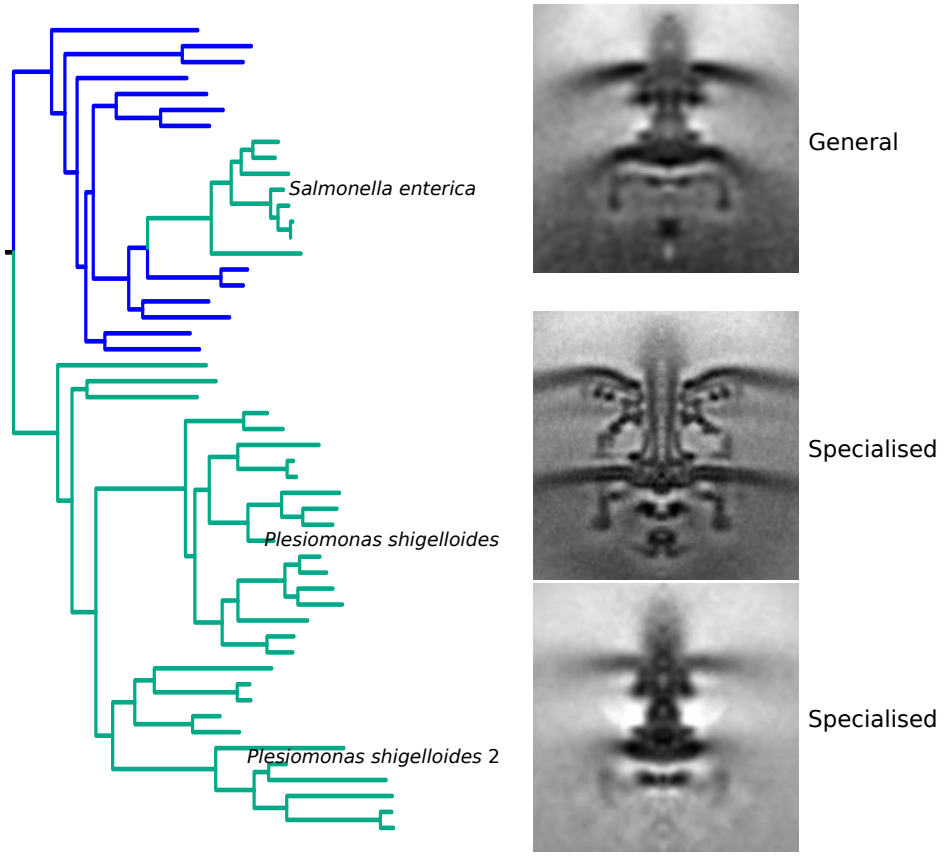


Fig. 2.18: *Salmonella* swapped two specialised flagellar motors for one more general motor.
Left: Flagellar tree. Right: The two highly specialised motors (bottom) were swapped for one general purpose motor (top).

2.4.2 Could the new flagellar motor have enabled colonisation of the gastrointestinal tract?

All bacteria closely related to the enterics are aquatic. The enteric bacteria are the exception to this and their new niche may have been enabled by the acquisition of the β-flagellar system. As all enteric bacteria have the new flagellar motors but *Plesiomonas* does not, and because it is unlikely to have occurred more than once, the HGT likely occurred after *Plesiomonas* diverged from the common ancestor of the enteric bacteria but prior to the divergence within the enteric bacteria. I speculate that the new flagellum may have enabled the colonisation of *Salmonella's* new gastrointestinal niche and highlight some of its key features below.

Stator occupancy

Moving from a motor with high-occupancy stators to one with dynamic stators could be a selective benefit of the HGT. This may provide selective benefits in the dynamic environment of the gut as the motor is primed for encountering different environmental viscosities, enabling it to swim very quickly (low torque, high speed) in low viscosities as well as allowing it to push its way through the thick gut mucous (high torque, low speed). This dynamic motor may be a more energy efficient, as ion channels are only open in the stator complexes when bound to the motor making re-establishment of ion gradients easier in low viscosities than the *Plesiomonas* motor that has higher occupancy stator complexes.

Flagellar position and response to viscosity

Another change is in the placement of motors. The general β-flagella are peritrichous, as opposed to polar. In bacteria with polar flagella, two proteins FlhF and FlhG are involved in placing the correct number of flagellar at the pole. The peritrichous location of flagella provides a very different form of motility and response by the chemotaxis system. Cells with peritrichous flagella swim with the well-known "run-tumble" mechanism of the enteric bacteria. Bacteria with polar flagella use the "forward-

reverse-flick" mode of swimming and responding to chemotactic signals. An increase in viscosity would slow down motor rotation in both cell types however, it also inhibits flagellar flicking for reorientation in polarly flagellated cells [96,109]. This means that the cells are not only slower, but are not as good at responding to chemotactic signals in high viscosity medium. The run-tumble chemotactic trajectory of the enteric bacteria with peritrichous motors however, is not affected by viscosity.

Ion motive force

A final change in the motors is the switch from Na^+- to H^+-driven motors. Moving from a Na^+-driven motor to one driven by protons may have enabled the switch from a high salt aquatic environment to the lower pH of the gut.

2.4.3 Why doesn't the *Plesiomonas shigelloides* lateral motor have a clear C-ring?

The lateral flagellar motor structure from *Plesiomonas shigelloides* does not have a clear C-ring (Fig. 2.14, 2.16). This is the first structure of a lateral flagellar motor and so no precedence from other structures can be used. One scenario is that the lack of a C-ring is due to its loss during lysis of the cells. However, this is unlikely due to a number of different lines of evidence. First, in the same tomograms from which the lateral motor subtomograms were extracted, the polar flagella have clear C-ring densities visible. Second, after lysing the cells and immediately prior to vitrification, the cells were examined under the light microscope and were still swimming. This is inconsistent with loss of a major component of the flagellar motor. Third, there does not appear to be a correlation between the appearance of C-ring densities in the subtomogram averages and the extent to which a cell was lysed. Fourth, the *Bordetella* cells were lysed and imaged in the same way and the *Bordetella* structure has a C-ring. And finally, I was following the protocol from previously solved subtomogram averages of the *E.coli* and *Salmonella* flagellar motors, which still have C-rings [5]. From this I am confident that the lack of a C-ring is not due to the sample preparation but rather a genuine feature of the lateral flagellar motor.

The next question is therefore, why doesn't the lateral motor have a clear C-ring and what is the significance of this? A likely explanation is the role of the C-ring in chemotaxis in polar and peritrichous motors. The lateral flagellar motors are not chemotactic [107] and therefore communication between the motor and the chemoreceptors via CheY's interaction with FliM is not necessary. This may mean that the C-ring in these motors are more dynamic and cyclically disassemble and assemble when needed. It may also be the case that instead of a continuous "ring" as in chemotactic motors, the C-ring in lateral motors may only be made of a set number of discrete columns, which are being lost in the averaging process due to the quality of the data. This is the case in the *Salmonella* SPI-1 injectisome, which has six discrete posts [110]. However, another role of the C-ring is to stabilise FliI via the extended helices of FliH. This should also be the case if the C-ring was made of a series of non-continuous posts, and a very clear FliI density is seen in the injectisome structure. However, in the lateral structure FliI is also absent, again pointing to a more dynamic C-ring (Fig. 2.19).

When phylogenetic trees were made of individual C-ring proteins, FliG and FliM, they were incongruent to the other flagellar gene trees (Fig. 2.9). The γ-proteobacterial lateral flagella C-ring proteins had long branches and have diverged faster due to different selective pressures. This may be due to losing the ability to act as a "switch-complex", communicating between the flagellum and the chemoreceptor arrays. The C-ring protein trees are consistent with not seeing clear C-ring densities in the subtomogram average of the *P. shigelloides* lateral flagellum.

2.4.4 What is the extra density in both of the *Plesiomonas* FlhAs?

One unusual feature that both flagellar motor structures of *P. shigelloides* have is an extra density in the FlhA ring (Fig. 2.19). This is not seen in any of the other flagellar motor structures studied to date however, in the structure of a homologous protein (InvA) in the SPI-1 injectisome an extra density is seen in the same place (Fig. 2.19) [110]. One

possibility is that this is a substrate, prior to secretion through the T3SS. Why this is only seen in *Plesiomonas* flagellar motors is unclear.

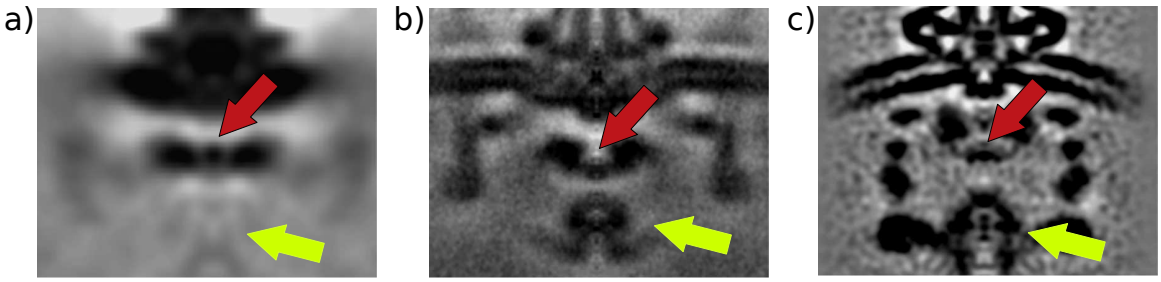


Fig. 2.19: Extra density in *Plesiomonas* FlhA is also seen in the SPI-1 injectisome homologue.
a) Plesiomonas lateral flagellar motor cytoplasmic components. b) Plesiomonas polar flagellar motor cytoplasmic components. c) SPI-1 injectisome cytoplasmic components (EMD-8544). Red arrows point to extra density. Yellow arrow points to FliI.

2.5 Materials and methods

Table 3: Chapter 2 list of strains

Strain	Source
Plesiomonas shigelloides ATCC 14029 WT	DSMZ (DSM-8224)
P. shigelloides Δ*fliC*	This study
Bordetella bronchiseptica WT RB50	DSMZ (DSM-13414)
Bordetella bronchiseptica RB54 Bvg-	Andrew Preston, University of Bath

2.5.1 Bacterial growth

Cells were grown overnight at 37°C, shaking at 290 RPM. A 1:100 dilution of the culture was then grown to an OD_{600} of 0.6. For lysis, Penicillin G (466 IU/ml) was added to samples when stated for half of one doubling event.

2.5.2 Phylogenetic analysis

Flagella (FlgI, FlgC, FliE, FliF, FlhA, FlhB, FliI, FliP, FliQ and FliR) and ribosomal protein (RplA, RplB, RplC, RplD, RplE, RplF, RplI, RplJ, RplK, RplM, RplN, RplO, RplP, RplQ, RplR) sequences were stored in WebApollo [111]. Sequences were aligned using Fast Statistical Alignment (FSA) [112]. The T-Coffee Suite was used to determine informative positions using the transitive consistence score (TCS) [113,114]. Sequences were concatenated in Seaview [115].The Maximum-likelihood approach was used within Garli [116] using the Jones, Taylor and Thornton (JTT) amino acid substitution rates [117].

Trees were created from the best of ten replicates. A topology improvement of 0.0001 in the lnL score and termination criterion of 100,000 were used. 1000 bootstraps were calculated with a topology improvement of 0.01 in the lnL score and termination criterion of 10,000. Bootstraps were added to the tree using SumTrees [118] and trees were visualised in FigTree [119].

2.5.3 Negative stain grid preparation

3µl of cells were placed on glow-discharged continuous-carbon grids (Taab Laboratory Equipment Ltd.). The grids were stained with 2% Uranyl Acetate and stored at room temperature prior to imaging.

2.5.4 Negative stain EM imaging

Negative stain images were collected on either an FEI Tecnai G2 Spirit BioTWIN (Tungsten) using an Eagle CCD camera or a Tecnai T12 TWIN (LAB6) using a TVIPS F216 CCD camera.

2.5.5 Cryo-grid preparation

Mini-cell pellets were mixed with gold fiducials coated in BSA. 3µl of the cell fiducial mixture was applied to freshly glow discharged R2/2, 300mesh gold Ultrafoil or copper Quantifoil R2/2 grids (Quantifoil Micro Tools GmbH, Germany). A Vitrobot Mark IV was used to freeze grids in an ethane/propane cryogen at 100% humidity.

2.5.6 Tilt-series collection

Tilt-series of *B. bronchiseptica* and *P. shigelloides* lateral motors were collected on an FEI F20 with a Falcon II detector (Thermo Fisher Scientific (formerly FEI), Hillsboro, OR, USA). A total fluence of 120e-/ $Å^2$ was used and a defocus of -4µm. Tilt-series were collected at a tilt range of +-53 degrees with 3° tilt increments and a pixel size of 8.28 Å.

Tilt-series of *P. shigelloides* polar motors were collected on a Titan Krios operating at 300 kV with a post-column GIF using a 20eV slit and a Gatan K2 summit (Gatan, Pleasanton, CA) collecting 4 frames per exposure. A pixel size of 2.713 Å with a total fluence of 54 e^-/A2 and a defocus range between -3 and -5.5µm was used. The bi-directional tilt series was collected using FEI's Tomo4 (Thermo Fisher Scientific (formerly FEI), Hillsboro, OR, USA) with a tilt range of ±53 degrees and a tilt-increment of 3°.

2.5.7 Tomogram reconstruction

Tomograms of *B. bronchiseptica* and *P. shigelloides* lateral motors were reconstructed automatically using RAPTOR [157].

For the *P. shigelloides* polar dataset, Frames were aligned using UnBlur [120]. Tomoctf [77] was used to estimate CTF-parameters (tomoctffind) and correct stacks (ctfcorrectstack). Fiducials were picked from CTF-corrected stacks and tracked in IMOD [89,121]. The aligned, CTF-corrected stacks and fiducial models were used with Tomo3d to reconstruct using SIRT or WBP [90,122].

2.5.8 Subtomogram averaging

Subtomograms were picked manually from binned tomograms. Template-free alignment was carried out in PEET by superimposing all manually picked subtomograms allowing no shifts or rotations for an initial reference. Initial alignment and averaging was achieved using binned subtomograms. Unbinned subtomograms were used for further refinement.

For *P. shigelloides* polar motor: As the rod length varied, sub-tomogram averaging was carried out twice with custom masks applied to either the top ring structures or the cytoplasmic structures. As clear 13-fold symmetry was observed, 13-fold rotational averaging was applied using custom scripts. The two individual averages for the top and bottom segments were then merged into a composite structure as in [34]. For comparisons, 13-fold rotational averaging was applied to the relic structure. FSC curves were determined from the final, unsymmetrised averages using PEET's calcFSC.

For the *B. bronchiseptica* and *P. shigelloides* lateral motors: As no symmetry was observed, 100-fold rotational averaging was applied using custom scripts.

2.5.9 Δ*fliC* strain construction

To generate deletion mutants in *P. shigelloides*, two 500-600 bp flanking regions upstream and downstream of the gene of interest were amplified and fused together using appropriate primers (TCTCTGCAGGATATCCAACAAACTGGTGACCGAAAGAGC

C, TAACCCAGAATAGCCATGCTTGTAATCTCCGTT, GGCTATTCTGGGTTAATT CTTTCTCAGCCAAG, GAATTCGTGGATCCAATATCTCGGTGCGTTATACTTCG GT). Delivery into *P. shigelloides* occurred by conjugation from *E. coli* WM3064 and markerless sequential crossover into the native site of the genes using the suicide plasmid pNPTS-138-R6K [123]. Correct deletions were verified by polymerase chain reaction (PCR) using appropriate primers (TTCATTTCATCACGTGAATAAATGATGATTTTT TTAGGGT, ACACTATTGCTCAGCGATAACGAATAAATGATGTAGGAAG).

Chapter 3

The switch to a sessile state: deactivation of the bacterial flagellum under nutrient depletion

3.1 Chapter Summary

Although the flagellum is a vital virulence factor, the majority of bacteria are in the sessile state and only intermittently switch to motile planktonic lifestyles under favourable conditions. When conditions are not ideal and nutrients become scarce, bacteria conserve energy by switching to stationary phase. This switch to stationary phase involves altering their metabolism and importantly stopping swimming. It is estimated that two-thirds of motile bacteria use the flagellum to swim and although much is known about the activation and assembly of this large molecular-machine, at present, the deactivation of the flagellum for entry into a sessile state remains poorly understood. Here, I describe the mechanism of switching from planktonic to sessile states in the polarly flagellated γ-proteobacteria. Using a combination of ECT, STA, swim assays and genetics, I demonstrate that γ-proteobacteria eject their polar flagella under nutrient depletion. Filaments with attached hooks accumulate in the growth medium of these bacteria and relics of previous flagellar motors remain in the outer membrane. Strikingly, these flagellar relics contain a novel protein density that I interpret as a "plug" that prevents leakage of the periplasmic components. By showing relic structures in five different γ-proteobacteria, *Plesiomonas shigelloides, Vibrio cholerae, Vibrio fischeri, Shewanella putrefaciens* and *Pseudomonas aeruginosa*, I demonstrate that this is a wide-spread phenomenon. Bacterial flagella are energetically costly in terms of both torque generation and continual assembly; these results reveal a previously unknown mechanism used by bacteria to abort flagellar motility in order to survive in low nutrient environments.

Relevant publication: Ferreira. JL, Gao. FZ, Rossmann. FM, et al. (2019) γ-proteobacteria eject their polar flagella under nutrient depletion, retaining flagellar motor relic structures. PLoS Biol 17(3): e3000165. [124]

3.2 Introduction

The γ-proteobacteria are a diverse group of bacteria that occupy a variety of ecological niches. This group can be broadly divided into two sets of bacteria, those with native Na^+-driven, polar flagella and the enteric bacteria with non-native proton driven peritrichous flagella. In Chapter 2, I showed that the *Salmonella* flagellar motor is not native and that these enteric bacteria inherited a flagellum from the β-proteobacteria. When analysing a close taxonomic relative of *Salmonella* which retained the native γ-proteobacterial motor, *P. shigelloides*, I noticed large differences between the swimming behaviour of *Salmonella* and *P. shigelloides* which led to the work in this chapter.

3.2.1 Motility in the γ-proteobacteria

The γ-proteobacteria include important human pathogens such as *Vibrio cholerae,* as well as opportunistic pathogens such as *Pseudomonas aeruginosa, Shewanella putrefaciens and Plesiomonas shigelloides.* It also includes other non-pathogenic aquatic bacteria such as the squid symbiont *Vibrio fischeri*. These cells have between one (*Pseudomonas aeruginosa, Shewanella putrefaciens, Vibrio cholerae)* and ~ four (V*ibrio fischeri) or even up to ~12 (Plesiomonas shigelloides)* polar flagella at one pole, unless they are about to divide when the second pole is flagellated in preparation for both daughter cells to swim.

The Na^+-driven flagellar motor is both faster [125] and has a higher torque than the H^+-driven motor [34]. The structures of these motors appear more complex than the enteric motors in sub-tomogram averages, with the most obvious structural differences being the extra rings or disks in the Na^+-driven motors [5,34,126]. These "accessory" proteins act as scaffolds to stabilise the stator complexes, keeping them engaged on the motor for longer than in the very dynamic enteric motor. The periplasmic rings (H- and T-rings) assemble on the P-ring and the basal disk assembles on the L-ring, under the outer membrane (Fig. 3.1). As these flagellar motors are driven by Na^+ ions, rather than protons, their rotation is

powered by the PomAB stator complexes (homologues of the H^+-driven stator complexes MotAB). The periplasmic T-ring is composed of the flagellar proteins MotX and MotY and stabilises PomAB on the motor. This means that these motors have a higher stator occupancy and can be seen in STA (unlike the stators of *Salmonella* – see Chapter 2 and 4). Some γ-proteobacterial flagellar filaments are sheathed by an extension of the outer membrane, and the basal disk and H-ring (FlgO, FlgP, FlgT) are suggested to assist in the growth of the flagellum within this sheath [127]. As many γ-proteobacteria do not have sheathed filaments but still contain an H-ring and basal disk however, the function of these rings is likely broader than this.

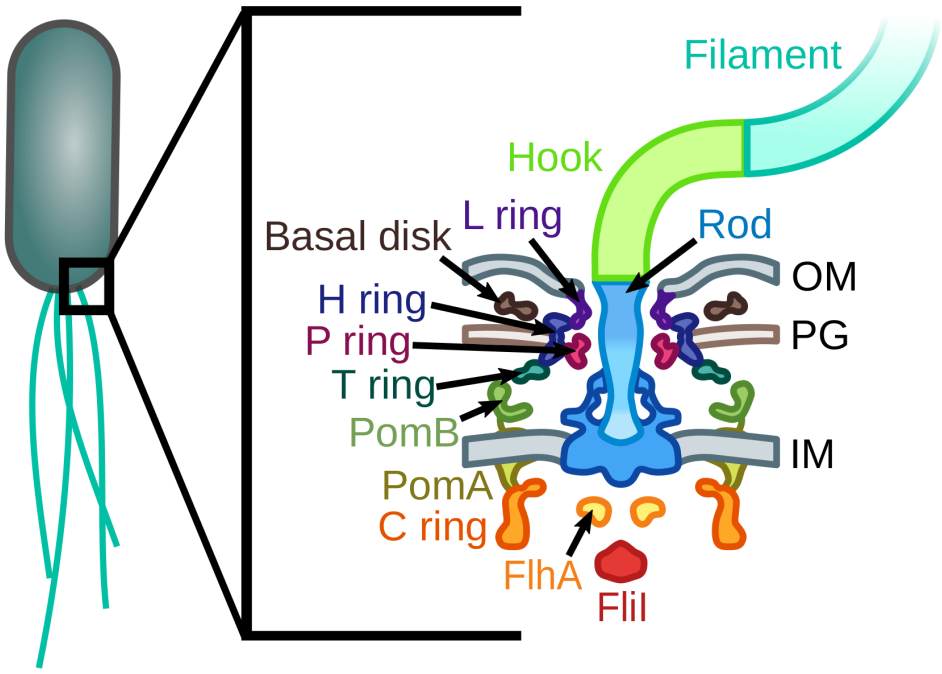


Fig. 3.1: The non-enteric γ-proteobacteria have polar Na+-driven flagella.
The most noticeable differences between the enteric motor and the other γ-proteobacterial motors are the addition of extra disks (Basal disk, H-ring and T-ring). OM = outer membrane, PG = peptidoglycan, IM = inner membrane

3.2.2 Transition from motile to sessile states

It is common for bacteria to switch between motile and sessile states dependent on a number of environmental factors. In stationary phase where nutrients become limited, for example, switching to a non-motile lifestyle conserves energy. Although the flagellum is vital, if nutrient limitation is extreme, it may become counterproductive for the cell to maintain a fully powering flagellum. In this case, putting a halt to motility is better than resource exhaustion.

Multiple examples of mechanisms for stopping swimming and entering a sessile state have been described in environments other than nutrient depletion. The enteric bacteria, *Salmonella* and *E. coli* have a "backstop brake", YcgR, which inactivates motility [128,129]. A homologue of YcgR, FlgZ, acts as a brake in the *Pseudomonas aeruginosa* flagellum [130]. The bacterial flagellum of *Rhodobacter sphaeroides* is unidirectional and also uses a brake to stop the flagellum [131]. Brownian motion then reorients the cell before it releases the brake and starts swimming in a new direction. Rather than a brake, *Bacillus subtilis* has a "molecular clutch" which disengages the motor in a reversible manor for the entry into a sessile biofilm state [132]. Finally, *Caulobacter crescentus* moves between a motile state and a stalked sessile state as part of its normal lifecycle [133]. In its sessile state it is a stalked cell, fixed by a holdfast at the tip of its stalk. When it divides, it buds off of a motile swarmer cell with one polar flagellum. In order for the motile cell to again enter the sessile state, the flagellum is ejected and a rearrangement of the cell morphology leads to the formation of the stalk at the pole where the ejected flagellum used to be [134].

Surprisingly, although the polarly-flagellated γ-proteobacteria have been intensely studied, little is known about how these bacteria switch between motile and sessile states. Here, I aim to identify how γ-proteobacteria deactivate their flagella for entry into a non-motile state shedding light on a novel mechanism for deactivation of motility for entry into a sessile state in nutrient depleted environments.

3.3 Results

3.3.1 γ-proteobacteria swim slower at increasing cell densities

Tracking the swimming speed of two γ-proteobacteria with polar Na^+-driven motors (*P. shigelloides* and *V. fischeri*) revealed that these cells have a drastic decrease in their swimming speeds at increasing cell densities (increasing growth stage). At low cell densities, these bacteria swim quickly (~ 30 -45 µm.s^{-1}) but this rapidly declines at higher cell densities (~10 µm.s^{-1}) (Fig.3.2a). This trend is unlike that of *Salmonella*, that uses H^+-driven enteric motors and swims the same or slightly better as cell density increases (Fig. 3.2a). As Na^+-driven motors are faster than proton-driven motors, a comparison of swimming speeds between bacterial species is not informative but rather the trend within a species as cell density increases. Speeds were therefore plotted relative to the initial speed at OD_{600} 0.2 (Fig. 3.2b). From this it is clear that while *Salmonella* swims better at higher cell densities than at low cell densities, *P. shigelloides* and *V. fischeri* swimming speeds are markedly slower at high cell densities than at low cell densities.

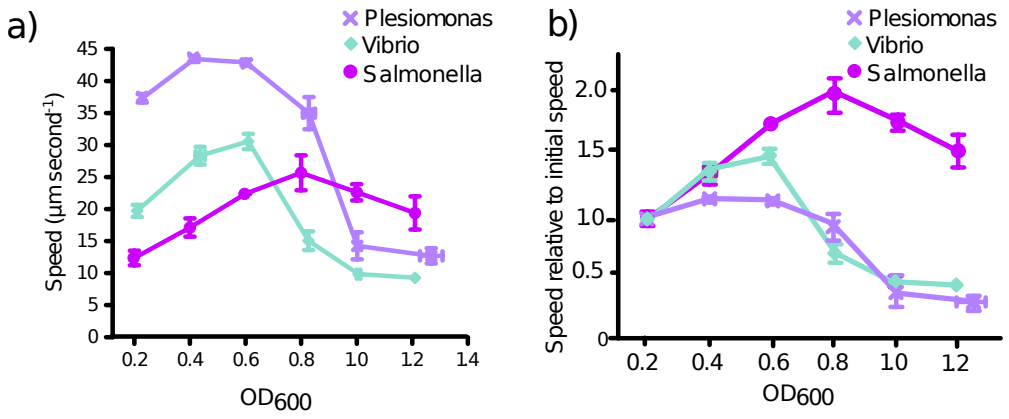


Fig 3.2. γ-proteobacteria with N+-driven polar flagellar motors swim slower at later growth stages.
a) Swimming speeds of P. shigelloides, V. fischeri and S. enterica grown to increasing cell densities. b) Swimming speeds from (a) plotted relative to the initial speed at OD_{600} 0.2.

3.3.2 Decrease in swimming speed coincides with loss in flagella

In order to investigate whether there were clear phenotypic changes to γ-proteobacterial cells at increasing cell density that could account for the trend in decreased swimming speed, negative stain EM was carried out. Three biological replicates were imaged over a time-course from OD_{600} 0.2 to OD_{600} 1.0. Strikingly, in both *P. shigelloides* and *V. fischeri*, the number of flagella per cell decreased with increasing cell density (Fig. 3.3a and b). This was not the case in *S. enterica*, where the number of flagella increased slightly or remained constant with increasing cell density.

I sought to distinguish between cells exclusively downregulating flagellar synthesis from cells losing or ejecting flagella. We can make assumptions about the state of flagellar assembly or disassembly using an estimate of the absolute number of flagella in a population, attached to cells. If assembly is occurring at a constant rate, the absolute number of flagella in the population will increase linearly. If flagella synthesis is inhibited, the absolute number of flagella in a population will remain constant. If, however, disassembly is taking place, the absolute number of flagella in the population will decline. A combination of flagella synthesis inhibition and disassembly of flagella would have a steeper decline. To calculate the absolute number of flagella in the population, the colony forming unit was calculated at each OD_{600} and multiplied by the mean number of flagella per cell (from negative stain EM data) (Fig. 3.3c). Again, *Salmonella* was used as a negative control. From these results it is clear that although *Salmonella* continues to synthesis flagella at high cell densities leading to an increasing absolute number of flagella in the population, the absolute number of flagella in the *P. shigelloides* and *V. fischeri* populations decrease as cell number increases, confirming the loss or ejection of flagella at high cell densities.

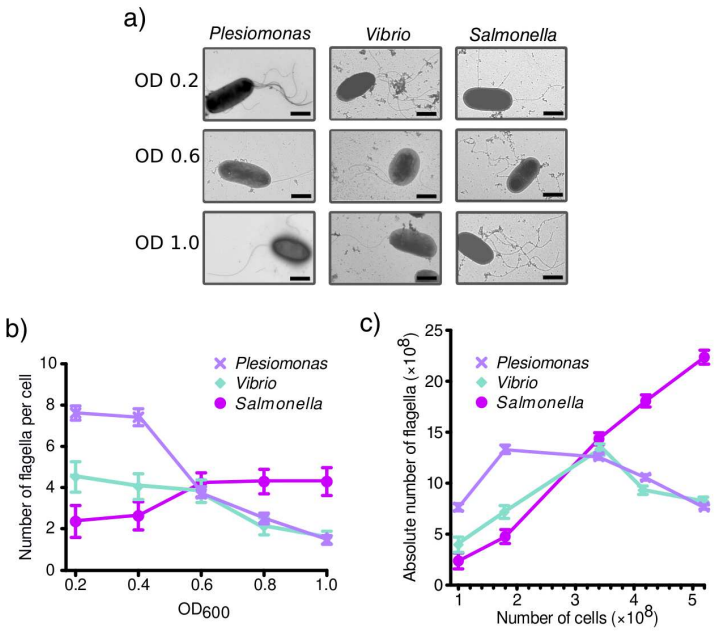


Fig 3.3. Decrease in swimming speed at later growth stages is due to loss of flagella. *a) Negative stain micrographs of Plesiomonas, Vibrio and Salmonella grown to increasing cell density (later growth stages). Scale bars are 1μm. b) The average number of flagella per pole counted from negative stain EM micrographs of cells harvested at different cell densities (150 cells counted for each OD_{600} – 50 per biological replicate). The error bars indicate a 95% t-based confidence interval. c) The absolute number of attached flagella in the population. Calculated from the mean number of flagella from (b) and the CFU at each OD_{600}. The error bars indicate a 95% t-based confidence interval. Adapted from Ferreira et al. [124]*

3.3.3 γ-proteobacteria eject flagella at the base of the distal rod

To confirm that *P. shigelloides* cells are losing flagella, and *Salmonella* cells are not, high OD_{600} cells were spun down and PEG precipitation was performed on the supernatant. The precipitate was analysed with negative stain EM. Unexpectedly, flagella were seen in both *P. shigelloides* and *Salmonella* precipitate. However, although hooks were seen on ~ 50% of flagellar ends (therefore 100% of flagella had a hook) in *P. shigelloides* (Fig. 3.4a), no hooks were seen on *Salmonella* filaments (Fig. 3.4b). *Salmonella* filaments are fragile and I expect that all filaments seen in the supernatant have been mechanically damaged. The appearance of hooks on all *P. shigelloides* filaments

confirms that the break point is consistently at the base of the hook or distal rod, unlikely to be caused by mechanical breakage.

To confirm the presence of hook (FlgE) and filament (FliC) proteins in the *P. shigelloides* supernatant but only filament protein in the *Salmonella* supernatant, an SDS-PAGE analysis of the precipitated supernatant was carried out. As expected the FliC band was stronger in *P. shigelloides* than in *Salmonella*. *P. shigelloides* also had a large FlgE band but no band was seen at the expected weight of the *Salmonella* hook protein (Fig. 3.4c). A faint band at the correct molecular weight for FlgG (distal rod) was also seen in the *P. shigelloides* supernatant. Together the negative stain and SDS-PAGE analysis shows that γ-proteobacteria with Na^+-driven polar motors lose flagellar filaments with attached hooks and distal rods, which accumulate in the supernatant at high cell density, while bacteria with enteric motors (*Salmonella*) do not.

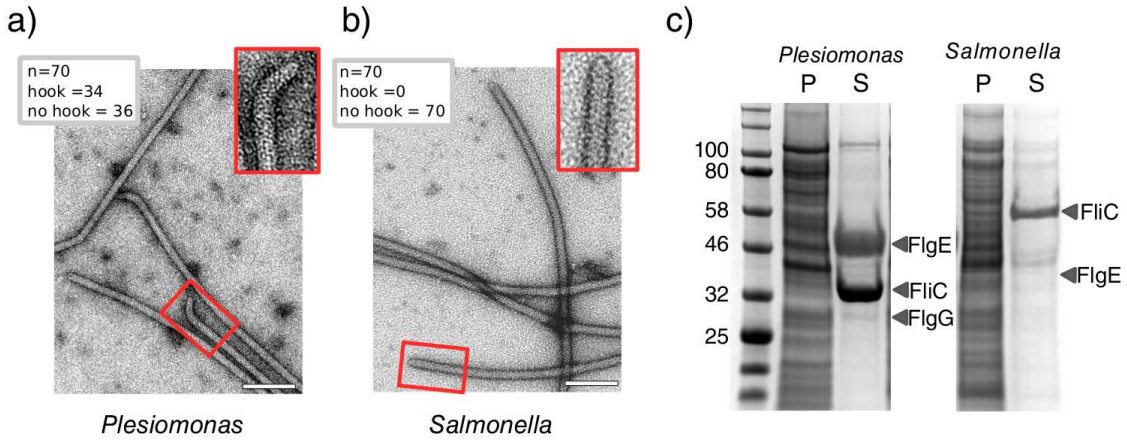


Fig 3.4: Ejected flagella with hooks accumulate in the supernatant of late growth stage *P. shigelloides*.
a) Negative stain EM micrographs of flagella recovered from the supernatant of P. shigelloides cells grown to stationary phase. Half of all imaged filament "ends" contained a hook, confirming consistent loss of flagella. Inset shows a hook. Scale bar is 100nm. b) Negative stain EM micrographs of flagella recovered from the supernatant of Salmonella cells grown to stationary phase. None of the imaged filament "ends" contained a hook, confirming random mechanical breakage. Inset shows a broken end. Scale bar is 100nm. c) SDS-PAGE gel of cells grown to stationary phase confirms hook protein (FlgE) is present in P. shigelloides supernatant but not Salmonella. FliC = flagellin, FlgG = distal rod, FlgE = hook, P = pellet, S = supernatant. Adapted from Ferreira et al. [124]

3.3.4 Ejected flagella leave behind a relic of a former motor which remains in the outer membrane of old poles

The knowledge that flagella are being ejected prompted the speculation that the remaining sub-structure of the flagellar motor may remain at the pole of cells after the hook and filament has been ejected. In order to asses this, I collected electron cryo-tomograms *of P. shigelloides* cells and as expected, clear partial flagellar structures were seen in the outer membrane of poles, alongside fully-formed flagellar motors (Fig. 3.5).

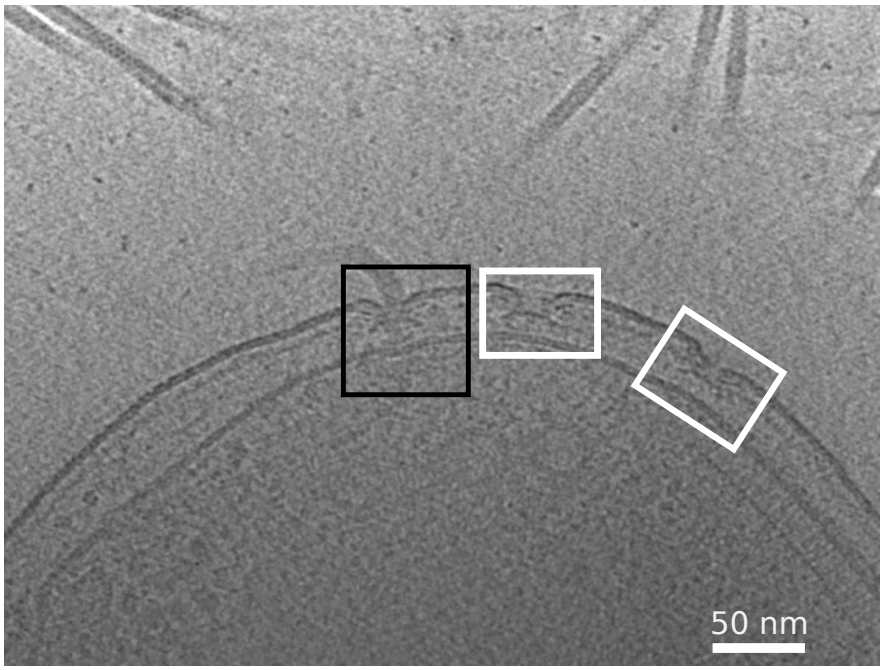


Fig. 3.5: Partial flagella structures appear alongside full flagella.
A slice through a tomogram of a pole of P. shigelloides. A full flagellar motor is boxes in black and two partial flagellar structures are boxed in white.

To link the partial structures to late growth stage, I compared tomograms of cells grown to low (OD_{600} 0.2) or high (OD_{600} 1.0) cell densities. Consistent with our hypothesis, more of these partial structures were seen at high cell density than at low cell density. The enrichment of partial structures at high cell density correlates with flagellar ejection (Table 4) pointing towards the structure being a "relic" of a former functional flagellar motor. 43.2% of poles at low cell density had solely intact flagella while a further 47.7% had both

intact flagella and relic structures. 9.1% had no structures. On cells with flagella, the average number was 5.5 and when cells had relics, the average number was 1.9. No cell poles at high OD_{600} had exclusively flagella while 52% of poles had no structures. 36% had both flagella and relics and 12% had solely relics. When poles had flagella, the average number was only 1.3, whereas if poles had relics, the average number was 3.3.

Relics are more difficult to detect in ECT than full motors because they lack a filament and are small. I therefore believe that I have not identified all relic structures. Consistent with this, when cells were grown to OD_{600} 1.0 and lysed with Penicillin G immediately prior to vitrification, providing thinner cells and therefore clearer tomograms, substantially more relics were seen at poles than detected in intact cells (up to 20 at a pole) (Fig. 3.6). As I was unable to deconvolute the effect of cell lysis on relic appearance, this dataset was not used in Table 4. Nevertheless, the lysed cells confirm that many relics can appear at a single cell pole.

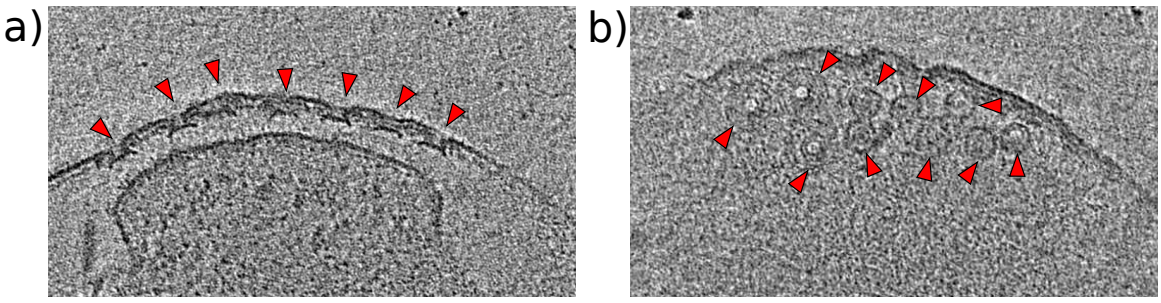


Fig. 3.6: *P. shigelloides* cells lysed prior to imaging show multiple relic structures at the pole.
a) A slice through a cryo-tomogram showing side views of relics. b) A different slice through the same cryo-tomogram as (a) showing more relic structures from the top. Red arrows point to relics. Adapted from Ferreira et al. [124]

The number of structures on poles at two different cell densities (Table 4) provides a link between the growth stage of cells and the presence of relic structures. From these results it is also clear that not only are filaments being ejected but assembly of flagella is also halted at high cell density as more than half of cell poles have neither relics nor intact flagella, indicating newly formed poles prior to assembly of a single flagellum.

Table 4: Number of outer membrane structures is related to growth stage of cells.

OD_{600}	Number of poles imaged (N)	Poles with filaments and relics (%)	Poles with only filaments (%)	Poles with only relics (%)	Poles with nothing (%)	Average number of filaments from all poles	Average number of relics from all poles	Average number of filaments for poles with filaments	Average number of relics for poles with relics
0.25	44	21 (47.7)	19 (43.2)	0 (0)	4 (9.1)	5	0.9	5.5	1.9
1	25	9 (36)	0 (0)	3 (12)	13 (52)	0.5	1.6	1.3	3.3

Number of filaments and outer membrane structures (relics) counted from cryo-tomograms of P. shigelloides cells at two different growth stages

3.3.5 Flagellar ejection is widespread in the γ-proteobacteria

To investigate whether the pattern of ejection and retaining relic structures is widespread in the γ-proteobacteria, ECT was carried out on 5 diverse species: *Plesiomonas shigelloides*, *Vibrio cholerae* (Tomogram collected by Dr Susanne Brenzinger (University of Leiden)) , *Vibrio fischeri* (Tomogram collected by Dr Morgan Beeby (Imperial College London)) , *Shewanella putrefaciens* (Tomogram collected by Amanda Wilson (Imperial College London) and *Pseudomonas aeruginosa* (Tomogram collected by Dr Rohola Hosseini (University of Leiden)). These species were selected as they had varying number of polar flagella, had both sheathed and non-sheathed filaments and were spread within the γ-proteobacteria (Fig. 3.7a). Remarkably, both flagella (Fig. 3.7c) and similar relic structures were seen in the outer membranes of all 5 species (Fig. 3.7b).

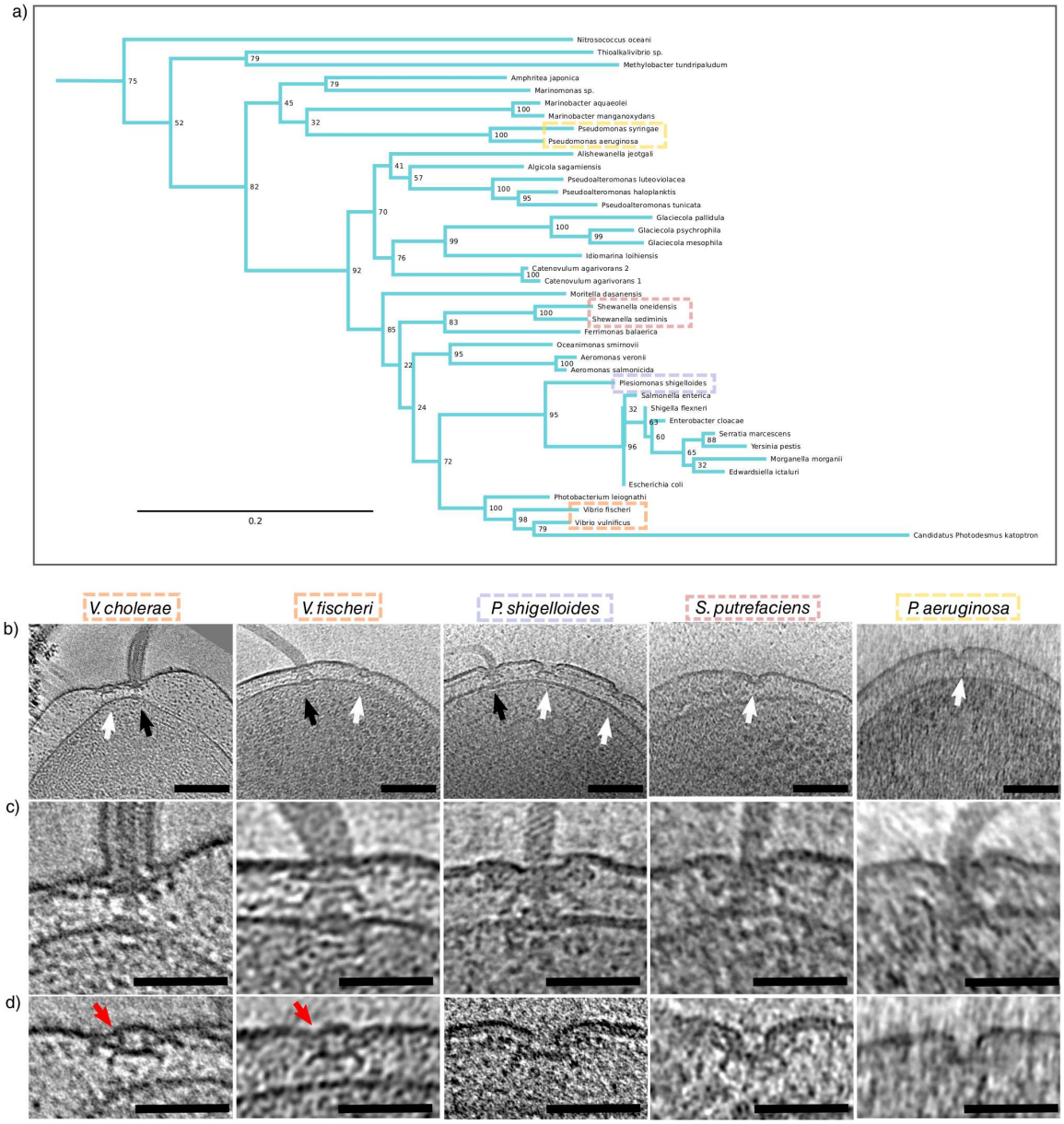


Fig 3.7: Relics of old flagella are seen at the poles of widespread γ-proteobacteria. *a) Phylogenetic tree of γ-proteobacteria (rooted using Campylobacter jejuni) highlighting the chosen species imaged by ECT. b) Slices through cryo-tomograms of five species identified in (a). Black arrows point to intact flagella and white arrows point to relics. Scale bar = 100 nm. c) Example sub-tomograms of intact flagella from the five species. Scale bar = 50 nm. d) Example sub-tomograms of relics from the five species. Red arrows highlight capped relics from sheathed flagella. Scale bar = 50 nm. Adapted from Ferreira et al. [124]*

3.3.6 Flagellar ejection and rebuilding occurs in bacteria with only a single polar flagellum

The most unexpected bacteria to see relic structures in were *V. cholerae, S. putrefaciens* and *P. aeruginosa* which only ever have a single polar flagellum. In one *V. cholerae* cell we observed four relic structures alongside one intact flagellum. Multiple rounds of ejection and rebuilding of flagella is remarkable and seems counter-productive as the synthesis and assembly of a flagellum is energy intensive.

3.3.7 Relics show differences between sheathed and unsheathed filaments

An interesting observation was the difference in outer membrane morphologies between relics from sheathed (*V. cholerae*, and *V. fischeri*) or unsheathed filaments (*P. shigelloides*, *S. putrefaciens* and *P. aeruginosa*). In bacteria with sheathed filaments, the relics were covered by a continuous outer membrane sealing over the relic whereas in unsheathed bacteria the relics had holes in the outer membrane (Fig. 3.7d). In sheathed bacteria the sheath must tear away from the outer membrane upon ejection followed by the healing of the outer membrane over the relic. In unsheathed bacteria, the L-ring holds a gap in the outer membrane acting as a bushing complex for the rotation of the flagellum within the outer membrane. During ejection this must remain unperturbed. This suggests a difference between sheathed and unsheathed flagellar L-rings, which is at present unidentified.

3.3.8 Subtomogram averaging reveals novel plug in relic structure

In order to gain a better understanding of the relic structure, as well as the connection between relics and full flagella, subtomogram averaging was carried out on intact flagella (see Chapter 2, Fig. 2.15)) and relics in *P. shigelloides* (Fig. 3.8, 3.9).

The relic structure had a high resemblance to the outer membrane structures of the intact flagellar motor. Measurements of the structures confirmed this. Both structures had a T-ring (MotXY) diameter of 44nm and a distance of 19nm between the T-ring and outer membrane. In both structures, the hole in the outer membrane had a diameter of 15nm, despite the relic structure lacking a rod. In the full motor, 13-fold symmetry was easily discernible in the T-ring (MotXY) and the stator complexes, as expected from previous studies [34,135].

Strikingly, the relic structure has a clear extra density in the P-ring which is filled by the rod in the intact flagellum. This density appears to plug the gap in the relic that is left behind after the ejection of the filament, hook and distal rod. No relic structures lacking a plug were seen in tomograms of all 5 species imaged, highlighting an obligate role of the plug. This is consistent with a mechanism for inhibition of leakage of periplasmic components after the ejection of flagella. A plug is seen in the relics from both sheathed and unsheathed filaments, emphasising the importance of the plug, regardless of outer membrane sealing.

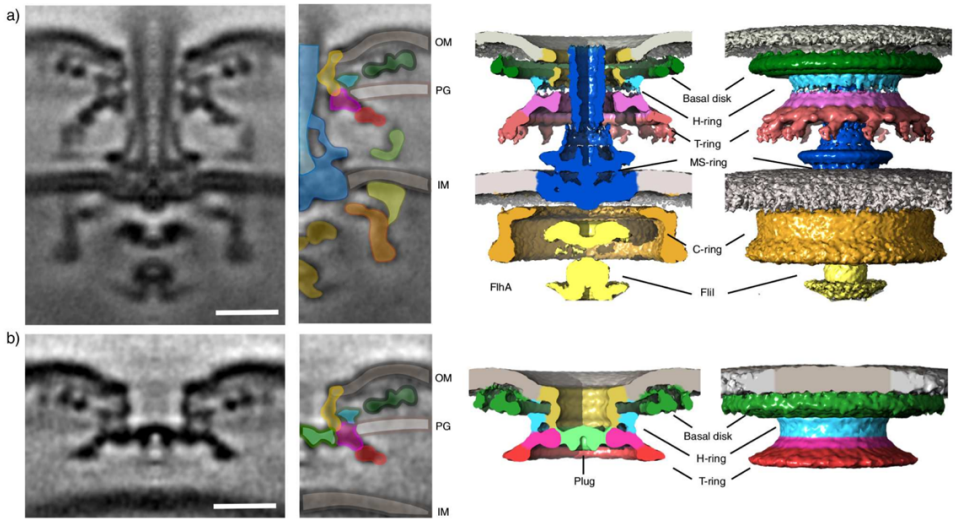


Fig 3.8: Subtomogram average of relic highlights novel plug protein.
a) Subtomogram average of P. shigelloides polar motor. Left to right: Central slice through subtomogram average, coloured overlay relating isosurface colours to subtomogram-average protein densities, cutaway isosurface rendering, full isosurface rendering. b) Subtomogram average of P. shigelloides relic. Left to right, as in (a). Note the extra "plug" density. (Scale bar = 15 nm). Adapted from Ferreira et al. [124]

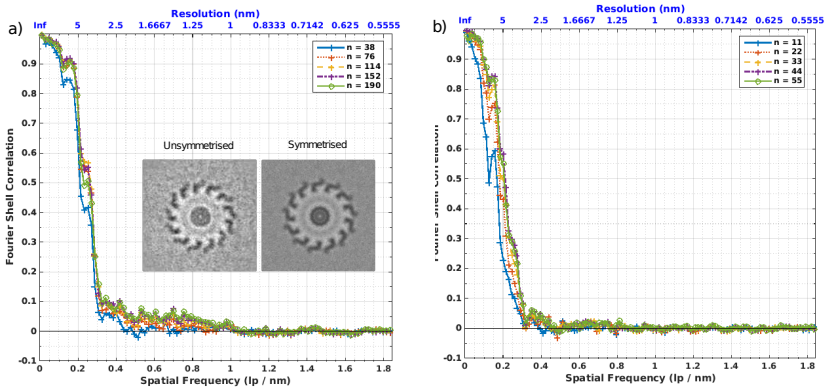


Fig. 3.9: Analysis of sub-tomogram averages.
a) Fourier shell correlation curve for unsymmetrised subtomogram average of full motor. Resolution at a 0.5 threshold of the unsymmetrised motor structure is ~3.5 nm. Inset shows unsymmetrised and 13-fold symmetrised slice through stator complexes. b) Fourier shell correlation curve for unsymmetrised subtomogram average of relic. Resolution at a 0.5 threshold of the unsymmetrised motor structure is ~4.7 nm. Adapted from Ferreira et al. [124]

3.3.9 Relics can be purified by a MotX (T-ring) affinity purification

MotX from *S. putrefaciens* was chromosomally tagged with a polyhistidine tag (Cloning performed by Dr Florian Rossmann (Imperial College London)). I used this to purify the relic structures using affinity purification from cells grown to a high OD_{600}. Negative stain micrographs of the Nickel-NTA eluate revealed structures resembling a series of concentric rings (top view) (Fig. 3.10) with the middle ring filled, a density interpreted as the plug protein seen in STA. A different view was also classified and appears to be a side view of a part of the relic structure also containing a density that may correspond to the plug. 2D-classification of the particles (Fig. 3.10c) allowed for the comparison of the dimensions of the rings with those of a sub-tomogram average of *S. putrefaciens* (Fig. 3.10d). The ring diameters matched that of the basal disk (50 nm), T-ring (37 nm) and MotY-ring (29 nm). Comparisons were also made with the relic structure in a single *P. shigelloides* tomogram (Fig. 3.10f), and the STA of the relic (Fig. 3.10g) and motor (Fig. 3.10h) from *P. shigelloides* (as in Fig. 3.8). This confirms that relics are made from the same proteins as full flagella.

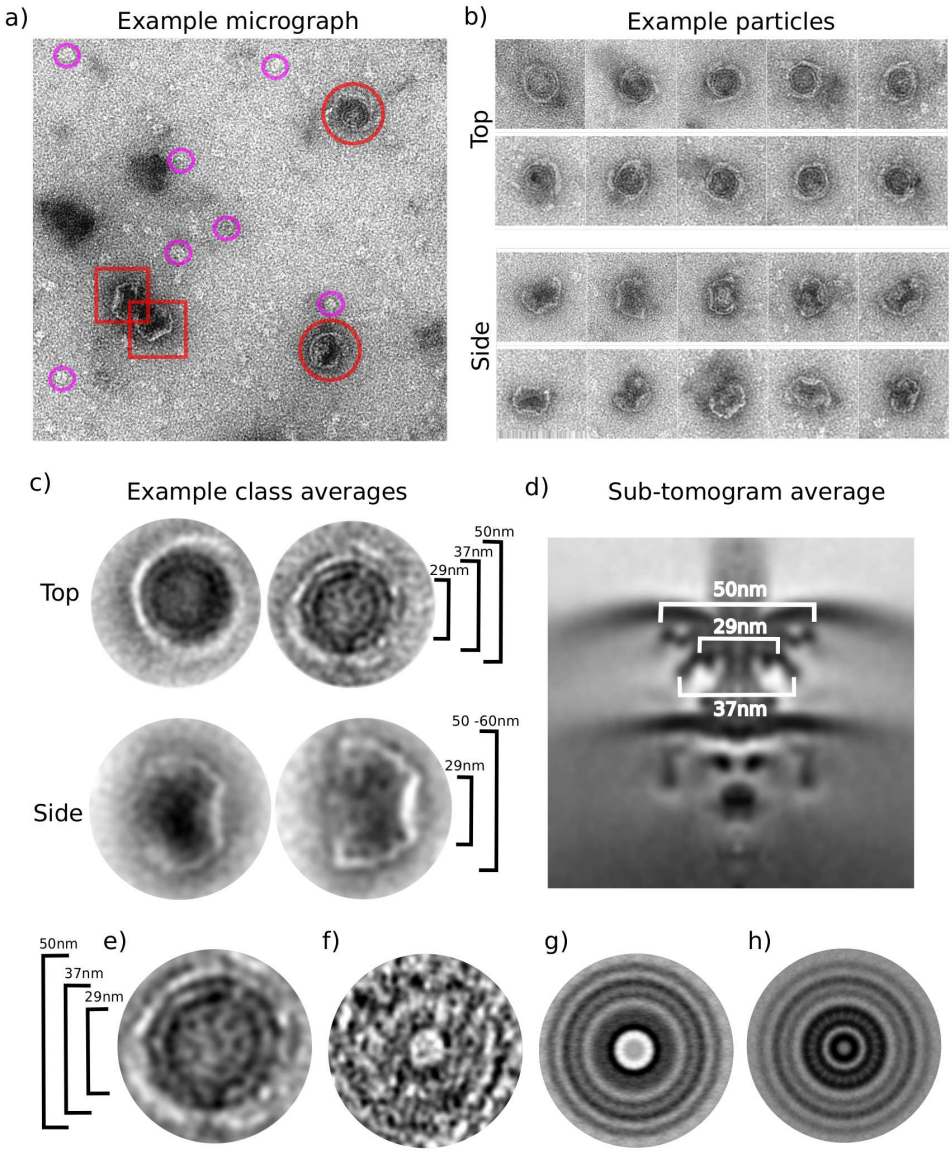


Fig 3.10: Relic structures are made of flagellar proteins and can be pulled-down and visualised by negative stain EM.
a) Example negative stain micrograph of purified relic proteins from S. putrefaciens MotX-HIS. Red circles show top views, red squares show side views and purple circles highlight many contaminating proteins. b) Example particles extracted from micrographs. c) 2 example 2D class-averages for each view. d) Central slice through sub-tomogram of full motor from S. putrefaciens with measurements that correspond to rings in (c). (STA produced by Dr Florian Rossmann, Imperial College London). e) Example top view 2D class-average from S. putrefaciens showing concentric rings. f) Top view of a relic from a slice through a single tomogram of P. shigelloides, showing concentric rings. g) Slice through a subtomogram average of the P. shigelloides relic structure (50 voxels thick). h) Slice through a subtomogram average of the P. shigelloides full motor structure (50 voxels thick). (e-h all at the same scale).

3.3.10 Revealing the protein that makes up the plug density

To try and identify the protein that makes up the plug density, the partially purified relic structures (Fig. 3.10) were sent for Liquid chromatography–mass spectrometry (LC-MS) analysis. However, no clear candidates were identified. This may be due to the plug being made of an already identified flagellar protein that has two-roles or undergoes a large conformational change to become a plug protein. However, this is unlikely as the plug density is large and there is no extra density in the STA of the full flagella that could be rationalised to change conformation so drastically. The purification protocol will need to be optimised to remove contaminating proteins before further LC-MS is attempted.

3.3.11 Confirmation that structures are relics and not assembly intermediates

In order to verify that the structures are relics and not assembly intermediates I tested the hypothesis that relics would require the rod to have been assembled whereas assembly intermediates could form independently from the rod. As the proteins that make up the relic are known to be secreted via the Sec-pathway and not the T3SS, a *S. putrefaciens* Δ*flhA* mutant strain that does not form a T3SS, was constructed to inhibit rod formation (Cloning performed by Florian Rossmann (Imperial College London)). The Δ*flhA* mutant was non-motile (Fig. 3.11a) and of the 68 tomograms that were collected no relics were seen (Fig. 3.11b), whereas 50% of cell poles are expected to have partial structures if they were assembly intermediates. This confirms that a functioning T3SS is required, despite the proteins being exported via the SEC pathway.

To ensure that the deletion had no effect on gene regulation of the other flagellar genes, I constructed a *flhA* over-expression plasmid and conjugated it into the Δ*flhA* strain to confirm complementation. Cells regained motility (Fig. 3.11a), flagella were confirmed to be polar and multiple flagella as well as one relic structure were seen in tomograms (3.11b). These results confirm that the structures are not assembly intermediates.

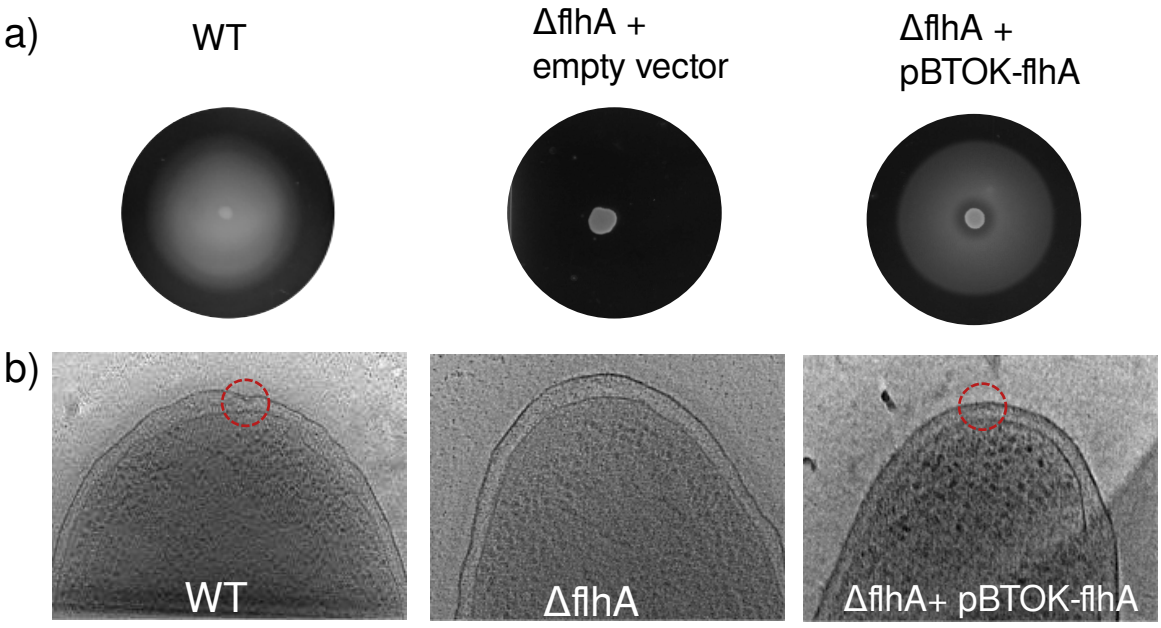


Fig 3.11: Partial flagella motors are not assembly intermediates.
a) Motility agar plates confirm that deletion of flhA leads to loss of motility and that this is rescued upon complementation. b) Relic structures seen in WT cells but not in the ΔflhA mutant return upon complementation.

3.3.12 Ejection "caught in the act" reveals immediate appearance of the plug density and break-point of ejection

While imaging *S. putrefaciens* WT cells with ECT, a cell was observed immediately after an ejection event, with the ejected flagellum still in close proximity (Fig. 3.12a) (Tomogram collected by Amanda Wilson (Imperial College London)). From this tomogram it is clear that the ejected filament has not only the hook but also the distal rod attached to it (Fig. 3.12a-b). The proximal rod remains behind with the MS-ring and cytoplasmic components (Fig. 3.12a, c). Remarkably, the plug density is clearly already in place suggesting an immediate cellular response.

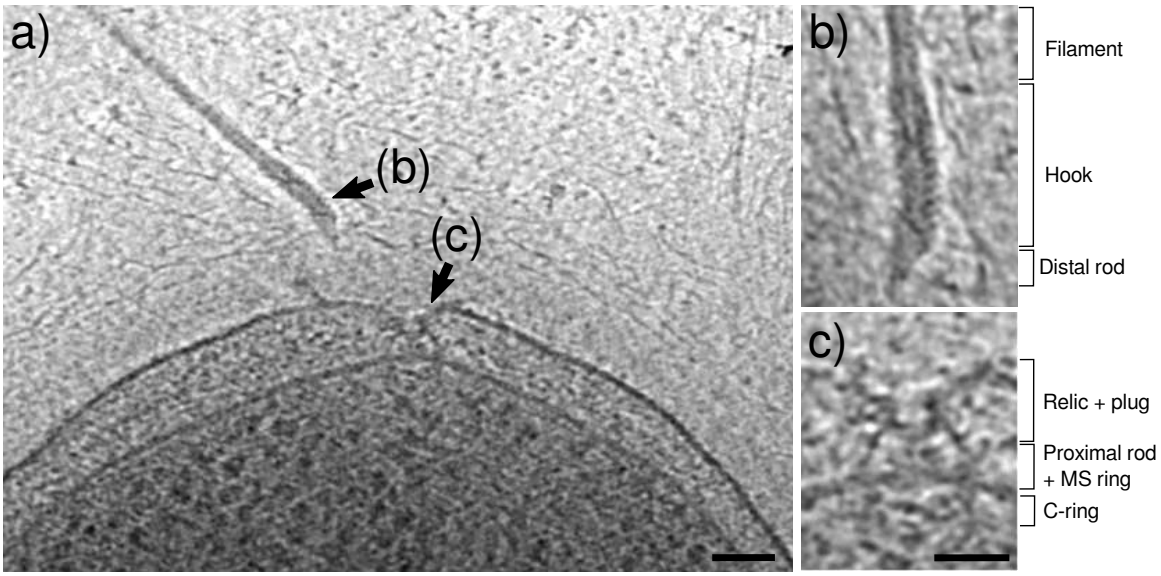


Fig 3.12: Ejection "caught in the act".
a) A slice through a tomogram of WT S. putrefaciens immediately after an ejection event occurred. From this the break-point of ejection appears to be between the distal and proximal rod and a plug density is already seen in place. Scale bar = 50 nm. b) Close-up view of filament immediately after ejection, with hook and distal rod attached. Scale as in (c). c) Close-up view of structure remaining in the cell immediately after filament ejection. The plug density is clearly in place, and the proximal rod, MS-ring and cytoplasmic components remain attached. Scale bar = 25 nm. Adapted from Ferreira et al. [124]

3.3.13 Relics are no longer connected to the inner membrane

I sought to establish whether a connection between the relics and the inner membrane exists by measuring the distance between the inner membrane and the outer-most disk in the outer membrane of relics and full motors. As was expected from previous work on the *V. alginolyticus* motor [127] the periplasmic distance varied at the full flagella, however, the range in distance was far greater at the relic (13.9nm range at relics and 7.9nm range at full flagella). The range in periplasmic distance is almost double at relics than at full flagella, suggesting that there is no connection between the inner membrane and the relic (Fig. 3.13).

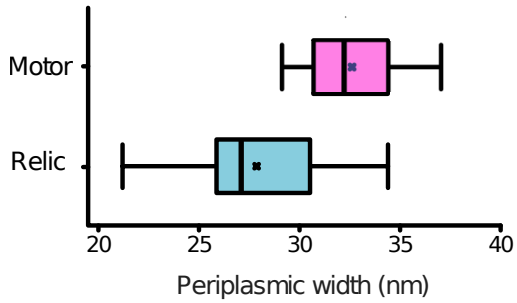


Fig 3.13: Relic structures are not attached to the inner membrane.
Periplasmic distances were measured from cryo-tomograms at sites with relics or full motors. The range in distances is much greater at relics suggesting that these structures are no-longer tethered to the inner membrane.

3.3.14 Relic and flagellar genes are interspersed in the same operon

Inspection of the flagellar operon shows that relic structures are interspersed with rod and hook genes throughout the same operon (Fig. 3.14). This operon structure makes the select expression and assembly of only relic structures very unlikely and is another piece of evidence which suggests that these structures cannot be assembly intermediates.

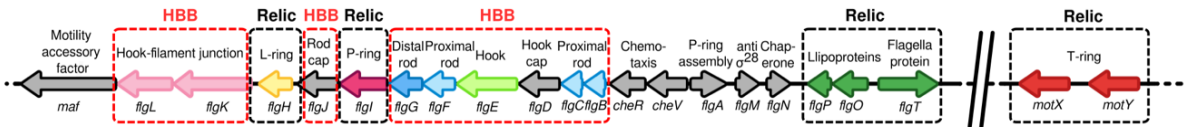


Fig 3.14: Relic genes are interspersed with core flagella genes in the same operon.
Genes encoding relics are interspersed with rod and hook genes. Colours as in Fig. 3.8 and Fig. 3.19. HBB = hook-basal body. Adapted from Ferreira et al. [124]

3.3.15 Placement of motors and relics is not random and suggests a common placement mechanism

When analysing 3D cell poles in tomograms of *P. shigelloides,* I noticed that the relics and full flagella appear evenly distributed in a common grid-like pattern (Fig. 3.15b). 3D coordinates were converted into 2D coordinates using custom scripts (Fig. 3.15a) and

the nearest neighbour distances were calculated for all relics and full flagella. The average nearest neighbour distance for relics and full flagella was 64nm. As the C-ring diameter is ~45nm, 20nm less than the average nearest neighbour spacing, it is unlikely that the placement of structures is constrained by steric clashes from the C-ring. In order to identify whether a common placement mechanism is used for both relics and full flagella, I plotted histograms of nearest neighbour distances for relics, full flagella and a random dataset (Fig. 3.15c). I generated the random dataset by calculating the area of each cell pole from the real data and matching this to the number of structures at each pole. For each real pole, I then wrote scripts to generate five new poles with the same dimensions and number of structures but with the structures placed at random 2D coordinates within the constrained pole dimensions. As expected from my observations, full flagella and relics had identical curves. The distribution of relics and full flagella motors was also much tighter than the random dataset. Together this is consistent with the relics and full flagella sharing a common placement mechanism.

As the nearest-neighbour analysis suggested a common placement mechanism and I predicted that relics and motors were part of a common grid, I quantified the dispersal of structures. Clark-Evans distribution analysis was used to quantify the distribution of structures on poles with more than 4 relics or full flagella (N=71) (Fig. 3.15d). This was compared to a synthesised random dataset. Clark-Evans distribution analysis compares the calculated mean nearest neighbour distance to the expected mean nearest neighbour distance if points were randomly distributed. A value of 1 (expected = measured) reveals that data is randomly distributed, whereas a value of 0 (measured distance = 0) reveals that points are clustered. A value above 1 (measured distance > expected distance) reveals that data is ordered with a value of 2.15 being a hexagonal grid where all points have six equidistant nearest neighbours. I calculated the Clark Evans distribution for all real poles and all poles generated with random structures. The synthesised random dataset had the expected mean of 1 whereas the *P. shigelloides* dataset had a mean close to 2. Relics and full flagella are therefore arranged in a non-random grid-like arrangement in a common grid. Although this was previously unknown in bacteria with polar flagella, similar analysis

was previously done on the peritrichous flagella of *B. subtilis,* and shown to have a Clark-Evans ratio greater than 1 [136]

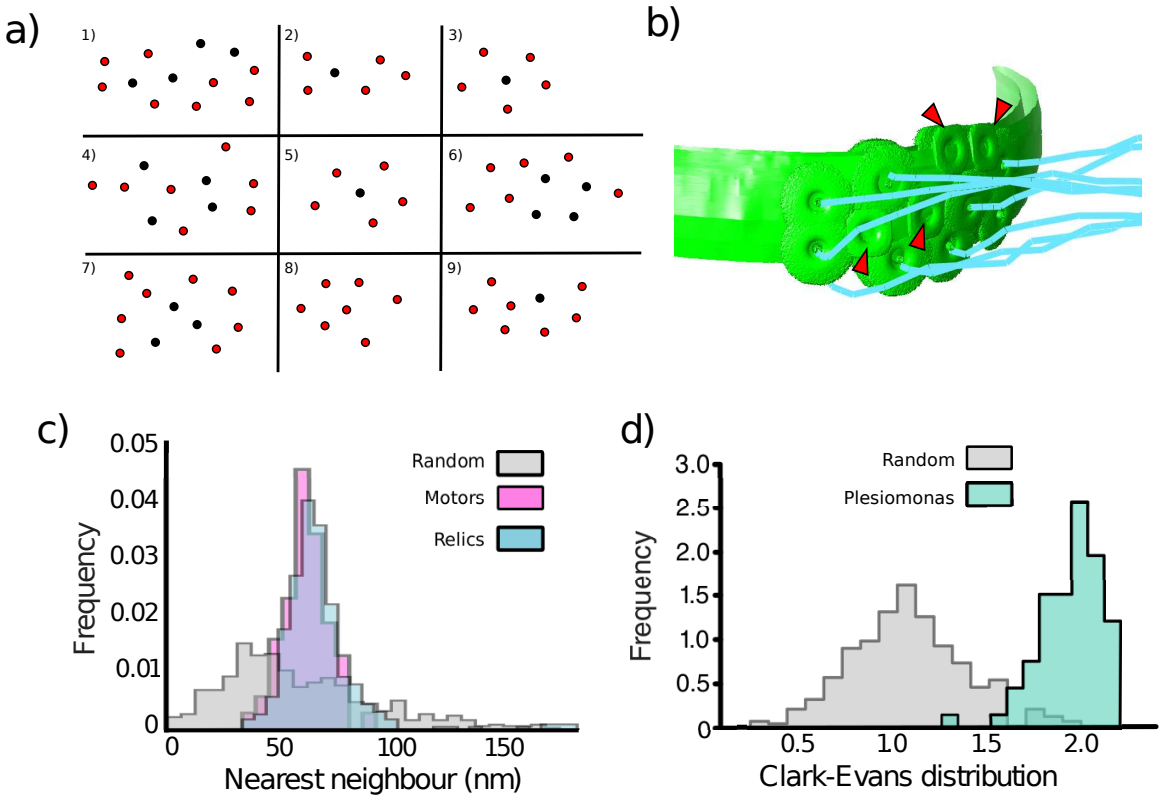


Fig 3.15: Positioning of relic and flagella is the same, suggesting a common placement mechanism.
a) Representative views looking down the long axis of nine P. shigelloides cells to show the 2D placement of intact flagella (red circles) and relics (black circles). b) Representative 3D isosurface of a P. shigelloides cell pole showing relics (red arrows) and flagella (blue lines). c) Histogram mapping all nearest neighbour points of relics, full motors and a randomly generated dataset. d) Clark-Evans distribution of all structures (relics and motors) in P. shigelloides compared to randomly placed structures. Adapted from Ferreira et al. [124]

3.3.16 Flagellar ejection is not caused by mechanical breakage or mechanosensing

From initial results (Fig. 3.2-3.4), the culture medium or growth conditions were indicated as being involved in triggering ejection, as cells lost flagella in late growth stages.

In late growth stages, the high cell density may lead to flagella physically interacting. To test if mechanosensitivity of the flagella load is detected as the trigger for ejection, I constructed a mutant lacking the polar filament protein FliC in *P. shigelloides*. When I imaged this by ECT, motors with just hooks and no filaments (Fig. 3.16a) as well as relics (Fig. 3.16b) were observed. This confirms that ejection of flagella does not require a flagellar filament. This also provides evidence of an active mechanism as ejection in the absence of a filament is incompatible with a mechanism that relies on mechanical shearing (a short hook will not feel shearing forces due to the Reynolds shell around the bacterium).

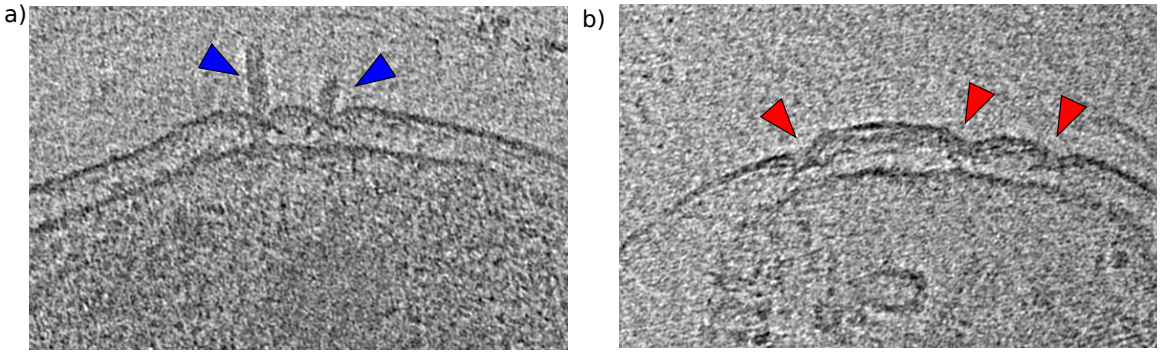


Fig 3.16: Ejection of flagella does not require a flagellar filament.
a) A slice through a cryo-tomogram of a ΔfliC P. shigelloides mutant showing flagella motors with hooks but no filaments (blue arrows). b) A slice through a cryo-tomogram of the same mutant as in (a) showing relics (red arrows). Adapted from Ferreira et al. [124]

3.3.17 Ejection occurs in response to nutrient depletion

Ejection of flagella occurs as cells grow to increasing cell density. To confirm that ejection is linked to cell density and to control for parameters such as time in the incubator, cells were continually diluted to below OD_{600} 0.2 with fresh LB alongside a control culture grown to OD_{600} 1.0. Negative stain EM was carried out and the number of flagella per cell were counted. Cells that were continually diluted retained flagella (mean of 5.3) while cells grown to OD_{600} 1.0 lost flagella (mean of 1.7) (Fig. 3.17a). This confirmed that ejection

occurs due to cell density and pointed to the signal for ejection being in the medium of old cells.

To assess whether the signal for ejection is in the medium from old cells, cells grown to low cell density were spun down and resuspended in the filtered supernatant from cells grown to high cell density (spent medium). After growth for one doubling time (OD_{600} 0.2 to 0.4), multiple flagella had been lost (mean flagella went from 6.7 to 1.2) while mean number of flagella remained constant in the control cells resuspended into fresh LB (Fig. 3.17b). This result, suggests that the trigger for ejection is in the supernatant of old cells, but does not differentiate between the signal being the depletion of something from the medium or a specific chemical secreted into the supernatant by cells at high cell densities.

To confirm whether the signal for ejection of flagella is a secreted chemical or the depletion of nutrients, the above experiment was carried out again but instead of transferring cells to *Plesiomonas* spent medium, cells were resuspended into *Salmonella* spent medium (from *Salmonella* cells grown to stationary phase). After one doubling time the number of flagella were counted and again the *P. shigelloides* cells had lost multiple flagella (mean from 6.2 to 1.6) (Fig 3.17c). This suggests that the signal is not a specific chemical signal secreted by *P. shigelloides* cells but the lack of a component of the medium or "nutrient depletion".

To confirm of that the signal for ejection of flagella is nutrient depletion, *P. shigelloides* cells grown to low OD_{600} in LB were resuspended in MOPS minimal medium. Within an hour cells had stopped swimming and the mean number of flagella had dropped from 5.8 to 1.6 within one doubling time (OD_{600} 0.2 to 0.4) (Fig. 3.17d). This was confirmed to be rescuable by the addition of yeast extract to the minimal medium (Fig. 3.17e).

As a more direct demonstration of an active mechanism, cells were grown in LB to low OD_{600} and then split into either MOPS minimal medium or fresh LB. After one doubling time the cells were spun down and PEG precipitation was carried out on the

supernatant. An SDS-PAGE gel showed significantly more flagellin (FliC) in the supernatant of the cells grown in minimal medium than those grown in fresh LB and only cells grown in minimal medium had a band for the hook protein (FlgE) (Fig. 3.17f) highlighting that these cells were actively ejecting flagella rather than losing them from random breakage. Together these results suggest that the signal for ejection of flagella, and entry into a sessile state in the in γ-proteobacteria, is the depletion of nutrients and that this is an active response.

3.3.18 Ejection mechanism is distinct from *Caulobacter crescentus*

Most motile bacteria move from motile to sessile states and back again. In many bacteria, including the α-proteobacterium *C. crescentus*, the entry into a sessile state is mediated by relative levels of cyclic di-GMP (cdG) [137]. I therefore sought to investigate whether cdiGMP concentrations play a role in the ejection of flagella in the in γ-proteobacteria. By over-expressing the cdiGMP-synthesising diguanylate-cyclase, VdcA, from *V. cholerae* in *P. shigelloides*, I assessed the effect that increasing the levels of cdiGMP had on *P. shigelloides* motility and flagellar number (Plasmid made by Dr Florian Rossmann (Imperial College London)). As expected, when cdG levels are increased, *P. shigelloides* cells stopped swimming but cells harbouring an empty vector continue to swim (Fig. 3.18a). Unexpectedly, however, the mean number of flagella on *P. shigelloides* cells remained constant (Fig. 3.18b). This result demonstrates that, although motility is abolished when cdiGMP levels are increased, a different pathway leads to the ejection of flagella in the γ-proteobacteria.

In *C. crescentus* the digestion of FliF by ClpA, co-occurs with the ejection of the flagellum, and is thought to be the trigger for ejection. To test whether this is the case in the γ-proteobacteria, *clpA* and *clpX* deletion mutants were constructed in *S. putrefaciens* (Mutants made by the lab of Kai Thormann). These cells were dropped onto motility agar made from spent medium. If ejection is caused by digestion of FliF by either ClpA (as in *C. crescentus*) or ClpX (another important proteasome component) then mutant cells would

be expected to swim better in spent medium than WT cells as ejection would not be occurring. However, no significant difference was seen between the three strains (Fig. 3.18c).

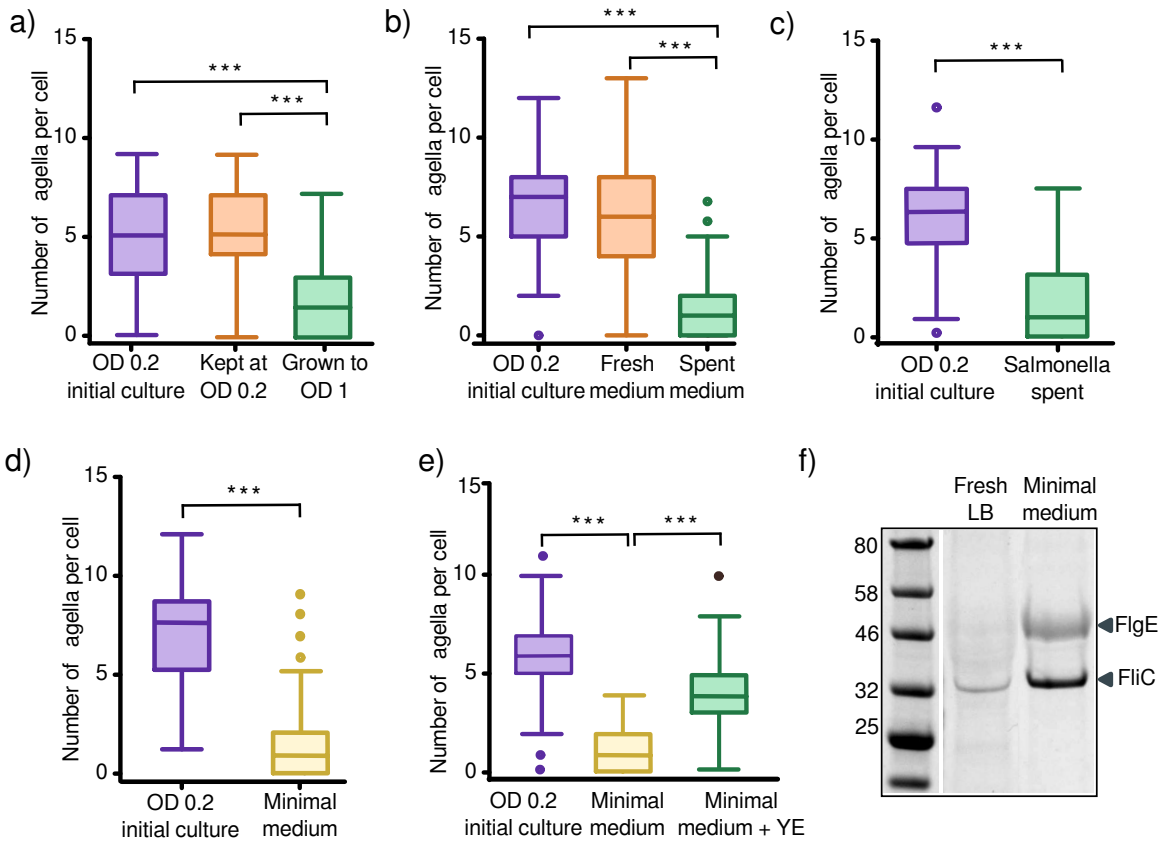


Fig 3.17: Ejection is triggered by nutrient depletion.
*a) P. shigelloides cells continually diluted to below OD_{600} 0.2 retain flagella (*** $p < 0.0001$, 1-way ANOVA). b) P. shigelloides cells at early growth stages moved into P. shigelloides spent medium eject flagella within one doubling time (*** $p < 0.0001$, 1-way ANOVA). Doubling time in fresh LB = 19 minutes and in spent medium = 38 minutes. c) P. shigelloides cells at early growth stages moved into Salmonella spent medium eject flagella within one doubling time. (*** $p < 0.0001$, Unpaired t-test). d) P. shigelloides cells at early growth stages moved into MOPS minimal medium eject flagella within one doubling time. (*** $p < 0.0001$, Unpaired t-test). e) Flagella ejection in MOPS minimal medium is rescued when yeast extract is added. (*** $p < 0.0001$, 1-way ANOVA). f) Early growth stage P. shigelloides cells were moved into either MOPS minimal medium or fresh LB and grown for one doubling time. The supernatant of cells grown in MOPS minimal medium has hook protein (FlgE) and more flagellin (FliC) than cells moved into fresh LB. All done in triplicate with at least 65 cells imaged per condition. Adapted from Ferreira et al. [124]*

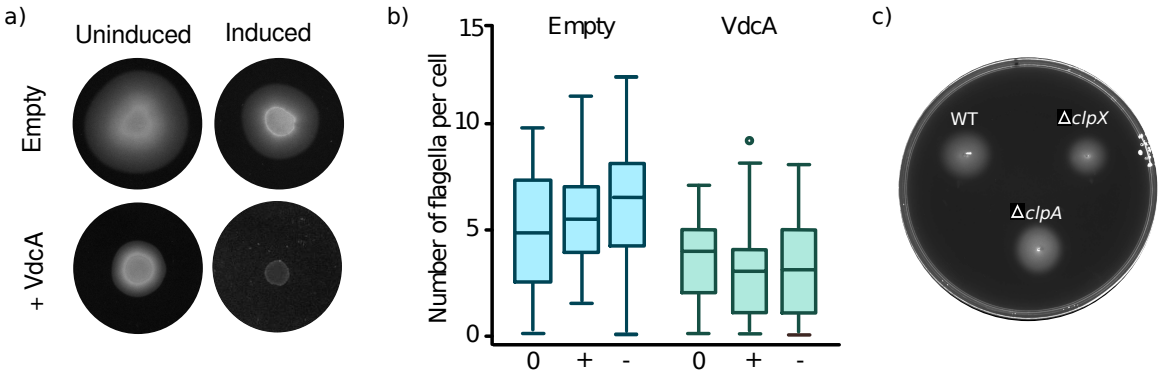


Fig 3.18: Ejection in γ-proteobacteria is not triggered by the same mechanism as *Caulobacter crescentus.*
a) P. shigelloides cells harbouring a plasmid overexpressing VdcA, a cdiGMP synthesising enzyme, stop swimming in motility agar when induced. b) The halting of swimming in P. shigelloides pBTOK-VdcA cells is not due to ejection of flagella. 0 = prior to induction, + = induced, - = not induced. No significant difference between induced and not induced cells. c) S. putrefaciens cells with key proteasome components deleted (ΔclpA and a ΔclpX) do not swim better in MOPS minimal medium soft motility agar.

3.3.19 Precursor and relic structures enable a model for assembly and ejection of the γ-proteobacterial flagellum to be proposed

From assembly and disassembly intermediates that I observed in tomograms (Fig. 3.19a), as well as the ejection event caught in one tomogram (Fig. 3.12) I am able to propose a model for the stages involved in building and disassembling a flagellum in the polarly flagellated γ-proteobacteria (Fig. 3.19b). The T3SS assembles in the inner membrane and the MS-ring and cytoplasmic components assemble around it. The rod proteins are secreted through a channel in the T3SS and fold and assemble. In sub-tomograms of this stage the rod is seen pushing on the outer membrane and forming a bulge perpendicular to it (Fig. 3.19a.1). Next, the P- and L-rings assemble around the distal rod, followed by the remaining relic proteins (FlgO, FlgP, FlgT, MotX and MotY). The L-ring opens a channel in the outer membrane and the hook and filament assembles through this, templating on the distal rod. With the attachment of the stator complexes, PomA and

PomB, and coupling to chemoreceptors, this is now a fully functional flagellar motor (Fig. 3.19a.2).

When nutrients become scarce, ejection of the distal rod, hook and filament into the growth medium is triggered. A plug protein immediately fills the hole left by the distal rod, presumably to stop periplasmic leakage (Fig3.19a.3). Finally, the proximal rod, MS-ring and cytoplasmic components and cleared away. Upon nutrient addition, new flagella are regrown and old relics remain at the pole (Fig. 3.19a.4).

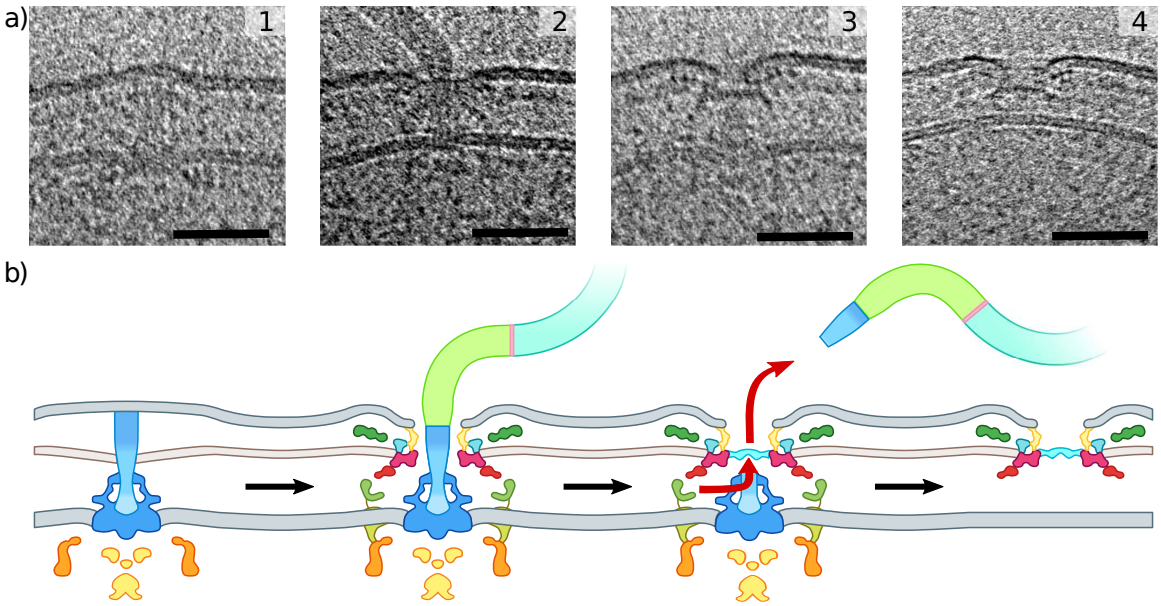


Fig 3.19: Multiple assembly intermediates provide the basis for a model of flagellar ejection.
a) Multiple assembly and disassembly intermediates. b) Schematic for the assembly and ejection of the Na^+-driven polar flagellum. Colours match genes in Fig. 3.13 and STA in Fig. 3.7. Adapted from Ferreira et al. [124]

3.4 Discussion

In this Chapter, I provide evidence for a novel mechanism for the deactivation of the flagellum resulting in a switch from a motile to a non-motile state in the polarly flagellated γ-*proteobacteria.* To accomplish this, species that showed characteristic decreases in swimming speeds when grown to late growth stages, distinct from the enteric bacterium *Salmonella*, were analysed for coincident morphological changes. I show that in response to depletion of nutrients in the growth medium, polarly flagellated γ-proteobacteria deactivate motility by ejecting their flagella. I found that the filament, hook and distal rod are ejected and accumulate in the supernatant while a relic of a previously functional flagellum remains at the cell pole. Importantly, I show that the rate of ejection increases when nutrients become limited and, as a mutant lacking a filament still ejects its hook and distal rod, it is clear that this is an active mechanism, not due to mechanical breakage. Subtomogram averaging of the relic structures that remain after ejection showed that they have an extra-density plugging the hole left by the ejected rod, hook and filament. This is likely a novel protein and was present in all polarly flagellated γ-proteobacterial species that we imaged: *Plesiomonas shigelloides, Vibrio cholerae, Vibrio fischeri, Shewanella putrefaciens*, and *Pseudomonas aeruginosa.*

3.4.1 Structures are relics and not assembly intermediates

A large amount of time went into showing, together with previous data from the literature, that these structures are relics of former flagellar motors and not assembly intermediates that form rings in the outer membrane before a rod, hook and filament assembles within the rings. I showed that in γ-proteobacteria swimming speeds decrease (Fig. 3.2) at the same time as there is a drop in the average number of flagella per cell (Fig. 3.3a, b) and the total number of flagella attached to cells in a population (Fig. 3.3c). This also co-occurs with flagella and hooks accumulating in the supernatant (Fig. 3.4a) and more relic structures appearing at cell poles (Table 4). The observation that bacteria that only ever have exactly one polar flagellum can have multiple relic structures at the same pole is consistent with a pattern of ejection and rebuilding over multiple generations, but does not

support structures being assembly intermediates as the regulation of a single flagellum occurs in the initial stages of flagellar formation [138]. This is even less likely taking into account the operon structure with relic genes interspersed with other flagellar genes (Fig. 3.14). Selectively assembling relic components FlgH, FlgI, FlgO, FlgP, FlgT, MotX and MotY in an operon with this structure is not likely, as it would face selective pressure to separate into discretely regulated modules as structure and co-occurrence of genes on an operon is predictive of structural co-assembly [139,140]. From previous studies in *Salmonella*, it is clear that the P- and L-rings (FlgI and FlgH) which form part of the relic structure in γ-proteobacteria with polar flagella, require a distal rod to be formed before they can assemble [141]. It has also been shown that multiple P-rings form around "polyrods" – mutants with extra-long distal rods – confirming that the rod is essential for P-ring assembly and not the outer membrane [142,143] (see also Chapter 5, Fig. 5.5). These studies suggest that the core of the relic (the P- and L-rings) cannot assemble without the prior assembly of a rod, at least in *Salmonella*. Nearest neighbour plots showed that relics and motors are positioned in a common-grid (Fig. 3.15), suggesting a common placement mechanism, which likely acts from the cytoplasm. As the periplasmic distance was shown to be far greater at relics (Fig. 3.13) suggesting no connection between relics and the inner membrane, these must have been positioned prior to ejection. A cell "caught in the act" immediately after flagellar ejection still has a filament in close proximity (Fig. 3.12) and finally, a *ΔflhA* mutant which lacks a T3SS does not produce relic structures (Fig. 3.11)

3.4.2 The appearance of a plug density suggests a specific cellular response

When subtomogram averages of the motor and relic were compared, a striking new feature of the relic was a large extra protein density plugging a hole in the outer membrane that was once occupied by the flagellar distal rod and hook (Fig. 3.8). Looking at individual tomograms of all five γ-proteobacterial species images, all relics have the plug density, even in sheathed flagella that have an outer membrane cap over the relic. No relics were ever seen without a plug. When an ejection event was caught in a cryo-tomogram (Fig. 3.12) the extra plug density was already in place, even with the filament still in very close

proximity to the cell. This is clearly an immediate and specific cellular response. This targeted response is significant, and may result in stopping periplasmic leakage.

At present the identity of the plug protein is unclear. The plug protein density is large, as seen from individual tomograms and the subtomogram average. If the plug was an already present protein that dropped down in a gate-like mechanism as seen in the secretin of the injectisomes [144], an extra protein density would be expected in the full motor STA to account for this, which is not seen. It is therefore likely that the plug is a novel protein that does not have a signal sequence for secretion via the T3SS. Although relic structures were partially purified by affinity purification, LC-MS did not lead to potential candidates. This may be due to the plug being an already annotated flagellar protein that has a second role in polarly flagellated γ-proteobacteria. A novel, enigmatic protein (or proteins) is more likely to form the plug protein as such a large conformational and functional change of a protein is unprecedented. As many contaminating proteins were seen in negative stain EM micrographs, this stage needs to be optimised before further LC-MS analysis can take place.

Although I show that the mechanism for triggering ejection is distinct from *Caulobacter crescentus,* I suggest that a similar mechanism of plugging must occur after flagellar ejection [145]. Due to the lack of large outer membrane disks in the *C. crescentus* flagellar motor [5] however, relics would be made of only the P- and L-rings and would therefore be difficult to visualise by ECT.

3.4.3 Evolution is a "tinkerer"

The accumulation of plugged relic structures at the pole with no apparent function is not the most elegant solution. However, if a plug protein did not exist, an alternative way for the cell to prevent leakage of cellular components would be to re-seal the outer membrane as is seen in the relics of bacteria with sheathed filaments. In bacteria with non-sheathed filaments (the majority of bacteria) the entire relic structure would need to be disassembled in order to reseal the outer membrane due to the L-ring acting to keep the

hole in the outer membrane open. This would require the evolution of sophisticated molecular machinery for proteolysis of all components. The plugging of a hole with a protein is a simpler solution to the problem, and as "evolution is a tinkerer" [146] it is therefore the more likely solution.

3.4.4 An active mechanism of flagellar ejection

The deactivation of the flagellum in γ-proteobacteria was shown to be an active mechanism. The ejection is triggered by the depletion of nutrients as demonstrated by an increased rate of ejection (and appearance of hook protein) under nutrient limited conditions (Fig. 3.17), ejection of hooks and distal rods even when flagellin (FliC) is not present (Fig. 3.16) and the appearance of a plug protein (Fig. 3.8). These results are not consistent with a random breakage mechanism, but are consistent with a mechanism of active ejection. At present the molecular mechanism for sensing and driving the ejection of flagella is not known, but was shown to be distinct from *C. crescentus* (Fig. 3.18).

3.4.5 Possible selective benefit of flagellar ejection

In nutrient limited environments, γ-proteobacteria with polar flagella deactivate their flagellar motors for switching into a non-motile state by ejecting their distal rod, hook and filament. This is not seen in the enteric γ-proteobacteria, such as *Salmonella*. Deactivation of the flagellum in response to a nutrient depleted environment may be an extreme form of energy conservation. The difference in ejection between *Salmonella* and the γ-proteobacteria with polar Na^+-driven motors may be due to the difference in flagellar placement in these bacteria. In *Salmonella*, flagella are peritrichous and therefore placed around the sides of the cell body, unlike at one pole in the γ-proteobacteria analysed here. This means that when *Salmonella* cells divide, the number of flagella on each daughter cell is half that of the mother cell. When *Salmonella* stops assembling flagella, flagella will be diluted with each cell division, but when polarly flagellated cells divide, one daughter cell inherits an entire set of flagella while the other (if flagella assembly has stopped) inherits

none. For the daughter cell that inherits an entire set of flagella, this is energetically draining, and ejection may be a drastic, but essential survival mechanism.

As flagellin triggers an immune-response, a possible selective advantage to ejection of the flagellum is escape from the host immune system. It has been shown that *V. cholerae* cells lose flagella upon penetration of mucin, priming them for host colonisation [147]. This may be beneficial even for non-pathogenic bacteria such as *V. fischeri* which is a squid endosymbiont. It has previously been shown to lose flagella upon entry into the squid light cavity, which may help it hide in the host, but regrows them within one hour of exposure to fresh sea water [148]. However, not all species imaged with relic structures have a host organism.

Although the assembly of a flagellum requires a lot of energy, maintaining one is also draining. Actively powering flagella use energy for the generation of torque and for constantly assembling the filament [149], which passes on a large energetic drain on the cell. A dramatic decrease in the number of flagella on a cell by ejection would be a drastic mechanism to conserve energy.

3.4.6 Potential applications and future work

The discovery of the ejection of the flagellum under nutrient depleted conditions could provide the basis for many potential applications. Firstly, as the flagellum is a virulence factor in many bacteria including *Vibrio cholerae*, identifying the molecular mechanism for triggering ejection may be an effective antimicrobial. More work is required to identify the molecular mechanism and how to effectively trigger it.

Secondly, on a more fundamental research level, this could be used to further study the assembly of the flagellum. By moving cells from low nutrients, where all flagella are lost to high nutrients where flagella re-grow, a time-resolved approach to imaging the assembly process of the flagellum could be developed.

3.5 Materials and methods

3.5.1 Cell Growth

Plesiomonas shigelloides was grown in LB (10 g/L tryptone, 10g/L NaCl, 5 g/L yeast extract) at 37°C, 200RPM overnight in 14 ml aeration tubes. The next day, cultures were diluted 1:100. Cells were grown to an OD of 0.2 unless specified.

Shewanella putrefaciens CN-32 was grown in LB (10 g/L tryptone, 10g/L NaCl, 5 g/L yeast extract) at 30°C, 200RPM overnight in 14 ml aeration tubes. The next day, cultures were diluted 1:100 for experiments. Cells were grown to an OD of 0.5.

Vibrio fischeri was grown in LBS + $MgSO_4$ (10g/L of tryptone, 5g/L of yeast extract, 20g/L of NaCl, 8.62g/L $MgSO_4$) at 30°C, 200RPM overnight in 14 ml aeration tubes. The next day, cultures were diluted 1:100 for experiments. Cells were grown to an OD of 0.3.

Vibrio cholerae N16961 was grown in LB for 18h, harvested by centrifugation and washed twice with sterile filtered and autoclaved environmental sea water before introduced into a 50ml sea water microcosm at an OD_{600} 2.5. Microcosms were kept at low agitation at 4°C for one month prior to imaging.

Pseudomonas aeruginosa PAOI persister cells were obtained from overnight stationary phase culture treated with Carbonyl cyanide *m*-chlorophenylhydrazone (CCCP) 200 μg/ml for 3 h in LB, followed by exposure to Ciprofloxacin 5 μg/ml for 3 h in sodium-phosphate buffer (10 mM, pH 7.4) as described previously [150].

Table 5. Strains and plasmids used in Chapter 3.

Strain or Plasmid	Source
Plesiomonas shigelloides ATCC 14029 WT	DSMZ (DSM-8224)
Shewanella putrefaciens CN-32 WT	[151]
Vibrio fischeri ES114 WT	Edward G. Ruby (University of Hawai‘i at Mānoa)
Vibrio cholerae N16961 WT	Simon Ringgaard (MPI Marburg)

Pseudomonas aeruginosa PAOI WT	Kylie Watts (Loma Linda University)
E.coli WM3064	W. Metcalf, (University of Illinois)
S. putrefaciens CN-32 Δ*flhA*	This study (Florian Rossmann)
S. putrefaciens CN-32 motX-mCherry-His	[106]
pBTOK	[152]
pBTOK-VdcA	This study (Florian Rossmann)
pBTOK-FlhA	This study
S. putrefaciens CN-32 Δ*clpA*	This study (Kai Thormann)
S. putrefaciens CN-32 Δ*clpX*	This study (Kai Thormann)
P. shigelloides Δ*fliC*	This study

3.5.2 Swimming Speed Videos

To measure bacterial swimming speeds at different cell densities, cells were grown as stated above and diluted in LB or LBS to an OD_{600} of 0.2 immediately prior to imaging. Cells were imaged at 100x oil immersion on a MT4000 series light microscope (Meiji Techno) with a DMK23G618 digital camera connected to IC Capture software. Bacterial cells were tracked for 10 seconds using Fiji [153] and converted to swimming velocities using custom scripts. Three videos were taken at each time point providing over 1000 traces and this was done in triplicate. Error bars indicate standard error (performed by myself and Forson Gao, Imperial College London).

3.5.3 Negative stain EM

3µl of cells or flagella, were placed on glow-discharged continuous-carbon grids (Taab Laboratory Equipment Ltd.). The grids were stained with 2% Uranyl Acetate and stored at room temperature prior to imaging. Negative stain micrographs were collected on either an FEI Tecnai G2 Spirit BioTWIN (Tungsten) using an Eagle CCD camera or a

Tecnai T12 TWIN (LAB6) using a TVIPS F216 CCD camera. Images were viewed using 3DMOD [89,121] and number of flagella per cell (or number of filaments with hooks) was counted manually.

3.5.4 Purification of relics

An *S. putrefacien*s MotX-mCherry-HIS strain was grown overnight at 30 degrees. The cultures were diluted 1:100 into 5L of LB and grown into stationary phase. Cells were pelleted and resuspended into MOPS minimal media and grown for a further 2 hours to ensure flagella were ejected. Cells were pelleted and resuspended into 150mM Tris pH 7.5, 150mM NaCl, 10% Sucrose, 10% glycerol, DNase and EDTA-free protease inhibitors. Cells were passed once through a cell-disrupter (27kpsi) and centrifuged at 15,000 x g for 15 minutes to remove unlysed cells. The supernatant was ultracentrifuged for 1 hour and the membrane pellet was washed in 150mM Tris pH 7.5, 150mM NaCl, 10% Sucrose, 10% glycerol before further centrifugation. Membrane pellets were flash frozen in 150mM Tris pH 7.5, 150mM NaCl, 10% Sucrose, 10% glycerol. Thawed membranes were solubilised in 1% DDM for 1 hour at 4 degrees before dilution in 150mM Tris pH 7.5, 150mM NaCl, 10% Sucrose, 10% glycerol, 0.03% DDM, 20mM imidazole. Soluble fraction was loaded onto a His-trap (GE Healthcare) and washed with buffer up to 100mM Imidazole. Relics were eluted with 300mM imidazole.

3.5.5 2D classification of relic particles

Negative stain grids were prepared as above. Images were collected on a Tecnai T12 TWIN (LAB6) using a TVIPS F216 CCD camera with a pixel size of 2.586 Å. Processing was done within Scipion 1.2 [154], particles were picked using Xmipp3 [155] and classification was done using Relion [156].

3.5.6 PEG precipitation to recover ejected flagella

Cells were spun down three times for 30 minutes at 3220×*g* and supernatant was carefully decanted. The supernatant was assessed with light microscopy to make sure no

cells remained. 3% PEG 20,000 was added to the supernatant and stirred at RT for >1 hour or at 4 degrees overnight. Flagella were recovered by centrifugation at 3220×*g* for 20 minutes.

3.5.7 SDS-PAGE gel electrophoresis of recovered flagella

After PEG precipitation, flagella were boiled in LDS and run on a 4-12% Bis-Tris gel (Thermo-Fisher, Hillsboro, OR, USA) and stained with InstantBlue (Sigma-Aldrich, Taufkirchen, Germany).

3.5.8 Mean number of flagella in a population

CFU at each OD was calculated by plating cells on LB or LBS agar and counting the number of colonies. The mean number of flagella at each time point, from negative stain images was multiplied by the total number of cells in the population. For all experiments at least three biological replicates with 30-50 cells per time point in each were imaged.

3.5.9 Electron Cryo-Tomography Sample Preparation

For *P. shigelloides, S. putrefaciens and V. fischeri*: Cells were pelleted by centrifugation at 3824×*g* for 5 minutes and resuspended to an OD_{600} of 11. Cells were mixed with gold fiducials coated in BSA and 3µl of the cell fiducial mixture was applied to freshly glow discharged R2/2, 200mesh gold Ultrafoil or copper Quantifoil R2/2 grids (Quantifoil Micro Tools GmbH, Germany). A Vitrobot Mark IV was used to freeze grids in an ethane/propane cryogen at 100% humidity.

V. cholerae (by Dr Susanne Brenzinger) and *P. aeruginosa* (by Dr Rohola Hosseini) cells from cultures were directly mixed with protein A-treated 10 nm colloidal gold solution (Cell Microscopy Core, Utrecht University, Utrecht, The Netherlands). After mixing, aliquots of 3 µl were applied to freshly plasma-cleaned R2/2, 200mesh copper Quantifoil grids (Quantifoil Micro Tools GmbH, Germany). Plunge freezing was carried out in liquid ethane using a Leica EMGP (Leica microsystems, Wetzlar, Germany). During

1 s blotting time, the blotting chamber was set at room temperature (20°C) with 95% humidity.

3.5.10 ECT Data Acquisition

Tomograms of *Plesiomonas, Shewanella* (By myself or Amanda Wilson) and *Vibrio fischeri* (by Dr Morgan Beeby) were collected on an FEI F20 with a Falcon II detector (Thermo Fisher Scientific (formerly FEI), Hillsboro, OR, USA). A total fluence of 120e^-/ $Å^2$ was used and a defocus of -3 to -4µm. Tomograms were collected at a tilt range of ±53 degrees with 3° tilt increments and a pixel size of 8.28 Å.

Tomograms of (by Dr Susanne Brenzinger) and *P. aeruginosa* (by Dr Rohola Hosseini) was performed on a Titan Krios transmission electron microscope (Thermo Fisher Scientific (formerly FEI), Hillsboro, OR, USA) operating at 300 kV. Tomograms were recorded with a Gatan K2 Summit direct electron detector (Gatan, Pleasanton, CA) equipped with a GIF-quantum energy filter (Gatan) operating with a slit width of 20eV. Images of *V. cholerae* and *P. aeruginosa* were taken at a nominal magnification of 42,000 and 26,000 respectively, which corresponded to a pixel size of 3.513 Å and 5.442 Å. Using UCSFtomo software, all tilt series were collected using a bidirectional tilt scheme of ±53 degrees (*V. cholerae*) and of ±60 degrees (*P. aeruginosa*), respectively. Defocus was set to -8 µm.

The *P. shigelloides* data-set for subtomogram averages were collected on a Titan Krios operating at 300 kV with a post-column GIF using a 20eV slit and a Gatan K2 summit (Gatan, Pleasanton, CA) collecting 4 frames per exposure. A pixel size of 2.713 Å with a total fluence of 54 e^-/A2 and a defocus range between -3 and -5.5µm was used. The bi-directional tilt series was collected using FEI's Tomo4 (Thermo Fisher Scientific (formerly FEI), Hillsboro, OR, USA) with a tilt range of ±53 degrees and a tilt-increment of 3°.

3.5.11 Tomogram reconstruction

For the *P. shigelloides* dataset, frames were aligned using UnBlur [120]. Tomoctf [77] was used to estimate CTF-parameters (tomoctffind) and correct stacks (ctfcorrectstack). Fiducials were picked from CTF-corrected stacks and tracked in IMOD

[89,121]. The aligned, CTF-corrected stacks and fiducial models were used with Tomo3d to reconstruct using SIRT or WBP [90,122]. For *V. fischeri* and *S. putrefaciens* Tomograms were reconstructed using RAPTOR [157]. For V. cholerae (by Dr Susanne Brenzinger) and *P. aeruginosa* (by Dr Rohola Hosseini), drift correction, fiducial-tracking based tilt series alignment of tomograms were done using the IMOD software package [89,121]. Tomograms were reconstructed using SIRT.

3.5.12 Subtomogram Averaging

Subtomograms were picked manually from binned tomograms. Template-free alignment was carried out in PEET by superimposing all manually picked subtomograms allowing no shifts or rotations for an initial reference. Initial alignment and averaging was achieved using binned subtomograms. Unbinned subtomograms were used for further refinement. As the rod length varied in the full motor, sub-tomogram averaging was carried out twice with custom masks applied to either the top ring structures or the cytoplasmic structures. As clear 13-fold symmetry was observed in the full motor, 13-fold rotational averaging was applied using custom scripts. The two individual averages for the top and bottom segments were then merged into a composite structure as in [34]. For comparisons, 13-fold rotational averaging was applied to the relic structure. FSC curves were determined from the final, unsymmetrised averages using PEET's calcFSC.

3.5.13 Segmentation

Semi-automatic segmentation of the membranes was performed in IMOD [89,121] using the Sculpt drawing tool followed by the linear interpolator (performed by myself and Forson Gao, Imperial College London).

3.5.14 Periplasmic distance measurements

Contours were drawn between the inner membrane and the first ring of the outer membrane disks manually in 3DMOD (IMOD package [89,121]) and distances were measured (performed by myself and Forson Gao, Imperial College London).

3.5.15 Clark-Evans distribution analysis

Clark-Evans ratios were calculated per cell with more than four flagella (N=70) [158]. To calculate the Clark-Evans distribution, the mean nearest neighbour distance was divided by half the square root of the mean cell pole density. The mean nearest neighbour distance was calculated using custom scripts and the cell pole area density was calculated for each pole. The area of each pole was calculated by adding the diameter of one C-ring (45 nm) to the maximum X and Y coordinates of any motor or relic structure and these coordinates were used to calculate the area of an ellipse. To calculate the mean cell pole density, each pole area was divided by the number of structures at that pole. The random dataset was made using custom scripts based on the area and number of structures on the real data cell poles but placed randomly.

3.5.16 Nutrient depletion assay

Cells grown overnight were removed from the supernatant by centrifugation. The supernatant was subsequently filtered using a 0.2µm filter. *Plesiomonas* cells grown to low OD_{600} (0.2) were spun down and resuspended in the filtered, spent medium. Negative stain grids were made prior to resuspension and after one doubling time in spent medium.

3.5.17 Minimal medium assay

Plesiomonas cells grown to low OD_{600} (OD 0.2) were spun down and resuspended in MOPS-minimal medium (40mM MOPS pH 7.4, 4 mM Tricine, 0.1 mM $FeSO_4 \cdot 7H_2O$, 9.5 mM NH_4Cl, 0.28 mM KCl, 0.53 mM $MgCl_2 \cdot 6H_2O$, 50 mM NaCl, 10mM KH_2PO_4, 0.005% $MgSO_4$, 0.0005% $MnCl_2 \cdot 4H_2O$, 0.0005% $FeCl_3$, 0.5% glucose). Cells were examined by light microscopy after one hour to see if they were swimming. Negative stain grids were made prior to resuspension and after one doubling time in spent medium.

3.5.18 Strain construction

Inducible expression of proteins in *Plesiomonas shigelloides* was carried out using the pBTOK vector [152]. DNA manipulations were carried out using appropriate kits

(VWR International GmbH, Darmstadt, Germany) and enzymes (Thermo Fisher, St Leon-Rot, Germany). The oligonucleotide pair CGCTCTAGAAGGAGGGCAAATGTGATG ACAACTGAAGATTTCAAAA and TCCGGGCCCTTAGAGCGGCATGACTCGATT G were used to amplify the gene encoding the diguanylate cyclase VdcA (VCA 0956) from *V. cholerae* (By Dr Florian Rossmann). Subsequently, the plasmid was constructed by restriction digest of the vector and the inserts with XbaI and PspOMI and subsequent ligation with Taq Ligase (Thermo Fisher, St. Leon-Rot, Germany). The oligonucleotide pair AATTCAGTCGGGCGACATCACCATCACCATCACTAAGCTTGGACTCCTGTTGAT and ATCAACAGGAGTCCAAGCTTAGTGATGGTGATGGTGATGTCGCCCGACTGAATT were used to amplify the gene encoding FlhA from *S. putrefaciens*. Subsequently, the plasmid was constructed using the Gibson assembly method. Plasmids were transformed into chemically competent *E.coli* cells. Subsequent delivery to *Plesiomonas shigelloides* was achieved by conjugation from E. coli WM3064.

3.5.19 Motility plates

P. shigelloides cells harbouring either empty pBTOK vector or expressing the diguanylate cyclase VdcA were stabbed into soft-agar plates (10g/L Bacto-Tryptone, 5 g/L NaCl, 3 g/L Bacto-Agar) containing 50µg/ml kanamycin and either no inducer or 2 ng/ml anhydrotetracycline and grown at 37°C for 6 hours.

3.5.20 cdiGMP over-expression

P. shigelloides cells harbouring either empty pBTOK vector or expressing the diguanylate cyclase VdcA were grown with 50µg/ml kanamycin to OD_{600} 0.2. Cells were then split in two and either not induced or induced with 2 ng/ml anhydrotetracycline until an OD_{600} of 0.4 was reached. Negative stain grids were made prior to and after induction.

Chapter 4

Mechanism of rotation: Structural studies of the flagellar stator complexes

4.1 Chapter Summary

The flagellar motor is powered by stator complexes in the inner membrane. Stator complexes are ion channels that convert electrochemical potential into torque to power the rotation of the flagellum. Although the flagellum has been studied for decades, providing a good biochemical understanding, the mechanism of action of the stator complexes remains poorly understood, partly due to a lack of structural information. This includes *in situ* details of the relative placement and number of stator complexes in the *Salmonella* motor, the dynamic nature of these complexes, and high resolution information to aid mechanistic insights into ion transfer and conformational changes. In this Chapter, I worked towards gaining an *in situ* structure of the *Salmonella* motor with a full set of stator complexes bound to it. By providing information on the number and relative placement of stator complexes, this would further our understanding of the dynamic mechanism of the stator complexes. To do this, I developed a strain to trap the stator complexes in place and demonstrate a proof of principle by the appearance of a protein density on the flagellar motor, positioned where the stator complexes are expected. I then worked towards gaining a high resolution structure of the stator complexes using SPA. Here, in collaboration with David Blair's lab at the University of Utah, I worked towards a purification protocol for studying purified stator complexes and did initial characterisation by SPA.

4.2 Introduction

At the heart of powering the rotation of the flagellar motor and eventually the cell, are the stator complexes. The torque for the motor is generated by the electrostatic interaction between FliG in the rotor and the collection of stator complexes [31]. At present an understanding of the mechanism of action of the stator complexes is hindered by the lack of detailed structural information.

In Chapter 2, I highlighted that the stator complexes in *Salmonella* are dynamic and are therefore not seen in the STA. This may be one of the selective advantages to the acquisition of the non-native β-proteobacterial motor found in modern day *Salmonella*. Due to this dynamic nature, however, the maximum number of stator complexes that can bind to the *Salmonella* flagellar motor, as well as the architecture and relative arrangement of the bound stator complexes, remains unclear. There is therefore a large gap in our understanding of the recruitment, binding capacity, stoichiometry and dynamic mechanism of stator complexes.

4.2.1 The stator complexes

Even without detailed structural analysis, decades of biochemical and biophysical experiments have led to well-established models. The stator complexes are each made up of four copies of a transmembrane protein, MotA, and two copies of a transmembrane protein, MotB (or PomA and PomB in sodium-powered motors). MotB, which when active, is non-covalently linked to peptidoglycan at its C-terminus [159] has a single transmembrane domain. MotA is a four transmembrane protein with two large cytoplasmic domains and two small periplasmic domains. Conserved residues in the cytoplasmic region between TM2 and 3 form electrostatic interactions with FliG charged residues. MotA and MotB form channels that utilise ion motive forces across the inner membrane [160–162] with the influx of ions thought to induce a large conformational change in the stators ("power-stroke") and leading to rotation of the rotor. Asp32 of MotB in *E. coli* likely

accepts a proton, to drive conformational changes in MotA [163]. Substitutions of Asp32 to anything other than D32E, results in complete loss of function [164]. As there are two MotB proteins per complex, it remains unclear whether one or two protons are needed to initiate the power stroke [165].

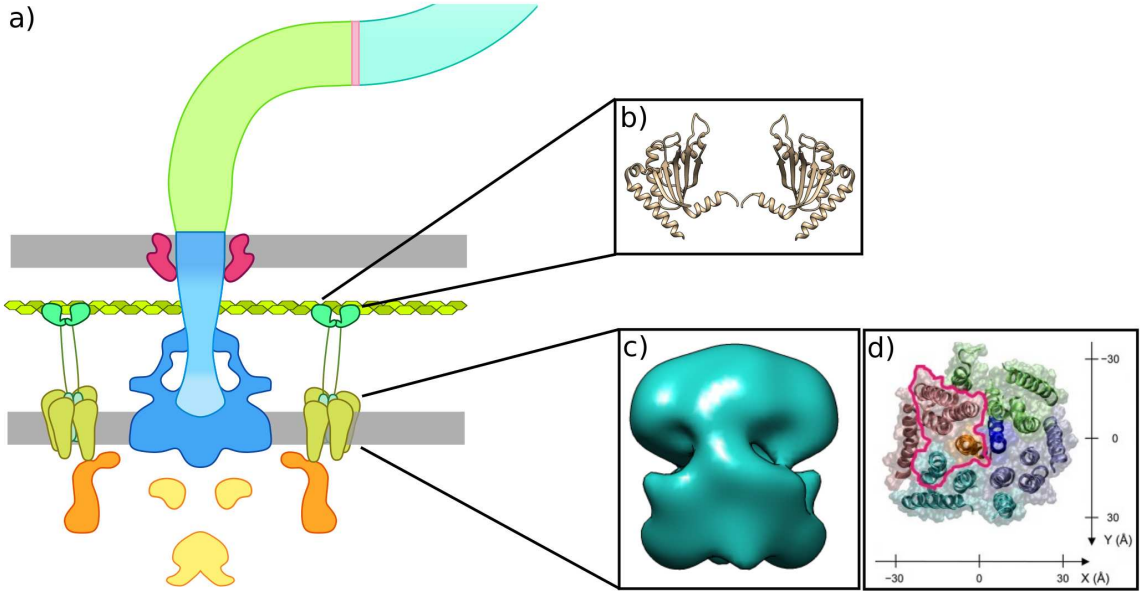


Fig 4.1: Structural analysis of the stator complex.
a) The stator complexes in the inner membrane are made of four copies of MotA and two copies of MotB. When engaged at the motor, MotA interacts with FliG in the C-ring and MotB interacts with peptidoglycan. b) The crystal structure of the peptidoglycan binding region of MotB (PDB-2zov). c) The 3D structure of $MotA_4$ from negative stain SPA (EMD-3417. d) Model of MotAB viewed from the periplasm, adapted from [166].

4.2.2 Experimental approaches to probe stator complex dynamics

The association of the stator complexes with the flagellar motor is dynamic. This dynamic interaction was first demonstrated in resurrection experiments [167,168]. These are an adaptation of the bead assay, where a cell is stuck to a glass slide and the relationship between speed and torque can be measured by altering the external load (changing the size of a bead attached to the hook or sheared filament) (Fig. 4.2a). The torque speed curves

have a characteristic shape where the motor switches from being mechanically limited (low speed, high torque) to being kinetically limited (high speed, low torque) (Fig. 4.2b) [35]. In the resurrection experiments, a stator complex deletion mutant cell is stuck to a glass slide and an external load is applied to the filament via a polystyrene bead. Stator complexes are then expressed from a plasmid in a controlled manner and the speed of the motor is measured. This established a relationship between speed and number of stator complexes at different external loads. The measured rotational speed of the motor was seen to have discrete increasing steps interpreted as the recruitment of additional torque-generating stator complexes. At high loads ~ 11 equally sized jumps were seen (Fig. 4.2c) whereas at low loads only a single increase was observed [169]. The size of the speed steps decreased with increasing stator complexes, suggesting the stator units are not equivalent. These results show that at high loads, multiple stator complexes are recruited to the flagellar motor to provide higher torque for pushing the bacterium through the more viscous environment while at low load the flagellum can power the cell with only one or two stator complexes providing torque. Importantly, overexpression of the stator complexes does not impair cell growth suggesting that there is tight control between the incorporation of stator complexes into the motor and the ion-conducting activity of MotAB [170]. A plug domain in MotB has been shown to stop premature ion leakage prior to full assembly around the MS-ring [171]. It is clear then that at low loads, where higher torque is not needed, the association of more than a couple of stators would be detrimental to the cell causing unnecessary proton leakage. The 11 discrete steps agree with early freeze-fracture images of the flagellar motor in *E. coli* which showed between 10 and 12 stator complexes per motor (Fig. 4.2d).

The stator complexes have a high turn-over rate and diffuse in and out of association with the motor. In single molecule fluorescent imaging of GFP-tagged MotB, ~22 copies of GFP-MotB were associated with each motor and a pool of ~200 GFP-MotB proteins were observed in the membrane. The turnover between the membrane pool and the motor-associated GFP-MotB had a rate constant of $0.04s^{-1}$, with a given stator complex remaining in the motor for ~ 30 seconds [172].

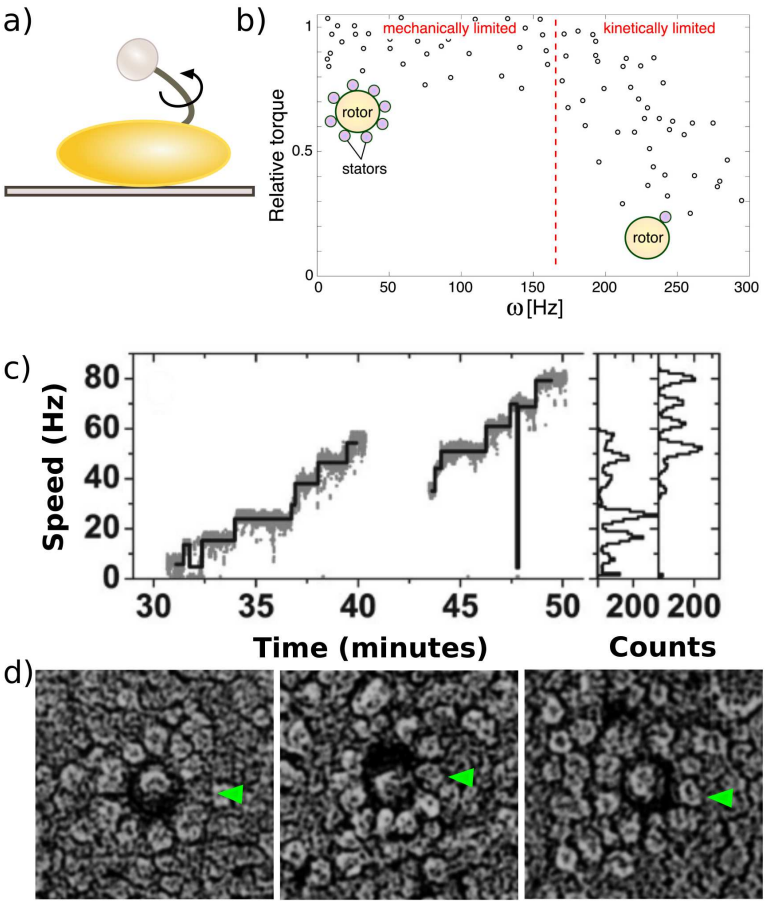


Fig. 4.2: Studying the dynamics of the stator complex.
a) "Bead-assay" experimental setup. A cell is attached to a glass slide and a polystyrene bead is fixed to the end of a truncated hook or flagellar filament. This allows characterisation of the motor across multiple external loads by altering the size of the bead. b) Example of a torque-speed curve. At low speed, the motor is at high torque and multiple stator complexes are associated with the motor to enable the high torque. At high speeds, the motor is at low torque and only a few stator complexes are associated with the motor. Adapted from [35]. c) Results from a resurrection experiment showing 11 discrete jumps in speed. Each speed increase is attributed to the recruitment of one stator complex. As 11 increases are seen, the maximum number of stator complexes that can bind to the Salmonella flagellar motor is expected to be 11. Adapted from [169]. Copyright (2006) National Academy of Sciences. d) Freeze-fracture images of rings of stator complexes in E. coli. Green arrows point to stator complex ring. Adapted from [173].

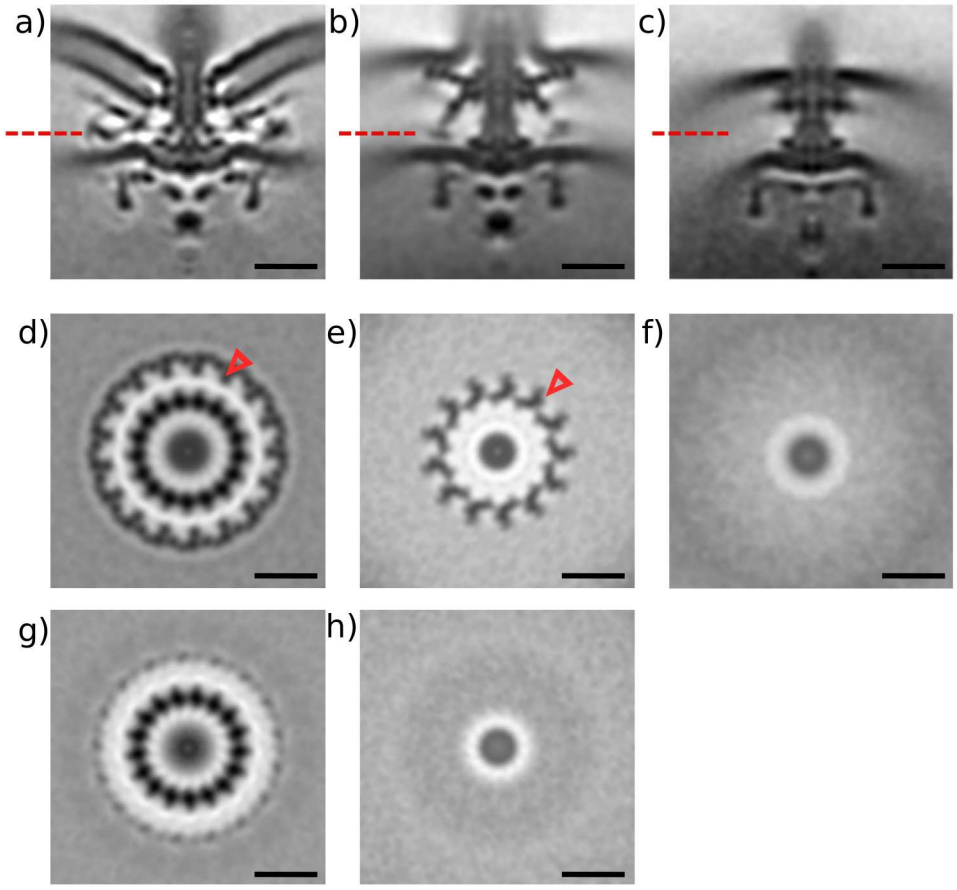


Fig. 4.3: The stator complexes are not seen in subtomogram averages of *Salmonella*. *a) Slice through a subtomogram average of the Campylobacter jejuni flagellar motor EMD-3150. b) Slice through a subtomogram average of the Vibrio fischeri flagellar motor. EMD-3155. c) Slice through a subtomogram average of the Salmonella enterica sv. Typhimurium flagellar motor EMD-3154. d) Average in (a) rotated 90° around the red dotted line in (a), to show the 17-fold symmetric stator complexes. e) Average in (b) rotated 90° around the red dotted line in (b), to show the 13-fold symmetric stator complexes. f) Average in (c) rotated 90° around the red dotted line in (c). No stator complexes are seen in the Salmonella enterica sv. Typhimurium flagellar motor. g) Slice through the stator complexes in a Campylobacter jejuni ΔmotB strain showing the disappearance of density marked with a red arrow in (d) (EMD-3157). h) Slice through the stator complexes in a Vibrio fischeri ΔmotB strain showing the disappearance of density marked with a red arrow in (e) (EMD-3156).*

4.2.3 Visualising the stator complexes *in situ*

When a STA of the *Salmonella* flagellar motor was acquired, no stator complexes were seen (Chapter 2, EMD-3514 [5,34]) although under the same imaging conditions, stator complexes were seen in *Vibrio fischeri* (EMD-3155) and *Campylobacter jejuni* (EMD-3150) (Fig. 4.3). As explained in Chapter 2 and above, this is due to the dynamic nature of the stator complexes in *Salmonella.* The stator complexes only assemble on the flagellar motor when an external force is applied to the motor and the cells are swimming at low speeds but need high torque (Fig. 4.2b). The cells imaged for the STA were frozen in a low viscosity medium and were therefore swimming at high speeds but needed low torque and therefore only a few stator complexes would be bound to each motor. These incomplete rings of stator complexes are averaged out in the STA process. Although the stator complexes are visible in *V. fischeri*, they are also likely to be dynamic, as in a close relative *Shewanella oneidensis* [174] but the occupancy rate of the stator complexes on the motor and their waiting time associated with the motor is likely higher.

Although resurrection experiments show at least 11 incremental speed steps and freeze fracture images of *E. coli* show between 10 and 12 stator complexes, because we can't visualise the stator complexes in *Salmonella in situ*, at present we do not know what the maximum number of stator complexes that can bind to the *Salmonella* flagellar motor is. This leaves large gaps in our understanding of how the stator complexes are arranged and what their stoichiometry is relative to the other flagellar motor protein stoichiometries.

4.2.4 The enigmatic protein, FliL

The highly conserved flagellum-associated protein, FliL, is enigmatic as in different bacterial species it has been associated with multiple different roles. It is however, likely involved in recruiting or stabilising the stator complexes. Phenotypes in deletion mutants range from complete inhibition of swimming [175,176] or swarming [177–179] to inhibition of flagellar ejection in *Caulobacter crescentus* [134,180]. In *Salmonella* and *E.*

coli, FliL was shown to interact with both the rotor and the stator complexes. Subtomogram averaging of the *Borrelia burgdorferi* flagellar motor in a WT and Δ*fliL* background showed that in *Borrelia*, FliL is positioned as a ring within the stator complex ring (Fig. 4.4). The deletion of *fliL* in these cells led to incorrect orientation of flagella as well as reduced swarming motility (but not swimming motility) [179]. Initial studies in *Salmonella* and *E. coli* attributed FliL to increased motor speed as well as establishing correct motor bias [181]. More recent studies however, saw no effect on motor torque or motor function in *E. coli* [182]. Although this protein remains enigmatic, the majority of evidence suggests that it plays a role in either recruiting or stabilising the stator complexes.

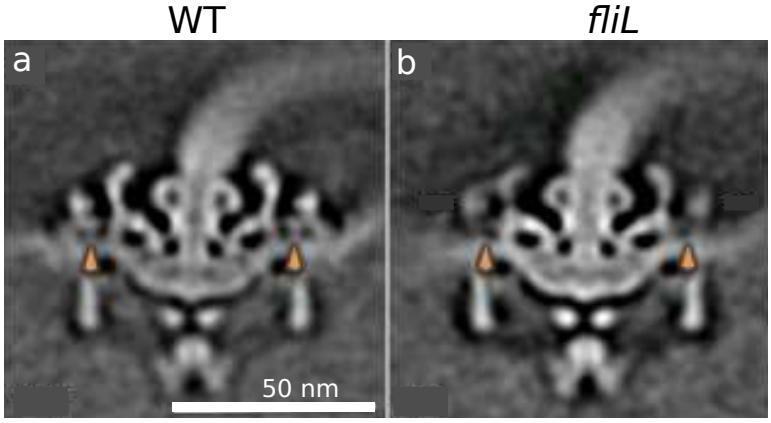


Fig. 4.4: FliL forms a ring within the stator complexes.
Slices through subtomogram averages of flagellar motors in WT and ΔfliL Borrelia burgdorferi cells. Orange arrows point to FliL density in WT and the missing FliL density in the ΔfliL strain. Figure adapted from [179].

In this Chapter, I aimed to gain a more detailed structural understanding of the flagellar motor stator complexes. Towards this goal I worked to develop the ideal strain for visualising the stator complexes *in situ* by ECT and used this strain to demonstrate the appearance of a protein density on the flagellar motor, positioned where the stator complexes are expected. I next worked towards establishing a purification protocol for gaining a high resolution structure of the stator complexes by SPA and performed initial structural characterisation with SPA.

4.3 Results

4.3.1 Towards visualising the stator complexes in *Salmonella in situ*

In order to provide a definitive answer to what the maximum number of stator complexes that can bind to the *Salmonella* flagellar motor is, and what their architecture is, I aimed to visualise the stator complexes *in situ* using ECT and STA. Because the stator complexes were not seen in a previous STA of the *Salmonella* flagellar motor [34], I worked towards producing a strain that would provide the highest chance of having all stator complexes bound to all motors when imaged. The challenges that needed to be overcome were:

1. The pool of stator complexes may not be sufficient for all flagellar motors to have all stator complexes bound at maximal capacity
2. *Salmonella* is over 1 micron thick and therefore too thick for high quality ECT
3. The stator complexes are dynamic and are only assembled on the motor under high load
4. The stator complexes disengage with the motor frequently, even under high load, and need to be stabilised in place once assembled

4.3.1a Ensuring sufficient building blocks

Firstly, to ensure that the pool of stator complexes was large enough to have the maximum number of stator complexes bound to all motors at once, I made a MotAB over-expression plasmid (pkG116_*motAB*) and ensured it complemented by producing a Δ*motAB* strain and looking for WT swimming levels in soft agar motility plates (Fig. 4.5a). The pkG116 plasmid is Chloramphenicol resistant and is sodium salicylate inducible. The flagellar protein FliL, is thought to increase the output of the flagellar motor by interacting with the stator complexes to either stabilise or recruit them, potentially contributing to

torque generation at high load [181]. I therefore produced a FliL over-expression plasmid (pBTOK_*fliL*), expecting that excess FliL might help to lock the stator complexes in place. The pBTOK plasmid is inducible with anhydrotetracycline and Kanamycin resistant. As I had no way to assess whether the FliL plasmid compliments a Δ*fliL* strain (as in our lab we cannot measure the phenotype of increased torque), I added an N-terminal polyhistidine tag and assessed expression with Western blot analysis (Fig. 4.5b).

To make the cells thinner for ECT, the plasmids were moved into a *Salmonella* strain that has inducible FtsZ expression from its chromosome, forming "mini-cells" when induced (described in Chapter 1). The production of mini-cells is random, and mini-cells with a large variation in size are produced. I therefore developed a purification protocol that uses a series of centrifugation steps at varying speeds to separate cells based on their size, and kept only the smallest mini-cells after inducing expression of MotAB, FliL and FtsZ.

Due to the overexpression of MotAB and FliL on top of WT expression levels, the mini-cell strain with both plasmids is expected to have a sufficient pool of stator complexes, as well as a sufficient pool of FliL for recruitment or stabilisation of the stator complexes. The cells should also be small enough for tomograms with good SNRs.

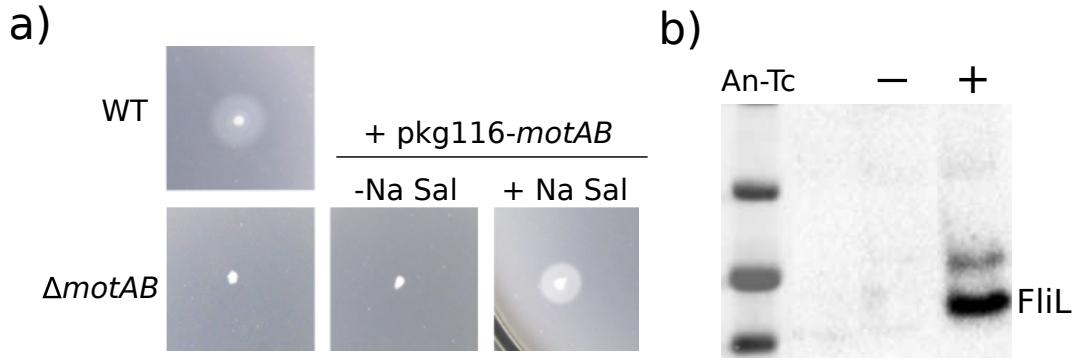


Fig. 4.5: Overexpression of MotAB and FliL.
a) Soft agar motility plates show that motility returns in a ΔmotAB strain when MotAB is expressed from an over-expression plasmid. b) FliL-His over-expression detected by a Western blot using an antibody against a histidine tag. (Na Sal = Sodium Salicylate, An-Tc = Anhydrotetracycline)

4.3.1b Mimicking a high-load environment

In *Salmonella*, the number of stator complexes assembled around the flagellar motor is dependent on the external load applied to the filament. As freezing highly viscous solutions would be detrimental to the quality of ice on cryo-grids, I needed to develop a method to mimic a high load environment while not increasing the viscosity of the solution. Importantly, the load could not be transient but needed to stay high ensuring that when the stator complexes disengage from the motor, they are immediately re-engaged or replaced.

Salmonella cells can be agglutinated by the addition of bivalent antibody against the flagellar filament protein, FliC. These bivalent antibodies are used for agglutination tests to identify the specific *Salmonella* serovar by detecting the flagellar H-antigen. We rationalised that if flagella from two different cells are tethered together, the force applied on the motors from the cells swimming in opposite directions would mimic a high-load environment. I optimised the concentration (1: 7500 dilution) of bivalent α-FliC antibody that did not cause the cells to agglutinate in large clumps but was high enough to inhibit swimming. By analysing the filaments by negative stain EM, and ECT, it was clear that the antibody was causing filaments to stick together (Fig. 4.6). Resurrection experiments previously showed that a high load needs to be applied to the motor for over 30 minutes before stator complexes start assembling on the motor and all are assembled after 50 minutes (Fig. 4.2c). Cells were therefore incubated with antibody at 37°C for 1 hour prior to vitrification.

4.3.1c Imaging the *Salmonella* stators *in situ*

The mini-cell strain with MotAB and FliL over-expressed was incubated with bivalent antibody for one hour at 37 ^{o}C. Under the light microscope, cells appeared to be pulling against each other, unable to swim apart. When tomograms of the strain were collected, flagella were tethered and multiple mini-cells were in each grid hole (Fig. 4.7a). However, due to the large number of flagella, which included flagella that had broken off from cells but were still tethered to other filaments with the bivalent antibody, targeting mini-cells specifically that have flagellar motors, for tilt series collection, was not possible

and the yield was very low (~ one motor in every five to six tomograms). Although, some motors were picked (examples in Fig. 4.7b), most mini-cells, although having many flagella in close proximity, did not have a flagellar motor (Fig. 4.7c). After six data collections , over 500 tomograms provided only 84 subtomograms, not enough to produce a STA of the small *Salmonella* flagellar motor.

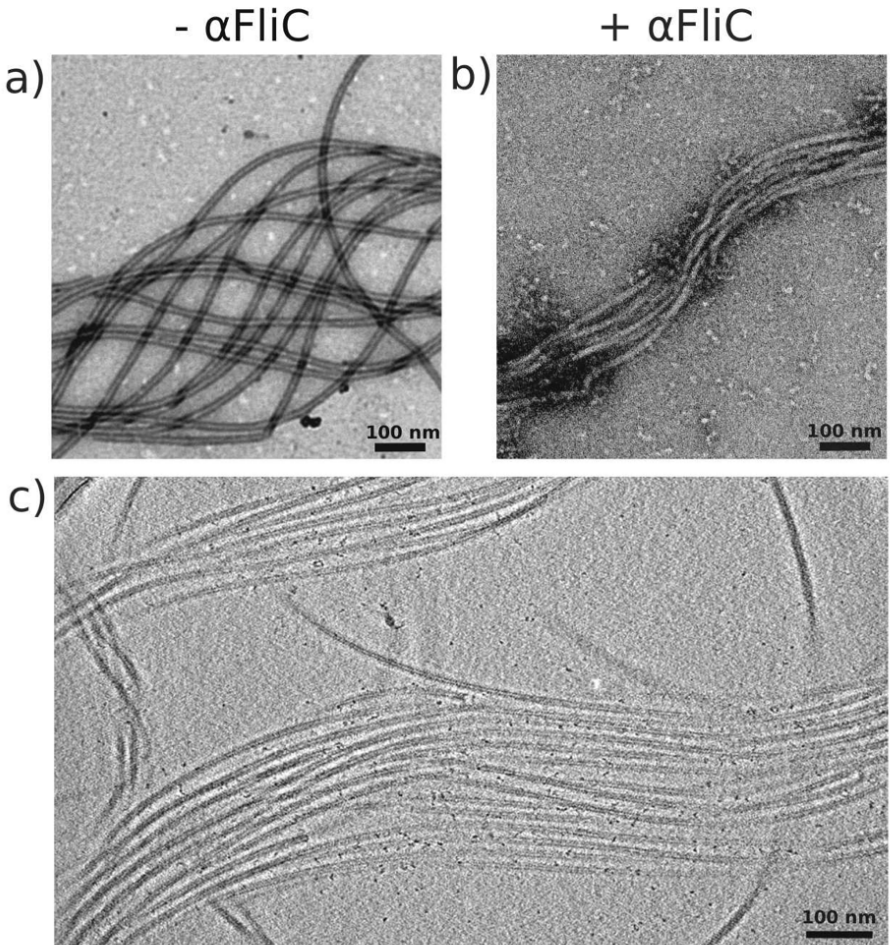


Fig. 4.6: Tethering flagellar filaments with a bivalent antibody sticks filaments together.
a) Negative stain micrograph of flagellar filaments without the addition of bivalent antibody. b) Negative stain micrograph of flagellar filaments with the addition of bivalent antibody. Filaments are stuck together. b) Slice through a tomogram of tethered filaments.

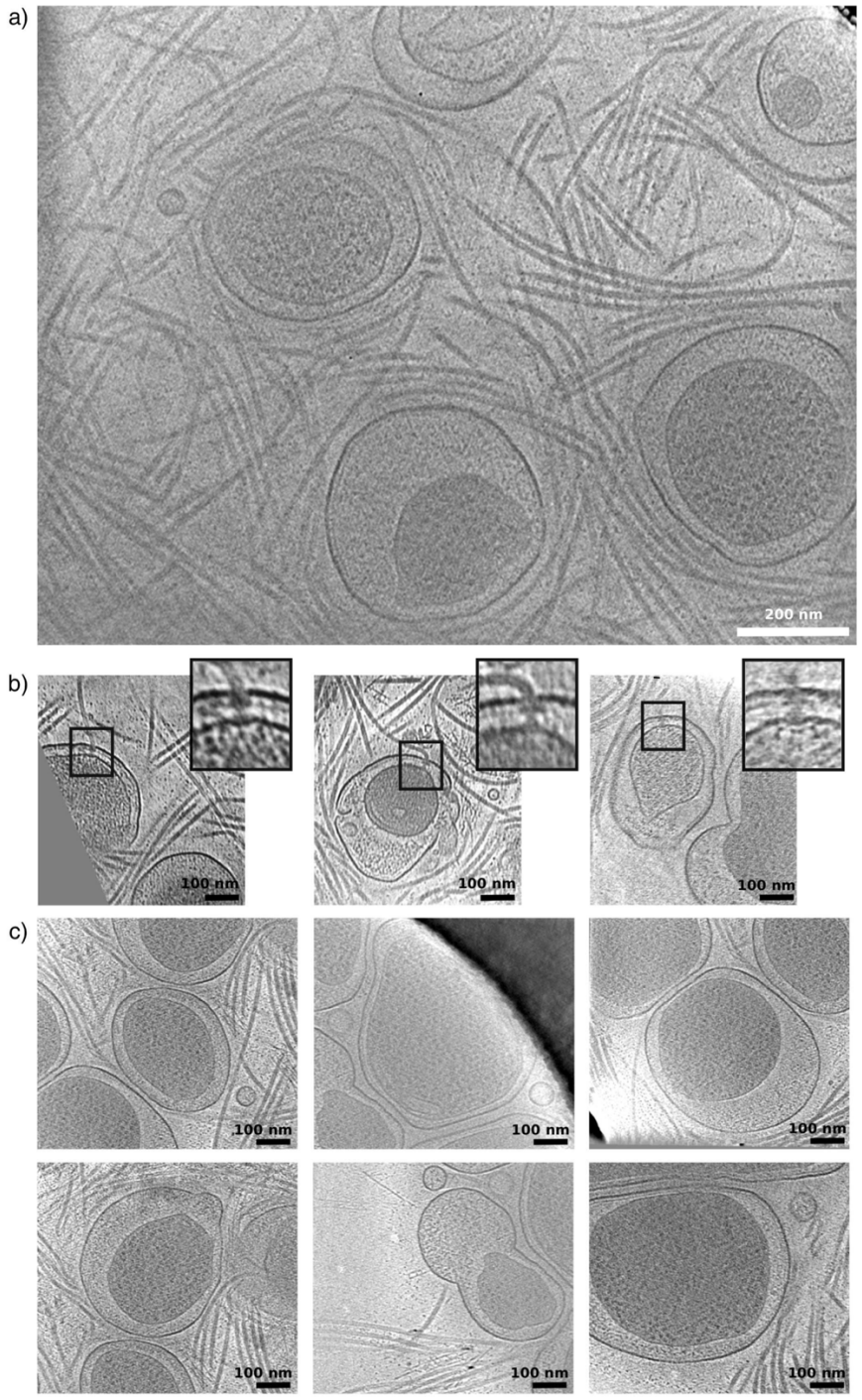


Fig. 4.7: Constructed strain has a low yield of motors per tomogram.
a) Slice through a representative tomogram. There are multiple mini-cells in one grid hole and many filaments, making targeting cells with flagellar motors for tilt series collection difficult. b) Example subtomograms with motors c) Example subtomograms of mini-cells with flagella in close proximity but which do not contain flagellar motors.

Although the low yield made collecting the large number of motors needed for a subtomogram average unfeasible, some of the initial subtomograms of this strain have clear densities where the stator complex is expected to be (Fig. 4.8b) and which is missing from the original *Salmonella* flagellar motor (Fig. 4.8a). The stator complex density is in the same place and orientation as the stator complexes from another β-like motor from *Hylemonella gracilis*, including the extra density that appears to be interacting with the C-ring, just below the inner membrane (Fig. 4.8c). This is a direct visualisation of the dynamic nature of the stator complexes.

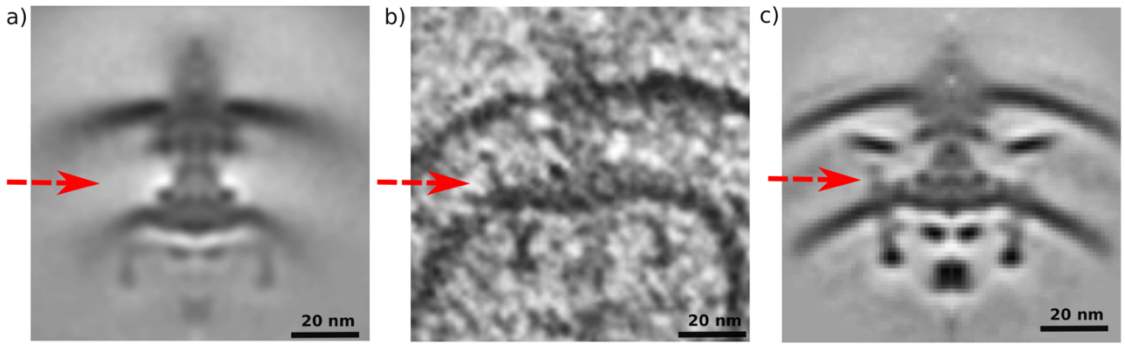


Fig. 4.8: Tethering filaments to increase load recruits stator complexes.
a) Subtomogram average of Salmonella flagellar motor imaged under low-load (EMD-3154). No stator complexes are seen where expected (red arrow). b) An example single subtomogram of the mini-cell Salmonella strain with MotAB and FliL overexpressed and imaged under high-load by the addition of bivalent antibodies against FliC. A clear protein density is seen where the stator complex is expected to be (red arrow). c) Subtomogram average of Hylemonella gracilis [5], a β-proteobacterium with clear stator complexes in the same place as seen in (b) (red arrow).

The low yield of motors is likely due to the random placement of division planes in the FtsZ over-expression strain. This results in many mini-cells without flagella and very few with more than one flagellum. To overcome this, I reasoned that instead of pinching off mini-cells from a WT cell at random places, a better method would be to limit the size that an individual cell can grow to. This would mean that the small cells still have the WT number of flagella. It was recently shown that bacterial cell size is regulated by fatty acid

biosynthesis [183] and that this is due to fatty acids altering the capacity of the cell envelope [184]. I therefore constructed a *fabH::Tc* knockout strain. FabH (Beta-ketoacyl-acyl carrier protein synthase III) is essential for the biogenesis of type II fatty acid [185]. The *fabH::Tc* knockout strain had a reduced growth rate, had a very small colony size, and many cells were considerably smaller than WT (Fig. 4.9). However, as with the FtsZ mini-cells, the cell size was not uniform but varied significantly. Surprisingly, initially the Δ*fabH* cells were non-motile however, after pricking into soft agar motility plates, motile revertant flares were seen, and in these cells WT motility was regained.

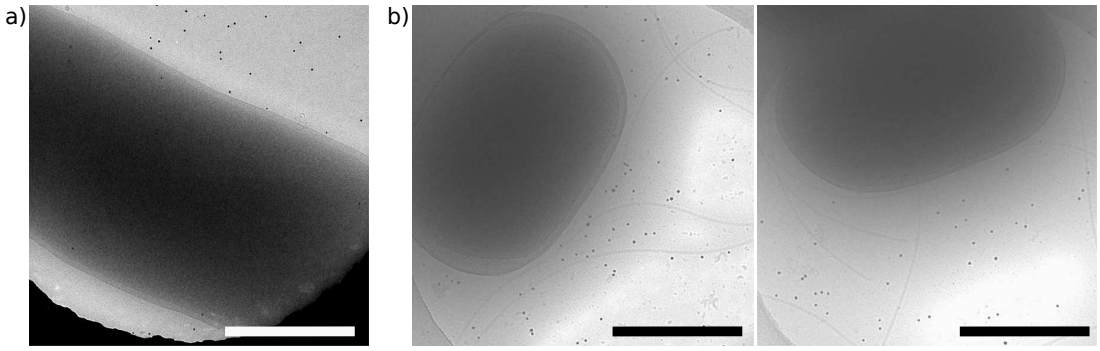


Fig. 4.9: FabH deletion limits cell size.
a) Example projection image of a WT Salmonella cell vitrified on an EM-grid. b) Two example projection images of the smallest ΔfabH cells seen. Each cell has multiple flagella, unlike in the FtsZ mini-cell strain however, although the cells are much shorter than WT cells, they are still over 500 nm thick. Scale bar = 500 nm.

The MotAB and FliL plasmids were moved into the Δ*fabH* stain by electroporation. Unsurprisingly, due to altering the outer membrane composition by stopping fatty acid synthesis, the strain had a reduced transformation efficiency by electroporation and needed large amounts of plasmid DNA. Once both plasmids were in the Δ*fabH* stain, the same protocol for tethering the filaments together using bivalent antibody against FliC was used (Fig. 4.10).

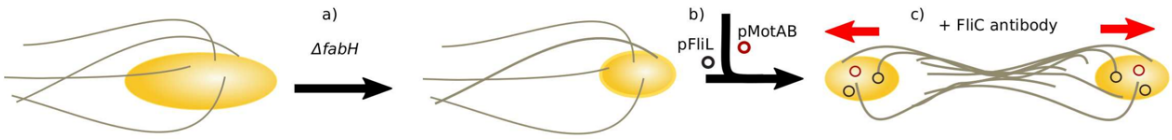


Fig. 4.10: Schematic showing final strain for imaging.
a) Deleting FabH leads to smaller cells. without decreasing number of flagella per cell. b) Over-expression of MotAB ensures a large pool of stator complexes and over-expression of FliL may lead to more stator complexes recruited to the motor or stabilised at the motor. c) Tethering flagella with anti-FliC bivalent antibody mimics a high load environment as the cells swim away from each other.

100 tomograms were collected of the Δ*fabH* strain overexpressing MotAB and FliL. There was a large range in cell morphology and cell size (Fig. 4.11). Due to the thickness of many cells, tethering of these cells led to thicker ice than on the mini-cell grids. Tomograms were therefore not as clear. Unfortunately, the yield of motors per tomogram did not increase, partly due to the decreased quality of tomograms and the thicker cells, making motors that were not perpendicular to the electron beam too obscure to identify.

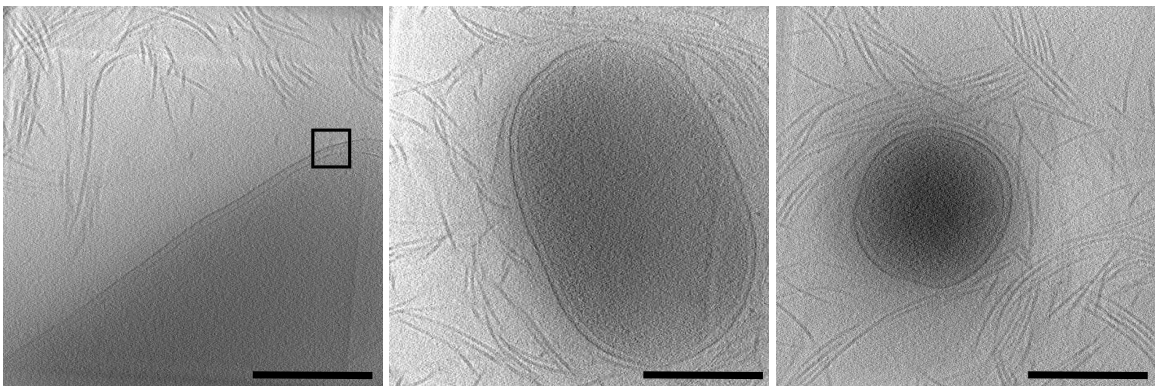


Fig. 4.11: Data collection of final strain.
Slices through three example tomograms showing the variety of sizes in the ΔfabH strain and many tethered flagellar filaments. The black box highlights a motor.

4.3.2 Towards a high resolution structure of the stator complex

The biggest leap in our understanding of the flagellar stator complexes will be gained from a high resolution structure of $MotA_4MotB_2$. Towards this goal, I collaborated with David Blair's lab at the university of Utah, whose focus is the biochemistry of the stator complexes.

Initially, the Blair lab sent purified stator complexes which I assessed by negative stain EM. After gel filtration (performed by Dr Kim Eun A, University of Utah) the protein was pure except for two faint contaminating bands (Fig. 4.12 a-b). When I assessed the protein with negative stain EM, there was some aggregation and the small protein complex was not homogeneous (Fig. 4.12 c). The small size of the stator complex (~170kDa total) makes assessing the quality of the protein, with negative stain EM and on our in-house microscopes, challenging.

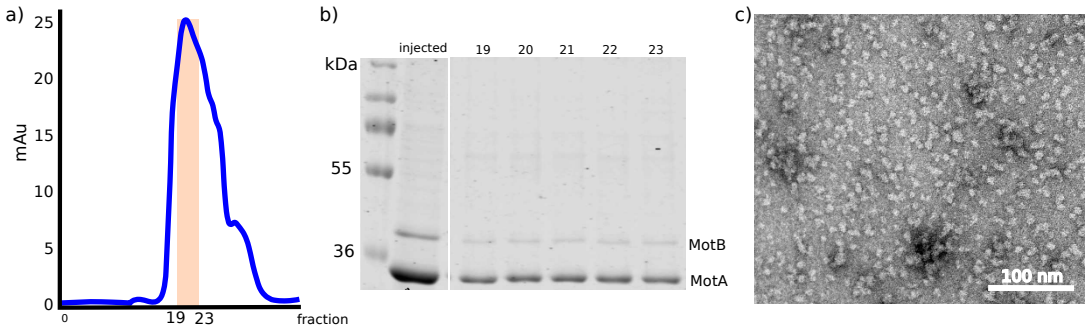


Fig. 4.12: Assessing purified MotAB from a collaborator by negative stain EM.
a) Gel filtration trace of MotAB after nickel affinity purification. b) Coomassie stained SDS-PAGE gel of protein before gel filtration (injected) and after gel filtration from orange area in (a). c) Example negative stain micrograph of purified MotAB.

To increase the size of the protein complex to aid with structural studies, the sequence for a maltose binding protein was added to the plasmid by our collaborators, in the flexible linker between the MotB plug region and the peptidoglycan binding domain. Again, the protein was pure after gel filtration (Fig. 4.13a-b) (performed by Dr Kim Eun

A, University of Utah). When I collected negative stain micrographs, the protein appeared homogenous and had limited amounts of aggregation (Fig. 4.13c) so I performed 2D classification. Although classes did converge on shapes of the expected size, no distinct structural features were seen in 2D class averages (Fig. 4.13d).

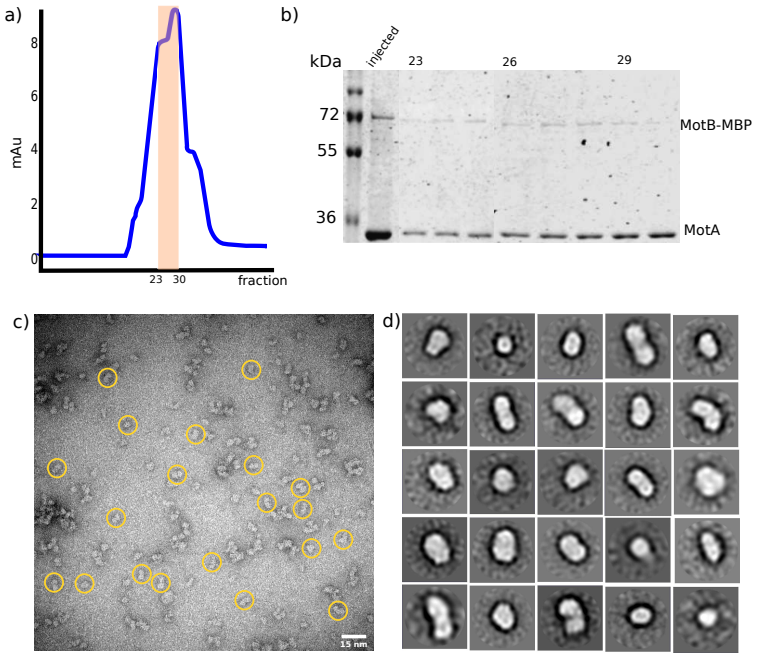


Fig. 4.13: Assessing purified MotAB-MBP from a collaborator by negative stain 2D class averaging.
a) Gel filtration trace of MotAB-MBP after nickel affinity purification. b) Coomassie stained SDS-PAGE gel of protein before gel filtration (injected) and after gel filtration from orange area in (a). c) Example negative stain micrograph of purified MotAB-MBP. Orange circles show examples of particles that were picked. d) 2D class averages of purified MotAB.

As the sample often precipitated while in transport, and to try and improve the quality of the protein, we moved towards in-house purification. When I expressed MotAB-MBP in-house however, the expression level was very low and the SEC column trace showed multiple peaks (Fig. 4.14a). On an SDS-PAGE gel contaminating bands were seen (Fig. 4.14b) however, when analysed by Western blot analysis using an anti-polyhistidine antibody, the main contaminating band was shown to be a MotA-dimer (Fig. 4.14c). All

peaks were assessed by negative stain EM (Fig. 4.14d) and the most homologous peak was taken forward for 2D class averaging (Fig. 4.14 e). Class averages appear different from previous samples and were more heterogeneous. Although multiple different approaches to improve the sample were tested (data not shown), no significant improvement was seen in negative stain 2D class averages.

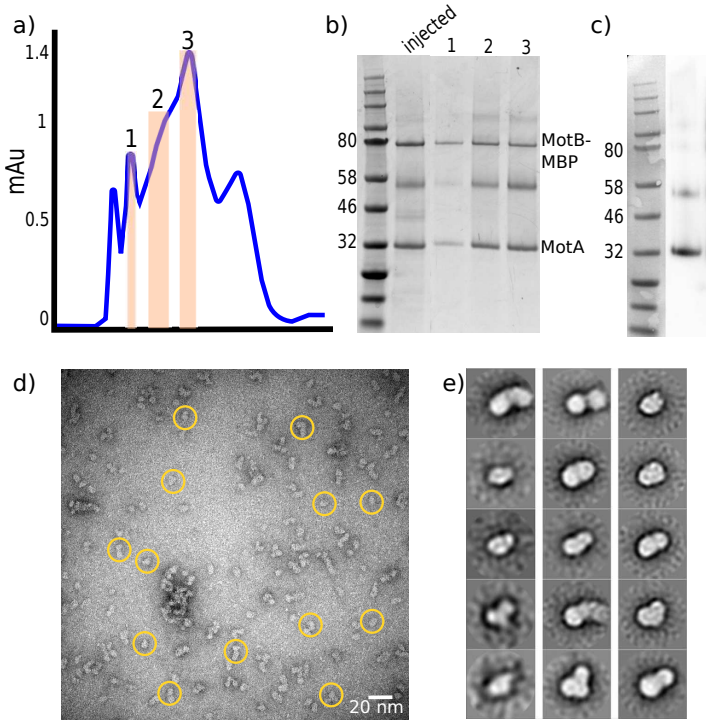


Fig. 4.14: Assessing MotAB-MBP purified in-house by negative stain 2D class averaging.
a) Gel filtration trace of MotAB-MBP after nickel affinity purification. b) Coomassie stained SDS-PAGE of protein after gel filtration from three peaks highlighted in orange in (a). c) Western blot showing that MotA is dimerising d) Example negative stain micrograph of purified MotAB-MBP. Orange circles show examples of particles that were picked. e) 2D class averages of purified MotAB.

4.3.3 Cryo-EM analysis of $MotA_4B_2$

Good sample arrived multiple times from the Blair lab, which I used to screen vitrification conditions. I wanted conditions which were reproducible and produced good

quality, uniform ice with homogenous sample that had not aggregated (Fig. 4.15a). The quality of the protein was difficult to assess on our in-house microscopes (120 – 200 keV) due to the small size of the complex (Fig. 4.15a). When the sample was loaded into a 300 keV microscope at the Francis Crick Institute, the clarity of the images made it clear that the protein was disassembling in thin ice and data needed to be collected in the thicker areas of the grid. This is not ideal for such a small protein and it was difficult to see particles in micrographs that were collected close to focus (Fig. 4.15b). Unfortunately, even in the thicker ice, a lot of dissociated complex was seen. After initial 2D-classes of the dataset looked promising (Fig. 4.15c), no improvements were made with further processing.

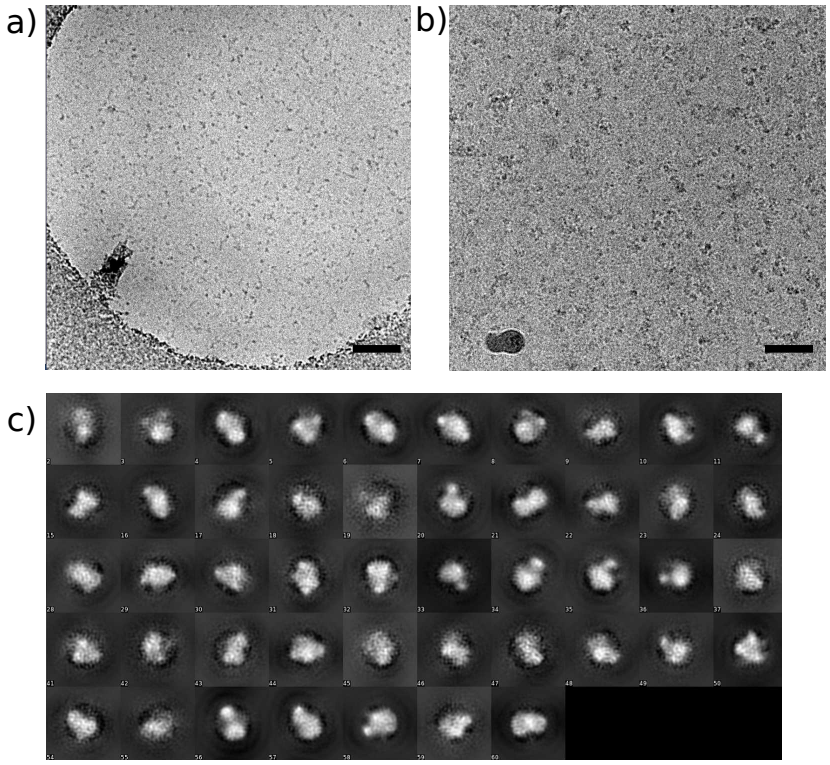


Fig. 4.15: Cryo-EM analysis of the stator complex.
a) Example high defocus image of one hole collected on a 120 keV Tecnai T12 microscope. Scale bar = 100 nm b) Example micrograph of stator complexes collected on a 300 keV Titan Krios. Scale bar = 40 nm c) 2D class averages from Titan Krios dataset.

4.4 Discussion

In this Chapter, I provide work towards visualising the *Salmonella* stator complexes *in situ* with ECT and gaining a high resolution structure of the stator complexes by SPA. Both projects, although promising require further work.

4.4.1 Direct visualisation of the dynamic nature of the stator complexes

The appearance of stator complexes in mini-cell subtomograms of flagellar motors when a high load was applied to the motor, is a direct visualisation of the dynamic nature of stator complex assembly (Fig. 4.8). This illustrates the mechanosensitivity of the motor, where stator complexes are only recruited to the motor when needed, to increase the torque in higher load or higher viscosity environments. In Chapter 2, I showed that the *Salmonella* motor is not native but was acquired via a HGT from the β-proteobacteria. The dynamic nature of the stator complexes, illustrated here by the appearance of stator complexes when an external load was applied to the filament, is a likely selective benefit of the new non-native motor.

4.4.2 So, how many stator complexes are there in the *Salmonella* flagellar motor?

From resurrection experiments, we expect the maximum number of stator complexes that can assemble on the motor to be at least 11. Freeze-fracture experiments confirm this, with between 10 and 12 stator complexes seen in *E. coli*. The freeze-fracture experiments were performed on cells grown in LB and are therefore under low load. This is not in agreement with the *in situ* tomography results and all biochemical and biophysical results showing the dynamic nature of the stator complexes. A possible explanation may be the selection regime the authors used for identifying motile cells (pricking into multiple rounds of motility plates), which may have resulted in a mutant with increased occupancy stator complexes. However, this may also be an artefact.

Although *Salmonella* is a γ-proteobacterium, it has a β-like flagellar motor (see Chapter 2). At present there are only two STA structures of flagellar motors from β-proteobacteria: *Bordetella bronchiseptica* (Chapter 2), and *Hylemonella gracilis* (Fig. 4.8c) [5]. Although no stator complexes were visualised in the *B. bronchiseptica* motor, 13 stator complexes were present in the *H. gracilis* flagellar motor. The ability to visualise the stator complexes in *H. gracilis* may be due to an extra disk present in the *H. gracilis* motor, acting to stabilise the stator complexes. From this it is therefore possible that *Salmonella* has a maximum number of 13 stator complexes that can bind to the flagellar motor, which would not be inconsistent with previous results.

4.4.3 Importance of visualising stator complexes *in situ*

There are large gaps in our knowledge of how stator complexes are recruited and stabilised on the flagellar motor. A large part of this gap could be filled by visualising the stator complexes *in situ*. This would provide the maximum number, architecture, the relative placement and the stoichiometry of the stator complexes, allowing informed mechanistic models to be made. There may, for example, be a symmetry mismatch which would help to explain how rotation is enabled or the arrangement and architecture could provide insights into how stator complexes are recruited.

4.4.4 Next steps for *in situ* visualisation

The appearance of stator complexes in the flagellar motors of mini-cells that have MotAB and FliL over-expressed and have been tethered, is a promising sign that using this approach could lead to resolving the stator complexes by STA. However, the low yield made data collection unfeasible. After six tomography data collections and over 500 tomograms, only 84 subtomograms of motors were acquired. To try and make up for this I attempted to make a strain that was smaller than WT cells which retained the same number of flagella, by deleting *fabH*. However, although many cells were smaller than WT, the population varied greatly in size. The larger size provided more difficulties than just

increased cell thickness. When filaments were tethered, the clumps of cells that formed produced much thicker ice on the grid than with mini-cells.

There are a few ways to progress for further studies. Firstly, in an attempt to get thinner ice on the EM grid, the smallest Δ*fabH* cells could to be purified before tethering, analogous to the purification protocol that I used for the mini-cells. A second option is to tether cells at very low cell density and then quench the antibody using monomeric FliC protein. This would stop large clumps of cells forming which creates thick ice on the EM grid. A third approach is to move back to a WT strain with the over-expression plasmids and to deflate the cells in a controlled manner using antibiotics. When I used this method to image *Bordetella* and *Plesiomonas* cells in Chapter 2, the cells kept swimming. This means that the recruitment of stator complexes was not affected by gentle lysis, and may be an easier way to provide a strain with multiple flagella per cell that is thin enough to provide good quality tomograms.

4.4.5 Future for single particle analysis studies

The purification protocol of the stator complexes needs to be improved before a high resolution structure with SPA can be gained. Although a detergent screen showed that Fos-Choline12 solubilised the most stator complexes while retaining activity [186], it is a very harsh detergent and may not be the best detergent for maintaining structural integrity for structural studies of a small protein complex with SPA. New developments in the field of membrane-protein purification should be tested, such as the use of SMALPs which both extract membrane proteins from the native membrane, and stabilise them [187]. As the protein was dissociating upon vitrification, this will also need to be optimised. Applying a support film to the grid, such as Graphene oxide may help stabilise the complex or a method for chemical crosslinking prior to vitrification could be used. It would be best to solve the native structure without the MBP-tag. As SPA on small proteins is becoming more routine due to microscopes, detectors and software improvements, this is becoming much more attainable.

4.5 Materials and methods

Table 6: Strains and plasmids used in Chapter 6

Strain or plasmid	Source
Salmonella LT2	Kelly Hughes (University of Utah)
Salmonella Δ*fabH*	This study
pKG116_MotAB	This study
pkBTOK_FliL	This study
LT2 pAra_ftsZ	Kelly Hughes (University of Utah)
pKD46	Kelly Hughes (University of Utah)

4.5.1 Bacterial growth

Cells were grown overnight at 37°C, shaking at 290RPM. A 1:100 dilution of the culture was then grown to an OD 600 of 0.6. If needed, cells were induced with Anhydro-tetracycline (20ng/ml), Arabinose (0.2%), Sodium Salicylate (10μM). When antibiotics were used the concentrations were, 25μg/ml Chloramphenicol, 50 μg/ml Kanamycin, 100 μg/ml Ampicillin.

4.5.2 Mini-cell purification

The MotAB plasmid was induced at OD_{600} 0.1-0.2 for 1 hour followed by FliL induction for a further hour and finally the induction of FtsZ for four hours.

15ml of arabinose induced mini-cells were pelleted at 8000RPM, 10min. Supernatant was pelleted again at 17000RPM, 15min and the pellet was resuspended in 30μl medium.

4.5.3 Negative stain grid preparation

3µl of cells were placed on glow-discharged continuous-carbon grids (Taab Laboratory Equipment Ltd.). The grids were stained with 2% Uranyl Acetate and stored at room temperature prior to imaging.

4.5.4 Negative stain EM imaging

Negative stain images were collected on either an FEI Tecnai G2 Spirit BioTWIN (Tungsten) using an Eagle CCD camera or a Tecnai T12 TWIN (LAB6) using a TVIPS F216 CCD camera.

4.5.5 FliC bivalent antibody tethering

Add 1:7500 dilution of antibody (*Salmonella* H antiserum - Disco 228241) to a 1.5 ml mini-cell sample and incubate for 45 minutes – 1 hour. Cells were pelleted and immediately plunge frozen.

4.5.6 Cryo-grid preparation

Cells were mixed with gold fiducials coated in BSA. 3µl of the cell fiducial mixture was applied to freshly glow discharged R2/2, 300 mesh gold Ultrafoil or copper Quantifoil R2/2 grids (Quantifoil Micro Tools GmbH, Germany). A Vitrobot Mark IV was used to freeze grids in an ethane/propane cryogen at 100% humidity with a 60 second wait time.

Purified MotAB protein was applied to freshly glow discharged R0.6/1, 300 mesh copper Quantifoil grids (Quantifoil Micro Tools GmbH, Germany). A Vitrobot Mark IV was used to freeze grids in an ethane/propane cryogen at 100% humidity with no wait time.

4.5.7 Tilt-series collection

Tilt-series were collected on an FEI F20 with a Falcon II detector (Thermo Fisher Scientific (formerly FEI), Hillsboro, OR, USA). A total fluence of 120e-/ $Å^2$ was used and a defocus of -4µm. Tomograms were collected at a tilt range of +-53 degrees with 3° tilt increments and a pixel size of 8.28 Å.

4.5.8 Tomogram reconstruction

Tomograms were reconstructed automatically using RAPTOR [157].

4.5.9 2D-classification

For negative stain grids, images were collected on a Tecnai T12 TWIN (LAB6) using a TVIPS F216 CCD camera with a pixel size of 2.586 Å. Processing was done within Scipion 1.2 [154], particles were picked using Xmipp3 [155] and classification was done using Relion [156].

For cryo-data. The cisTEM program was used [188]. Within cisTEM, frames were aligned with unBlur [120] and CTF estimation was done with CTFFIND4 [189] before 2D classification was carried out.

4.5.10 Δ*fabH* and Δ*motAB* strain construction

The Δ*fabH* and Δ*motAB* strains were constructed using the lambda red system. Briefly, a linear fragment of the TetRA cassette with complementary fragments was amplified using the primers DfabH::TetR and DfabH::TetA (ACCGAAAAGTGACTGAGCGTACATGTATACGAAGATTATTTTAAGACCCACT TTCACATT and TCATGTTTAAATCCTTATACTAGAAACGAATCAGCGCGG ACTAAGCACTTGTCTCCTGTT) or motBstopTetA and motAstartTetR (TGTCTGATAAAAATCGCTAATATCCATGCTCACGCTATCACTAAGCACTTGT CTCCTG and TTACACTTTCACCCAGAATTGTGCTGTAGTAGGAAGGCGACAA

CTGATACTGTCCTACGC). 250 ng of the linear fragment was electroporated into *Salmonella* LT2 harbouring the PKD46 plasmid and cells were recovered in LB for 1 hour at 37 °C. Recovered cells were plated onto LB and grown at 42 °C overnight. Single colonies were picked and patched onto Tetracycline plates. Picked colonies and patched onto LB plates and then onto Amp plates (to make sure PKD46 has been lost) and grown at 37 °C overnight.

4.5. 11 FliL plasmid construction

The pBtok plasmid was linearised with reverse PCR. FliL was amplified with the primers FliL_for and FliL_rev (GGTCCCGAATTCGAGATGACTGACTCCGCGATT and TCCCCGGGTACCGAGTTAATGATGGTGATGATGATGCCGCAGAATAAAA GC) with 6 histidines added to C-terminus. The in-fusion cloning kit (Takara Bio, USA) was used to anneal plasmid.

4.5.12 MotAB plasmid construction

The pKG116 plasmid was linearised with restriction enzymes knpI and NdeI. MotAB was amplified with the primers MotA_for and MotB_rev (TAGCGCATCGAGCTCATATGCTTATCTTATTAGGTTACCTG and TTTTTTTTTT TTGGTACCTCACCTCGGTTCCGCTTT). T4 ligase was used to anneal the fragment and cut vector.

4.5.13 Protein purification (adapted from protocol from the Blair lab)

The plasmid, pEk541 containing MotA(His)MotB-MBP, was transformed chemically competent C41 (De3) *E. coli* cells. Colonies from LB agar plates containing 100 μg/mL ampicillin were picked and grown overnight in LB at 37°C and 290 RPM. 6L of Terrific Broth (TB) containing 100 μg/mL ampicillin was inoculated 1:100 dilution of overnight culture and grown at 24°C, 160 RPM until an OD_{600} of 0.1-0.2 was reached. Culture was induced with 400 μM of Isopropyl β-D-1-thiogalactopyranoside (IPTG) and

grown until an OD_{600} of 0.6-0.8 was reached. The cells were then harvested by centrifugation at 5000xg for 45 min at 4°C and the pellets were flash-frozen in liquid nitrogen and stored at -80°C.

The thawed pellets were resuspended in 45 mL of membrane buffer (50 mM Tris pH 7.5, 50 mM NaCl, 250 mM sucrose, 10% glycerol, 2 mM $CaCl_2$, 0.5 mM DTT, protease inhibitor complete EDTA free, DNase). The cells were lysed using a Constant Cell Disruption System (Constant Systems Ltd., UK) at 27 KPSI for 3 cycles. To get rid of unlysed cell, the sample was centrifuged at 8000 xg for 20 min at 4°C.

Next, the supernatant was ultracentrifuged at 195,000xg for 1 h at 4°C. The membrane pellets were resuspended with 8 mL of Buffer A1 (20 mM Tris pH 8, 300 mM NaCl, 20% glycerol, 5 mM imidazole) before flash-freezing and storage at -80°C. The thawed membrane samples were diluted into 50 mL of Buffer A2 (20 mM Tris pH 8, 300 mM NaCl, 20% glycerol, 20% glucose, 0.05% DPC, 5 mM imidazole) and solubilised for 15 min at 4°C. Membrane samples were then diluted 4-fold into Buffer A3 (20 mM Tris pH 8, 300 mM NaCl, 20% glycerol, 0.03% DPC, 5 mM imidazole) and solubilisation continued for a further 10 min at 4°C. Next, the samples were spun down at 70,000 xg for 30 min to remove unsolubilised sample.

The supernatant was mixed with 6 mL of Ni-NTA resin (prewashed in Buffer A1) and incubated for 1h at 4°C. The sample was poured into a gravity flow column and washed with 10 column volumes of Buffer A3 followed by 10 column volumes of Buffer A4 (20 mM Tris pH 8, 300 mM NaCl, 0.03% DPC, 60 mM imidazole). The protein was eluted in 1 ml fractions with elution Buffer (20 mM Tris pH 8, 300 mM NaCl, 0.03% DPC, 300 mM imidazole). Eluted fractions were pooled and concentrated using Amicon 50k Centrifugal Filter Units (Merck). The presence of purified MotAB-MBP was analysed by SDS-PAGE, western blot and native-PAGE.

The eluate was mixed 1:10 with amphipol A3-85 (protein:amphipol). The amphipol exchange mixture was rotated overnight at 4°C. Bio-BeadsTM SM-2 Resin (Bio-Rad) added for 2 h at 4°C to remove unbound detergent.

The sample in amphipol was concentrated and loaded onto a pre-equilibrated (in 20 mM Tris pH 8, 300 mM NaCl) gel filtration column HiLoad 16/600 Superdex 200 column

(GE Healthcare). Sample from peaks were analysed by SDS-PAGE, western blot and negative stain EM.

4.5.14 SDS-PAGE electrophoresis

Sample was boiled in LDS, run on a 4-12% Bis-Tris gel and stained with InstantBlue.

4.5.15 Western blot analysis

After SDS-gel electrophoresis and prior to staining, the protein was transferred onto a nitrocellulose membrane using a iblot system (Thermo Fisher Scientific, USA). Membrane was blocked with 5% skimmed milk in PBST (PBS + 0.05% Tween 20) for 1 hour at RT. After 3 washes with PBST, the sample was incubated with an HRP conjugated α-HIS antibody at RT for 1 hour. Membrane was washed again in PBST and then developed using ECL and imaged using a BioRad system (BioRad, USA).

Chapter 5

Assembly of the flagellar rod and broader implications of periplasmic architecture

5.1 Chapter Summary

The bacterial flagellum extends from the cytoplasm to multiple microns beyond the cell body. At its base, the flagellar motor sits within the periplasm, anchored in both the inner and outer membranes. The Gram-negative periplasm is a vital cellular compartment. It protects cells from unpredictable environments, selectively traffics nutrients into the cytoplasm and toxins out, couples established gradients to energy production, and provides a rapid signalling response to stress. The flagellar motor is just one of many periplasm-spanning protein complexes, however, despite their abundance, the importance of the correct periplasmic architecture has not been studied.

In this Chapter, I show that the width of the periplasm can be altered by changing the length of an abundant lipoprotein, Lpp (Braun's lipoprotein). Using this methodology, I show that the length of the flagellar motor's distal rod in *Salmonella* is controlled by the periplasmic distance. When the rod length is altered via manipulation of the periplasmic distance, motility is affected and in some cases completely abolished. By finding a reliable method for altering the periplasmic distance, I looked at the broader implications of the periplasmic architecture and show here that the periplasmic distance is tightly controlled for proper functioning of another cellular process, the Rcs stress-response network in *E. coli*. Periplasmic width increase or decrease eliminates the ability of cells to detect and respond to envelope integrity defects however, signalling could be restored by complementing the increased distance by simultaneously increasing the length of the lipoprotein RcsF involved in stress-sensing. Finally, I provide evidence for the role of Lpp in controlling periplasmic architecture– speculating that this abundant lipoprotein acts both as a tether and a column in Gram-negative bacteria.

This Chapter is a combination of work conducted by myself and two other PhD students in collaborating groups, Eli Cohen (University of Utah) and Abir Asmar (Universite catholique de Louvain).

Relevant publications:

1. *Cohen EJ, Ferreira JL, Ladinsky MS, et al., (2017) Nanoscale-length control of the flagellar driveshaft requires hitting the tethered outer membrane. Science 356, 197–200 [27]*
2. *Asmar AT, Ferreira JL, Cohen EJ, et al. (2017) Communication across the bacterial cell envelope depends on the size of the periplasm. PLoS Biol 15(12): e2004303. [190].*

5.2 Introduction

The bacterial flagellum is a complex molecular machine which self-assembles within the context of the bacterial cell envelope. The flagellar motor, which powers the flagellum is anchored within both the inner and outer membranes and couples the influx of ions from the periplasm via the stator complexes, to rotation of the flagellar motor. All life is contained within biological membranes [191], and the periplasm is a specialised cellular compartment which surrounds Gram-negative cells. Although historically the bacterial envelope was presumed to be "simple" due to the relative simplicity of this domain of life, bacteria face harsh, unpredictable and, often dilute environments [191]. Bacterial cells have therefore evolved complex cell envelopes containing a periplasm, not only for protection but also for separation of molecules, the selective, directional trafficking of nutrients and toxins and the establishment of gradients coupled to energy production.

5.2.1 Flagellar assembly within the context of the cell envelope

Gram-negative bacteria are enveloped by a complex, multi-layered structure in which the flagellar motor assembles (Fig. 5.1). The T3SS is assembled within the inner membrane, a phospholipid bilayer separating the cytoplasm from the periplasm. The rod reaches across the periplasm through the semi-rigid peptidoglycan layer, which is made of a network of repeating disaccharides cross-linked by pentapeptide side chains [192]. The P-ring is thought to interact with the peptidoglycan. On the tip of the rod, the L-ring assembles within the outer membrane. The outer membrane, acts as a barrier between the periplasm and the external environment and is an asymmetric bilayer. The inner-leaflet is made of phospholipids and the outer leaflet is composed of glycolipids, most prominently lipopolysaccharide (LPS). LPS acts as an effective barrier for Gram-negative bacteria [193]. When cations are present (Mg^{2+}), LPS molecules bind to each other and pack tightly in a non-fluid barrier. This makes the outer membrane impermeable to hydrophobic molecules and diffusion of small hydrophilic molecules (< ~700 Da) occurs only via β-

barrel proteins such as porins [194]. The L-ring acts as a bushing in this tightly packed outer-membrane, allowing the flagellum to rotate.

The flagellar motor depends on the accurate assembly of component pieces, allowing the system as a whole to function properly. Due to the intimate relationship between the flagellar motor and the cell envelope, it is clear that for the proper assembly and therefore correct function of the flagellum, the cell envelope and periplasm architecture must be strictly maintained.

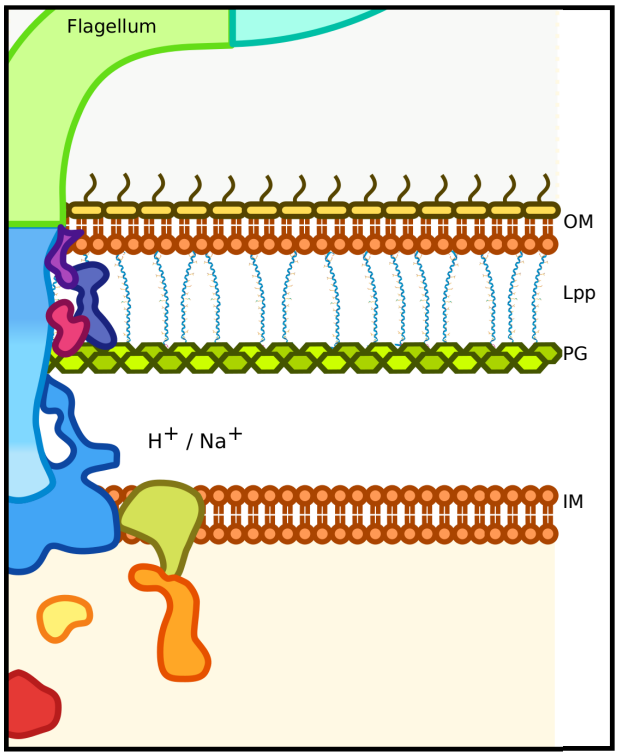


Fig. 5.1: The Gram-negative cell envelope.
The envelope is made of three layers, a phospholipid bilayer inner membrane, a peptidoglycan layer and a lipopolysaccharide/ phospholipid bilayer outer membrane. Lpp extends between the peptidoglycan layer and outer membrane. (OM = outer membrane, PG = peptidoglycan, IM = inner membrane)

The flagellar motor is composed of a series of axial components, which each need to be length controlled. One way to measure linear filaments in biology is the use of "molecular rulers". For example, a molecular ruler is used to control the length of the flagellar hook. The ruler protein FliK, is secreted through the growing rod and hook intermittently. When the hook reaches the desired length, the C-terminus interacts with FlhB and initiates the next stage in flagellar assembly, assembly of the filament [195]. Another axial component of the flagellar motor that needs to be accurately measured is the flagellar rod. The flagellar rod crosses the entire periplasm, from the T3SS in the inner membrane to the L-ring in the outer membrane. However, no rod molecular ruler has been identified. The proximal rod is made from 4 different proteins (FlgB, FlgC, FlgF, FliE) that extend from the inner membrane about 7 nm. The distal rod of *Salmonella* is made of ~50 copies of a single protein, FlgG and extends to ~ 18 nm. As FlgG has been shown to have self-stacking or polymerising capabilities, and because no rod-length molecular ruler has been identified, the question that emerges is what stops FlgG polymerisation once it is initiated?

5.2.2 Length control of the flagellar rod

Due to the known self-stacking ability of the FlgG protein, and because reported point mutations in FlgG (FlgG*) lead to extra-long (~ 60 nm rather than ~ 25 nm) rod structures [142,196], a mechanism for rod-length control was thought to be based on intrinsic interactions between FlgG monomers. However, for a model of rod-length control based on intrinsic interactions between FlgG proteins to be correct, flagellar rod length should be unaffected by the over-expression of FlgG. But, when *flgG* is over-expressed, rod length increases from ~22 nm to ~26 nm [27]. Therefore, it is likely that the rod has an external factor measuring its length.

The FlgG* point mutants which produce extra-long rods are non-motile [142,196]. The ~60 nm long rods are assumed to bend within the periplasm causing the rod tip to form parallel to the outer membrane, preventing the L-ring from forming a pore in the outer

membrane. Flagella in the FlgG* mutants therefore do not exit the outer membrane but rather assemble within the periplasm. The non-motile phenotype of these cells, allowed the lab of Kelly Hughes (University of Utah) to look for FlgG* suppressor mutants which regained motility, in an attempt to understand what controls the termination of FlgG proteins and therefore rod length. Unexpectedly, many of the mapped mutations in the suppressor mutants were not in flagellar operons but rather in the *lpp* gene, which codes for an abundant lipoprotein (Braun's lipoprotein or Lpp) linking the peptidoglycan to the outer membrane. In *Salmonella*, two genetic tandem repeats are present (*lppA* and *lppB*) however, *lppB* is not expressed under standard lab conditions and *lppA* is equivalent to the single *lpp* of *E. coli*.

To confirm that the regained motility of the suppressor mutants was due to mutations in *lpp,* the Hughes lab deleted *lppA* and *lppB* in WT *Salmonella* and the FlgG* mutant background. When *lppA* was deleted in an otherwise WT strain, swimming motility decreased, however, when *lppA* was deleted in a FlgG* mutant with abolished motility, swimming motility was rescued to two-thirds WT (Fig. 5.2) and cells again had extracellular flagella. From this it appears that Lpp is involved in coupling rod-length with flagella forming properly and exiting the outer membrane, and therefore motility. Due to this relationship, Lpp may be involved in establishing or maintaining the correct periplasmic architecture.

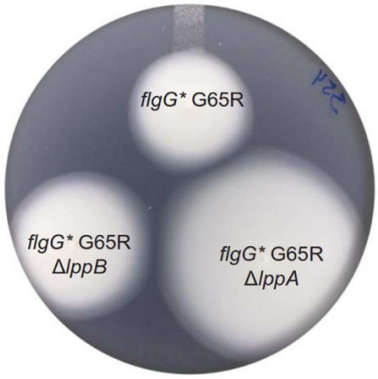


Fig. 5.2: Δ*lppA* rescues motility in FlgG* mutants.
FlgG mutants form extra-long rods and periplasmic flagella. Deletion of lppA, but not lppB, results in motile cells with more extra-cellular flagella than the single FlgG* mutant. From Cohen et al. [27]. Reprinted with permission from AAAS.*

5.2.3 Braun's lipoprotein

Lpp (Braun's lipoprotein) is an abundant lipoprotein, which reaches between the peptidoglycan and the outer membrane [197]. Lpp is the most abundant protein in *E. coli*, with each cell estimated to have 10^6 copies of the protein and making up ~ 10% of all cellular mRNA [198]. Lpp is a 58 amino acid protein made of heptad repeats. About one-third of Lpp is covalently linked to peptidoglycan via a C-terminal Lysine, and two-thirds are free in the outer membrane [199], likely surface exposed [200] (Fig. 5.3). The *E. coli* Lpp protein crystallises as a trimeric, α-helical coiled-coil [201,202] with a strip of hydrophobic residues running down the length of each monomer, interacting to zip the trimer together (Fig. 5.3). However, the biological significance of this trimer has been questioned due to the ability of Lpp to flip between peptidoglycan and free forms which would require overcoming multiple Van der Waals forces.

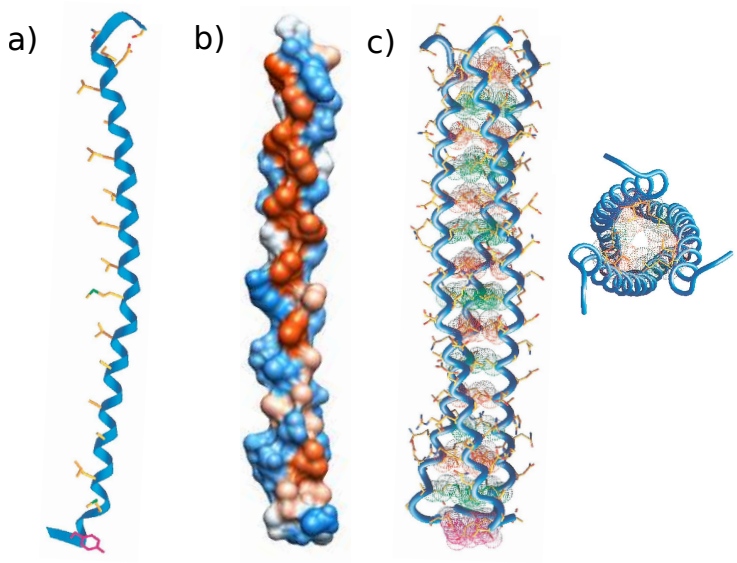


Fig. 5.3: The structure of Braun's lipoprotein (Lpp).
a) Crystal structure showing single Lpp strand. b) Single Lpp showing hydrophobic strip where trimer interactions occur. c) Lpp trimer side and top view. All from: PDB-1EQ7 [202]

5.2.4 Rcs stress response

As the cell envelope is critically important for the survival of cells, monitoring and maintaining its integrity is vital. Complex pathways provide a constant source of envelope components and multiple signal transduction systems are set up to respond to environmental stresses and membrane damage.

One of these signal transduction systems is the Rcs stress response system, which provides a watchful eye over the peptidoglycan and outer membrane. The phosphorelay system is induced by drugs that make changes to the LPS barrier or affect the assembly of peptidoglycan (Fig. 5.4). It responds by inhibiting flagellar motility by repressing *flhDC* and activating secretion of colonic acid for the formation of a protective biofilm [203]. The Rcs stress response network is composed of six components [204]. Signals are sensed by the lipoprotein RcsF, anchored in the outer membrane [205,206]. When stress is sensed, RcsF forms an interaction with IgaA in the inner membrane and the complex activates the autophosphorylation of RcsC, a histidine kinase in the inner membrane [207]. Phosphorylated RcsC activates phosphorylation of the transcription factor RcsB, via RcsD, resulting in the regulation of multiple genes. Via its six components, the Rcs network effectively transfers information across both membranes and into the cytoplasm (Fig. 5.4).

5.2.5 Other periplasm spanning complexes

The flagellar motor, Rcs network and Lpp are just three of multiple proteins or complexes spanning the periplasm. Some, like the flagellum are large complexes spanning the entire periplasm to outside the cell (e.g.: injectisomes [208]). Some, like Lpp cross just from the peptidoglycan to the outer membrane (e.g.: OmpA [209]). Others, like the Rcs network have components in both membranes that need to interact (e.g.: Tol/Pal system [210]). These periplasm spanning protein complexes are involved in a large range of functions including virulence, removal of toxins or maintenance of outer membrane integrity. The abundance of periplasm spanning complexes with multiple vital functions

all rely on their correct assembly. Due to the intimate relation between these periplasmic spanning machines and the cell envelope, their correct assembly may rely on the correct architecture of the periplasm.

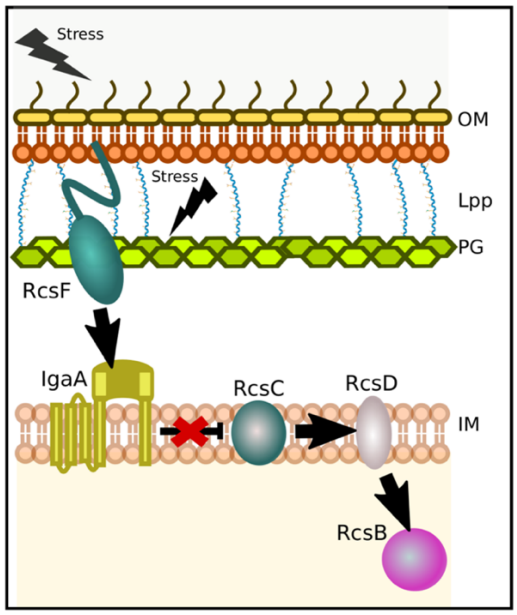


Fig. 5.4: Rcs stress response network.
Stress to the outer membrane or peptidoglycan is sensed by RscF in the outer membrane. When stressed, RcsF forms an interaction with IgaA in the inner membrane leading to the autophosphorylation of RcsC. This in turn leads to the phosphorylation of the transcription factor RcsB, via RcsD, resulting in regulation of many genes involved in motility and biofilm formation. (OM = outer membrane, PG = peptidoglycan, IM = inner membrane)

Biological systems depend on accurate assembly of component pieces, allowing the system as a whole to function properly. For periplasmic biological systems, their assembly is intimately linked to the architecture of the periplasm and therefore correct assembly of these components must rely on correct periplasmic architecture. In this Chapter I show that the correct architecture of the periplasm is important for termination of rod assembly and hence flagellar function. To show the broader importance of periplasm architecture, I then show that the Rcs-stress response network also relies on a tightly controlled periplasmic architecture.

5.3 Results

5.3.1 FlgG* polyrods do not interact with the outer membrane

To understand the impact of the periplasmic architecture on the control of flagellar rod length, I imaged the FlgG* point mutants that have extra-long rods and periplasmic flagella using Cryo-EM and ECT. Due to the thickness of *Salmonella* cells and therefore decreased quality of tomograms, the FlgG* mutant was moved into a mini-cell strain with overexpression of FtsZ (By Kelly Hughes, University of Utah). When I imaged these cells using ECT, it was clear that the periplasmic flagella were inhibiting cell division and production of mini-cells and the results were difficult to interpret (Fig. 5.5a-b). In order to make analysis easier, the hook and filament proteins (FlgE and FliC) were deleted leaving flagellar motors that only assemble rods (performed by Kelly Hughes). When I imaged these strains with ECT, although the flagellar rods were longer than in WT flagella, as expected there was no interaction between the rod and the outer membrane (Fig. 5.5c, d, h, i). Mini-cells provide a good system for imaging biological systems *in situ* however, due to the induced defects in their cell division cycle, the mini-cells have morphological abnormalities. A common defect is in the periplasmic width, which often varies greatly in these cells. When flagella are assembled properly however, they hold the inner and outer membranes in place due to their anchoring in both membranes, such as the *Salmonella* mini-cells imaged in Chapter 4 (Fig. 4.7). In the FlgG* mutants this is not the case due to the incorrect length of the rods and therefore incorrect assembly of the P- and L-rings (Fig. 5.5c-d). On the same mini-cells however, where an injectisome was seen the periplasmic distance was held correctly due to the proper assembly of the injectisomes, which are also anchored in both membranes (Fig. 5.5e).

As expected, the FlgG* mutant had long rods and no interaction between the rod and the outer membrane was seen. However, the morphological abnormalities in the cells made interpretation of the FlgG* mutant strains difficult, and the tomograms did not provide enough information to understand the cause of extra-long rods and hence the mechanism for rod length determination.

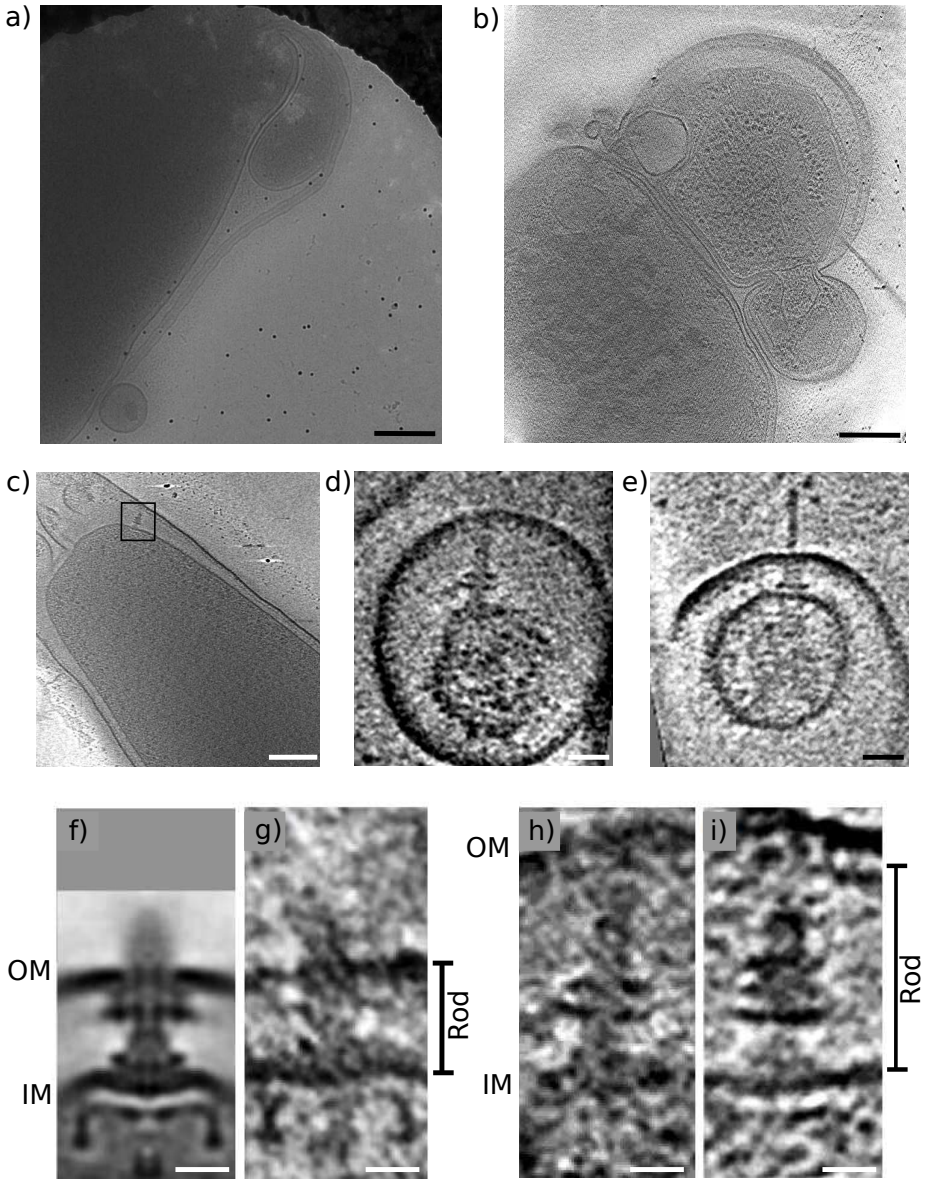


Fig. 5.5: FlgG* mutants produce long rods *in situ.*
a) *Projection image of a FlgG* mutant in a mini-cell strain. b) Slice through a tomogram of a FlgG* mutant in a mini-cell strain. c) Slice through a tomogram of a FlgG* mutant without the flagellar filament close to a cell pole. d) Slice through a tomogram of a FlgG* mutant without the flagellar filament in a mini-cell with wide periplasm. e) An injectisome on the same mini-cell as in (d). f) Subtomogram average of WT Salmonella flagellar motor (EMD-3154). g) Subtomogram of a WT Salmonella flagellar motor with the correct length rod. h, i) Subtomograms of FlgG* mutant flagellar motors with increased rod length. The flagellar motor in (h) has one P-ring and one L-ring and the motor in (i) has two P-rings and one L-ring. Neither L-rings are anchored in the outer membrane. Scaled as in (g). Scale bars, a-c = 100 nm, d-e = 25 nm, f-i = 20 nm. (IM = inner membrane, OM = outer membrane)*

5.3.2 Lpp provides membrane stability in *Salmonella*

Due to previous results from the Hughes lab showing that loss of *lppA* enables flagellar mutants with extra-long rods (FlgG*) to form external filaments, I sought to understand the role of LppAB in *Salmonella*. In order to do this, I imaged *lppAB* deletion mutants using cryo-EM (Fig. 5.6) and ECT and compared them to WT *Salmonella*. In the Δ*lppAB* strain, the outer membrane had pulled-away from the cell in many areas forming large taut outer membrane blebs (Fig. 5.6, middle row). To assess the relative effects of LppAB and another abundant lipoprotein, Pal, which non-covalently binds peptidoglycan, I imaged a Δ*lppAB*Δ*pal* double deletion mutant. In these cells, even greater morphological defects were seen with larger outer membrane blebs and many outer membrane vesicles completely separate from the cell (Fig. 5.6). These mutants also showed severe growth defects. From this it is clear that LppA plays a role in maintaining periplasmic architecture.

We hypothesised that due to large areas of increased periplasmic distance in the Δ*lppAB* strain, the ~60 nm long rods in the FlgG* mutants, could in some areas meet the outer membrane at a right angle, correctly positioned for formation of the L-ring pore. A mechanism for rod-length control therefore may be physical interaction of the rod with the outer membrane, and we hypothesised that by altering the periplasmic distance, the length of the flagellar rod would change concurrently.

5.3.3 Length of LppA dictates periplasmic distance in *Salmonella*

To test the hypothesis of rod-length control by periplasmic width, a system to reliably alter the periplasmic distance by specific amounts without compromising the integrity of the outer membrane or causing growth defects of the cells was needed. As Lpp contains heptad-repeat motifs, we deleted or inserted amino acids in multiples of 7 (1 heptad repeat), creating *lpp*-21, *lpp*+21, *lpp*+42, *lpp*+63 mutants (genetics performed by Eli Cohen). I vitrified *lpp*-21, *lpp*+21 and WT cells and imaged them by cryo-EM and ECT. Importantly, no morphological changes were seen (Fig 5.7).

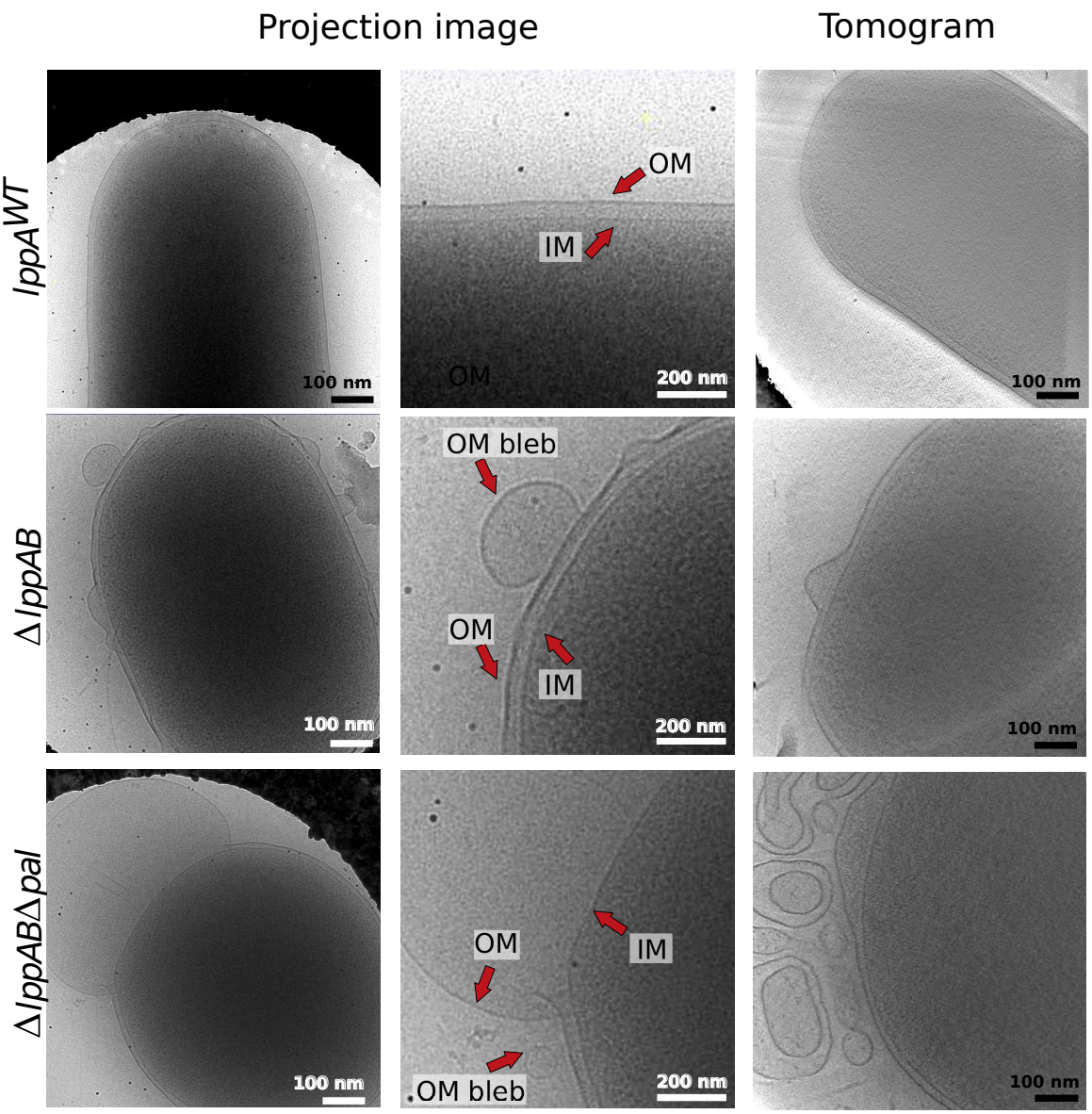


Fig. 5.6: LppAB maintains outer membrane integrity in *Salmonella* by tethering it to peptidoglycan.
Representative examples of cryo-EM micrographs and slices through tomograms of WT cells, ΔlppAB and ΔlppABΔpal cells. Column 1 contains projection images highlighting the cell morphology in the three strains. Column 2 provides a close-up view of micrographs in column 1, highlighting the inner membrane (IM), outer membrane (OM) and outer membrane blebs (OM bleb) that have pulled away from the cell. Column 3 show slices through cryo-tomograms of the three strains. The severity of membrane instability in ΔlppABΔpal cells is clear from the large amount of outer membrane blebs.

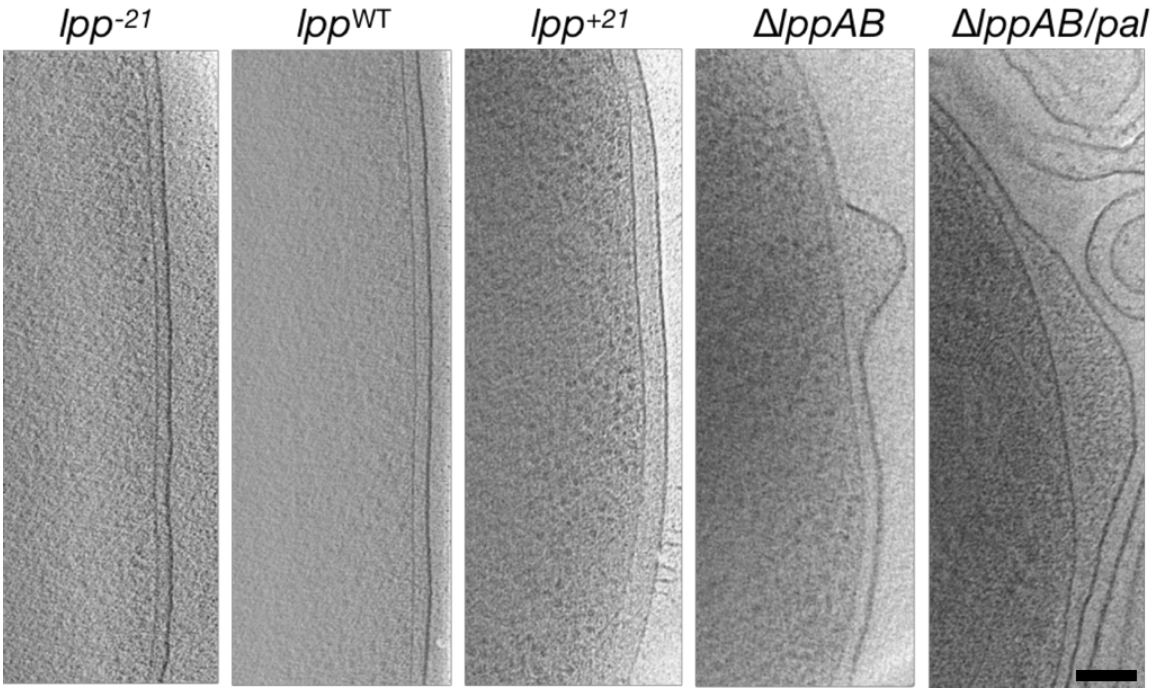


Fig 5.7: Periplasmic integrity is lost in *lpp* deletion strains but not in *lpp* length variants.
Slice through tomograms of all five strains at the same scale. Addition or deletion of amino acids to lppA does not affect membrane integrity, however deletion of lppAB or lppAB and pal results in deformation of outer membrane and loss of periplasmic integrity. Scale bar = 100nm. Adapted from Cohen et al. [27]. Reprinted with permission from AAAS.

In order to assess the periplasmic distance, I needed to develop an assay to accurately measure the inner membrane to outer membrane distance. I collected projection images of cells vitrified at OD_{600} 0.6 on a 200 keV FEI Tecnai TF20 FEG transmission electron microscope at a nominal magnification of 25000x and a defocus of - 5 µm. I then manually drew contours down the centre of each double membrane. Using custom scripts, the contours were converted into a series of points and then used to find the shortest distance between the two contours every 0.5 nm.

Using this assay, I measured the periplasmic distances for each strain (*lpp*-21, *lpp*+21 and WT) every 0.5 nm. As predicted, the periplasmic distance changed with respect

to the alteration of *lppA* length. When 21 amino acids (3 heptad repeats) were deleted from *lppA* the periplasmic distance was decreased by ~3 nm. When 21 amino acids were added to the length of *lppA* the periplasmic distance was increased by ~3 nm (Fig. 5.8). Although the histograms of a population of cells was quite broad, it was interesting to note that the histograms of individual cells are much tighter (Fig. 5.9). At present, little is known about expression levels and localisation of LppA, but variation of periplasmic distance within a population may be due to differential expression levels at different points in the division cycle. This would be an interesting follow up study. These results show that one of the main determinants in the periplasmic width is LppA and that *lppA* length variants are a reliable system to study the effects of changing periplasmic distances.

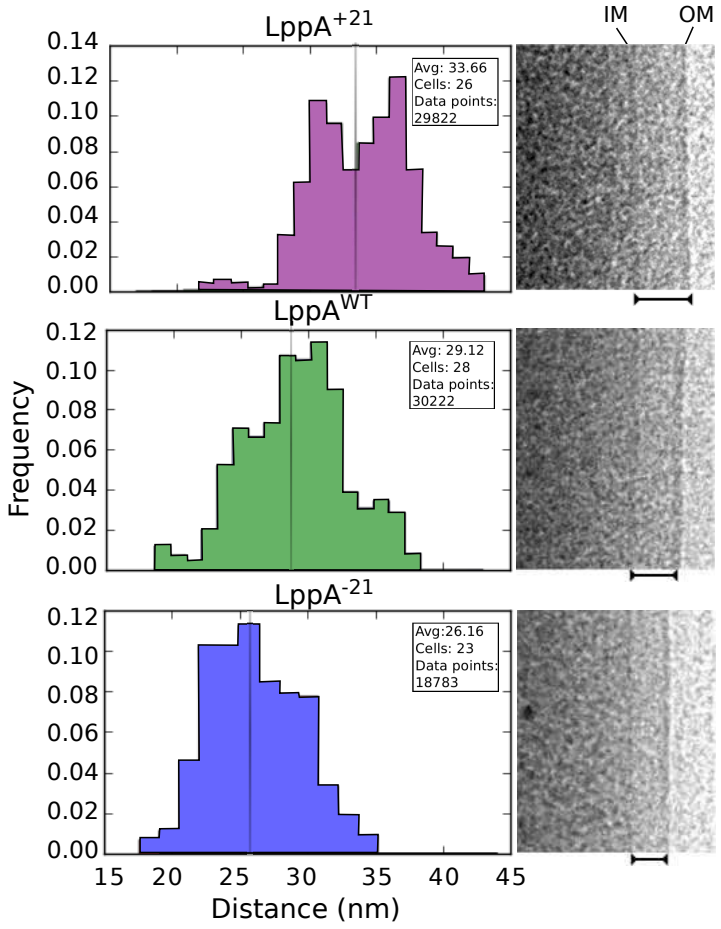


Fig 5.8: The periplasmic distance changes with LppA length variants in *Salmonella.* *Histograms representing the periplasmic width for all cells measured every 0.5 nm. The mean periplasmic width changed with respect to LppA length. ($p < 0.0001$, Student's two-tailed t test). Adapted from Cohen et al. [27]. Reprinted with permission from AAAS.*

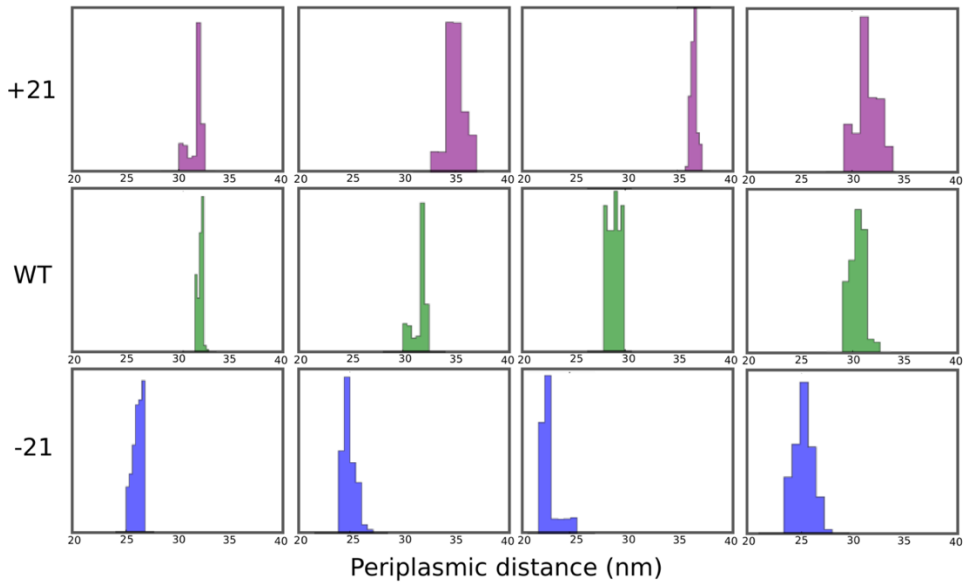


Fig. 5.9: Periplasmic distance within an individual cell is tightly controlled
Four examples from each strain of the variation in periplasmic distance within individual cells. The range in periplasmic widths is much narrower than in the population (Fig.5.8).

5.3.4 Periplasmic distance controls rod length

As *lppA* length variants were shown to be a good system for reliably altering the periplasmic distance without any observed morphological defect, we used this system to assess whether altering the periplasmic distance had an effect on the length of the flagellar rod (Experiment performed by Eli Cohen). Flagellar basal bodies were purified from each mutant and the length of the rod was measured in over 100 basal bodies per mutant (Fig. 5.10a). Significantly, the average rod length varied with the changes in *lppA* length (Fig. 5.10b). This means that altering the periplasmic distance in turn alters the length of flagellar rods. This points towards the termination of FlgG stacking being dependent on interaction with the outer membrane. By increasing the periplasmic width, the interaction of the rod with the outer membrane is delayed and FlgG polymerises for a longer time, resulting in longer rods.

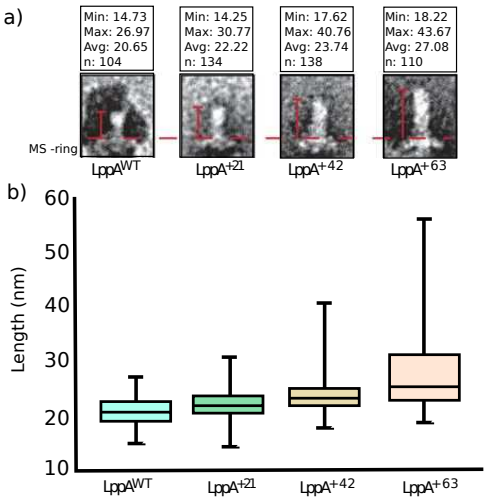


Fig. 5.10: Rod length is altered by periplasmic distance.
a) Examples of negatively stained flagellar basal bodies purified from WT cells and three different LppA length variants (+21, + 42 and +63 amino acids). Red lines delineate area where measurements were taken. b) Plots of data collected from measurements in (a). ($p < 0.0001$, one-way ANOVA, $N \geq 3$, data in b = mean ± SEM). Adapted from Cohen et al. [27]. Reprinted with permission from AAAS.

5.3.5 Altering the length of the flagellar rod affects *Salmonella* motility

Is the tight regulation of the periplasmic distance and therefore rod length required for motility in *Salmonella*? To answer this, soft agar plates were used to assess the relative swimming ability of all *lppA* length variants compared to WT *Salmonella* (Experiment performed by Eli Cohen). Deletion of 21 amino acids from *lppA* completely abolished swimming (Fig. 5.11). Addition of 42 or 63 amino acids to *lppA* also impaired swimming to ~ 60% and ~ 10% of WT swimming respectively. Unexpectedly, when 21 amino acids were added to *lppA* the swim diameter increased by ~ 10%.

Although there was a slight increase in swim diameter in the *lppA*+21 strain, another vital flagellar function, swarming on a solid surface, was completely abolished in all *lppA* length variants (Performed by Eli Cohen. Data not shown). These results highlight that proper length control of the rod, via control of the periplasmic space by LppA, is essential for maintaining the function of the flagellar motor.



Fig. 5.11: Altering the length of the rod affects *Salmonella* motility.
Soft agar plates were used to assess motility in lpp length-variants. a) Motility plate of different lpp length variants. All variants had altered motility. Adapted from Cohen et al. [27] Reprinted with permission from AAAS

The result that the periplasmic width is important for the proper assembly of the rod suggested that there may be other systems controlled by the correct periplasmic architecture. To explore the wider ramifications of periplasmic width, I collaborated with colleagues at the Universite´ Catholique de Louvain to study the Rcs stress-response system. As this system requires communication across the periplasm, between proteins in the inner and the outer membrane, it is a good model system to study the role of the periplasmic width.

5.3.6 LppA maintains outer membrane stability in *E. coli*

I sought to confirm that LppA behaves in the same way in *E. coli* as it does in *Salmonella*. First WT *E. coli* cells were compared to a Δ*lpp* mutant, as well as a *lpp*ΔK58 mutant which lacks a key Lysine residue required for covalent linkage of Lpp to peptidoglycan. As this mutant still expresses Lpp and integrates it into the outer membrane, it may be a better system to study membrane stability, as any other processes that Lpp is involved in should not be effected. If Lpp functions the same as in *Salmonella*, the *lpp*ΔK58 mutant should not play a role in establishing periplasmic width as it does not attach to the peptidoglycan layer.

When I imaged the strains by cryo-EM, both the Δ*lpp* mutant and the *lpp*ΔK58 mutant had irregular outer membranes (Fig. 5.12). As in *Salmonella* Δ*lppAB*, the outer membranes were wavy and blebs of outer membrane pulled away from the cells. From this I was confident that in *E. coil* Lpp acts like LppAB in *Salmonella* to maintain outer membrane stability.

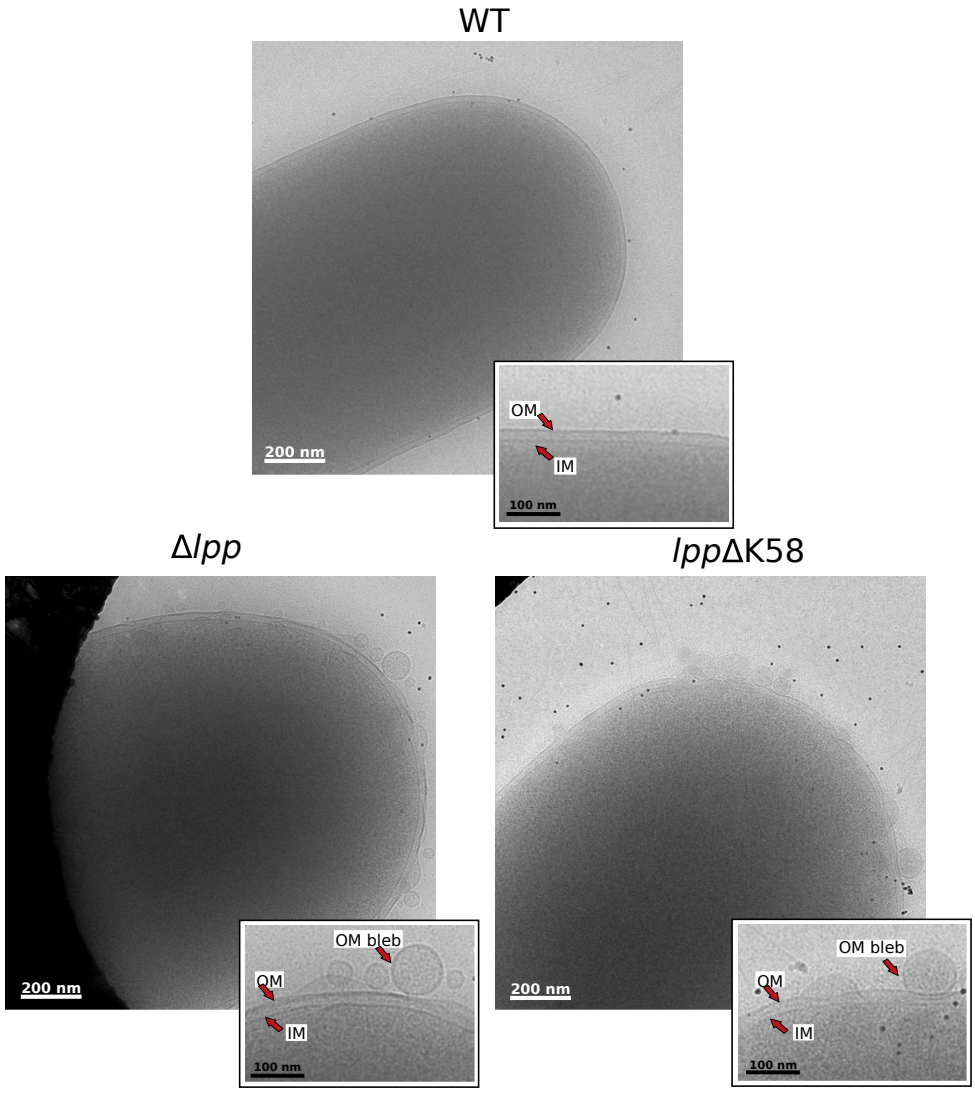


Fig. 5.12: Lpp is involved in membrane maintenance in *E. coli*.
Cryo-EM micrographs of a representative WT E. coli cell compared with a Δlpp mutant and a lppΔK58 mutant that cannot covalently link to peptidoglycan. Both mutants have outer membranes that have pulled away from the cell body and formed outer membrane blebs.

5.3.7 Instability of outer membrane results in impaired Rcs network activity

To test whether the morphological changes to the outer membrane, imparted by the *lpp*ΔK58 mutant, have an effect on the Rcs stress response, we monitored the response to two stresses compared to WT (Performed by Abir Asmar). A22 (S-(3,4-Dichlorobenzyl)isothiourea) is a chemical compound which binds to MreB, disrupting the bacterial actin cytoskeleton [211]. Mecillinam is a ß-lactam antibiotic which targets penicillin binding protein 2 (PBP2), preventing peptidoglycan elongation [212]. Both compounds cause cells to become spherical and eventually cause cell death by lysis. The *lpp*ΔK58 mutant had impaired response to both compounds compared to WT (Fig. 5.13a).

It has previously been reported that deletion of *mdoG* constitutively activates the Rcs system via RcsF [213]. MdoG is a protein involved in the biosynthesis of osmoregulated periplasmic glucan [214], and its deletion leads to the absence of membrane-derived oligosaccharides. We confirmed that deletion of *mdoG* constitutively activates the Rcs system (Fig. 5.13b), and found that the *mdoG* deletion in a *lpp*ΔK58 mutant background had impaired stress response, almost back to uninduced WT levels (Fig. 5.13b) (performed by Abir Asmar). These results indicate that Lpp needs to be attached to peptidoglycan in order for the Rcs stress response network to function.

5.3.8 Constitutive Rcs response in Δ*mdoG* cells is due to a decreased periplasmic width

At present it is not known why deletion of *mdoG* results in constitutively activated Rcs response. To investigate this, I vitrified Δ*mdoG* cells and imaged them with cryo-EM. As with *Salmonella*, I measured the periplasmic distance and compared it to WT *E. coli* (Fig. 5.13c). The periplasm in Δ*mdoG* cells was 1.7 nm narrower than in WT cells, but no other morphological changes were observed. This decrease in periplasmic width may bring RcsF in the outer membrane into close contact with IgaA in the inner membrane, even without the need for a conformational change from RcsF sensing stress.

This result indicates for the first time that the periplasmic width is important for proper functioning of the Rcs stress response.

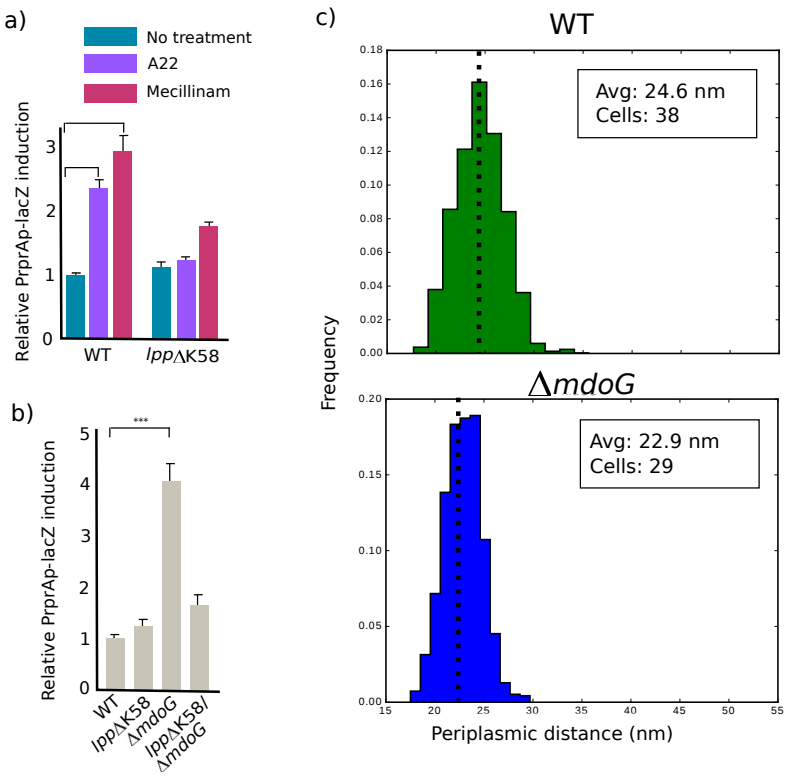


Fig. 5.13: Lpp must be linked to peptidoglycan for Rcs network to function.
*Rcs activity was monitored using a PrprA-LacZ fusion. a) lppΔK58 mutant cells have impaired activation of the Rcs system in response to stress from A22 or Mecillinam (*** $p < 0.0001$, 2-way ANOVA) (n =6 for A22 and n=3 for mecillinam). b) The ΔmdoG mutant has the Rcs network constitutively activated in a WT background, however in a lppΔK58 mutant background Rcs stress response is also impaired. (*** $p < 0.0001$, 1-way ANOVA). Values are normalised to mean value of untreated WT cells. Error bars are SEM c) ΔmdoG cells have a narrower periplasm than WT cells which may be the cause for continuous Rcs activity. Values are normalised to mean value of untreated WT cells. Error bars are SEM (n =6). (a and b are adapted from Asmar et al. [190])*

5.3.9 Length of Lpp dictates periplasmic distance in *E. coli*

Next, guided by the results from the Δ*mdoG* cells, I wanted to establish whether the disruption of the Rcs response in the *lpp*ΔK58 mutant cells is due to an increased periplasmic distance. Firstly, it needed to be established whether the length of Lpp dictates the width of the periplasm in *E. coli*, as it does in *Salmonella*.

Lpp length variants (made by Eli Cohen) were moved into WT *E. coli* (by Abir Asmar). Again, I imaged these with cryo-EM and used custom scripts to measure the periplasmic width compared to WT cells. As in *Salmonella,* no morphological defects were seen in the +14 and +21 cells (Fig. 5.14a). As expected, when 14 or 21 amino acids were added to the Lpp linker region the periplasmic distance increased by 3 and 4 nm respectively (from 24.6 nm in WT, to 27.6 nm in +14 and 28.5 nm in +21 mutant) (Fig. 5.14b). Surprisingly, the histograms of *E. coli* were much narrower than those in *Salmonella* (Fig. 5.8). This tighter range may be the result of Lpp playing a greater role in *E. coli* periplasmic width and other lipoproteins, such as Pal, contributing more in *Salmonella*. When the periplasmic distance of the ΔK58 mutant was measured, as expected the range in widths was much higher than any of the WT or Lpp length variant cells, and the average distance was wider than WT (27.7 nm) (Fig. 5.14b).

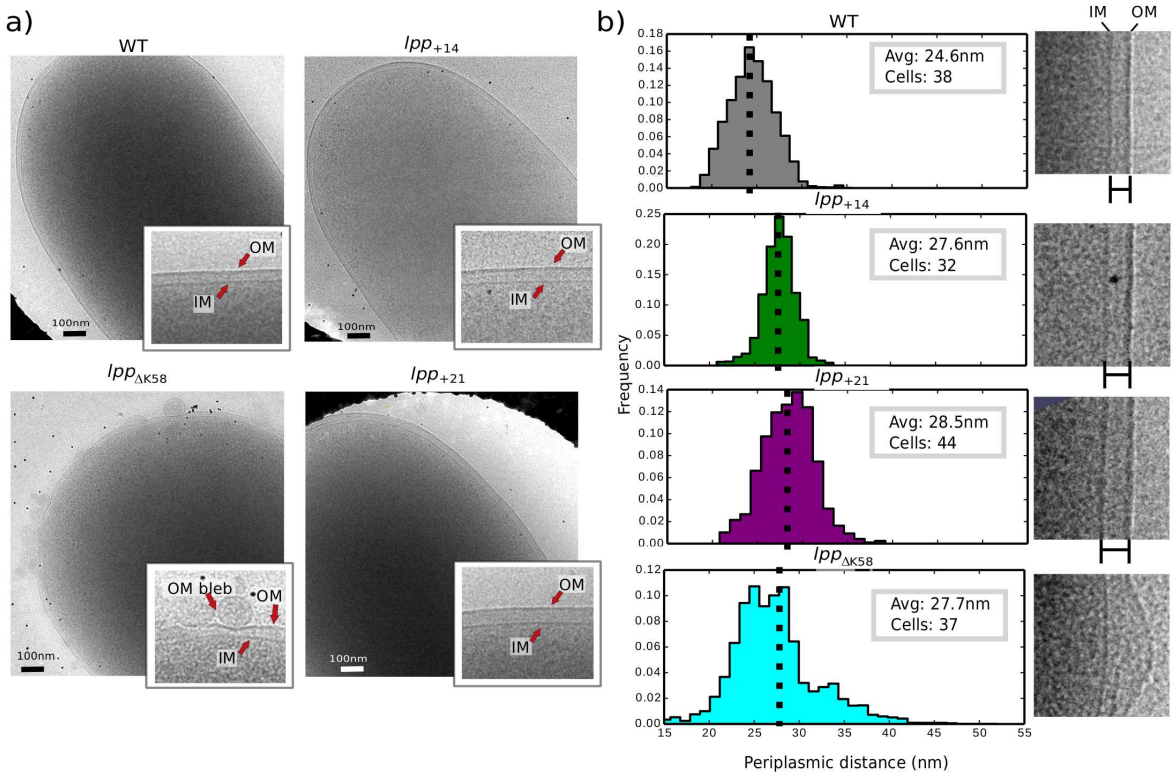


Fig. 5.14: *lpp* length dictates periplasmic distance in *E. coli*.
a) Example cryo-EM micrographs of four strains. Inset shows close up). b) Histograms representing the periplasmic distance measured from cryo-EM micrographs. The periplasmic distance varies with lpp length. IM = inner membrane, OM = outer membrane, OM bleb = outer membrane bleb. Adapted from Asmar et al. [190]

5.3.10 Increasing the periplasmic distance inhibits activation of Rcs network in response to stress

We next wanted to establish whether the same disruption of the Rcs response network seen in the *lpp*ΔK58 mutant occurs in the Lpp length variants, to identify whether increased periplasmic distance is responsible for the disruption. Adding either 14 or 21 amino acids to WT Lpp, corresponding to no morphological abnormalities except increased periplasmic width (+3 nm and + 4nm, respectively), completely abolished the ability of cells to trigger the Rcs network in response to stress from A22, Mecillinam or *mdoG* deletion (Fig. 5.15) (performed by Abir Asmar).

These results, together with the measurements from Δ*mdoG* mutant cells (Fig. 5.13c) indicates that the periplasmic distance is essential for proper functioning of the Rcs stress response network.

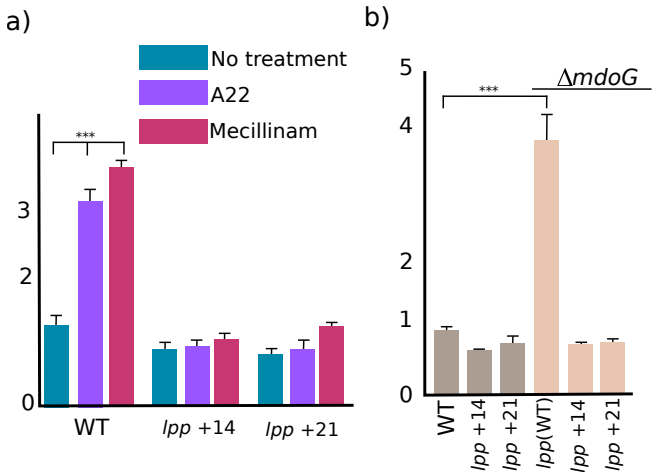


Fig. 5.15: Increased periplasmic distance inhibits the Rcs response to stress.
*Reporter for activity of Rcs response is β-galactosidase activity. a) Activity of the Rcs network in response to stress from A22 or Mecillinam is impaired in mutants with wider periplasmic distances. (*** p < 0.0001, 2-way ANOVA. No significant difference found in mutants). b) Stress response to deletion of mdoG is impaired in mutants with larger periplasms. (*** p < 0.0001, 1-way ANOVA). Adapted from Asmar et al. [190]*

5.3.11 Increased periplasmic distance can be compensated for by increasing RcsF linker length

If an increased periplasmic width is responsible for abolishing the ability of cells to respond to stress, this is indicative of a mechanism where RcsF is not long enough to reach IgaA in the inner membrane. If this hypothesis is correct, increasing the length of the RcsF linker might compensate for the increased periplasm and enable cells to sense stress again.

Upstream of the signalling domain, RcsF contains a 32-amino acid linker region with no predicted secondary structure [215,216]. We added 7 amino acids to the C-terminus of the linker region, predicted to add 2-3 nm to the linker, which should compensate for the increased periplasmic distance in the *lpp*+14 mutant (Performed by Abir Asmar).

Amazingly, activation of the Rcs network in response to A22, Mecillinam or *mdoG* deletion was restored in the RcsF(+7)Lpp(+14) double mutant, indicating that the width of the periplasm and the length of RcsF are perfectly coordinated (Fig. 5.16). In the Lpp+21 cells with 4 nm wider periplasms, the extra 7-amino acids in RcsF only partially compensated for the increased periplasmic distance. These results are consistent with the hypothesis that the activation of the Rcs network is dependent on the ability of RcsF to reach across the periplasm to be able to interact with IgaA.

5.3.12 Lpp acts as both a tether and a column

These results can also be used to assess the function of Lpp in Gram-negative bacteria. As deletion of *lppAB* in *Salmonella*, and *lpp,* in *E. coli* resulted in blebs of membrane pulling away from the cell body we reason that Lpp must act as a tether, pulling on the outer membrane and holding it in place.

When analysing the periplasmic distance of the *lpp*ΔK58 mutant however, I was surprised that the histogram appears bimodal and that although the spread of data is greater and the mean periplasmic distance is also greater than WT, there is also a peak at WT

periplasmic distance (Fig. 5.17). This may be due to the role of other lipoproteins that non-covalently bind peptidoglycan (e.g.: Tol-Pal/ OmpA) in sustaining the regular WT periplasmic width. It was therefore unexpected to not see the bimodal histogram in cells where the length of Lpp had been increased, if proteins such as Tol-Pal and OmpA contribute to WT periplasmic distance (Fig. 5.17). This led us to hypothesise that Lpp not only acts as a tether but also as a support column, and due to the abundance of Lpp, Lpp mutants with increased length can override the non-covalent interactions between the peptidoglycan and Tol-Pal or OmpA, pushing away the outer membrane and increasing the periplasmic width.

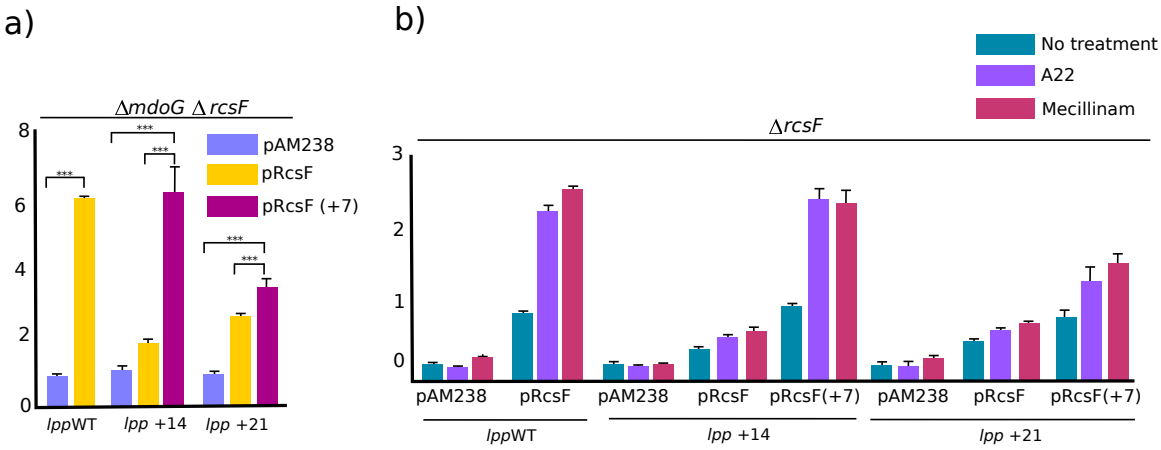


Fig. 5.16: Extending the RcsF linker compensates for increased periplasmic distance.

*a) In lpp length variant mutants, stress response to ΔmdoG is restored when the linker of RcsF is extended by 7 amino acids. (*** $p < 0.0001$, 1-way ANOVA) b) In lpp length variant mutants, response to A22 or Mecillinam is restored (or partially restored in Lpp +21) when the linker of RcsF is extended by 7 amino acids. There was a significant increase in activity ($p < 0.0001$, 2-way ANOVA) for all cells with RcsF+7 compared to empty vector or WT RcsF. Values are normalised to mean value of untreated WT cells. Error bars are SEM (n = 6). Adapted from Asmar et al. [190]*

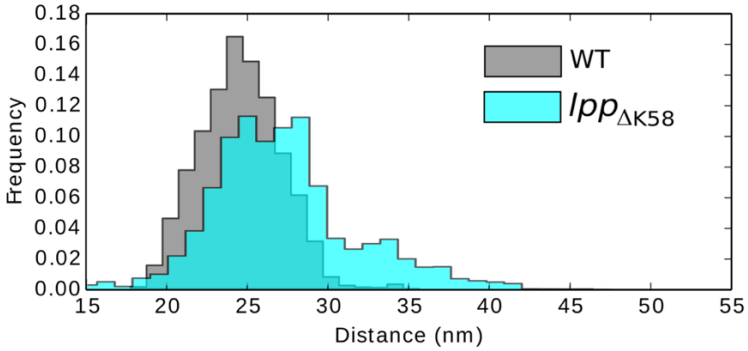


Fig. 5.17: Lpp acts as both a tether and a support column.
Histograms representing the periplasmic distance measured from cryo-EM micrographs of WT overlapped with lppΔK58. Both strains have a peak at ~ 25 nm.

5.4 Discussion

The periplasm is a vital compartment of the Gram-negative cell and is responsible for multiple cellular processes. Due to the abundance of proteins crossing the periplasm (either from inner to outer membranes, or between the peptidoglycan and either membrane) the distance between the inner and outer membranes (periplasmic width) was presumed to be relatively constant. However, experimental measurements of the periplasmic volume have varied significantly, mainly due to artefacts from chemical fixation and sectioning in EM studies [217].

The results presented here in *Salmonella* and *E. coli*, provide insight into the role of Lpp in Gram-negative bacteria. For the first time, it is clear that Lpp plays a role in establishing the periplasmic width. I show here that maintaining a tightly regulated periplasmic width is important for regulating the correct assembly of the *Salmonella* flagellar motor, which affects the proper functioning of the flagellar motor for swimming and swarming. Next, I show the importance of periplasmic distance regulation for stress sensing in the Rcs system. The flagellum and Rcs-network are the first two such systems to be reported, but as the periplasm and the systems held within it have co-evolved, I expect many other periplasmic spanning systems to also be highly dependent on the periplasmic distance.

5.4.1 Flagellar length control

The length control of the flagellar rod has remained enigmatic due to the self-stacking capabilities of FlgG and the lack of a molecular ruler. Here, I show that in *Salmonella*, polymerisation of FlgG stops when the rod tip hits the outer membrane. *lppA* length variants were shown to alter the periplasmic distance and the length of flagellar rods purified from these mutants varied with respect to the changes in *lppA* length. This provides a major advance in our understanding of the assembly of the *Salmonella* flagellar motor.

The results presented here are consistent with a model for distal rod termination requiring contact of the rod with the outer membrane. The growing distal rod continues to polymerise until it hits into the outer membrane. As WT cells have tightly controlled periplasmic distances, the WT distal rod is always ~18 nm long when it interacts with the outer membrane (Fig. 5.18). If, however the periplasmic distance is lengthened via *lppA* length variants, the rod will continue to polymerise until it hits the outer membrane resulting in longer rod structures (Fig. 5.18)

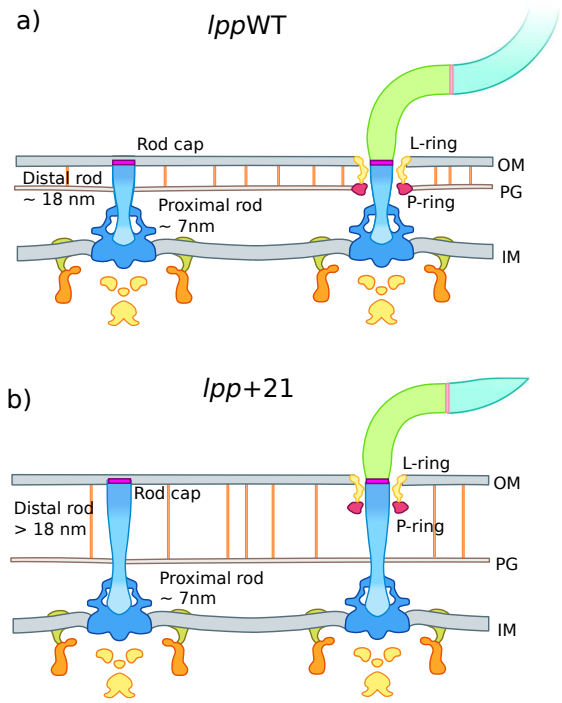


Fig. 5.18: Model for flagellar rod length control in *Salmonella*.
a) In WT cells the periplasmic distance is kept at a specific distance (average 29.12 nm, see Fig. 4b) and the distal rod (FlgG) stops polymerising when it hits into the outer membrane. The P- and L- rings can then assemble around it before the hook and filament assemble. b) In mutant cells where the periplasmic distance is increased the rod grows longer before polymerisation is stopped by the outer membrane and the P- and L-rings can assemble.

In Chapter 3, I show subtomograms identifying steps in the assembly of the flagellum in the γ-proteobacteria with polar flagella (*P. shigelloides*) (Fig. 3.18). In the

early intermediate structure (Fig. 3.18.1), the rod is shown to be pushing on the outer membrane. I believe that the same mechanism for FlgG termination as in *Salmonella,* occurs in these bacteria. The poles of bacteria with Lpp have much greater variation in periplasmic distance than the sides, and poles were therefore not used in the analysis in this Chapter (Chapter 5). This may be due to specific localisation of LppA. In γ-proteobacteria with polar flagella, this range in periplasmic width, corresponds to flagellar motors with large variations in rod length (Chapter 3, Fig. 3.12). In *Salmonella*, tight regulation of the periplasmic distance, and hence maintaining the correct rod length, is important for swimming motility and is vital for swarming (Fig.5.11). In *P. shigelloides* however, this is not the case.

5.4.2 Rcs response

Identifying the role of the periplasm in controlling flagellar rod length provided the basis for hypothesising that the periplasmic distance must be of critical importance to many other periplasm spanning systems, and lead me to work on an unexpected system: the Rcs stress response.

The results in this chapter, allowed us to devise a model for the tight regulation of the RcsF stress-response by the periplasmic distance (Fig. 5.19). In a WT cell the linker region of RcsF is long enough for RcsF to reach across the periplasm and interact with IgaA in the inner membrane (Fig. 5.19a) and turn the Rcs network on. When LppA is mutated (Δ*lpp* or ΔK58), Lpp is no longer covalently linked to the peptidoglycan layer. The outer membrane pulls away from the inner membrane (Fig. 5.12) and the periplasmic distance increases (Fig. 5.13). The RcsF linker is no longer long enough to reach IgaA in the inner membrane (Fig. 5.19b) and the Rcs network cannot get switched on. Analogously, in a mutant where the length of *lpp* is increased by 14 amino acids, although the outer membrane is stable, the periplasmic distance increases by 3 nm (Fig. 5.13) and the RcsF linker is again too short to reach across the periplasm to interact with IgaA. Again, the Rcs network cannot be activated (Fig. 5.19c). If, however, the RcsF linker length is increased

to match the increased periplasmic distance, RcsF can again reach across the periplasm and activate the Rcs network via interaction with IgaA (Fig. 5.19d). These results provide direct evidence that the Rcs-stress response requires a tightly regulated periplasmic distance.

The results presented here demonstrate that without regulation of the periplasmic width, cells lose the ability to sense envelope stress. When the periplasmic width is decreased (Δ*mdoG*), the Rcs system is constitutively activated. With even small increases in periplasmic width the surveillance system is disrupted. The work in this chapter shows that the length of the RscF linker is perfectly coordinated with the width of the periplasm.

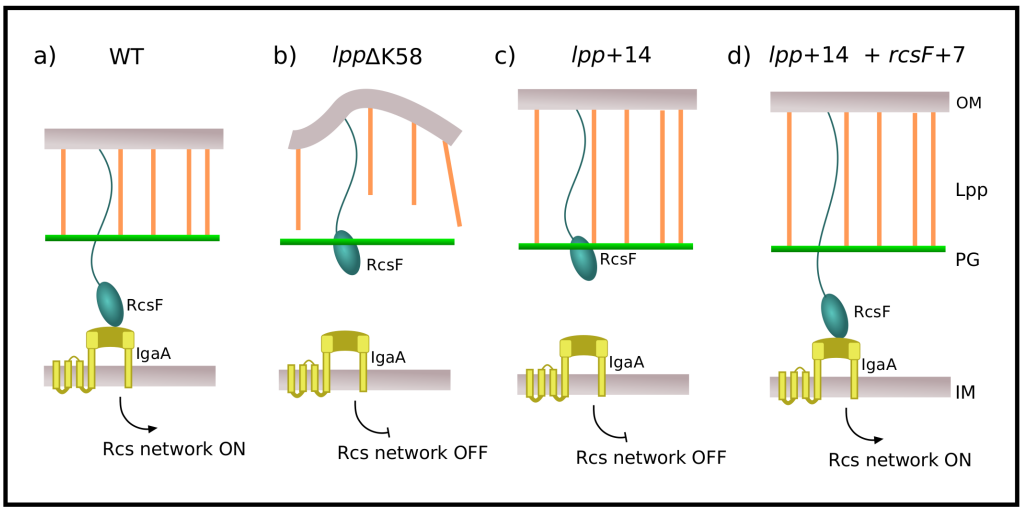


Fig. 5.19: Model for control of Rcs response by periplasmic width.
Activation of the Rcs network depends on RcsF in the outer membrane interacting with IgaA in the inner membrane. a) WT cells have an RcsF linker that is long enough to reach across the WT periplasmic distance and interact with IgaA. b) In the lppΔK58 mutant, Lpp cannot covalently link to peptidoglycan. In these cells the outer membrane pulls away from the cell and forms outer membrane blebs. The average periplasmic distance in these cells increases and the RcsF linker is no longer long enough to reach IgaA in the inner membrane. c) In an lpp length variant where 14 amino acids have been added to it, the average periplasmic distance increased by ~ 3 nm. In these cells the RcsF linker is not long enough to cross the extra-wide periplasm and cannot activate the Rcs network via IgaA. d) In the same mutant background as (c), the linker of RcsF is increased by 7 amino acids. IgaA is now long enough to reach across the extra-wide periplasm and can again activate the Rcs network via interactions with IgaA in the inner membrane.

5.4.3 Role of Lpp

The work in *Salmonella* and *E. coli* uncovered another interesting result. I show that Lpp is not only important for maintenance of outer membrane integrity by acting as a tether between the outer membrane and the peptidoglycan but, also that it is the major determinant of periplasmic distance and hence a principle player in controlling periplasmic spanning complexes and inter-membrane communication.

I was surprised by the apparent large range in periplasmic distance in *Salmonella* cells as a population (Fig. 5.8), but found that if histograms were made for individual cells, the range in periplasmic width became much lower (Fig. 5.9). One reason for this may be that Lpp levels may change at different times in a cell division cycle. It has already been shown that at different stages in a population growth, the ratio of Lpp bound to peptidoglycan and free Lpp changes. In stationary phase, for example, the proportion of Lpp bound to the peptidoglycan increases by 70%, compared to cells in exponential growth [218]. Little is known about this and it would be of interest to the field to identify whether periplasmic width correlates with cell length, as a proxy for point in division cycle.

5.4.4 Gram-negative cells without Lpp

Not all Gram-negative cells have the lipoprotein Lpp. Future work will need to be done to understand how these cells maintain a tightly regulated periplasmic distance. In these cells, other lipoproteins such as the Tol/Pal system may play bigger roles in periplasmic distance maintenance.

5.4.5 Relevance to other systems and future work

The Gram-negative cell is just one of many examples of cellular compartments surrounded by a double membrane. Eukaryotic organelles such as mitochondria, chloroplasts and other plastids are also surrounded by two membranes. The chloroplasts

from some algae, such as Glaucophytes, still contain peptidoglycan between their two membranes, believed to be a remnant from their endosymbiotic origin from cyanobacteria [219]. All of these systems need communication between the two membranes. The importance of the inter-membrane space for maintenance of membrane-spanning complexes or inter-membrane communication highlighted here, hints at similar mechanisms playing a role in these systems. To fully understand the significance of the tightly controlled periplasmic width, the effect of altering the periplasmic width on other membrane spanning complexes will need to be probed.

5.5 Materials and Methods

5.5.1 Strain growth

Strains were grown aerobically in LB at 37℃ until an OD_{600} of 0.6 was reached. Cells were spun for 5 min at 6,000 × *g* at 4℃ and resuspended to an OD_{600} of about 12.

Table 7: Strains and plasmids used in Chapter 5.

Strain or plasmid	Source
TH437 (*S. enterica* WT LT2)	Kelly Hughes, University of Utah
TH22117 (LT2 FlgG(G65R) polyrod)	Kelly Hughes, University of Utah
TH21911 (LT2 Δ*lppAB)*	This study
TH22638 (LT2 Δ*lppAB,* Δ*pal)*	This study
TH22549 (LT2 lpp_{+21})	This study
TH22550 (LT2 lpp_{+42})	This study
TH22551 (LT2 lpp_{+63})	This study
TH22552 (LT2 lpp_{-21})	This study
DH300 (E. coli WT)	This study
DH300 Δ*lpp*	This study
DH300 Δ*lpp::*$lpp_{\Delta K58}$	This study
DH300 Δ*lpp::*lpp_{+14}	This study
DH300 Δ*lpp::*lpp_{+21}	This study
DH300 Δ*lpp::*lpp_{+14}*,* Δ*rcsF*	This study
DH300 Δ*lpp::*lpp_{+21}*,* Δ*rcsF*	This study
DH300 Δ*lpp::*$lpp_{\Delta K58}$, Δ*mdoG*	This study
DH300 Δ*lpp::*lpp_{+14}*,* Δ*mdoG*	This study
DH300 Δ*lpp::*lpp_{+21}*,* Δ*mdoG*	This study
DH300 Δ*lpp::*lpp_{+14}*,* Δ*rcsF,* Δ*mdoG*	This study
DH300 Δ*lpp::*lpp_{+21}*,* Δ*rcsF,* Δ*mdoG*	This study
DH300 Δ*mdoG*	This study
DH300 Δ*rcsF*	[220]
DH300 Δ*rcsF,* Δ*mdoG*	This study
pAM238 (IPTG-regulated Plac, pSC101-based, spectinomycin)	[221]
pAM238 with *rcsF*	[220]
pAM238 with $rcsF_{+7}$	This study

5.5.2 Cryo-EM data collection

UltraAuFoil R2/2 grids (200 mesh; Quantifoil Micro Tools GmbH) were glow-discharged for 60 s at 10 mA. Cells were mixed with a solution of 10 nm colloidal gold (Sigma) immediately before freezing. A 2.5-µl droplet of sample was applied to the grid and plunge frozen using a Vitrobot Mk IV (FEI Company) with a wait time of 60 s, a blot time of 5 s, a blot force of 3, and a drain time of 1s at a constant humidity of 100%. Grids were stored under liquid nitrogen until required for data collection.

Projection images were collected on a 200 keV FEI Tecnai TF20 FEG transmission electron microscope (FEI Company) equipped with a Falcon II direct electron detector (FEI Company) using a Gatan 626 cryogenic-holder (Gatan). Leginon automated data-collection software 3.0 was used to acquire images with pixel size of 0.828 nm (nominal magnification 25,000×) with a defocus of −5 µm.

5.5.3 Membrane measurements

3dmod from the IMOD package [89] and custom scripting were used to manually segment inner and outer membranes of projection images of ~25 cells per mutant in *Salmonella* and ~35 cells per strain in *E. coli*, measuring the periplasmic width at 0.5nm intervals, resulting in tens of thousands of data points per mutant to produce width histograms.

5.5.4 Construction of *lpp* length mutants (Performed by Eli Cohen and Abir Asmar)

lpp length mutants were constructed in *E. coli* K12 F^- λ^- cells harbouring the λRed recombination plasmid (pKD46). Briefly, a tetracycline-resistance cassette (*tetRA*) was inserted between codons 42 and 43 of *E. coli lpp*. Replacement of the *tetra* cassette with insertions of 14 or 21 residues (2 and 3 heptad repeats, respectively) was accomplished by introducing dsDNA fragments bearing 40 bp of homology to *E. coli lpp* directly flanking the 5’ and 3’ ends of the *tetRA* cassette. Tetracycline-sensitive transformants (*lpp* length mutants) were selected by plating on medium containing anhydrotetracycline (0.2 mg/ ml)

and fusaric acid (2.4 mg/ml). Chromosomal *lpp* length mutations were moved into the MG1655 background through standard λRed recombination.

5.5.5 Construction of the *lpp*ΔK58 mutant (Performed by Abir Asmar)

The *lpp*ΔK58 mutant was constructed using site-directed mutagenesis of WT *lpp* cloned into pBad18. *lpp*ΔK58 was moved onto the chromosome of MG1655 cells via standard λRed recombination.

5.5.6 Construction of RcsF+7 (Performed by Abir Asmar)

To create a longer version of RcsF, we used pSC202 (the RcsF ORF in the low-copy vector pAM238) as a template [222]. The extended linker fragment was synthesised with flanking restriction sites RsrII and PstI using gene fragments (sequence available upon request). The fragment and vector pSC202 were digested and ligated to yield pRcsF+7.

5.5.7 β-Galactosidase assay (Performed by Abir Asmar)

Cells harbouring P*rprA-lacZ* at the *att*B phage lambda site on the chromosome were diluted 1:100 from over- night cultures in Luria broth (LB), then incubated at 37℃. When needed, the cultures were treated with 0.3 μg/ml mecillinam or 5 μg/ml A22 at OD_{600} = 0.2. Cells were further grown for 1 h (with mecillinam treatment) or 40 min (with A22 treatment). Otherwise, cells were harvested at OD_{600} = 0.6. 20 μm of cells were harvested and incubated with 80 μl of permeabilisation solution for 30–45 min at room temperature. Then, 600 μl of substrate (1 mg/ml O-nitrophenyl-β-d-galactoside, 50 mM β-mercaptoethanol) was added. The mixture was further incubated at 30℃ for 20–25 min. 700 μl of 1 M Na_2CO_3 were added to stop the reaction, and the optical density was measured at 420 nm. The standardised amount of β-galactosidase activity was reported in Miller units. The ratio of P*rprA-lacZ* induction was calculated relative to the basal level in a WT strain.

5.5.8 Swimming and Swarming Motility Assays (Performed by Eli Cohen)

Swimming motility was assayed by stabbing single colonies into swimming motility plates (0.2% agar with 10 g/L tryptone and 5 g/L NaCl added) and incubated face-up at 37° C for 8-12 hours. For swarming motility assays, 1 µl of overnight cultures were spotted on swarming motility agar (0.5% agar with 10 g/L tryptone, 5 g/L yeast extract, 10 g/L NaCl and 0.5% glucose added) followed by incubating face-up at 37° C for 16-18 hours.

5.5.9 Isolation, Transmission Electron Microscopy and Measurement of Flagellar Structures (Performed by Eli Cohen)

Hook basal body (HBB) isolation was carried out by methods described previously [223], with minor modifications. Structures were not collected by CsCl or sucrose gradient centrifugation but were pelleted at 60,000 x g for 1 h using a Beckman 50.2Ti and/or S80-AT3 rotor at 12 °C. Purified structures were applied to glow discharged carbon-coated formvar copper grids (Cu-FCF-300H grids, Electron Microscopy Sciences) and stained with 2% aqueous phosphotungstic acid (pH ~7.0). Images were captured using a JEOL JEM-1400 electron microscope at an acceleration voltage of 120 kV coupled to a Gatan CCD camera. Rod lengths were measured using NIH ImageJ 1.50i software.

Chapter 6

Summary and recent developments

6.1 Thesis summary

Salmonella is a sophisticated pathogen with a complex lifestyle. It infects hosts via contaminated food and becomes intracellular in the gut epithelial layer. One of *Salmonella's* important virulence factors is its dynamic, H^+-driven flagellum. This flagellum is poised to encounter multiple different environments and viscosities encountered in the gut. Interestingly, *Salmonella* and the other enteric bacteria occupy a very different niche to many closely related species. *Salmonella* is a γ-proteobacterium, closely related to species such as *Vibrio, Shewanella* and *Plesiomonas*. All of these species, and most other γ-proteobacteria are aquatic with polar, Na^+-driven flagellar motors for swimming. Some also have a second, lateral H^+-driven flagellar system for swarming.

Inferring from its close relatives, it is likely that an ancestor of *Salmonella* was a free-living aquatic species that once had two flagellar systems. In Chapter 2, I show that the flagellar motor in modern-day *Salmonella* is not native, but was acquired via a HGT from the β-proteobacteria. By using phylogenetic analysis, I show that *Salmonella* acquired its motor from an ancestor of *Bordetella*. Combining this with ECT and STA, I confirmed this result by showing that the model "donor strain", *B. bronchiseptica*, has a motor which is structurally very similar to that from modern-day *Salmonella*. The model "acceptor strain" *P. shigelloides*, which is taxonomically closely related, has two flagellar motors which are structurally very different from that of modern-day *Salmonella*. From this I can propose that an ancestor of modern-day *Salmonella,* from which *Plesiomonas'* motor is a direct descendant, once had a motor more similar to *Plesiomonas* than the motor *Salmonella* has today. The acquisition of the non-native β-proteobacterial flagellar motor, and subsequent loss of the two native flagellar motors, may have played a role in *Salmonella*'s path from a free-living aquatic species to a highly specialised gut pathogen.

The two flagellar systems in γ-proteobacteria are highly specialised, and by acquiring the new, non-native flagellar motor from an ancestor of *Bordetella*, *Salmonella* received a more generalist motor. But what selective advantage did the new motor provide? One of the main differences, seen in STA, between *Salmonella's* new motor and the native polar γ-proteobacterial motor of *P. shigelloides,* is the lack of stator complexes in the new motor. While the polar motor has high occupancy stators and is always firing at high torque, even when this is not needed in low viscosity medium, *Salmonella's* motor can adapt to its environment, only recruiting stator complexes when they are truly needed. This may be a selective advantage as the new flagellar motor is both energy efficient, and poised to encounter multiple environments. Due to this dynamic nature however, we can't visualise the stator complexes in STA and therefore still do not know what the maximum number of stator complexes that can assemble on the *Salmonella* flagellar motor is, and how these are arranged. In Chapter 4, I show a direct visualisation of the dynamic nature of the stator complexes by showing the appearance of a stator complex density in a subtomogram when load is applied to the filament.

The energy efficient, general purpose motor may have been a selective advantage, but not only is the native polar flagellum more energy intensive, it also fares poorly at high cell densities. When measuring the swimming speeds of different γ-proteobacteria, I noticed that cells with native, polar flagella (*V. fischeri* and *P. shigelloides*) stop swimming when they are grown to later growth stages. As a cell population grows, nutrients become limited and in Chapter 3, I show that under nutrient limited environments, polarly flagellated γ-proteobacteria eject their flagella and enter a sessile state. The filaments with attached hook and distal rod accumulate in the supernatant of cells, and this ejection can be triggered by moving cells from fresh LB into spent or minimal medium. The ejected flagella leave behind partial flagella structures in the outer membrane and a novel protein plugs the hole left behind from the ejected rod. This specific cellular response is remarkable and I show that it is wide-spread in the non-enteric γ-proteobacteria (*V. fischeri, V. cholerae, S. putrefaciens, P. aeruginosa*). This is limited to polar flagella however, and *Salmonella* cells with their non-native peritrichous flagella, do not exhibit the same behaviour.

Ejecting a flagellum, which required a large amount of energy to build, seems counter-productive. Due to the placement of these flagella on the pole however, during division, one daughter cell inherits an entire set of powering flagella. Ejection may therefore be a drastic, but essential mechanism to save energy. During division of *Salmonella* cells however, each daughter cell receives half of the flagella. If flagellar assembly is stopped, the flagella will be diluted with each division. *Salmonella's* new, non-native motor provided by the β-proteobacteria, is located laterally, is not ejected at high cell densities and is energy efficient.

There is an impressive amount of diversity in flagella, particularly in their structures and placement on the cell. I have shown that diverse flagella behave differently and that by swapping flagellar motors, cells can seek out new niches. However, all flagella have a common core of conserved proteins and all flagella self-assemble within the confines of the bacterial cell envelope. The Gram-negative cell envelope is made up of three main structures, a phospholipid bilayer inner membrane, a peptidoglycan layer and a phospholipid/ glycolipid bilayer outer membrane. Each layer is held at a specific distance by many proteins that cross between them. Each component of the flagellum needs to be carefully assembled within the cell envelope and this self-assembly is therefore intimately linked to the periplasmic architecture.

Although the self-assembly of the flagellar motor within the cell envelope has been well studied, one of the outstanding questions in the field was what the mechanism for rod-length control is. It was already known that the hook is measured by a molecular ruler protein, FliK, and that the filament was self-limiting at ~10 μm due to the rate of diffusion, but the length-control for the last axial component, the rod, had not yet been identified. In Chapter 5, I show that the periplasmic distance is the size-determining factor for the flagellar rod. By altering the periplasmic distance, the length of the rod was also altered. The altered rod length impaired the swimming and swarming ability of the flagellum.

The flagellar motor is just one of many systems which assemble and function within the cell envelope. Upon finding that the periplasmic width is tightly controlled and can be manipulated, I sought to understand the greater implications for a tightly controlled periplasmic width by studying the Rcs stress-response system. This system requires the interaction of two proteins, one in the inner membrane and one in the outer membrane. In Chapter 5, I show that the Rcs stress-response system is inhibited if the periplasmic width is increased, but this can be complemented by simultaneously increasing the length of the outer membrane component, RcsF. Together the flagellar rod length control and stress response control highlight the importance of the tight regulation of the periplasmic width.

The work presented in this thesis, provides a better understanding of the *Salmonella* flagellar motor and more generally the Gram-negative cell envelope. While building on a long history of flagellar research, the new techniques available today, such as ECT, have enabled novel insights into the acquisition, mechanism of rotation, assembly and regulation of motility.

This thesis also provides insight into the more general theme of evolution. In Chapter 2, the use of HGT to provide new machinery for bacteria to adapt to different environments, and colonise new niches is highlighted. The two native polar and lateral flagellar systems that *Salmonella* had before the HGT are highly specialised. The only way to move from highly specialised systems back to a more general system is to acquire one from a different bacterium. *Salmonella's* acquisition of three T3SSs via HGT has allowed it to colonise the gut, live intracellularly and infect new hosts.

In Chapter 3, evolution is shown as a "tinkerer". The hole in the outer membrane which is left by the ejected filament is filled by a protein plug. The relic structures accumulate at the cell pole with, as far as I know, no function. If we were to design this process, we might think it necessary to remove all left-over components. However, evolving proteolysis enzymes to do this is a much more complex solution to the problem than merely plugging the hole and moving on. The simple solution is more likely; evolution does not wait for the perfect solution.

In Chapter 5, the idea of co-evolution is introduced. The periplasm and protein complexes within it are perfectly coordinated. These systems have all co-evolved to reach the optimal functional level as a whole. This was shown simply with two systems, the flagellar motor and the Rcs stress-response. The periplasmic width and the length of the RcsF-linker are perfectly co-ordinated. This periplasmic width in turn controls the length of the flagellar motor's rod. Alterations in the periplasmic width leads to a loss of function in both systems.

6.2 Developments in ECT which would benefit this work

New developments in the field of ECT give the promise of collecting data in thicker cells (FIB-milling), much faster (continuous tilt-series collection) and closer to focus with more contrast (phase plate).

6.2.1 FIB-milling

For thick samples, a focussed ion beam (FIB) can be used, in a virtually artefact-free way, to whittle away biological material leaving only a thin lamella (typically 60-350nm for ECT), supported by the surrounding un-eroded sample. The sputtering of sample from above or below the object of interest is carried out in a precisely controlled and systematic way, typically using Gallium ions (Ga^{+}) while allowing the biological sample to remain in a vitreous state [224].

FIB-milling could be used to study eukaryotic cells infected with *Salmonella* to provide an understanding of the intracellular infection process. Imaging *Salmonella* cells inside FIB-milled SCVs would provide a way to image the final *Salmonella* T3SS, the SPI-2 injectisome, *in situ.*

6.2.2 Phase plates

Phase plates apply a phase shift to the scattered electrons, increasing the contrast of the image. This allows data collection at or close to focus and decreases the required dose [225]. The decreased dose needed is hugely advantageous for ECT, decreasing specimen damage and increasing precision of tilt series alignment due to decreased specimen movement. The Volta Phase plate, which is now routinely used for automated data acquisition has shown huge improvements in the definition of features in ECT [226] and is now often used for small proteins using SPA.

Collecting cryo-EM SPA data of the stator complexes would be assisted by the use of a phase plate (Chapter 4). The small size of the stator complex protein would benefit from the extra contrast gained.

6.2.3 Continuous tilt-series collection

Collecting tilt-series' is time consuming and takes between 15 minutes and an hour to collect one. This is partly due to the sample being tilted in discrete tilt steps. After each tilt the microscope refocuses, re-centres and has a wait time for the sample to settle, reducing sample movement. The development of continuously recording detectors and stable microscope stages that can move through a tilt-series in one continuous run without the need to refocus or re-centre would dramatically increase the through-put of data collection [227].

This would be particularly useful for imaging the stator complexes *in situ* in *Salmonella* (Chapter 4) as the yield of flagellar motors in this sample is very low. It would also, more generally mean that more data can be collected for each STA, allowing further processing such as classification. Heterogeneity in biological samples is inevitable and STA assumes all subtomograms are homogenous. STA of heterogonous samples greatly reduces the resolution as multiple states are being averaged into one. If enough data has

been collected, the individual subtomograms can be classified into discrete states and these can be averaged to give multiple STAs. This has the benefit of increasing the resolution but can also provide important mechanistic understanding by giving multiple states of each structure, providing insights into the dynamics of complexes *in situ*.

References

1. Purcell EM. Life at low Reynolds number. Am J Phys. 1977;45: 3–11. doi:10.1119/1.10903

2. Schwarz US. Physical constraints for pathogen movement. Semin Cell Dev Biol. 2015;46: 82–90. doi:10.1016/j.semcdb.2015.09.025

3. Mattick JS. Type IV pili and twitching motility. Annu Rev Microbiol. 2002;56: 289–314. doi:10.1146/annurev.micro.56.012302.160938

4. Spormann AM. Gliding Motility in Bacteria: Insights from Studies of Myxococcus xanthus. Microbiol Mol Biol Rev. 1999;63: 621–641.

5. Chen S, Beeby M, Murphy GE, Leadbetter JR, Hendrixson DR, Briegel A, et al. Structural diversity of bacterial flagellar motors. EMBO J. 2011;30: 2972–2981. doi:10.1038/emboj.2011.186

6. Ferreira JL, Matthews-Palmer TRS, Beeby M. Electron Cryo-Tomography. Cellular Imaging. Springer, Cham; 2018. pp. 61–94. Available: https://link.springer.com/chapter/10.1007/978-3-319-68997-5_3

7. Berg HC, Anderson RA. Bacteria Swim by Rotating their Flagellar Filaments. Nature. 1973;245: 380–382. doi:10.1038/245380a0

8. Erhardt M, Namba K, Hughes KT. Bacterial Nanomachines: The Flagellum and Type III Injectisome. Cold Spring Harb Perspect Biol. 2010;2: a000299. doi:10.1101/cshperspect.a000299

9. Kutsukake K, Ohya Y, Iino T. Transcriptional analysis of the flagellar regulon of Salmonella typhimurium. J Bacteriol. 1990;172: 741–747.

10. Chevance FFV, Hughes KT. Coupling of Flagellar Gene Expression with Assembly in Salmonella enterica. Methods Mol Biol Clifton NJ. 2017;1593: 47–71. doi:10.1007/978-1-4939-6927-2_4

11. Imada K, Minamino T, Kinoshita M, Furukawa Y, Namba K. Structural insight into the regulatory mechanisms of interactions of the flagellar type III chaperone FliT with its binding partners. Proc Natl Acad Sci. 2010;107: 8812–8817. doi:10.1073/pnas.1001866107

12. Minamino T, Macnab RM. Components of the Salmonella flagellar export apparatus and classification of export substrates. J Bacteriol. 1999;181: 1388–1394.

13. Yonekura K, Maki-Yonekura S, Namba K. Complete atomic model of the bacterial flagellar filament by electron cryomicroscopy. Nature. 2003;424: 643–650. doi:10.1038/nature01830

14. Akeda Y, Galán JE. Chaperone release and unfolding of substrates in type III secretion. Nature. 2005;437: 911–915. doi:10.1038/nature03992

15. Erhardt M, Mertens ME, Fabiani FD, Hughes KT. ATPase-Independent Type-III Protein Secretion in Salmonella enterica. PLOS Genet. 2014;10: e1004800. doi:10.1371/journal.pgen.1004800

16. Hara N, Namba K, Minamino T. Genetic Characterization of Conserved Charged Residues in the Bacterial Flagellar Type III Export Protein FlhA. PLoS ONE. 2011;6. doi:10.1371/journal.pone.0022417

17. Minamino T, Namba K. Distinct roles of the FliI ATPase and proton motive force in bacterial flagellar protein export. Nature. 2008;451: 485–488. doi:10.1038/nature06449

18. Paul K, Erhardt M, Hirano T, Blair DF, Hughes KT. Energy source of flagellar type III secretion. Nature. 2008;451: 489–492. doi:10.1038/nature06497

19. Terashima H, Kawamoto A, Tatsumi C, Namba K, Minamino T, Imada K. In Vitro Reconstitution of Functional Type III Protein Export and Insights into Flagellar Assembly. mBio. 2018;9. doi:10.1128/mBio.00988-18

20. Delalez NJ, Berry RM, Armitage JP. Stoichiometry and Turnover of the Bacterial Flagellar Switch Protein FliN. mBio. 2014;5. doi:10.1128/mBio.01216-14

21. Lele PP, Branch RW, Nathan VSJ, Berg HC. Mechanism for adaptive remodeling of the bacterial flagellar switch. Proc Natl Acad Sci U S A. 2012;109: 20018–20022. doi:10.1073/pnas.1212327109

22. Yuan J, Branch RW, Hosu BG, Berg HC. Adaptation at the output of the chemotaxis signalling pathway. Nature. 2012;484: 233–236. doi:10.1038/nature10964

23. Hosu BG, Berg HC. CW and CCW Conformations of the E. coli Flagellar Motor C-Ring Evaluated by Fluorescence Anisotropy. Biophys J. 2018;114: 641–649. doi:10.1016/j.bpj.2017.12.001

24. Ibuki T, Imada K, Minamino T, Kato T, Miyata T, Namba K. Common architecture of the flagellar type III protein export apparatus and F- and V-type ATPases. Nat Struct Mol Biol. 2011;18: 277–282. doi:10.1038/nsmb.1977

25. Imada K, Minamino T, Tahara A, Namba K. Structural similarity between the flagellar type III ATPase FliI and F1-ATPase subunits. Proc Natl Acad Sci U S A. 2007;104: 485–490. doi:10.1073/pnas.0608090104

26. Pallen MJ, Bailey CM, Beatson SA. Evolutionary links between FliH/YscL-like proteins from bacterial type III secretion systems and second-stalk components of the FoF1 and vacuolar ATPases. Protein Sci Publ Protein Soc. 2006;15: 935–941. doi:10.1110/ps.051958806

27. Cohen EJ, Ferreira JL, Ladinsky MS, Beeby M, Hughes KT. Nanoscale-length control of the flagellar driveshaft requires hitting the tethered outer membrane. Science. 2017;356: 197–200. doi:10.1126/science.aam6512

28. Erhardt M, Singer HM, Wee DH, Keener JP, Hughes KT. An infrequent molecular ruler controls flagellar hook length in Salmonella enterica. EMBO J. 2011;30: 2948–2961. doi:10.1038/emboj.2011.185

29. Kim HJ, Yoo W, Jin KS, Ryu S, Lee HH. The role of the FliD C-terminal domain in pentamer formation and interaction with FliT. Sci Rep. 2017;7: 4418. doi:10.1038/s41598-017-02664-6

30. Renault TT, Abraham AO, Bergmiller T, Paradis G, Rainville S, Charpentier E, et al. Bacterial flagella grow through an injection-diffusion mechanism. eLife. 2017;6. doi:10.7554/eLife.23136

31. Zhou J, Lloyd SA, Blair DF. Electrostatic interactions between rotor and stator in the bacterial flagellar motor. Proc Natl Acad Sci U S A. 1998;95: 6436–6441.

32. Ito M, Takahashi Y. Nonconventional cation-coupled flagellar motors derived from the alkaliphilic Bacillus and Paenibacillus species. Extremophiles. 2017;21: 3–14. doi:10.1007/s00792-016-0886-y

33. Thomas D, Morgan DG, DeRosier DJ. Structures of Bacterial Flagellar Motors from Two FliF-FliG Gene Fusion Mutants. J Bacteriol. 2001;183: 6404–6412. doi:10.1128/JB.183.21.6404-6412.2001

34. Beeby M, Ribardo DA, Brennan CA, Ruby EG, Jensen GJ, Hendrixson DR. Diverse high-torque bacterial flagellar motors assemble wider stator rings using a conserved protein scaffold. Proc Natl Acad Sci. 2016; 201518952. doi:10.1073/pnas.1518952113

35. Nirody JA, Berry RM, Oster G. The Limiting Speed of the Bacterial Flagellar Motor. Biophys J. 2016;111: 557–564. doi:10.1016/j.bpj.2016.07.003

36. Berg HC, Brown DA. Chemotaxis in Escherichia coli analysed by Three-dimensional Tracking. Nature. 1972;239: 500–504. doi:10.1038/239500a0

37. Silverman M, Simon M. Flagellar rotation and the mechanism of bacterial motility. Nature. 1974;249: 73–74. doi:10.1038/249073a0

38. Lee SY, Cho HS, Pelton JG, Yan D, Henderson RK, King DS, et al. Crystal structure of an activated response regulator bound to its target. Nat Struct Biol. 2001;8: 52–56. doi:10.1038/83053

39. Lele PP, Roland T, Shrivastava A, Chen Y, Berg HC. The flagellar motor of Caulobacter crescentus generates more torque when a cell swims backward. Nat Phys. 2016;12: 175–178. doi:10.1038/nphys3528

40. Armitage JP, Macnab RM. Unidirectional, intermittent rotation of the flagellum of Rhodobacter sphaeroides. J Bacteriol. 1987;169: 514–518.

41. Berg HC. How spirochetes may swim. J Theor Biol. 1976;56: 269–273.

42. Greenberg EP, Canale-Parola E. Motility of flagellated bacteria in viscous environments. J Bacteriol. 1977;132: 356–358.

43. Kimsey RB, Spielman A. Motility of Lyme disease spirochetes in fluids as viscous as the extracellular matrix. J Infect Dis. 1990;162: 1205–1208.

44. Klitorinos A, Noble P, Siboo R, Chan EC. Viscosity-dependent locomotion of oral spirochetes. Oral Microbiol Immunol. 1993;8: 242–244.

45. Ruby JD, Charon NW. Effect of temperature and viscosity on the motility of the spirochete Treponema denticola. FEMS Microbiol Lett. 1998;169: 251–254. doi:10.1111/j.1574-6968.1998.tb13325.x

46. Lux R, Miller JN, Park NH, Shi W. Motility and chemotaxis in tissue penetration of oral epithelial cell layers by Treponema denticola. Infect Immun. 2001;69: 6276–6283. doi:10.1128/IAI.69.10.6276-6283.2001

47. WHO. 9789241565240-eng.pdf. In: Interventions for the Control of Non-typhoidal Salmonella spp. in Beef and Pork: METING REPORT AND SYSTEMATIC REVIEW [Internet]. 2016 [cited 26 Mar 2017]. Available: http://apps.who.int/iris/bitstream/10665/249529/1/9789241565240-eng.pdf

48. Gal JE. Salmonella interactions with host cells: Type III Secretion at Work. Annu Rev Cell Dev Biol. 2001; 53–86.

49. Abby SS, Rocha EPC. The non-flagellar type III secretion system evolved from the bacterial flagellum and diversified into host-cell adapted systems. PLoS Genet. 2012;8: e1002983. doi:10.1371/journal.pgen.1002983

50. Erhardt M, Namba K, Hughes KT. Bacterial nanomachines: the flagellum and type III injectisome. Cold Spring Harb Perspect Biol. 2010;2: a000299. doi:10.1101/cshperspect.a000299

51. Kawamoto A, Morimoto YV, Miyata T, Minamino T, Hughes KT, Kato T, et al. Common and distinct structural features of Salmonella injectisome and flagellar basal body. Sci Rep. 2013;3: 3369. doi:10.1038/srep03369

52. Galán JE, Lara-Tejero M, Marlovits TC, Wagner S. Bacterial type III secretion systems: specialized nanomachines for protein delivery into target cells. Annu Rev Microbiol. 2014;68: 415–438. doi:10.1146/annurev-micro-092412-155725

53. Chaban B, Hughes HV, Beeby M. The flagellum in bacterial pathogens: For motility and a whole lot more. Semin Cell Dev Biol. 2015;46: 91–103. doi:10.1016/j.semcdb.2015.10.032

54. Schraidt O, Lefebre MD, Brunner MJ, Schmied WH, Schmidt A, Radics J, et al. Topology and organization of the Salmonella typhimurium type III secretion needle complex components. PLoS Pathog. 2010;6: e1000824. doi:10.1371/journal.ppat.1000824

55. Kuhle V, Hensel M. Cellular microbiology of intracellular Salmonella enterica: functions of the type III secretion system encoded by Salmonella pathogenicity island 2. Cell Mol Life Sci CMLS. 2004;61: 2812–2826. doi:10.1007/s00018-004-4248-z

56. Stecher B, Hapfelmeier S, Müller C, Kremer M, Stallmach T, Hardt W-D. Flagella and chemotaxis are required for efficient induction of Salmonella enterica serovar Typhimurium colitis in streptomycin-pretreated mice. Infect Immun. 2004;72: 4138–4150. doi:10.1128/IAI.72.7.4138-4150.2004

57. Misselwitz B, Barrett N, Kreibich S, Vonaesch P, Andritschke D, Rout S, et al. Near Surface Swimming of Salmonella Typhimurium Explains Target-Site Selection and Cooperative Invasion. PLOS Pathog. 2012;8: e1002810. doi:10.1371/journal.ppat.1002810

58. Harshey RM. Dimorphic transition in Escherichia coli and Salmonella typhimurium: surface-induced differentiation into hyperflagellate swarmer cells. PNAS. 1994;91: 8631–8635.

59. La Ragione RM, Cooley WA, Velge P, Jepson MA, Woodward MJ. Membrane ruffling and invasion of human and avian cell lines is reduced for aflagellate mutants of Salmonella enterica serotype Enteritidis. Int J Med Microbiol IJMM. 2003;293: 261–272. doi:10.1078/1438-4221-00263

60. Dibb-Fuller MP, Allen-Vercoe E, Thorns CJ, Woodward MJ. Fimbriae- and flagella-mediated association with and invasion of cultured epithelial cells by Salmonella enteritidis. Microbiol Read Engl. 1999;145 (Pt 5): 1023–1031. doi:10.1099/13500872-145-5-1023

61. Schmitt CK, Ikeda JS, Darnell SC, Watson PR, Bispham J, Wallis TS, et al. Absence of All Components of the Flagellar Export and Synthesis Machinery

Differentially Alters Virulence of Salmonella enterica Serovar Typhimurium in Models of Typhoid Fever, Survival in Macrophages, Tissue Culture Invasiveness, and Calf Enterocolitis. Infect Immun. 2001;69: 5619–5625. doi:10.1128/IAI.69.9.5619-5625.2001

62. Silverman M, Simon M. Phase variation: Genetic analysis of switching mutants. Cell. 1980;19: 845–854. doi:10.1016/0092-8674(80)90075-6

63. Bonifield HR, Hughes KT. Flagellar phase variation in Salmonella enterica is mediated by a posttranscriptional control mechanism. J Bacteriol. 2003;185: 3567–3574.

64. McQuiston JR, Fields PI, Tauxe RV, Logsdon Jr JM. Do Salmonella carry spare tyres? Trends Microbiol. 2008;16: 142–148. doi:10.1016/j.tim.2008.01.009

65. Gewirtz AT, Navas TA, Lyons S, Godowski PJ, Madara JL. Cutting edge: bacterial flagellin activates basolaterally expressed TLR5 to induce epithelial proinflammatory gene expression. J Immunol Baltim Md 1950. 2001;167: 1882–1885.

66. Zeng H, Carlson AQ, Guo Y, Yu Y, Collier-Hyams LS, Madara JL, et al. Flagellin is the major proinflammatory determinant of enteropathogenic Salmonella. J Immunol Baltim Md 1950. 2003;171: 3668–3674.

67. Sierro F, Dubois B, Coste A, Kaiserlian D, Kraehenbuhl JP, Sirard JC. Flagellin stimulation of intestinal epithelial cells triggers CCL20-mediated migration of dendritic cells. Proc Natl Acad Sci U S A. 2001;98: 13722–13727. doi:10.1073/pnas.241308598

68. Stecher B, Robbiani R, Walker AW, Westendorf AM, Barthel M, Kremer M, et al. Salmonella enterica serovar typhimurium exploits inflammation to compete with the intestinal microbiota. PLoS Biol. 2007;5: 2177–2189. doi:10.1371/journal.pbio.0050244

69. Dubochet J. Cryo-EM—the first thirty years. J Microsc. 2012;245: 221–224. doi:10.1111/j.1365-2818.2011.03569.x

70. Tivol WF, Briegel A, Jensen GJ. An Improved Cryogen for Plunge Freezing. Microsc Microanal Off J Microsc Soc Am Microbeam Anal Soc Microsc Soc Can. 2008;14: 375–379. doi:10.1017/S1431927608080781

71. Crowther RA, Klug A. ART and science or conditions for three-dimensional reconstruction from electron microscope images. J Theor Biol. 1971;32: 199–203.

72. Crowther RA, DeRosier DJ, Klug A. The Reconstruction of a Three-Dimensional Structure from Projections and its Application to Electron Microscopy. Proc R Soc Lond Math Phys Eng Sci. 1970;317: 319–340. doi:10.1098/rspa.1970.0119

73. De Rosier DJ, Klug A. Reconstruction of three dimensional structures from electron micrographs. Nature. 1968;217: 130–134.

74. Penczek PA. Fundamentals of three-dimensional reconstruction from projections. Methods Enzymol. 2010;482: 1–33. doi:10.1016/S0076-6879(10)82001-4

75. Henderson R. The potential and limitations of neutrons, electrons and X-rays for atomic resolution microscopy of unstained biological molecules. Q Rev Biophys. 1995;28: 171–193.

76. Stokes D., Owen G. An introduction to low dose electron tomography- from specimen preparation to data collection. Mod Res Educ Top Microsc. 2007; 939–950.

77. Fernández JJ, Li S, Crowther RA. CTF determination and correction in electron cryotomography. Ultramicroscopy. 2006;106: 587–596. doi:10.1016/j.ultramic.2006.02.004

78. Orlova EV, Saibil HR. Structural analysis of macromolecular assemblies by electron microscopy. Chem Rev. 2011;111: 7710–7748. doi:10.1021/cr100353t

79. Schröder RR, Hofmann W, Ménétret J-F. Zero-loss energy filtering as improved imaging mode in cryoelectronmicroscopy of frozen-hydrated specimens. J Struct Biol. 1990;105: 28–34. doi:10.1016/1047-8477(90)90095-T

80. Leapman RD, Kocsis E, Zhang G, Talbot TL, Laquerriere P. Three-dimensional distributions of elements in biological samples by energy-filtered electron tomography. Ultramicroscopy. 2004;100: 115–125. doi:10.1016/j.ultramic.2004.03.002

81. de Bruijn WC, Sorber CW, Gelsema ES, Beckers AL, Jongkind JF. Engery-filtering transmission electron microscopy of biological specimens. Scanning Microsc. 1993;7: 693–708; discussion 709.

82. Li X, Mooney P, Zheng S, Booth CR, Braunfeld MB, Gubbens S, et al. Electron counting and beam-induced motion correction enable near-atomic-resolution single-particle cryo-EM. Nat Methods. 2013;10: 584–590. doi:10.1038/nmeth.2472

83. Carragher B, Kisseberth N, Kriegman D, Milligan RA, Potter CS, Pulokas J, et al. Leginon: an automated system for acquisition of images from vitreous ice specimens. J Struct Biol. 2000;132: 33–45. doi:10.1006/jsbi.2000.4314

84. Mastronarde DN. Automated electron microscope tomography using robust prediction of specimen movements. J Struct Biol. 2005;152: 36–51. doi:10.1016/j.jsb.2005.07.007

85. Hagen WJH, Wan W, Briggs JAG. Implementation of a cryo-electron tomography tilt-scheme optimized for high resolution subtomogram averaging. J Struct Biol. 2017;197: 191–198. doi:10.1016/j.jsb.2016.06.007

86. Turoňová B, Schur FKM, Wan W, Briggs JAG. Efficient 3D-CTF correction for cryo-electron tomography using NovaCTF improves subtomogram averaging resolution to 3.4 Å. J Struct Biol. 2017;199: 187–195. doi:10.1016/j.jsb.2017.07.007

87. Noble AJ, Stagg SM. Automated batch fiducial-less tilt-series alignment in Appion using Protomo. J Struct Biol. 2015;192: 270–278. doi:10.1016/j.jsb.2015.10.003

88. Fernandez J-J, Laugks U, Schaffer M, Bäuerlein FJB, Khoshouei M, Baumeister W, et al. Removing Contamination-Induced Reconstruction Artifacts from Cryo-electron Tomograms. Biophys J. 2016;110: 850–859. doi:10.1016/j.bpj.2015.10.043

89. Kremer JR, Mastronarde DN, McIntosh JR. Computer visualization of three-dimensional image data using IMOD. J Struct Biol. 1996;116: 71–76. doi:10.1006/jsbi.1996.0013

90. Agulleiro JI, Fernandez JJ. Fast tomographic reconstruction on multicore computers. Bioinformatics. 2011;27: 582–583. doi:10.1093/bioinformatics/btq692

91. Castaño-Díez D. The Dynamo package for tomography and subtomogram averaging: components for MATLAB, GPU computing and EC2 Amazon Web Services. Acta Crystallogr Sect Struct Biol. 2017;73: 478–487. doi:10.1107/S2059798317003369

92. Rosenthal PB, Henderson R. Optimal determination of particle orientation, absolute hand, and contrast loss in single-particle electron cryomicroscopy. J Mol Biol. 2003;333: 721–745.

93. Briegel A, Ladinsky MS, Oikonomou C, Jones CW, Harris MJ, Fowler DJ, et al. Structure of bacterial cytoplasmic chemoreceptor arrays and implications for chemotactic signaling. eLife. 2014;3: e02151. doi:10.7554/eLife.02151

94. Frazer AC, Curtiss R. Production, properties and utility of bacterial minicells. Curr Top Microbiol Immunol. 1975;69: 1–84.

95. Adler HI, Fisher WD, Cohen A, Hardigree AA. MINIATURE escherichia coli CELLS DEFICIENT IN DNA. Proc Natl Acad Sci U S A. 1967;57: 321–326.

96. Xie L, Altindal T, Chattopadhyay S, Wu X-L. Bacterial flagellum as a propeller and as a rudder for efficient chemotaxis. Proc Natl Acad Sci. 2011;108: 2246–2251. doi:10.1073/pnas.1011953108

97. Kearns DB. A field guide to bacterial swarming motility. Nat Rev Microbiol. 2010;8: 634–644. doi:10.1038/nrmicro2405

98. Liu R, Ochman H. Origins of flagellar gene: Operons and secondary flagellar systems. J Bacteriol. 2007;189: 7098–7104. doi:10.1128/JB.00643-07

99. Woese CR. There must be a prokaryote somewhere: microbiology's search for itself. Microbiol Rev. 1994;58: 1–9.

100. Hug LA, Baker BJ, Anantharaman K, Brown CT, Probst AJ, Castelle CJ, et al. A new view of the tree of life. Nat Microbiol. 2016;1: 16048. doi:10.1038/nmicrobiol.2016.48

101. Woese CR, Kandler O, Wheelis ML. Towards a natural system of organisms: proposal for the domains Archaea, Bacteria, and Eucarya. Proc Natl Acad Sci U S A. 1990;87: 4576–4579.

102. Ochman H, Lawrence JG, Groisman EA. Lateral gene transfer and the nature of bacterial innovation. Nature. 2000;405: 299–304. doi:10.1038/35012500

103. Doolittle WF. Phylogenetic classification and the universal tree. Science. 1999;284: 2124–2129.

104. Hogeweg P, Hesper B. The alignment of sets of sequences and the construction of phyletic trees: an integrated method. J Mol Evol. 1984;20: 175–186.

105. Akerley BJ, Monack DM, Falkow S, Miller JF. The bvgAS locus negatively controls motility and synthesis of flagella in Bordetella bronchiseptica. J Bacteriol. 1992;174: 980–990.

106. Bubendorfer S, Held S, Windel N, Paulick A, Klingl A, Thormann KM. Specificity of motor components in the dual flagellar system of Shewanella putrefaciens CN-32. Mol Microbiol. 2012;83: 335–350. doi:10.1111/j.1365-2958.2011.07934.x

107. Bubendorfer S, Koltai M, Rossmann F, Sourjik V, Thormann KM. Secondary bacterial flagellar system improves bacterial spreading by increasing the directional persistence of swimming. Proc Natl Acad Sci. 2014;111: 11485–11490. doi:10.1073/pnas.1405820111

108. Kojima M, Kubo R, Yakushi T, Homma M, Kawagishi I. The bidirectional polar and unidirectional lateral flagellar motors of Vibrio alginolyticus are controlled by a single CheY species. Mol Microbiol. 2007;64: 57–67. doi:10.1111/j.1365-2958.2007.05623.x

109. Stocker R. Reverse and flick: Hybrid locomotion in bacteria. Proc Natl Acad Sci. 2011;108: 2635–2636. doi:10.1073/pnas.1019199108

110. Hu B, Lara-Tejero M, Kong Q, Galán JE, Liu J. In Situ Molecular Architecture of the Salmonella Type III Secretion Machine. Cell. 2017;168: 1065–1074.e10. doi:10.1016/j.cell.2017.02.022

111. Lee E, Helt GA, Reese JT, Munoz-Torres MC, Childers CP, Buels RM, et al. Web Apollo: a web-based genomic annotation editing platform. Genome Biol. 2013;14: R93. doi:10.1186/gb-2013-14-8-r93

112. Bradley RK, Roberts A, Smoot M, Juvekar S, Do J, Dewey C, et al. Fast Statistical Alignment. PLOS Comput Biol. 2009;5: e1000392. doi:10.1371/journal.pcbi.1000392

113. Notredame C, Higgins DG, Heringa J. T-Coffee: A novel method for fast and accurate multiple sequence alignment. J Mol Biol. 2000;302: 205–217. doi:10.1006/jmbi.2000.4042

114. Di Tommaso P, Moretti S, Xenarios I, Orobitg M, Montanyola A, Chang J-M, et al. T-Coffee: a web server for the multiple sequence alignment of protein and RNA sequences using structural information and homology extension. Nucleic Acids Res. 2011;39: W13–17. doi:10.1093/nar/gkr245

115. Gouy M, Guindon S, Gascuel O. SeaView version 4: A multiplatform graphical user interface for sequence alignment and phylogenetic tree building. Mol Biol Evol. 2010;27: 221–224. doi:10.1093/molbev/msp259

116. Bazinet AL, Zwickl DJ, Cummings MP. A gateway for phylogenetic analysis powered by grid computing featuring GARLI 2.0. Syst Biol. 2014;63: 812–818. doi:10.1093/sysbio/syu031

117. Jones DT, Taylor WR, Thornton JM. A Model Recognition Approach to the Prediction of All-Helical Membrane Protein Structure and Topology. Biochemistry (Mosc). 1994;33: 3038–3049. doi:10.1021/bi00176a037

118. SumTrees: Phylogenetic Tree Summarization and Annotation — DendroPy 4.4.0 documentation [Internet]. [cited 3 Apr 2019]. Available: https://dendropy.org/programs/sumtrees.html

119. FigTree [Internet]. [cited 2 Apr 2017]. Available: http://tree.bio.ed.ac.uk/software/figtree/

120. Grant T, Grigorieff N. Measuring the optimal exposure for single particle cryo-EM using a 2.6 Å reconstruction of rotavirus VP6. eLife. 2015;4: e06980. doi:10.7554/eLife.06980

121. Mastronarde DN. Dual-Axis Tomography: An Approach with Alignment Methods That Preserve Resolution. J Struct Biol. 1997;120: 343–352. doi:10.1006/jsbi.1997.3919

122. Agulleiro J-I, Fernandez J-J. Tomo3D 2.0 – Exploitation of Advanced Vector eXtensions (AVX) for 3D reconstruction. J Struct Biol. 2015;189: 147–152. doi:10.1016/j.jsb.2014.11.009

123. Lassak J, Henche A-L, Binnenkade L, Thormann KM. ArcS, the cognate sensor kinase in an atypical Arc system of Shewanella oneidensis MR-1. Appl Environ Microbiol. 2010;76: 3263–3274. doi:10.1128/AEM.00512-10

124. Ferreira JL, Gao FZ, Rossmann FM, Nans A, Brenzinger S, Hosseini R, et al. γ-proteobacteria eject their polar flagella under nutrient depletion, retaining flagellar motor relic structures. PLOS Biol. 2019;17: e3000165. doi:10.1371/journal.pbio.3000165

125. Magariyama Y, Sugiyama S, Muramoto K, Maekawa Y, Kawagishi I, Imae Y, et al. Very fast flagellar rotation. Nature. 1994;371: 752. doi:10.1038/371752b0

126. Chaban B, Coleman I, Beeby M. Evolution of higher torque in Campylobacter-type bacterial flagellar motors. Sci Rep. 2018;8: 97. doi:10.1038/s41598-017-18115-1

127. Zhu S, Nishikino T, Hu B, Kojima S, Homma M, Liu J. Molecular architecture of the sheathed polar flagellum in Vibrio alginolyticus. Proc Natl Acad Sci U S A. 2017;114: 10966–10971. doi:10.1073/pnas.1712489114

128. Boehm A, Kaiser M, Li H, Spangler C, Kasper CA, Ackermann M, et al. Second Messenger-Mediated Adjustment of Bacterial Swimming Velocity. Cell. 2010;141: 107–116. doi:10.1016/j.cell.2010.01.018

129. Paul K, Nieto V, Carlquist WC, Blair DF, Harshey RM. The c-di-GMP Binding Protein YcgR Controls Flagellar Motor Direction and Speed to Affect Chemotaxis by a "Backstop Brake" Mechanism. Mol Cell. 2010;38: 128–139. doi:10.1016/j.molcel.2010.03.001

130. Baker AE, Diepold A, Kuchma SL, Scott JE, Ha DG, Orazi G, et al. PilZ Domain Protein FlgZ Mediates Cyclic Di-GMP-Dependent Swarming Motility Control in Pseudomonas aeruginosa. J Bacteriol. 2016;198: 1837–1846. doi:10.1128/JB.00196-16

131. Pilizota T, Brown MT, Leake MC, Branch RW, Berry RM, Armitage JP. A molecular brake, not a clutch, stops the Rhodobacter sphaeroides flagellar motor. Proc Natl Acad Sci. 2009;106: 11582–11587. doi:10.1073/pnas.0813164106

132. Blair KM, Turner L, Winkelman JT, Berg HC, Kearns DB. A Molecular Clutch Disables Flagella in the Bacillus subtilis Biofilm. Science. 2008;320: 1636–1638. doi:10.1126/science.1157877

133. Goley ED, Iniesta AA, Shapiro L. Cell cycle regulation in Caulobacter: location, location, location. J Cell Sci. 2007;120: 3501–3507. doi:10.1242/jcs.005967

134. Aldridge P, Jenal U. Cell cycle-dependent degradation of a flagellar motor component requires a novel-type response regulator. Mol Microbiol. 1999;32: 379–391. doi:10.1046/j.1365-2958.1999.01358.x

135. Liu J, Zhu S, Nishikino T, Kojima S, Homma M. The Vibrio H-ring facilitates the outer membrane penetration of polar-sheathed flagellum. bioRxiv. 2018; 358820. doi:10.1101/358820

136. Guttenplan SB, Shaw S, Kearns DB. The cell biology of peritrichous flagella in Bacillus subtilis. Mol Microbiol. 2013;87: 211–229. doi:10.1111/mmi.12103

137. Brown PJB, Hardy GG, Trimble MJ, Brun YV. Complex regulatory pathways coordinate cell cycle progression and development in Caulobacter crescentus. Adv Microb Physiol. 2009;54: 1–101. doi:10.1016/S0065-2911(08)00001-5

138. Kusumoto A, Shinohara A, Terashima H, Kojima S, Yakushi T, Homma M. Collaboration of FlhF and FlhG to regulate polar-flagella number and localization in Vibrio alginolyticus. Microbiol Read Engl. 2008;154: 1390–1399. doi:10.1099/mic.0.2007/012641-0

139. Marsh JA, Hernández H, Hall Z, Ahnert SE, Perica T, Robinson CV, et al. Protein Complexes Are under Evolutionary Selection to Assemble via Ordered Pathways. Cell. 2013;153: 461–470. doi:10.1016/j.cell.2013.02.044

140. Wells JN, Bergendahl LT, Marsh JA. Operon Gene Order Is Optimized for Ordered Protein Complex Assembly. Cell Rep. 2016;14: 679–685. doi:10.1016/j.celrep.2015.12.085

141. Kubori T, Shimamoto N, Yamaguchi S, Namba K, Aizawa S-I. Morphological pathway of flagellar assembly in Salmonella typhimurium. J Mol Biol. 1992;226: 433–446. doi:10.1016/0022-2836(92)90958-M

142. Chevance FFV, Takahashi N, Karlinsey JE, Gnerer J, Hirano T, Samudrala R, et al. The mechanism of outer membrane penetration by the eubacterial flagellum and implications for spirochete evolution. Genes Dev. 2007;21: 2326–2335. doi:10.1101/gad.1571607

143. Fujii T, Kato T, Hiraoka KD, Miyata T, Minamino T, Chevance FFV, et al. Identical folds used for distinct mechanical functions of the bacterial flagellar rod and hook. Nat Commun. 2017;8: 14276. doi:10.1038/ncomms14276

144. Hu J, Worrall LJ, Hong C, Vuckovic M, Atkinson CE, Caveney N, et al. Cryo-EM analysis of the T3S injectisome reveals the structure of the needle and open secretin. Nat Commun. 2018;9: 3840. doi:10.1038/s41467-018-06298-8

145. Jenal U. Signal transduction mechanisms in Caulobacter crescentus development and cell cycle control. FEMS Microbiol Rev. 2000;24: 177–191. doi:10.1111/j.1574-6976.2000.tb00538.x

146. Jacob F. Evolution and tinkering. Science. 1977;196: 1161–1166. doi:10.1126/science.860134

147. Liu Z, Miyashiro T, Tsou A, Hsiao A, Goulian M, Zhu J. Mucosal penetration primes Vibrio cholerae for host colonization by repressing quorum sensing. Proc Natl Acad Sci U S A. 2008;105: 9769–9774. doi:10.1073/pnas.0802241105

148. Ruby EG, Asato LM. Growth and flagellation of Vibrio fischeri during initiation of the sepiolid squid light organ symbiosis. Arch Microbiol. 1993;159: 160–167. doi:10.1007/BF00250277

149. Paradis G, Chevance FFV, Liou W, Renault TT, Hughes KT, Rainville S, et al. Variability in bacterial flagella re-growth patterns after breakage. Sci Rep. 2017;7: 1282. doi:10.1038/s41598-017-01302-5

150. Grassi L, Di Luca M, Maisetta G, Rinaldi AC, Esin S, Trampuz A, et al. Generation of Persister Cells of Pseudomonas aeruginosa and Staphylococcus aureus by Chemical Treatment and Evaluation of Their Susceptibility to Membrane-Targeting Agents. Front Microbiol. 2017;8: 1917. doi:10.3389/fmicb.2017.01917

151. Fredrickson JK, Zachara JM, Kennedy DW, Dong H, Onstott TC, Hinman NW, et al. Biogenic iron mineralization accompanying the dissimilatory reduction of hydrous ferric oxide by a groundwater bacterium. Geochim Cosmochim Acta. 1998;62: 3239–3257. doi:10.1016/S0016-7037(98)00243-9

152. Rossmann F, Brenzinger S, Knauer C, Dörrich AK, Bubendorfer S, Ruppert U, et al. The role of FlhF and HubP as polar landmark proteins in Shewanella putrefaciens CN-32. Mol Microbiol. 2015;98: 727–742. doi:10.1111/mmi.13152

153. Schindelin J, Arganda-Carreras I, Frise E, Kaynig V, Longair M, Pietzsch T, et al. Fiji: an open-source platform for biological-image analysis. Nat Methods. 2012;9: 676–682. doi:10.1038/nmeth.2019

154. de la Rosa-Trevín JM, Quintana A, Del Cano L, Zaldívar A, Foche I, Gutiérrez J, et al. Scipion: A software framework toward integration, reproducibility and validation in 3D electron microscopy. J Struct Biol. 2016;195: 93–99. doi:10.1016/j.jsb.2016.04.010

155. Abrishami V, Zaldívar-Peraza A, de la Rosa-Trevín JM, Vargas J, Otón J, Marabini R, et al. A pattern matching approach to the automatic selection of particles from low-contrast electron micrographs. Bioinforma Oxf Engl. 2013;29: 2460–2468. doi:10.1093/bioinformatics/btt429

156. Scheres SHW. RELION: implementation of a Bayesian approach to cryo-EM structure determination. J Struct Biol. 2012;180: 519–530. doi:10.1016/j.jsb.2012.09.006

157. Amat F, Moussavi F, Comolli LR, Elidan G, Downing KH, Horowitz M. Markov random field based automatic image alignment for electron tomography. J Struct Biol. 2008;161: 260–275. doi:10.1016/j.jsb.2007.07.007

158. Clark PJ, Evans FC. Distance to Nearest Neighbor as a Measure of Spatial Relationships in Populations. Ecology. 1954;35: 445–453. doi:10.2307/1931034

159. Kojima S, Imada K, Sakuma M, Sudo Y, Kojima C, Minamino T, et al. Stator assembly and activation mechanism of the flagellar motor by the periplasmic region of MotB. Mol Microbiol. 2009;73: 710–718. doi:10.1111/j.1365-2958.2009.06802.x

160. Glagolev AN, Skulachev VP. The proton pump is a molecular engine of motile bacteria. Nature. 1978;272: 280–282.

161. Larsen SH, Adler J, Gargus JJ, Hogg RW. Chemomechanical Coupling without ATP: The Source of Energy for Motility and Chemotaxis in Bacteria. Proc Natl Acad Sci U S A. 1974;71: 1239–1243.

162. Manson MD, Tedesco P, Berg HC, Harold FM, Van der Drift C. A protonmotive force drives bacterial flagella. Proc Natl Acad Sci U S A. 1977;74: 3060–3064.

163. Kojima S, Blair DF. Conformational change in the stator of the bacterial flagellar motor. Biochemistry (Mosc). 2001;40: 13041–13050.

164. Zhou J, Sharp LL, Tang HL, Lloyd SA, Billings S, Braun TF, et al. Function of Protonatable Residues in the Flagellar Motor of Escherichia coli: a Critical Role for Asp 32 of MotB. J Bacteriol. 1998;180: 2729–2735.

165. Kim EA, Price-Carter M, Carlquist WC, Blair DF. Membrane Segment Organization in the Stator Complex of the Flagellar Motor: Implications for Proton Flow and Proton-Induced Conformational Change. Biochemistry (Mosc). 2008;47: 11332–11339. doi:10.1021/bi801347a

166. Nishihara Y, Kitao A. Gate-controlled proton diffusion and protonation-induced ratchet motion in the stator of the bacterial flagellar motor. Proc Natl Acad Sci U S A. 2015;112: 7737–7742. doi:10.1073/pnas.1502991112

167. Blair DF, Berg HC. Restoration of torque in defective flagellar motors. Science. 1988;242: 1678–1681. doi:10.1126/science.2849208

168. Sm B, Hc B. Successive incorporation of force-generating units in the bacterial rotary motor. Nature. 1984;309: 470–472. doi:10.1038/309470a0

169. Reid SW, Leake MC, Chandler JH, Lo C-J, Armitage JP, Berry RM. The maximum number of torque-generating units in the flagellar motor of Escherichia coli is at least 11. Proc Natl Acad Sci U S A. 2006;103: 8066–8071. doi:10.1073/pnas.0509932103

170. Stolz B, Berg HC. Evidence for interactions between MotA and MotB, torque-generating elements of the flagellar motor of Escherichia coli. J Bacteriol. 1991;173: 7033–7037.

171. Hosking ER, Vogt C, Bakker EP, Manson MD. The Escherichia coli MotAB Proton Channel Unplugged. J Mol Biol. 2006;364: 921–937. doi:10.1016/j.jmb.2006.09.035

172. Leake MC, Chandler JH, Wadhams GH, Bai F, Berry RM, Armitage JP. Stoichiometry and turnover in single, functioning membrane protein complexes. Nature. 2006;443: 355–358. doi:10.1038/nature05135

173. Khan S, Dapice M, Reese TS. Effects of mot gene expression on the structure of the flagellar motor. J Mol Biol. 1988;202: 575–584. doi:10.1016/0022-2836(88)90287-2

174. Paulick A, Delalez NJ, Brenzinger S, Steel BC, Berry RM, Armitage JP, et al. Dual stator dynamics in the Shewanella oneidensis MR-1 flagellar motor. Mol Microbiol. 2015;96: 993–1001. doi:10.1111/mmi.12984

175. Jenal U, White J, Shapiro L. Caulobacter flagellar function, but not assembly, requires FliL, a non-polarly localized membrane protein present in all cell types. J Mol Biol. 1994;243: 227–244. doi:10.1006/jmbi.1994.1650

176. Suaste-Olmos F, Domenzain C, Mireles-Rodríguez JC, Poggio S, Osorio A, Dreyfus G, et al. The Flagellar Protein FliL Is Essential for Swimming in Rhodobacter sphaeroides. J Bacteriol. 2010;192: 6230–6239. doi:10.1128/JB.00655-10

177. Attmannspacher U, Scharf BE, Harshey RM. FliL is essential for swarming: motor rotation in absence of FliL fractures the flagellar rod in swarmer cells of Salmonella enterica. Mol Microbiol. 2008;68: 328–341. doi:10.1111/j.1365-2958.2008.06170.x

178. Cusick K, Lee Y-Y, Youchak B, Belas R. Perturbation of FliL Interferes with Proteus mirabilis Swarmer Cell Gene Expression and Differentiation. J Bacteriol. 2012;194: 437–447. doi:10.1128/JB.05998-11

179. Motaleb MA, Pitzer JE, Sultan SZ, Liu J. A Novel Gene Inactivation System Reveals Altered Periplasmic Flagellar Orientation in a Borrelia burgdorferi fliL Mutant▽. J Bacteriol. 2011;193: 3324–3331. doi:10.1128/JB.00202-11

180. Christen M, Christen B, Allan MG, Folcher M, Jenö P, Grzesiek S, et al. DgrA is a member of a new family of cyclic diguanosine monophosphate receptors and controls flagellar motor function in Caulobacter crescentus. Proc Natl Acad Sci. 2007;104: 4112–4117. doi:10.1073/pnas.0607738104

181. Partridge JD, Nieto V, Harshey RM. A new player at the flagellar motor: FliL controls both motor output and bias. mBio. 2015;6: e02367. doi:10.1128/mBio.02367-14

182. Chawla R, Ford KM, Lele PP. Torque, but not FliL, regulates mechanosensitive flagellar motor-function. Sci Rep. 2017;7: 5565. doi:10.1038/s41598-017-05521-8

183. Yao Z, Davis RM, Kishony R, Kahne D, Ruiz N. Regulation of cell size in response to nutrient availability by fatty acid biosynthesis in Escherichia coli. Proc Natl Acad Sci U S A. 2012;109: E2561–2568. doi:10.1073/pnas.1209742109

184. Vadia S, Tse JL, Lucena R, Yang Z, Kellogg DR, Wang JD, et al. Fatty Acid Availability Sets Cell Envelope Capacity and Dictates Microbial Cell Size. Curr Biol. 2017;27: 1757–1767.e5. doi:10.1016/j.cub.2017.05.076

185. Lai C-Y, Cronan JE. Beta-ketoacyl-acyl carrier protein synthase III (FabH) is essential for bacterial fatty acid synthesis. J Biol Chem. 2003;278: 51494–51503. doi:10.1074/jbc.M308638200

186. Kojima S, Blair DF. Solubilization and Purification of the MotA/MotB Complex of Escherichia coli. Biochemistry (Mosc). 2004;43: 26–34. doi:10.1021/bi0354051

187. Postis V, Rawson S, Mitchell JK, Lee SC, Parslow RA, Dafforn TR, et al. The use of SMALPs as a novel membrane protein scaffold for structure study by negative stain electron microscopy. Biochim Biophys Acta BBA - Biomembr. 2015;1848: 496–501. doi:10.1016/j.bbamem.2014.10.018

188. Grant T, Rohou A, Grigorieff N. cisTEM, user-friendly software for single-particle image processing. Egelman EH, editor. eLife. 2018;7: e35383. doi:10.7554/eLife.35383

189. Rohou A, Grigorieff N. CTFFIND4: Fast and accurate defocus estimation from electron micrographs. J Struct Biol. 2015;192: 216–221. doi:10.1016/j.jsb.2015.08.008

190. Asmar AT, Ferreira JL, Cohen EJ, Cho S-H, Beeby M, Hughes KT, et al. Communication across the bacterial cell envelope depends on the size of the periplasm. PLOS Biol. 2017;15: e2004303. doi:10.1371/journal.pbio.2004303

191. Silhavy TJ, Kahne D, Walker S. The Bacterial Cell Envelope. Cold Spring Harb Perspect Biol. 2010;2. doi:10.1101/cshperspect.a000414

192. Vollmer W, Blanot D, de Pedro MA. Peptidoglycan structure and architecture. FEMS Microbiol Rev. 2008;32: 149–167. doi:10.1111/j.1574-6976.2007.00094.x

193. Raetz CRH, Whitfield C. Lipopolysaccharide endotoxins. Annu Rev Biochem. 2002;71: 635–700. doi:10.1146/annurev.biochem.71.110601.135414

194. Nikaido H. Molecular Basis of Bacterial Outer Membrane Permeability Revisited. Microbiol Mol Biol Rev. 2003;67: 593–656. doi:10.1128/MMBR.67.4.593-656.2003

195. Erhardt M, Hirano T, Su Y, Paul K, Wee DH, Mizuno S, et al. The Role of the FliK Molecular Ruler in Hook-length Control in Salmonella enterica. Mol Microbiol. 2010;75: 1272–1284. doi:10.1111/j.1365-2958.2010.07050.x

196. Hirano T, Mizuno S, Aizawa S-I, Hughes KT. Mutations in Flk, FlgG, FlhA, and FlhE That Affect the Flagellar Type III Secretion Specificity Switch in Salmonella enterica. J Bacteriol. 2009;191: 3938–3949. doi:10.1128/JB.01811-08

197. Braun V. Covalent lipoprotein from the outer membrane of escherichia coli - ScienceDirect. Biochim Biophys Acta BBA - Biomembr. 1975;415: 335–377.

198. Li G-W, Burkhardt D, Gross C, Weissman JS. Quantifying absolute protein synthesis rates reveals principles underlying allocation of cellular resources. Cell. 2014;157: 624–635. doi:10.1016/j.cell.2014.02.033

199. Inouye M, Shaw J, Shen C. The assembly of a structural lipoprotein in the envelope of Escherichia coli. J Biol Chem. 1972;247: 8154–8159.

200. Cowles CE, Li Y, Semmelhack MF, Cristea IM, Silhavy TJ. The free and bound forms of Lpp occupy distinct subcellular locations in Escherichia coli. Mol Microbiol. 2011;79: 1168–1181. doi:10.1111/j.1365-2958.2011.07539.x

201. Liu J, Cao W, Lu M. Core side-chain packing and backbone conformation in Lpp-56 coiled-coil mutants. J Mol Biol. 2002;318: 877–888. doi:10.1016/S0022-2836(02)00138-9

202. Shu W, Liu J, Ji H, Lu M. Core structure of the outer membrane lipoprotein from Escherichia coli at 1.9 å resolution1. J Mol Biol. 2000;299: 1101–1112. doi:10.1006/jmbi.2000.3776

203. Ferrières L, Clarke DJ. The RcsC sensor kinase is required for normal biofilm formation in Escherichia coli K-12 and controls the expression of a regulon in response to growth on a solid surface. Mol Microbiol. 2003;50: 1665–1682.

204. Majdalani N, Gottesman S. THE RCS PHOSPHORELAY: A Complex Signal Transduction System. Annu Rev Microbiol. 2005;59: 379–405. doi:10.1146/annurev.micro.59.050405.101230

205. Farris C, Sanowar S, Bader MW, Pfuetzner R, Miller SI. Antimicrobial peptides activate the Rcs regulon through the outer membrane lipoprotein RcsF. J Bacteriol. 2010;192: 4894–4903. doi:10.1128/JB.00505-10

206. Laubacher ME, Ades SE. The Rcs phosphorelay is a cell envelope stress response activated by peptidoglycan stress and contributes to intrinsic antibiotic resistance. J Bacteriol. 2008;190: 2065–2074. doi:10.1128/JB.01740-07

207. Sato T, Takano A, Hori N, Izawa T, Eda T, Sato K, et al. Role of the inner-membrane histidine kinase RcsC and outer-membrane lipoprotein RcsF in the activation of the Rcs phosphorelay signal transduction system in Escherichia coli. Microbiol Read Engl. 2017;163: 1071–1080. doi:10.1099/mic.0.000483

208. Cornelis GR. The type III secretion injectisome. Nat Rev Microbiol. 2006;4: 811–825. doi:10.1038/nrmicro1526

209. Park JS, Lee WC, Yeo KJ, Ryu K-S, Kumarasiri M, Hesek D, et al. Mechanism of anchoring of OmpA protein to the cell wall peptidoglycan of the gram-negative bacterial outer membrane. FASEB J Off Publ Fed Am Soc Exp Biol. 2012;26: 219–228. doi:10.1096/fj.11-188425

210. Lloubès R, Cascales E, Walburger A, Bouveret E, Lazdunski C, Bernadac A, et al. The Tol-Pal proteins of the Escherichia coli cell envelope: an energized system required for outer membrane integrity? Res Microbiol. 2001;152: 523–529. doi:10.1016/S0923-2508(01)01226-8

211. Bean GJ, Flickinger ST, Westler WM, McCully ME, Sept D, Weibel DB, et al. A22 disrupts the bacterial actin cytoskeleton by directly binding and inducing a low-affinity state in MreB. Biochemistry (Mosc). 2009;48: 4852–4857. doi:10.1021/bi900014d

212. Spratt BG. The mechanism of action of mecillinam. J Antimicrob Chemother. 1977;3: 13–19. doi:10.1093/jac/3.suppl_B.13

213. Castanié-Cornet M-P, Cam K, Jacq A. RcsF Is an Outer Membrane Lipoprotein Involved in the RcsCDB Phosphorelay Signaling Pathway in Escherichia coli. J Bacteriol. 2006;188: 4264–4270. doi:10.1128/JB.00004-06

214. Bohin J-P. Osmoregulated periplasmic glucans in Proteobacteria. FEMS Microbiol Lett. 2000;186: 11–19. doi:10.1111/j.1574-6968.2000.tb09075.x

215. Leverrier P, Declercq J-P, Denoncin K, Vertommen D, Hiniker A, Cho S-H, et al. Crystal structure of the outer membrane protein RcsF, a new substrate for the periplasmic protein-disulfide isomerase DsbC. J Biol Chem. 2011;286: 16734–16742. doi:10.1074/jbc.M111.224865

216. Rogov VV, Rogova NY, Bernhard F, Löhr F, Dötsch V. A disulfide bridge network within the soluble periplasmic domain determines structure and function of the outer membrane protein RCSF. J Biol Chem. 2011;286: 18775–18783. doi:10.1074/jbc.M111.230185

217. Stock JB, Rauch B, Roseman S. Periplasmic space in Salmonella typhimurium and Escherichia coli. J Biol Chem. 1977;252: 7850–7861.

218. Glauner B, Höltje JV, Schwarz U. The composition of the murein of Escherichia coli. J Biol Chem. 1988;263: 10088–10095.

219. Keeling PJ. The endosymbiotic origin, diversification and fate of plastids. Philos Trans R Soc Lond B Biol Sci. 2010;365: 729–748. doi:10.1098/rstb.2009.0103

220. Cho S-H, Szewczyk J, Pesavento C, Zietek M, Banzhaf M, Roszczenko P, et al. Detecting envelope stress by monitoring β-barrel assembly. Cell. 2014;159: 1652–1664. doi:10.1016/j.cell.2014.11.045

221. Gil D, Bouché JP. ColE1-type vectors with fully repressible replication. Gene. 1991;105: 17–22.

222. Datsenko KA, Wanner BL. One-step inactivation of chromosomal genes in Escherichia coli K-12 using PCR products. Proc Natl Acad Sci U S A. 2000;97: 6640–6645. doi:10.1073/pnas.120163297

223. Aizawa SI, Dean GE, Jones CJ, Macnab RM, Yamaguchi S. Purification and characterization of the flagellar hook-basal body complex of Salmonella typhimurium. J Bacteriol. 1985;161: 836–849.

224. Marko M, Hsieh C, Moberlychan W, Mannella CA, Frank J. Focused ion beam milling of vitreous water: prospects for an alternative to cryo-ultramicrotomy of frozen-hydrated biological samples. J Microsc. 2006;222: 42–47. doi:10.1111/j.1365-2818.2006.01567.x

225. Guerrero-Ferreira RC, Wright ER. Cryo-electron tomography of bacterial viruses. Virology. 2013;435: 179–186. doi:10.1016/j.virol.2012.08.022

226. Fukuda Y, Laugks U, Lučić V, Baumeister W, Danev R. Electron cryotomography of vitrified cells with a Volta phase plate. J Struct Biol. 2015;190: 143–154. doi:10.1016/j.jsb.2015.03.004

227. Chreifi G, Chen S, Metskas LA, Kaplan M, Jensen GJ. Rapid Tilt-Series Acquisition for Electron Cryotomography. bioRxiv. 2018; 454587. doi:10.1101/454587

Appendix 1: Custom script for periplasmic width

```
#!/usr/bin/python
#
# getPeriplasmWidth.py
#
# Takes a model file with pairs of contours (first of pair is
# inner membrane, second is outer membrane), and returns periplasm
# diameters.

import sys
sys.path.append("/beebylab/tomography_db/bin")
import os
import math
import imod
import re
import automation
from optparse import OptionParser

def getPeriplasmWidth(model):
    output = []
    for count in range(model.max.z):
        output.append([])
    objectCount = 0
    if model.units != "nm":
        sys.stderr.write("ERROR: Model units not in nm! (are in "+model.units+"!)\n")
        sys.exit(1)

    for object in model.objects:
        if len(object.contours) % 2 == 1:
            sys.stderr.write("ERROR! Odd number of contours
("+str(len(object.contours))+") in object #"+str(objectCount)+"\n")
            sys.exit(1)
        for contourCount in range(0,len(object.contours),2):
            IM = contourCount
            OM = contourCount + 1

            # Loop through all points in IM, and for each find closest point in OM
            for IMpoint in object.contours[IM].points:
                minDist = -1
                for OMpoint in object.contours[OM].points:
                    dist = (imod.distance(IMpoint,OMpoint)) * model.pixsize
                    if (minDist == -1) or (dist < minDist):
                        minDist = dist
```

```
            finalDist = "{:.1f}".format(minDist)
            output[int(IMpoint.z)].append(finalDist)
        objectCount += 1

    max = 0
    for column in output:
        if len(column)> max:
            max = len(column)

    for row in range(max):
        line = []
        for column in output:
            if row >= len(column):
                line.append("")
            else:
                line.append(column[row])
        sys.stdout.write(",".join(line)+"\n")

def main():
    parser = OptionParser("usage: %prog <model file>")
    parser.add_option("-i", "--interval", action="store", type="float", dest="interval",
default=0.5, help="Interval resampled along contour using addModPts")
    (options,args) = parser.parse_args()

    if len(args) != 1:
        parser.error("Incorrect number of arguments! ("+str(len(args))+": "+",
".join(args)+")")
    modelFile  = args[0]

    model      = imod.modelClass()
    automation.execute(["addModPts", modelFile, str(options.interval)], verbose=0)
    (base,ext) = os.path.splitext(modelFile)
    newModel   = base+"_PtsAdded.mod"
    model.load(newModel)
    getPeriplasmWidth(model)
    automation.execute(["rm", newModel], verbose=0)

main()
```

Appendix 2: Permissions to reprint figures

Fig no.	Type of work	Name of work	Source of work	Copyright holder	permission requested on	I have permission yes /no	Permission note
5.2, 5.7, 5.8, 5.10, 5.11	Figure	Adapted Fig 2 and figures from supplemental data	Cohen EJ, Ferreira JL, Ladinsky MS, et al., *(2017) Nanoscale-length control of the flagellar driveshaft requires hitting the tethered outer membrane. Science 356, 197–200 [27]*	The American Association for the Advancement of Science	09/04/2019	yes	Written permission
1.4	Figure	Adapted Fig 1	Ferreira JL, Matthews-Palmer TRS, Beeby M. Electron Cryo-Tomography. Cellular Imaging. Springer, Cham; 2018. pp. 61–94.	Springer Nature	09/04/2019	yes	Written permission
1.7c	Figure	Fig 9	Orlova EV, Saibil HR. Structural analysis of macromolecular assemblies by electron microscopy. Chem Rev. 2011;111: 7710–7748. doi:10.1021/cr100353t Link: https://pubs.acs.org/doi/10.1021/cr100353t	ACS	09/04/2019	yes	Written permission
4.2b	Figure	Fig 2	Nirody JA, Berry RM, Oster G. The Limiting Speed of the Bacterial Flagellar Motor. Biophys J. 2016;111: 557–564.doi:10.1016/j.bpj.2016.07.003	Elsevier	09/04/2019	yes	Written permission
4.2d	Figure	Fig 4	Khan S, Dapice M, Reese TS. Effects of mot gene expression on the structure of the flagellar motor. J Mol Biol. 1988;202: 575–584. Doi:10.1016/0022-2836(88)90287-2	Elsevier	09/04/2019	yes	Written permission
Fig 4.4	Figure	Fig 4	Motaleb MA, Pitzer JE, Sultan SZ, Liu J. A Novel Gene Inactivation System Reveals Altered Periplasmic Flagellar Orientation in a Borrelia burgdorferi fliL Mutant▽. J Bacteriol. 2011;193: 3324–3331. doi:10.1128/JB.00202-11	Elsevier	09/04/2019	yes	Written permission

All further permissions related to the material listed above should be directed to the copyright holder